WETLAND EROSION IN GALVESTON BAY BY OCEAN WAVES

A Dissertation

by

JIN YOUNG KIM

Submitted to the Office of Graduate and Professional Studies of
Texas A&M University
in partial fulfillment of the requirements for the degree of

DOCTOR OF PHILOSOPHY

Chair of Committee,	James M. Kaihatu
Co-Chair of Committee,	Kuang-An Chang
Committee Members,	Russell A. Feagin
	Jens Figlus
Head of Department,	Robin Autenrieth

May 2021

Major Subject: Civil Engineering

ABSTRACT

Wave energy has been identified as a major cause of wetland edge erosion in general. This dissertation focuses on the numerical modeling of wind-wave and sediment transport affecting erosion and accretion of salt marsh edges and experimental investigations on the relationship between wave and salt marsh edge erosion.

First, the physical aspect of cold front-induced waves on salt-marsh erosion was investigated. We modeled changes in water level and wave conditions during the passage of cold fronts on Galveston Island, Texas. We found that wind gusts and abrupt direction shifts produced high energy wave events, propagated toward the wetland edge during the simulation period. Field measurements agreed with the modeled predictions in terms of both tidal water level and significant wave heights. We also calculated the wave power during the entire measurement period and found that cold front-induced waves significantly increased the potential erosion of salt marsh edges.

Second, a laboratory experiment investigated the resistance of the salt marsh to wave energy. Wave properties affecting salt marsh core samples were investigated. The wave power of the input waves was calculated based on spectrum analysis. Then the relationship between wave power and erosion rate was discussed based on dimensional analysis. As the input wave height increased, erosion generally increased, and more erosion was found in the portion of the samples where the wave breaking was frequent.

Third, surveys using Unmanned Aerial Vehicle (UAV) were conducted to identify salt marsh boundary erosion and potential wind-wave vulnerability. Using UAV images

and Global Navigation Satellite System receivers, the wetland areas located on the bay side of Galveston Bay were photographed over a year to observe the change in the boundary. Erosion rates have been calculated for several wetlands on Galveston Island. An average of 0.76 m of lateral erosion was recorded over the measurement period. Through the wave simulation during this period, the relationship between wave energy and erosion rate was derived.

Lastly, sediment transport and processes along the wetland edge were investigated based on the large scale and detailed model. Sediment fluxes along the Galveston Bay entrance and West Bay area were quantified during the cold front passages. Erosion and accretion along the salt marsh boundary by tides, currents, and waves were investigated. In the relative sea level rise simulation model, it was found that the wetland edge region had the ability to adapt to a relatively high sea level, not lowering their platform level significantly.

DEDICATION

With Love and Respect,
To My Parents, Wife, Son, and parents-in-law

ACKNOWLEDGEMENTS

I could not fulfill this study without the support and encouragement of many people. I would like to express my deep gratitude to my advisors and mentors, Dr. James Kaihatu and Dr. Kuang-An Chang, for continuous financial support and advice on this course of research and all aspects of an academic career. I am very grateful to Dr. Chang and Dr. Kaihatu for being patient and giving me countless guidance. And I would like to thank my committee members, Dr. Feagin and Dr. Figlus, for their guidance and support throughout this research. Dr. Feagin made me interested in salt marsh research and always kindly answered related questions. Dr. Figlus gave me good comments relate to my research. Thanks also go to the department faculty and staff for making my time at Texas A&M University a great experience. I would like to thank Dr. Won-Hyun Lee as a former office mate for letting me know about simulation input methodology. I also would like to thank Mr. Jaewon Kim for helping me during my Ph.D. studies, especially for drone research. I am grateful to Shih-heng Sun and Dr. Thomas P. Huff, who let me participate in the lab and drone experiments. Thank you Dr. Wei-Liang Chuang, Inchul Kim and Shin-yu Huang for working with me. I sincerely appreciate all of my friends and lab mates.

Finally, I am grateful to my parents, parents-in-law, wife, and son, who supported me and encouraged me when times got tough.

CONTRIBUTORS AND FUNDING SOURCES

Contributors

This work was supervised by a dissertation committee consisting of Dr. James Kaihatu (chair), Kuang-An Chang (co-chair) of the Department of Civil Engineering, Dr. Russell A. Feagin of the Department of Ecology and Conservation Biology, and Dr. Jens Figlus of the Department of Ocean Engineering. Chapter 2 work was supported by Dr. Russell A. Feagin and Dr. Thomas P. Huff of the Department of Ecology and Conservation Biology at Texas A& M University. They performed an on-site measurement and collected water level and wave data. The work of Chapter 3 was supported by Chair and Co-Chair, and Dr. Russell A. Feagin. We together performed wetland core samples extraction and laboratory settings. Dr. Feagin's group performed a LiDAR analysis for erosion calculation. All other chapter works conducted for the dissertation was completed by the student independently.

Funding Sources

This research was supported by the Texas Sea Grant College Program, National Oceanic and Atmospheric Administration via the project entitled “Study of Wetland Erosion due to Storms through Combined Field, Laboratory, and Numerical Investigations.” The Texas General Land Office partially supported this research via the project entitled “Developing UAV and Satellite Tools for Ocean Currents and Oil Transport.” Part of the graduate study was supported by American Bureau of Shipping Scholarship (ABS), and Dr. Chester P. Jelesnianski Memorial Fellowship.

TABLE OF CONTENTS

Page

LIST OF FIGURES

Page

LIST OF TABLES

Page

1. INTRODUCTION

1.1. Motivations and objectives

The interaction between the earth's surface and the ocean has been the subject of active research in many disciplines such as oceanography, geology, hydrology, ecology, and coastal engineering. Processes of mass, momentum, and energy transfer between the earth's surface and the ocean are shown to have a significant impact on the land boundary. The land boundary where oceans meet the land is referred to as the nearshore, which includes the intertidal zone, the subtidal zone, and the backshore zone. These coastal zones maintain essential ecosystem services in coastal protection, fisheries and other living resources, rich agricultural lands, high aesthetic value areas, and are typically held as a public resource connecting land and sea. The coastal area is also regarded as the most endangered social ecosystem on the planet (Ramesh et al., 2015).

The saltmarsh wetlands are one of the important ecosystems in the nearshore. Salt marshes are flat lands covered mainly by halophytic vegetation. They are found in warm to cool latitudes (Duarte et al., 2008). They are periodically flooded by the sea due to tides (Allen, 2000). Marsh vegetation has a potential role in inland protections as a barrier from the attenuating waves.

However, their sustainability is now threatened by human interference such as global sea level rise and land subsidence. According to a study based on 25 years of NASA and European satellite data, global sea-level rise is accelerating over time rather than increasing at a steady rate (Nerem et al., 2018). As this trend continues, salt marshes located in shallow bays are under increasing threat.

Here, the overarching research question is as follows: What are the hydrodynamic causes of wetland erosion, and what will happen in the near future?

Understanding the processes driving the salt marsh erosion and its future trajectory is necessary to manage and protect the salt marshes. Thus, both observations and models for these processes are essential to understand the processes of erosion. However, observations and models have provided inconsistent answers to these questions, likely in part because of comparisons among sites and/or models that differ significantly in their characteristics and processes (Wiberg et al., 2020). Therefore, improved hydrodynamic and morphological predictive skill of a numerical model is key to understanding the interaction between salt marshes and oceans.

Wind-induced waves propagating toward salt marsh boundaries are considered to be a major cause of lateral wetland erosion. It is imperative to accurately model the waves and hydrodynamics at the shallow bays to verify the processes. Observing the erosion by remote sensing can also play a key role in further understanding the process. The processes of sediment transport, especially suspended sediment concentration, is a critical factor that greatly influences whether wetlands survive or diminish (Kirwan et al., 2010).

Even though the cause and process of salt marsh erosion have been studied for decades, many questions remain. What is the effect of wind and tides on the wetland erosion process in the field? How does wave energy play a role in salt marsh lateral erosion? What kind of weather conditions can accelerate salt marsh edge erosion? How do salt marshes respond to relative sea level rise?

This dissertation investigated cold front or winter storm induced wave energy and sediment transport affecting salt marsh edge lateral erosion based on the above questions. Moreover, field measurements using UAV were done to verify the above questions. A large scale hydrodynamic model combining with a high-resolution wetlands model was used to understand better the impact of wind-induced waves and sediment transport in shallow bays affecting salt marsh boundaries. In addition, a laboratory experiment was done to test the wave vulnerability of the salt marsh edge. Observations of the natural salt marsh areas using Unmanned Aerial Vehicle were done to verify the wind waves induced erosion.

To summarize, the goals of this dissertation are as follows: 1) to verify the impact of wind-induced waves on salt marsh edge erosion based on large scale hydrodynamic and wave models, with a specific focus on how cold front induced waves impact the salt marsh edge, 2) to build the relationship between the wave energy and the salt marsh lateral erosion based on the 3D flume experiment and drone survey, 3) to monitor the salt marsh boundary evolution around the Galveston Bay area using a drone, and track the status of wetland vegetations, 4) simulate the potential of sediment transport's effect on the accretion and erosion of the morphology at the salt marsh boundary. A significant part of this thesis work will focus on coastal salt marshes at Galveston Bay.

1.2. Synthesis

This thesis studies the lateral erosion of salt marsh edge caused by ocean waves through numerical, laboratory, and field experiments. Chapter 2~4 detail the investigation of the waves impacting salt marsh and their effect on the erosion of salt marsh edges. Chapter 5 describes an investigation into sediment transport by tide and waves affecting salt marsh boundary morphological change, such as accretion by flooding and erosion by bed shear stress. Chapter 2 verifies and quantifies the wave energies to the salt marsh through high-resolution hindcast simulation. Chapter 3 investigates the effect of wave energy on salt marsh surface erosion to connect wave energy calculation in Chapter 2 with the lateral erosion rate of salt marsh. In Chapter 4, observation of salt marsh boundaries in Galveston Bay was done over a year through actual field UAV surveys. Chapter 4 tried to verify the investigations of Chapter 2 and Chapter 3 related to wave power and erosion rate relationships from the UAV survey results.

Chapter 2 describes a large scale numerical simulation for waves in a shallow bay affecting salt marsh edge lateral erosion. The focus is to understand the role of cold fronts induced water levels and waves in shaping the salt marsh edge. Wind gusts affecting the wave energy in the shallow bay are quantified and compared to averaged wind. Effective wave power to the north-facing salt marshes based on the wave properties was evaluated as a potential cause of erosion.

Chapter 3 describes a laboratory experiment to verify the effect of wave energy on the erosion of wetlands core samples. Different incident wave heights were tested in a

three dimensional wave basin. Based on the results, the relationship between wave power and erosion rate was investigated through dimensional analysis.

Chapter 4 is dedicated to examining field wetlands boundary mapping and lateral erosion rate analysis based on Unmanned Aerial Vehicle (UAV) images. A specific focus was on salt marsh boundary changes compared with cumulative wave power calculated by the wave model.

Chapter 5 investigates the role of sediment transport around the salt marsh in a shallow bay during the cold front passages, via sediment transport simulation by expanding the numerical model in Chapter 2. Relative sea level rise (RSLR) effect on morphodynamic of salt marshes are also tested.

Chapter 6 concludes the entire thesis and suggests future research directions.

Materials included in Chapter 2 have already been published. Full reference is given below:

Chapter 2: Kim, J.Y., Kaihatu, J., Chang, K.A., Sun, S.H., Huff, T.P., & Feagin, R.A. (2020). Effect of cold front-induced waves along wetlands boundaries. Journal of Geophysical Research: Oceans. 125e2020JC016603. https://doi.org/10.1029/2020JC016603

2. COLD FRONT INDUCED WAVES ACTING ON THE WETLANDS BOUNDARY[1]

2.1. Introduction

Saltmarsh wetlands are an important component of coastal ecosystems. Marsh vegetation has a significant role in inland protections as a barrier to storm waves. Dampened estuarine currents allow the estuaries to serve as nursery habitats for numerous shellfish and fish species (Mathieson et al., 2000). Additionally, tidal hydrodynamics facilitate the transport of vital nutrients and tracers into and out of the wetlands (during flood and ebb tides), affecting both inshore and onshore vegetation and animals (Mann and Lazier, 2013).

However, salt marsh edges are continuously affected by sea conditions such as storm surge (Cahoon, 2006), natural and/or human-induced regional subsidence (van der Wal and Pye, 2004) and sea-level rise (Alizad et al., 2016). It has been previously shown that wind-wave activity near saltmarsh wetlands is a potential factor in accelerating wetland loss rates (Schwimmer and Pizzuto, 2000; Schwimmer, 2001; Marani et al., 2011; Karimpour et al., 2016; Leonardi et al., 2016). Moreover, a combination of increased water levels and energetic wind-wave conditions can lead to more wave breaking, amplifying the marsh edge erosion (Tonelli et al., 2010).

---

[1] Reprinted with permission from "Effect of Cold Front-Induced Waves Along Wetlands Boundaries" by Kim, J.-Y., Kaihatu, J., Chang, K.-A., Sun, S.-H., Huff, T. P., & Feagin, R. A., 2020. Journal of Geophysical Research: Oceans, 125, e2020JC016603, Copyright [2020] by American Geophysical Union, Further reproduction or electronic distribution is not permitted.

Numerous studies (Schwimmer, 2001; Marani et al., 2011; Leonardi et al., 2016; Leonardi et al., 2016) have shown a linear relationship between wave energy flux and lateral rates of salt marsh boundary retreat although marsh edge erosion is dependent on processes of wetlands such as root effects, soil characteristics, and bioturbation. The wave energy flux is strongly related to the volumetric erosion rates of the marsh edges and is considered a critical factor in overall marsh loss (McLoughlin et al., 2015). Moreover, frequent, moderately energetic weather conditions, rather than less-frequent extreme weather events (e.g., hurricanes), can have a greater impact on salt marsh retreat (Roberts et al., 1987; Leonardi and Fagherazzi, 2015; Roberts et al., 2015). Passing cold fronts are thus important drivers for shoreline changes of low-energy coasts (Keen, 2002)

Cold fronts are generally active from autumn to spring and move from north to south in the northern hemisphere (DiMego et al., 1976). These fronts are accompanied by gusty winds that can cause energetic waves over water. Winds ahead of a cold front tend to blow from the south and southwest, and then shift toward the northwest after the frontal passage. Subsequently, coastal water levels would change because of cold front-driven currents and Ekman transport before and after the arrival of northwest winds with the frontal passage. Cold front-driven currents are mainly caused by across-Gulf coast winds that can drive across-shelf flow to shallow bays. Ekman transport is caused by the balance between along-Gulf coast winds generated stress and Coriolis force in the deep water and the direction of the flows is directed 90° clockwise rightward with respect to

the wind direction (Walker and Hammack, 2000; Tilburg and Garvine, 2004; Fagherazzi et al., 2010).

The water level increase in shallow tidal basins can cause a monotonic increase in wave power, thus causing additional potential marsh edge erosion (Young and Verhagen, 1996; Fagherazzi and Wiberg, 2009; Valentine and Mariotti, 2019). However, this increase in wave power with water level is true up to a point; further increase in water level can reduce erosion rates by weakening the wave thrust (defined as the depth-integrated dynamic pressure due to waves) at the edge of the salt marsh when the wetland platform is submerged. If the instantaneous water level is higher than the height of the edge of the wetland, the wave thrust on the wetland decreases sharply due to wave "overshoot" (Tonelli et al., 2010; Valentine and Mariotti, 2019). Subsequently, these overshooting waves become attenuated in the marsh platform, and thus no additional lateral erosion occurs (Möller and Spencer, 2002; Möller et al., 2014). As such, the wave and water level both needed to be considered simultaneously to evaluate the erosion potential of wetlands.

Hydrodynamic and wave models have been applied to evaluate the lateral erosion of salt marsh in shallow bays. Fagherazzi and Wiberg (2009) simulated wave evolution in the shallow tidal basins based on the formulation presented by Young and Verhagen (1996). McLoughlin et al. (2015) and Priestas et al. (2015) compared the shoreline changes of Virginia Coast (USA) to the wave model results based on the numerical model Simulating WAves Nearshore (SWAN) (Booij et al., 1999).

In areas populated by coastal wetlands, such as the barrier islands in shallow bays, wind-driven currents, and astronomical tides jointly control water fluxes (Lester et al., 2002; Duran-Matute et al., 2016). To model this, a large-scale hydrodynamics and wave model is necessary. In previous studies, coupled ADCIRC-SWAN models were applied to identify changes in the coastal environment under hurricane conditions in the Gulf of Mexico due to waves, tides, and surge inundation (Hope et al., 2013; Kerr et al., 2013; Sebastian et al., 2014). Hurricane-induced hydrodynamics and morphological changes in wetlands were also investigated by Liu et al. (2018) using the Delft3D model. However, no prior work has been done to model the impacts of cold-front-induced waves and hydrodynamics to the salt marsh boundary in a shallow bay. In the present study, we utilize a large-scale coupled modeling system (Delft3D) to investigate processes (including wind, surge, and waves) in Galveston Bay along the Texas coast induced by two different cold front passages. The model is also validated with in-situ data, an advance over many similar previous studies relate to the investigation of wave climate along salt marsh edges (Leonardi et al., 2016).

The purpose of this study is to show how cold front-driven wave and water level changes impact marshes and affect potential marsh edge erosion rates in coastal microtidal bays such as Galveston Bay. The objectives of this study are threefold: (1) to investigate the meteorological condition changes during the cold front passage that affect the wave and hydrodynamic environment in Galveston Bay; (2) to investigate the wave response to these fronts (and attendant impact on erosion), with a focus on the impact of wind gustiness during cold front passage; and (3) to quantify the effect of inundation in

the marsh boundary areas on wave energy during times of simultaneous high tide and cold-front driven surge.

2.2. Study area

2.2.1. Site description

Galveston Island is a barrier island on the Texas Gulf Coast, located about 80.5 km southeast of Houston, Texas, U.S.A. The island stretches 43.5 km long by 4.8 km wide at its widest point. The island is oriented northeast-southwest, with the Gulf of Mexico bordering on the east and south, West Bay and San Luis Pass on the west, and Galveston Bay toward the north (Figure 2-1c).

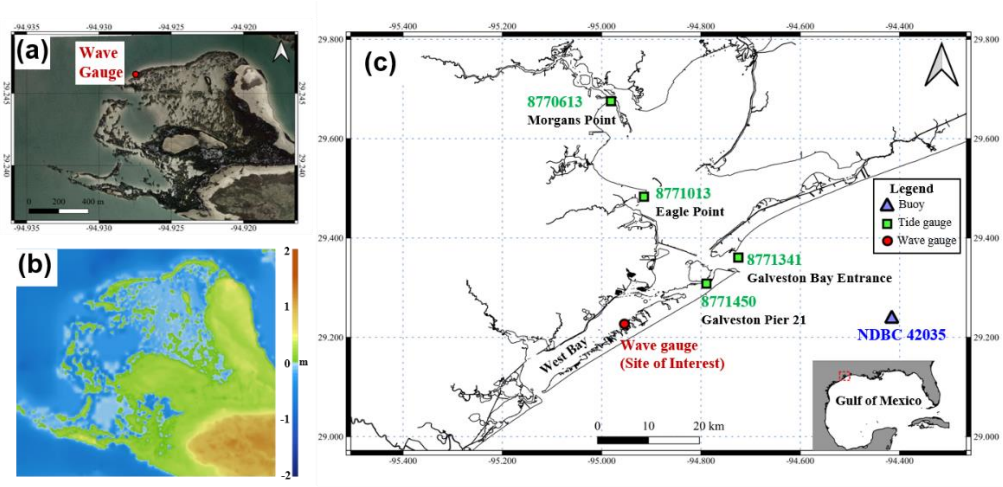

Figure 2-1 (a) The image of the Galveston Bay wetland in the study site and tide and wave gauge location, (b) topography and bathymetry of the study site in the model, and (c) tide gauges and buoy locations around the Galveston Bay for model validation

The bay has an average water depth of 1.8m with respect to mean sea level. West Galveston Bay is classified as a micro-tidal lagoon. Along the immediate shorelines of Galveston Bay, *Spartina alterniflora* grows. This plant is well-known for its extensive

roots and below-ground production, and grows along many of the world's bay shorelines (Feagin et al., 2009). The platform elevation of salt marshes along the area was calculated to range from 0.3 to 0.45 m NAVD88 in both LIDAR imagery and survey-grade GNSS (Feagin et al., 2010; Kulawardhana et al., 2015)

A field site was established on the bayside of Galveston Island along West Galveston Bay. The site is located between Melager Cove and Oxen Bayou, about 6 km from Galveston Island State Park. (Figure 2-1a). This site was chosen since it is typical of eroding north-facing barrier island wetlands, and is therefore exposed to the impacts of northerly winds from cold fronts.

The wetlands in the area are affected by mixed (diurnal and semidiurnal) tides and waves generated by cold front winds acting across the 6 km (width of West Bay) to 26 km (length of a northeast-southwest line delineating the long axis of West Bay) fetch. Northerly winds may lead to water level difference as high as 1.0 m between east and west sides of the bay (Lester et al., 2002).

The loss of Galveston Bay salt marshes (estuarine marshes) has occurred at a rate of 0.7% from 1979 to 2002 (White et al., 2004). This is higher than the national wetland loss, estimated to be about 0.5 % (59,400 acres) annually in the decade before 1986 (Dahl and Johnson, 1991). From 2006 to 2011, a total of 5.1 % of Galveston county wetlands (Yearly average 1.02 %) have been eroded in terms of surface area (Entwistle et al., 2018). The majority of losses were the result of subsidence, sea-level rise, wave action, sediment deficit, dredging, and filling (Moulton et al., 1997; Ravens et al., 2009). Across our study location, the long-time rate measured by Gibeaut (2003) from 1930 to

1995 was 0.58 m per year (Feagin et al., 2010). This rate includes shoreline facing both the predominant fetch direction and peripheral, protected shorelines. The rate accelerated in the later portion of this time range, largely due to sea level rise (Ravens et al., 2009). For shorelines facing the predominant fetch direction only, we also measured the lateral erosion rate using Google Earth images for dates from 1954 to 2018 and found a consistent linear rate with minimal outliers, arriving at 1.13 m per year. On these same stretches of shoreline, Huff et al. (2019) also recorded erosion in the field, also finding 1.13 m per year.

2.2.2. Cold fronts passage along Galveston Bay

From September to May, Galveston Bay is influenced by cold fronts, evidenced by a sudden drop in temperature and strong gusty winds highly variable in direction. After the cold front passage, the Galveston Bay area experiences cool and dry weather brought by the northerly or westerly winds. These changes affect the wave and circulation of the Galveston Bay system. These changes affect the wave and circulation of the Galveston Bay system. The change in hydrodynamic conditions due to cold fronts in the Galveston Bay were discussed in Cox et al. (2002).

Changing environmental conditions associated with cold front passages can be classified as prefrontal, frontal passage, and postfrontal (Roberts et al., 2015). The mean water level of Galveston Bay is strongly influenced by cold front-driven currents, in addition to the astronomical tide. As the front approaches the coast, winds become more southerly which causes the water level to increase slightly, due to the influx of water from the Gulf of Mexico (prefrontal). Immediately after the cold front passage (frontal

passage), the northerly or westerly wind dominates over the entire bay; there is a resulting drop in water level as the water in the Galveston Bay fetch is pushed to the offshore side (postfrontal).

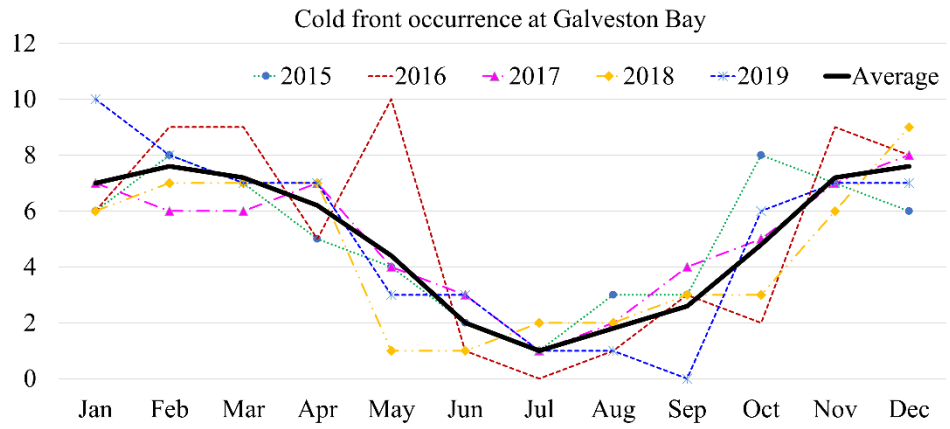

Figure 2-2 Monthly cold front passage at Galveston Bay from 2015 to 2019 and its all year average

The number of cold front passages from 2015 to 2019 are shown in Figure 2-2. The number of cold fronts that passed through Galveston Bay from 2015 to 2019 was determined based on the analysis of infrared satellite imagery produced by the Weather Prediction Center (WPC) of NOAA. Analysis consisted of manual recognition and counting of surface front locations passing through the Galveston Bay, and was performed at 3-hour intervals. Most of the cold fronts moved from North to South or from Northwest to Southeast. During the period, the months where the cold front passed most often were from November to February. From June to August, the lowest number of cold frontal passages were observed. The average return period of the cold fronts in Galveston Bay was calculated as 6 days during the months in which they occur. Cold

front gust generation, their directionality, and their forcing of waves are quantifiable, so it is important to investigate the effect of waves generated by these climatic events on the salt marsh.

2.2.3. Field Measurement

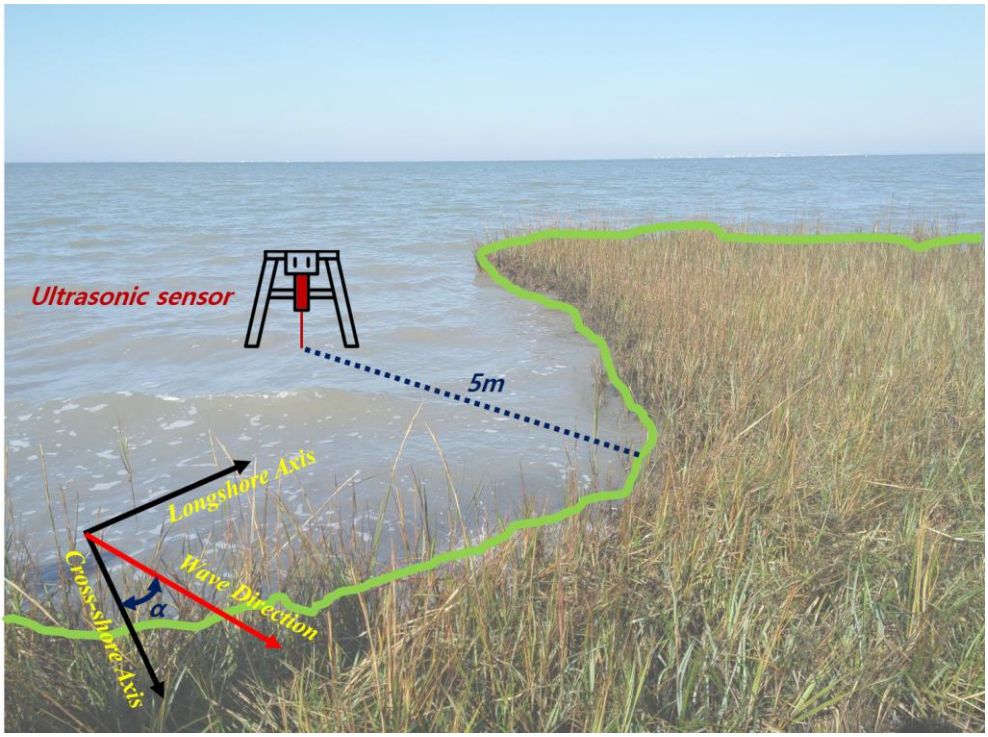

Figure 2-3 Wetland boundary at the site of interest and sensor configuration in the field (primary wave direction from cold fronts -NW)

The study site, located at 29°14'46.55" N and 94°55'38.26" W, is near Melager Cove (Figure 2-1a), where the salt marshes present along the West Galveston Bay side of Galveston Island are exposed to northerly winds and waves. To measure wave energy, an ultrasonic wave sensor (T30UXUB, Banner Engineering, Inc.) was placed approximately 5 meters offshore from the edge for a duration of nine days (December 10 to December 18, 2015), with a sample rate of 20 Hz with no bursts (Figure 2-3). During

this period, a large range of sea state conditions was encountered, with wind arriving from every direction and speeds ranging from 1.6 m/s to 10.8 m/s, arising across a maximum fetch of approximately 6.25 km (the width of West Bay near the site).

Spectral wave analysis was performed for the water elevation records. The total record period is 8 days, 7 h, 16 min, and 28 s. The time series are divided into 1,993 realizations of 7,200 data points apiece, resulting in frequency bins of 4097 with a resolution of 0.0025 Hz. Each realization is input into the periodogram function, which yields the frequency vector. This function computes the FFT from the input water elevation vector. These initial spectra were truncated at f_{min}=0.05 Hz, as the signal errors and some unrealistic low-frequency parts were recorded during the frontal edge crossing mainly caused by the increased water level. The high-cutoff frequency was set equal to f_{max}=1.00 Hz. The average water level data was extracted by applying a moving average of 72,000 data points (1 h) window to the raw ultrasonic gauge data.

2.2.4. Wave power (Wave energy flux)

Schwimmer (2001) found that the marsh regression rate is correlated to the averaged wave power, defined as:

$$P_w = \left(\frac{\rho g H_s^2}{8}\right) C_g \qquad 2\text{-}1$$

where H_s is significant wave height, ρ is the water density, and C_g is the wave group velocity, where:

$$C_g = \frac{1}{2}\sqrt{\frac{g}{k}\tanh kh}\left(1 + \frac{2kh}{\sinh(2kh)}\right) \qquad 2\text{-}2$$

where k is wave number (k=2$\pi\lambda$, λ being the wavelength). The wavelength λ is calculated using the mean absolute wave period $T_{m-1,0}$ ($T_{m-1,0}$= m_{-1}/m_0, m_{-1} being the -1 order moment integral of the power spectrum) based on the dispersion relation ($\omega^2 = gk\tanh(kh)$, where ω =2πT). The mean absolute average wave period (often called a mean energy wave period) is used to determine the wave energy flux per unit of wave-crest length (Hofland et al., 2017). For a marsh edge oriented at an angle to the wave propagation direction, the instantaneous incident wave power density is:

$$P_i = P_w \cos\alpha \qquad 2\text{-}3$$

where α is the mean wave direction relative to the direction normal to the marsh edge. Since the wave direction cannot be deduced using a single gauge, the P_i was calculated using the wind direction records at the Eagle Point wind station for the effective wave power calculation in the measurements, under the assumption that the waves are collinear with the wind direction. The average wave direction is assumed to be very close to the averaged wind direction records, and it is not considered to be a source of error since the direction of wind and waves were very similar in the model results. In addition, P_i < 0 represents times when the winds are directed away from the marsh edge, and as such do not generate waves that impact it; for these occurrences we set P_i =0. The water depth at the site was not sufficiently small for the shallow water approximation of the linear dispersion relation to be used. The time series of the significant wave height, H_s , water level, and mean energy wave period, $T_{m-1,0}$, extracted from the wave gauge time series data, were used to calculate group velocity C_g in Equation 2-2. The short distance between the gauge and the wetland edge is

insufficient for additional wind-wave generation, so the wave energy at the gauge was assumed to be representative of what occurred at the marsh edge. Wave reflection from the edge of the steep wetlands would likely be detected by the gauge; however, since it is a single gauge, there would be no way to extract it from the time series. While this reflection is not modeled, its neglect is not expected to be a significant source of error since the effective wave power value does not include waves directed away from the marsh edge.

Based on findings from Tonelli et al. (2010), McLoughlin et al. (2015) calculated the effective wave power by setting P =0 when the extracted averaged water level was above the top elevation of the marsh edge platform. In a later section, we define three wetlands platform thresholds for calculation of effective wave power in line with this prior work. However, this definition excludes frictional effects generated by wavefront orbital velocity passing through the edge of a wetland, which can affect the salt marsh edge erosion (Karimpour et al., 2016). Other studies consider this effect by exponentially reducing the wave thrust as water level increases above the marsh scarp (Leonardi et al., 2016; Donatelli et al., 2019)

2.3. Numerical models

2.3.1. Model description

Due to the focus on wind-generated waves, a phase averaged wave energy (or action) balance model is required. The SWAN model (Booij et al., 1999) is widely used for coastal regions and was used here. SWAN was used with DELFT 3D-FLOW within the DELFT3D model suite, thus allowing coupled wave and hydrodynamic modeling.

The DELFT3D-FLOW module solves the unsteady shallow-water equations in two (depth-averaged) or three dimensions (Lesser et al., 2004). The system of equations consists of the horizontal momentum equations, the continuity equation, the transport equation, and a turbulence closure model. The vertical momentum equation is reduced to the hydrostatic pressure relation as vertical accelerations are assumed to be small compared to gravitational acceleration and are not taken into account. Although the 3-D model has the advantage in resolving the vertical flow structure, a validated 2-D model can achieve similar accuracy in tidal current prediction with much higher computational efficiency (Horstman et al., 2013). Therefore, the 2-D version of the Delft3D model was used in the study to focus on depth-averaged currents in the shelf-bay-wetland system. In addition, we employed domain decomposition in the Delft3D-FLOW model. Domain decomposition is a technique in which a model is divided into several smaller model domains, with parallel computation occurring among all domains. In simultaneous computation with SWAN, nesting from a coarse grid to finer grids is used. In the outer boundary of the Gulf of Mexico grid, periodic conditions are applied at the open ocean boundary along the entrance of the Gulf of Mexico. Astronomical tidal constituents (K1, O1, Q1, P1, M2, S2, N2, and K2) are forced on the open ocean boundary using the TPXO 8.0 tidal atlas (Egbert and Erofeeva, 2002).

2.3.2. Bathymetry and grids

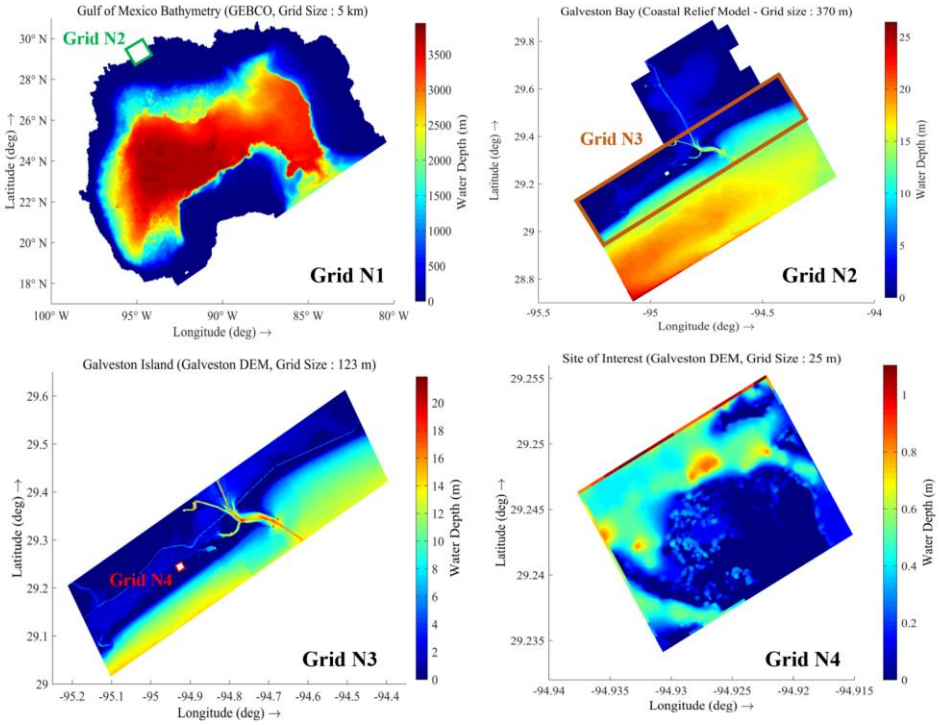

Figure 2-4 Model grid and bathymetry of Gulf of Mexico (N1), Galveston Bay(N2), Galveston Island(N3), and study area (N4) in Delft3D-FLOW and SWAN model

For improved fidelity of the model, four model grids, spanning from the Gulf of Mexico to the wetlands in the bayside of Galveston Island, were adopted. The bathymetric grid for the Gulf of Mexico (Figure 2-4, Grid N1) was based on GEBCO-08 (Becker et al., 2009), a global bathymetry and elevation database at 30 arc seconds spatial resolution. The bathymetric grid for Galveston Bay (Figure 2-4, Grid N2) was constructed using a nearshore digital elevation model at 3 arc seconds spatial resolution (U.S. Coastal Relief Model, National Centers for Environmental Information NOAA, U.S. Department of Commerce, Boulder, CO, September 2010). For Galveston Island (Figure 2-4, Grid N3) and the site of interest (Figure 2-4, Grid N4), the Galveston

Digital Elevation Model 1/3 arc-second (10 m) high-resolution topography and bathymetry (Taylor et al., 2008) was adopted for the representation of the salt marsh boundaries located at the bay side of Galveston Island (Figure 2-1b). Because the Galveston DEM was originally transformed to Mean High Water level (MHW) for the vertical datum, bathymetric and topographic data for Grid N3 and Grid N4 were adjusted to the NAVD88 datum using NOAA Vertical Datum Transformation (VDatum) software (Parker et al., 2003). The difference between MHW and NAVD88 at the study site is 0.3 m. However, the uncertainty regarding the difference between the MHW level and NAVD88 presented in VDatum is 0.11 m.

Grid resolutions for the Gulf of Mexico, Galveston Bay, Galveston Island, and wetlands in the Galveston Island grid are 5 km, 370 m, 123 m, and 25 m, respectively. Each equidistant grid was rotated such that the positive x-direction is oriented 30° clockwise from the west-to-east direction. The datum of the bathymetric data is important since the water depth defined by bathymetry is directly related to wave shoaling and refraction and thus to the wave power at the salt marsh boundary. It should be noted that the present model resolution (25 m, Figure 2-4, Grid N4) cannot resolve the fine detail of highly variable bathymetry around the salt marsh edge.

2.3.3. Wind input

NCEP Climate Forecast System Version 2 (CFSv2) 6-hourly Products (Analysis data) were applied (Saha et al., 2014) for the entire Gulf of Mexico (Grid N1) as well as the offshore side of Galveston Bay. These winds had a spatial resolution of 0.205 degrees. The comparison showed good agreement between NCEP offshore winds and NDBC buoy station 42035, located outside of Galveston Bay entrance.

For the N2, N3, and N4 grids, 6 min intervals winds and gusts from the nearest NOAA weather station in Eagle Point (Station ID: EPTT2, 8771013), Houston, Texas, were input to the model over the measurement period. Averaged wind speed was determined by a 2-min scalar average of 1-s wind speed measurements collected prior to each tenth hour. The wind gusts were determined from the maximum 5-s moving scalar average of wind speed that occurred during the previous 6 min at the station. Winds from Eagle Point, measured at 5.7 m above mean sea level, were corrected to the standard 10 m height (NOAA, 2020). Scholes International Airport weather station (77551), Galveston, Texas, is located 7.3 km east of the wave sensor location in Galveston Island. However, this weather station has low-directional resolution and frequent data gaps, precluding its use for modeling. Wind data from Eagle Point and Scholes Field International Airport were compared to confirm the similarity between two locations. It is found that the difference between the Scholes Field International Airport and Eagle Point was minimal, particularly during the cold front passage.

2.3.4. Parameter selection for model

The DELFT3D model suite was configured to allow the hydrodynamic flow model (Delft3D-FLOW) and the SWAN wave model to communicate every 6 min during the simulation, with the consideration of 6 min interval wind input of the model. The time step of the DELFT3D-FLOW model was 12 seconds and the SWAN time step and coupling interval with the flow is 6 min. The time step of 12 seconds was chosen as a compromise between the Courant number (<10 is recommended, Deltares Hydraulics (2006))in Grid N4 bathymetry and computational efficiency. Hydraulic friction is parameterized in the DELFT3D-FLOW model using a spatially varying Manning's *n* value based on the water depth. Offshore, areas with sandy/gravel bottoms such as the Florida shelf are set to n=0.022, and areas with muddy bottoms like the Texas-Louisiana shelf are set to n=0.012 (Buczkowski et al., 2006). These values are applied at depths greater than 5 m, and they are increased linearly to n=0.022 toward the shoreline. The SWAN time step of 6 min is determined by the time interval of the wind input, allowing the immediate update of the wind velocity and the subsequent wind-wave conditions in the model. The wave directional spectra are discretized into 72 directional bins of a constant 5-degree width, and the frequencies are discretized over 24 frequency bins, in the range of 0.05-1 Hz, which is the default in SWAN. The hindcast uses the wind input formulation based on Snyder et al. (1981), the modified whitecapping expression of Rogers et al. (2003), and quadruplet nonlinear interactions via the discrete interaction approximation (Hasselmann et al., 1985). For the shallow-water source terms, depth-

induced breaking is computed with a spectral version of the model of Battjes and Janssen (1978) with the breaking index γ= 0.73. Wave refraction is enabled in regions where the resolution of the bathymetry is sufficient to prevent spurious wave refraction. Both models were run on the same computational grid, thus eliminating the need for interpolation between models. In the study area, an inner nest was included in the simulations to provide higher resolution in the wetlands of Galveston Island. The nest position is shown in Figure 2-4. Additional details on the SWAN wave model design are:

- Stationary computations, with default setting for numerics (Rogers et al., 2003)
- Default settings for nonlinear interactions (Snl4)
- Bottom friction for JONSWAP (Hasselmann et al., 1973), set to 0.067 $m^2 s^{-3}$

The time series of the significant wave height, H_s mean absolute wave period, $T_{m-1,0}$, and averaged wave direction θ as outputs from the SWAN model combined with the Delft3D-FLOW results of the water level time series, were used to calculate wave power.

2.3.5. Skill Metrics

Model validation was quantified using the following skill metrics: Root Mean Square Error (E_{RMS}, which is a measure of the magnitude of error, with an ideal value of zero), Coefficient of Determination (R^2, which describes how well a regression line fits a set of data, with an ideal value of one), Normalized Bias (which is a measure of the model's magnitude of overprediction or underprediction normalized to the observed value, with an ideal value of zero), Scatter Index (SI, The standard deviation of E_i is SI

which indicates how much the predicted variation pattern deviates from the observed one, with an ideal value of zero), and Mean Normalized Error (E_{NORM}, which is the mean error normalized by the mean observed value, with an ideal value of zero; Hanson et al., 2009; Kerr et al., 2013). Taking N as the number of observation points in the time series and $E_i = S_i - O_i$ as the difference between the model result S_i and the observation O_i, the equation for Mean Normalized Bias is

$$Bias = \frac{\frac{1}{N}\sum_{i=1}^{N} E_i}{\frac{1}{N}\sum_{i=1}^{N}|O_i|} \quad 2\text{-}4$$

and the equation for Scatter Index is

$$SI = \sqrt{\frac{\frac{1}{N}\sum_{i=1}^{N}(E_i - E)^2}{\frac{1}{N}\sum_{i=1}^{N}|O_i|}} \quad 2\text{-}5$$

Additionally, the equation for Mean Normalized Error is

$$E_{NORM} = \sqrt{\frac{\frac{1}{N}\sum_{i=1}^{N}(E_i)^2}{\frac{1}{N}\sum_{i=1}^{N}(O_i)^2}} \quad 2\text{-}6$$

2.4. Results

Two cold fronts were observed during the measurement period. Figure 2-5(a) illustrates the frontal passage and first cold front, approaching Galveston Bay around DEC 13, 2015 14:30 (UTC) with peak average wind speed of 14.2 m/s and gusting of 21.4 m/s. During the prefrontal phase, winds at Eagle Point were directed from south to north (arriving from 170 - 180°). As the leading edge passed the weather station, the primary wind direction quickly changed to northerly (arriving from 320 - 360°) (Figure 2-5b). A drop in temperature of 8.5°C was recorded at the weather station after the frontal passage. A maximum gust of 10 m/s gust was recorded during the postfrontal phase. Gusty winds continued for nearly 7 hours from the frontal passage.

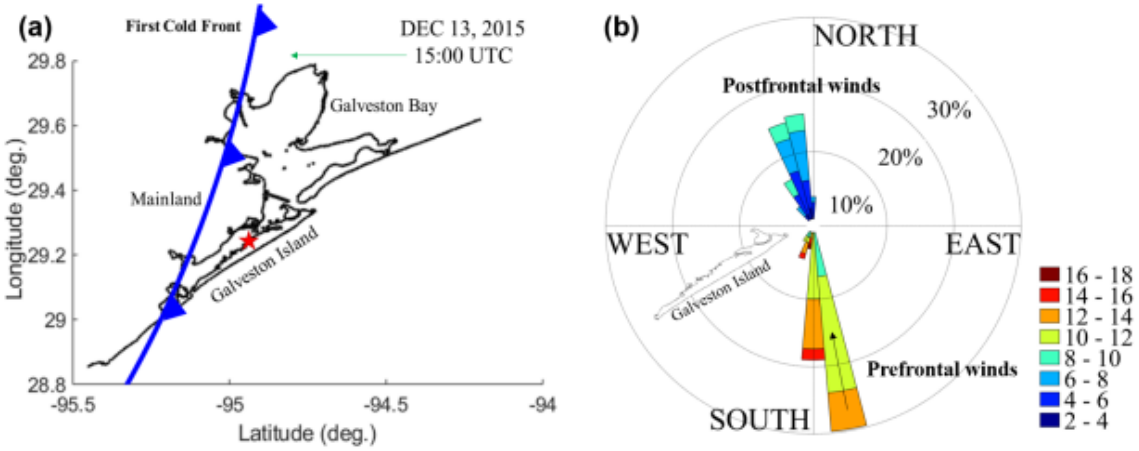

Figure 2-5 (a) History of movement and (b) Eagle Point (8771013) wind rose during the First cold front (13 May, 2015) across the coast of Texas

The second front approached Galveston Bay around 12:00 (UTC) on DEC 16, 2015 (Figure 2-6a), with a peak average wind speed of 10.2 m/s and gusts of 13.1 m/s. In contrast to the first cold front, this second front is oriented nearly parallel with the

shoreline. It also passed slowly over the region relative to the first cold front. The speed of winds coming from the south during the prefrontal phase of this second cold front was also lower relative to the first cold front. After the frontal passage, the gusty winds accompanying the cold fronts continued from DEC 16, 2015 12:00 to DEC 17, 2015 20:00 (UTC), overall duration of 32 h of northerly gusts winds whose directions ranging from 360° to 35° (Figure 2-6b) during the postfrontal phase. During this period the range of gusts was recorded from 5 to 11 m/s.

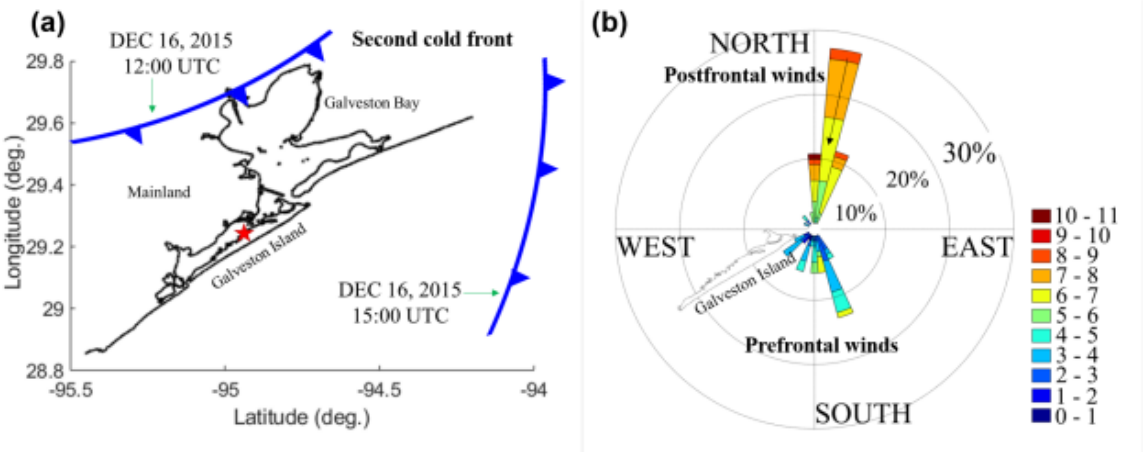

Figure 2-6 (a) History of movement and (b) Eagle Point (8771013) wind rose during the First cold front (13 May, 2015) across the coast of Texas

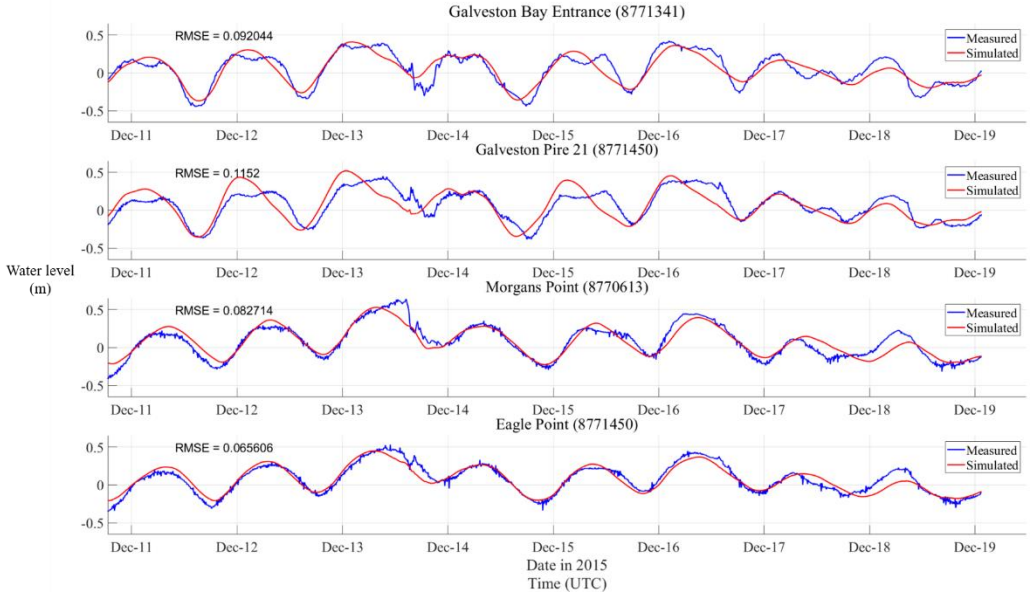

Figure 2-7 Measured and simulated water level at tide stations in Galveston Bay

Table 2-1 The accuracy of model predictions of water level time series

Geographic Location	Water level (m)				
	$E_{RMS}\ (m)$	SI	$Bias$	R^2	E_{NORM}
Galveston Bay Entrance	0.09	0.005	-0.21	0.81	0.45
Galveston Pier 21	0.11	0.005	0.17	0.65	0.60
Eagle Point	0.07	0.000	-0.44	0.88	0.45
Morgan Point	0.08	0.001	0.29	0.85	0.45
Site of Interest	0.04	0.006	-0.68	0.88	0.61

Figure 2-7 shows the measured and simulated water level at the tide stations at Galveston Bay (Figure 2-1c). The measured water level showed a 0.6 m overall tidal range, with diurnal variation, at the site. As seen in the water level record, winds from

the south during the prefrontal phase served to increase the water level of the entire extent of Galveston Bay. From Dec 13, 00:00, wind-driven currents from prefrontal winds were shown to increase the overall Galveston Bay water level by approximately 0.2 m. Due to cold front-driven currents and coincident high astronomical tide, the water level over the measurement period was highest during the passage of the first cold front at Dec 13, 12:00 (UTC) and lowest at Dec 14, 23:00 (UTC). The model results show accurate predictions during most of the measurement period. However, some discrepancies in water level records at the Galveston Bay Entrance and the Galveston Pier 21 tide stations were apparent. It is thought that this is due to the lower temporal resolution of wind conditions in the N2 grid (wind input: NCEP model) at the Galveston Bay entrance compared to the N3 grid (wind input: Eagle Point wind records). The metrics reflecting the accuracy of the modeled water level in the tide stations are summarized in Table 2-1.

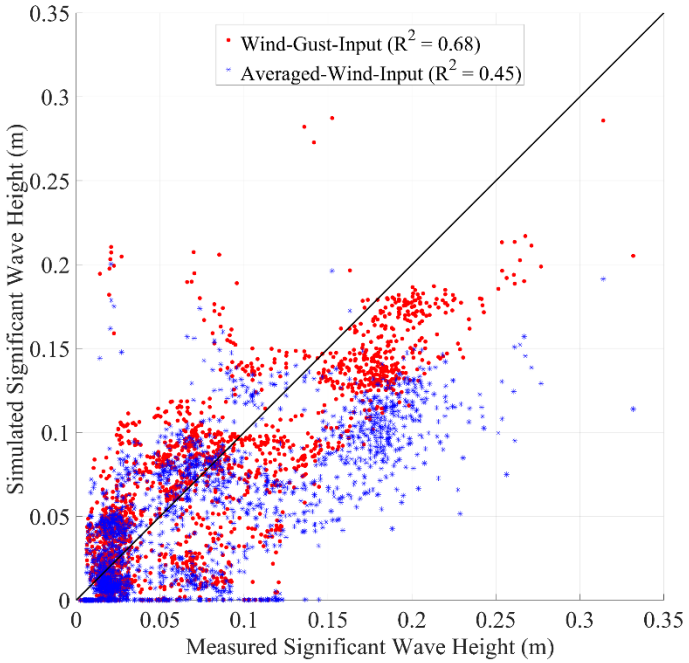

Figure 2-8 Comparison of modeled significant wave height results at the site of interest to the measured significant wave height results between two different wind inputs (Gust and Averaged wind)

To evaluate the effect of gusts on wave generation in West Galveston Bay, the model was run using the wind gust record and the results compared to that using averaged wind. The comparison also confirmed the wind data suitable for cold front-induced wave model prediction in the SWAN model. Significant wave height results by the average wind data and wind gust data input were compared to measured significant wave height data, as shown in Figure 2-8. Use of the wind gust record as input results in better prediction (R^2=0.68) than use of the averaged wind as input (R^2=0.45). Therefore, the model result forced by wind gust input was used for all comparisons with the measurement result to be described here later.

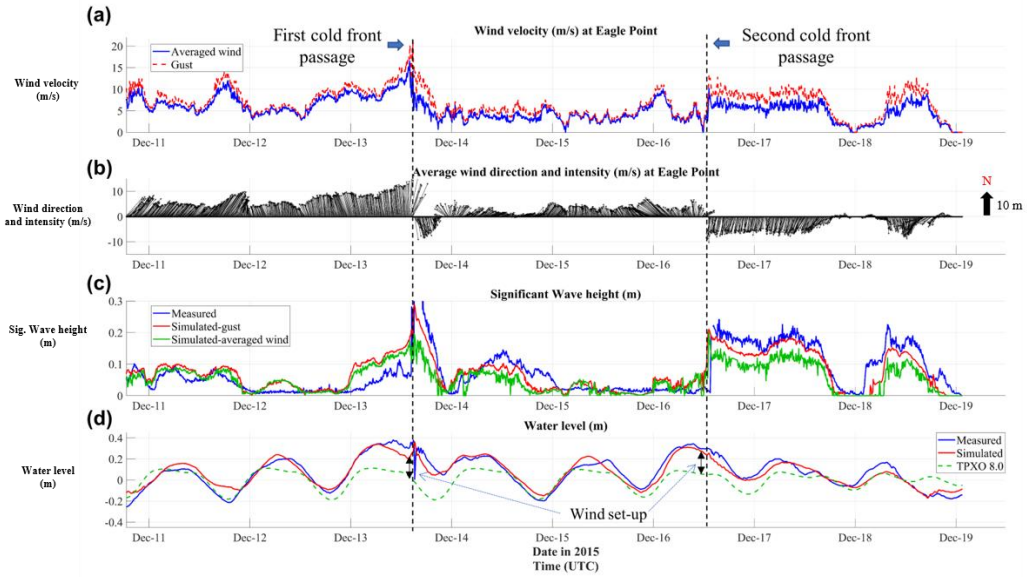

Figure 2-9 (a) Averaged wind velocities and wind gusts at Eagle Point, (b) averaged wind direction records at Eagle Point, (c) comparison of significant wave height results between measured and modeled records, and (d) results of measured and modeled water level records compare to TPXO8.0 model.

Water level results in Figure 2-9 show the measured and simulated water level changes during the measurement period at the site of interest as well as the generated water level signal from the global astronomical tide model TPXO 8.0. As seen in the water level records, winds from the south during the prefrontal phase served to increase the water level (wind set-up) of the entire extent of Galveston Bay. The water elevation was the highest during the approach of the first cold front at Dec 13, 12:00 (UTC). Both cold fronts passed through Galveston Bay during the end of the high astronomical tide condition, maximizing the water level of the Galveston Bay area. Under maximized water level conditions, it is likely that the wetlands boundary area switches from partially depth-limited (in which wave generation or wave height is limited by water depth) conditions to entirely fetch-limited (in which wave energy is limited by the size

of the wave generation area) conditions. The lowest water level occurred around DEC 15 00:00 (UTC), which accompanied a low tide. The result of the significant wave height at the site of interest is shown in Figure 2-9 along with the wind inputs.

From Dec 11 to Dec 12, significant wave heights were less than 0.1 m at the site even though most of the wind speeds were above 5 m/s during this period. This is because most of the winds were not directed toward the salt marsh boundary. In the prefrontal phase of the first cold front, from Dec 13, the southerly wind speed increased from 5 m/s to 10 m/s, and the wind arrived from the south which increases the influx of water into Galveston Bay. However, the significant wave height only increases from 0.05 m to 0.1 m, likely due to the winds moving away from the north-facing wetlands.

During the frontal passage, a peak wind gust value of 20 m/s was recorded. The maximum significant wave height recorded during the first cold front passage in the model was 0.29 m. In the postfrontal phase, wind speeds decreased significantly after the leading edge of the front passed the Galveston Bay area. The significant wave heights dropped to a very low level on Dec 14; from Dec 14 to 16, the significant wave height was below 0.1 m.

The second cold front, observed Dec 16-17, abruptly changed the wind velocity; it was accompanied by gusts and generated 0.12 - 0.21 m significant wave heights during the passage on Dec 16. The gusty winds lasted almost two days at the site and the wave direction was close to the normal direction of the salt marsh boundary. During the postfrontal phase after the second cold front passage, the TPXO 8.0 tide model showed

low tide on Dec 17 at 00:00 (UTC). During this low astronomical tide condition, the significant wave height slightly decreased to below 0.12 m.

Table 2-2 The accuracy of model predictions of significant wave height time series

Geographic Location	Significant wave height				
	$E_{RMS}\ (m)$	SI	$Bias$	R^2	E_{NORM}
Site of Interest (Gust)	0.03	0.001	0.00	0.68	0.40
Site of Interest (Ave. Wind)	0.03	0.006	0.26	0.45	0.53
NDBC-42035	0.17	0.021	0.42	0.83	0.42

The accuracy of model predictions of water level and wave heights time series are summarized in Table 2-1 and Table 2-2. The model performance between two different wind inputs at the site of interest are also presented in Table 2-2. The average of E_{RMS} (m) and R^2 of the best fit of water level at all of the stations were 0.08 and 0.81, respectively.

The modeled significant wave heights and mean wave directions for different phases of the cold front passage are presented in Figure 2-10. The trend of mean wave direction change between the first cold front and second cold front period was very similar. However, However, the waves during the first cold front passage were more energetic (Figure 2-10b, e). During the postfrontal phase, the significant wave height of the second cold front was slightly higher than the first cold front (Figure 2-10c, f) and the duration of the postfrontal phase of the second cold front lasted longer.

Wave power estimates calculated from the SWAN model results was tested against the observed wave power values at the wave gauge deployment site. For the

calculation of the effective wave power in the simulation, the water depth of the nearest marsh edge grid point most similar to the depth at the measurement was used (R^2=0.88). In addition, the direction corresponding to that of the mean spectrum was used as the wave direction result in SWAN for the calculation of the wave power. For the calculation of the effective wave power in the measurement, wind direction records of the Eagle Point winds were used to represent the wave direction. The modeled bulk wave power includes wave energy from all directions, whereas effective wave power only contains wave energy directed towards the edge of the wetland.

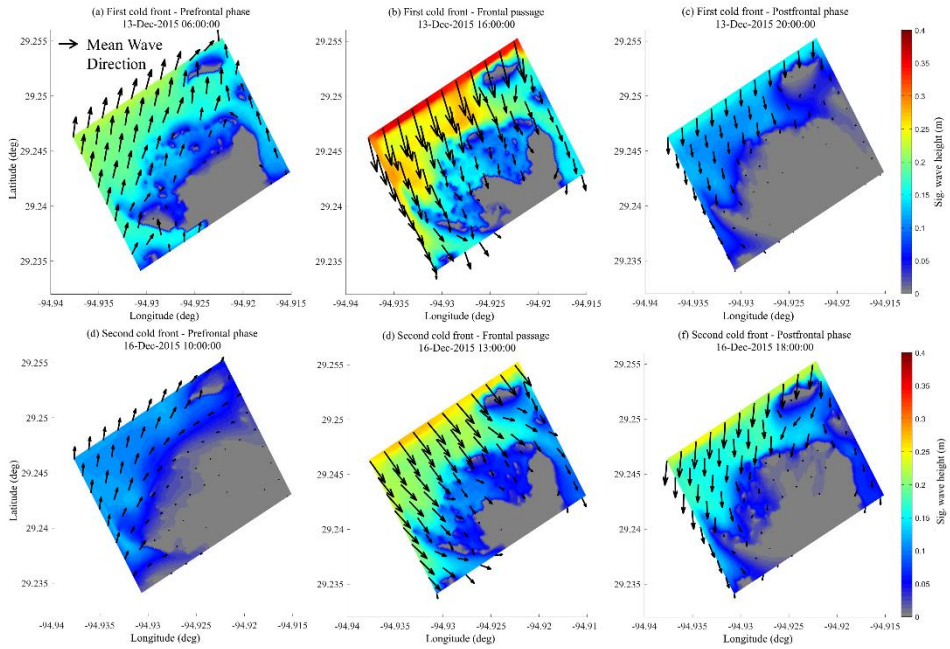

Figure 2-10 Significant wave height and its direction in different phases during the first cold front passage, (a) Dec 13 06:00 UTC (Prefrontal phase), (b) Dec 13 17:00 UTC (Frontal Passage), (c) Dec 13 20:00 UTC (Postfrontal phase) and during the second cold front passage, (d) Dec 16 10:00 UTC (Prefrontal phase), (e) Dec 16 13:00 UTC (Frontal Passage), (f) Dec 16 18:00 UTC (Postfrontal phase)

In addition to effective wave power, inundation of the wetlands also required consideration since the flooding of the wetlands to elevations higher than the marsh edge elevation can reduce the erosion of waves (termed “overshooting”). However, to determine the marsh elevations, a detailed topographic survey of marsh edge elevation based on NAVD88 datum would be required; such a survey is not available. We did initially investigate LIDAR elevation data, and in general the marsh is quite flat in this location. Still, to illuminate the effect of inundation without this data, three estimated inundation cases were calculated for the estimation of the wave effect at the marsh edge while inundated. The water depth at the site immediately after sensor installation (Dec 10, 2015 18:36:00 (UTC)) was approximately 0.1 m, and the maximum water depth during the measurement period was 0.72 m. Data loss due to the extreme high tide exceeding the wave gauge measurement range occurred twice during the measurement period, which means at least two inundation events were observed. Based on the model grid of the marsh edge platform, inundation can be determined, but the simulated records might not represent the actual inundation at the site due to the inability to resolve the distance between the instrument and the marsh edge at the present grid cell size (25 m). To account for this, the critical water depth at which flooding of the marsh platform occurs (thereby nullifying the wave energy impact on the marsh) is set to three values of 0.55, 0.60, and 0.65 m, which were estimated based on measured water depth.

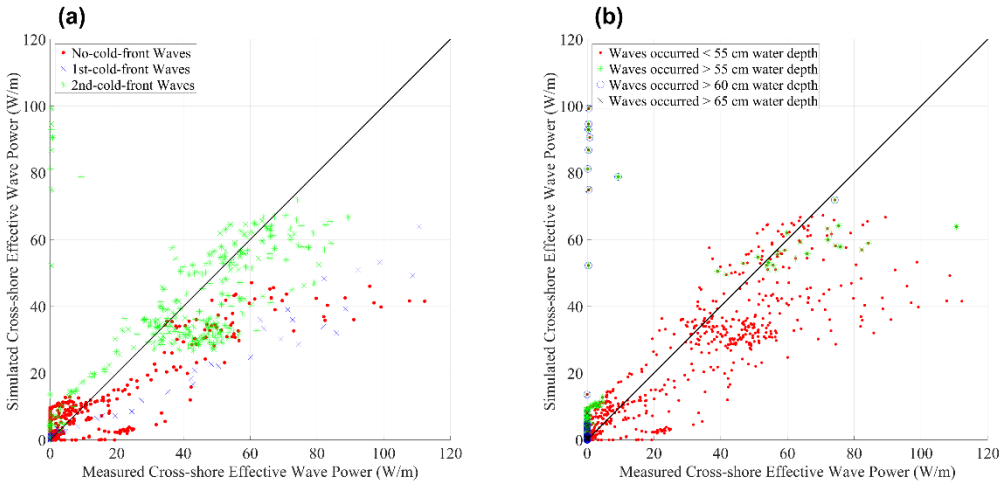

Figure 2-11 Comparison of effective wave power between measurement and model based on the "no-cold-front" period and cold front period (a) and classification of effective wave power based on different water depth thresholds (b)

The comparison between the measurements and the modeled results for cross-shore components of wave power during the entire time period is shown in Figure 2-11. Underestimation of the modeled effective (shore-normal direction) wave power shown in Figure 2-11 is seen in the slightly underestimated significant wave heights and mean absolute wave periods in the model results. Wave power estimates during the second cold front have a lower wave power range of 40 - 60 (W/m), compared to the range of 40 - 110 (W/m) from the first cold front. However, the inundation caused by the strong southerly winds during the prefrontal phase of the first cold front reduced the impact of the high wave power (Figure 2-11b). In contrast, the second cold front had a longer duration, and a relatively low-water level, exacerbating the impact of the wave power on the marsh edge. The values in the y-axis in Figure 2-11(b) represent the waves in measurements during the extremely high-water depth, abnormal data recorded due to

exceeding the gauge measurement range, excluded in measurement records here. These values are considered to have minimal effects on the salt marsh lateral erosion since they have occurred during extreme high water depth.

2.5. Discussion

2.5.1. Sources of model input uncertainty

The results from the DELFT3D-FLOW and SWAN model show accurate predictions of the water level oscillations and significant wave heights during most of the measurement periods at the site. Some disparity with measurements of significant wave height was found, especially during Dec 13, the prefrontal phase of the first cold front. The likely cause of the model errors was the spatial difference between the model output location and the location of the measurement since the 25 m grid resolution was coarser than the 5 m distance between the measurement location and marsh edge. Because of this disparity, the modeled results likely included more waves in the opposite direction of the salt marsh edge. It is believed that the significant change in topographic data by wetlands shoreline retreat around the study site between 2007 (when the topographic survey was done) and 2015 (measurement period) could have also contributed to the discrepancy between the modeled and observed significant wave height. The salt marsh erosion for the change in the estuarine hydrodynamics is considered to influence tidal amplitude and asymmetry. Moreover, the marsh deterioration can reduce the sediment stock in back-barrier basins and therefore compromise the resilience of salt marshes (Donatelli et al., 2020). Bathymetric data fit to the 25 m resolution grid around the wetlands boundary could also cause inconsistency in

the significant wave height calculation since there would likely be discrepancies in shoaling rates and wave breaking locations between model and measurement. Wind input used in the model was also 7 km away from the site of interest, which may cause errors in simulating the modeled wave properties. A significant difference in wind velocity during Dec 11 was found, but differences in averaged winds and wind gusts during the cold front passages were minimal. Moreover, the SWAN model usually overestimates the wave energy for waves of lower wave height; causing a discrepancy in significant wave height difference. Seibt et al. (2013) determined that SWAN simulations with measured wind fields tend to overestimate waves with low wave amplitudes and to underestimate waves with higher wave amplitudes regardless of the modification of the specified parameters. The SWAN results in this study using default parameters for JONSWAP bottom friction (0.067 $m^2 s^{-3}$) and depth-induced wave breaking γ ratio (= 0.73) also showed this tendency in the significant wave height results. In this study, the wind gust data that was used was slightly higher than the averaged wind during the cold front passages and may offset the effect of underestimation of the significant wave heights.

2.5.2. Characteristics of cold front induced wave climate

A similar pattern of cold front induced hydrodynamic forcing was observed in the water level and the significant wave height during prefrontal, front passage, and postfrontal phases. The water level was highest at the end of the prefrontal phase, and the significant wave height was the highest immediately after the prefrontal phase, and thus during the postfrontal phase. High water level conditions during the prefrontal

phase allowed the generation of larger significant wave heights, which were critical to the potential marsh edge erosion. However, this situation was abated by the fact that the marsh edge is completely inundated by the higher water level. It is hypothesized that the wave energy affecting the marsh edge is highest when the water level is the same or just above the marsh edge ground level, and that the wave environment along the north-facing marsh at the site is most energetic during the postfrontal phase of cold fronts. During the second cold front, higher significant wave heights in the postfrontal phase continued for two days with minimal (or no) inundation after its passage at the Galveston Bay. This combination of strong waves and lower water levels allowed the marsh edge to be intercepted with greater wave energy for a longer duration. The wind direction was usually close to shore-normal relative to the north-facing marsh edge immediately after the frontal passage and during the postfrontal phase, and this period had the most critical effect on the potential erosion of the marsh. However, it should be noted that the favorable model comparisons realized by using gust wind input may be related to the characteristics of the default wave generation mechanisms and parameters employed in this study.

2.5.3. Potential impact of results

To analyze the most significant likely cause of the marsh erosion at the site of interest, cumulative effective wave power from both measurement and model during three periods (“No-cold-front", first cold front, and second cold front) are shown in Figure 2-12 (a), (c). To distinguish wave power invalidated by the inundation of the

marsh platform, four immersion thresholds (No inundation, 0.65 m, 0.60 m, and 0.55 m) are also presented.

Overall, the measurements and model values were in good agreement. Because only one wave gauge was used, the wave direction was not measured but instead assumed to be the same as the wind direction. This can lead to potential errors in the measurement results of effective wave power. However, according to the results of the model, the errors were considered minimal, especially during the passage of the cold front since the wave direction closely coincided with the wind direction when the winds blew in the same direction for more than a given time. From the cumulative effective wave power results (Figure 2-12a, b), it was likely that cold front induced waves were a significant driver of potential marsh edge retreat in the Galveston Bay wetlands considering its short duration (first cold front - 24.6 hours, second cold front - 30 hours). The first cold front showed the highest wind gusts for a relatively short time, but after its passage, the duration of the postfrontal phase over which the waves approached the marsh boundary was short. This results in less cumulative effective wave power of the first cold front to the site of interest even though its bulk wave power was 110 % higher than the effective wave power.

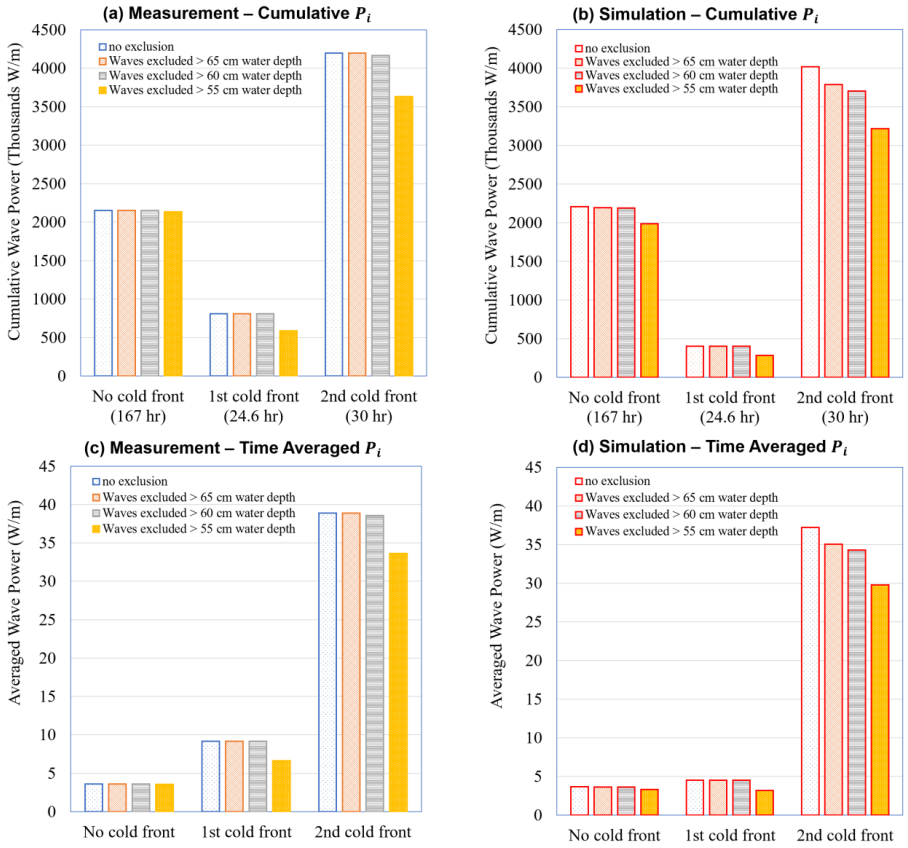

Figure 2-12 Plot of cumulative effective wave power with different salt marsh platform thresholds in measurement (a) and simulation (b), plot of averaged effective wave power with different salt marsh platform thresholds in measurement (c) and simulation (d)

On the other hand, the second cold front arrived with moderate wind gusts for a relatively long time, with limited flooding affecting the marsh edges with elevated wave energy over a long duration. Unlike the first cold front, the winds during the postfrontal phase were much higher than that of the prefrontal phase (Figure 2-6b), which results in a significant effect on the accumulation of wave energy toward the north-facing salt marshes (Figure 2-12).

The duration of time without a cold front (“no-cold-front" period), the first cold front, and the second cold front were 167 hours, 24.6 hours, and 30 hours, respectively. The time-averaged effective wave power of the second cold front was the highest among the three periods, likely due to its duration (Figure 2-12c,d).

In the comparison of the wave power along with the immersion thresholds, there was no sudden cumulative wave power reduction except in the scenario of flooding at 0.55 m. Using estimated flood elevations of 0.65 m and 0.60 m, the effective wave power reduction was minimal, due to the postfrontal winds which contributed to the rapid reduction of the water depth in the Galveston Bay. Therefore, after passing through the cold front, the possibility of flooding is greatly reduced, so that the wave energy can affect the edge of the salt marsh without loss.

Leonardi et al. (2016) suggested that winter cold fronts called winter storms which accompany strong winds, can lead to more erosion than hurricanes and found that waves with a return period of 2.5 months have the highest effect on salt marsh deterioration. In connection with these findings, additional parameters such as the presence of wind gusts, the wind direction change, and water level change during cold fronts may need to be considered together as factors in determining the cause of wetland erosion in shallow bays.

2.6. Summary and conclusions

The model successfully reproduced the observed tides and waves in the relatively shallow depths of West Galveston Bay. This case study demonstrates the effect of cold-front-induced wave and water level amplification on the edge of bounding wetlands.

Compared to that of storm surge, the role of seasonal cold fronts and the generated waves on impact and erosion of wetlands has not been as well identified. From the measurement and the model results, the following findings can be derived. First, wind gusts during the cold front passage affect the wave conditions in the area, making its use essential for modeling wind input. Furthermore, from the prefrontal phase to the passage of cold frontal edge, an increase in water elevation in the coastal microtidal bay was observed both in first and second cold fronts which are caused by wind-driven currents to the bay during the prefrontal passage. Increased water level changes the wind-wave growth characteristics within the bay from partially depth limited condition to fully fetch limited condition, ensuring additional wave growth. During the passage of the frontal edge, increased gustiness of the winds increases the significant wave heights to a level in which the erosion of the salt marsh edge was possible. However, when high tide coincided with the prefrontal phase, the water level in the microtidal bay increased to the point where the inundation of the wetlands occurred, which reduced the possible erosive impact of the generated waves. Additionally, considering the time-averaged wave power of the second cold front, we determined that the cumulative wave power increase at a faster rate when a cold front was moving through the area relatively slowly. Under the assumption that the waves move in line with the wind (applicable for wind-generated waves), the waves during the “no-cold-front" period had no distinct directionality, limiting its impact on the marsh edge.

In contrast, the cold front-induced waves had a clear preferential direction throughout the prefrontal, frontal passage, and postfrontal period. This is indicated by the high cumulative wave power value of the second cold front (4,200,000 W/m) compared to the no-cold-front period (2,150,000 W/m) even though the measurement period of the no-cold-front period (167 hours) was much longer than the second cold front (30 hours). We confirmed that the second cold front-induced waves had a greater impact on north-facing salt marsh erosion during the frontal passage and postfrontal with its high cumulative wave power at the site of interest. In this study's investigation of cold front induced surge and waves, high gusts and winds from cold fronts increased tide and waves along the shallow bay. The occurrence of gusts and dynamical changes in wind direction during the cold front passage can have a significant impact on changes in water depth, wave amplitude, and ultimately on the potential erosion rate of salt marshes in shallow bays. Considering that the number of times that cold fronts pass per year is higher compared to that of hurricanes, the potential impact on lateral erosion of coastal wetlands is thought to be significant. Moreover, prefrontal winds and postfrontal winds that occur as the cold front passes through can significantly affect the salt marsh edges facing the opposite of their wind directions, evidenced by the postfrontal wind's effect on the north-facing salt marshes in the study. Subsequently, the characteristics of these cold fronts can have a lasting effect on salt marshes in specific locations in shallow bays.

Now that the model has been verified for this application, it can be used to gauge the effect of wave action on barrier island salt marshes, and further also be used to determine the cumulative wave power of the entire cold front passing each year to

associate with the annual salt marsh retreat rate. The model can provide wave data to identify the role of wave energy affecting total salt marsh erosion. However, such modeling work could be coupled with extensive field measurements of marsh platform height, soil, and vegetation properties.

3. INVESTIGATION FOR WETLAND LATERAL EROSION BY WAVES IN LABORATORY EXPERIMENT

3.1. Introduction

Salt marshes exist in protected coastal saltwater environments at the interface between the uplands and the coastal ocean. Their characteristics change with latitude, and a broad range of salt marsh types can be identified based on vegetation, composition, and community structure (Adam, 1993).

In recent years, increasing rates of sea-level rise (Alizad et al., 2016), human-induced subsidence (van der Wal and Pye, 2004), and the loss of marsh around the world (Gedan et al., 2009), have emphasized the importance of understanding the response of these environments to human-induced climate changes. It is essential to understand the relationships among these physical and biological processes to protect and promote the management of these environments (Bendoni et al., 2014).

Previous studies on these systems have focused on the fundamental mechanisms that trigger the morphological change in salt marshes. Schwimmer (2001) found a linear relationship between wave power and salt marsh edge erosion. Mariotti and Fagherazzi (2010) showed that retreat/progradation of a marsh scarp results from the interaction among vegetation, sediment supply, and sea-level rise.

Marani et al. (2011) investigated the waves acting on marsh edges through dimensional analysis and showed that the incident wave power density is linearly related to marsh edge erosion rate. McLoughlin et al. (2015) also measured the lateral erosion

and calculated wave power using the SWAN model. However, these results are based on modeled wave data which may not fully reflect the actual mechanics in the field. The potential discrepancy is largely due to a lack of bathymetry and topography in these models. An additional problem can be that model resolution (grid size) is insufficient to accurately reproduce wave-based processes.

Only a few studies have been published on the physical mechanisms at the interaction of the wetland edge and the pore water pressure fluctuations by wind-waves and by tides. Feagin et al. (2009) investigated the role of soil types and vegetation in the bank retreat in salt marsh systems by wave force. Francalanci et al. (2013) conducted a laboratory experiment using bank models and hydrodynamic forcing to identify the bank retreat rates with and without vegetation. They found that the impulsive effects associated with wave energy dissipation affect bank instability. Bendoni et al. (2014) found that critical conditions causing bank topping failure are associated with low water level conditions and water present within tension cracks.

There are three types of lateral marsh edge erosion—particle by particle erosion, small-scale slides on the bank, and toppling failures. When hydrodynamic stress on the soil surface is sufficient to remove particles, particle-by-particle erosion can occur. The shape of the bank can slightly influence this process. Slides occur as a combination of a detachment of material under tensile stress along an arcuate surface and a contemporary slide. Toppling (slab) failures often occur due to the presence of deep tension cracks (Francalanci et al., 2013). It is assumed that one of the main causes of salt marsh erosion

is particle-by-particle erosion by waves. Therefore, in this chapter, particle-by-particle erosion through the wave flume experiment was investigated.

The experimental methods used in this study have the potential to determine the mechanisms of salt marsh surface erosion by waves through visual and instrumental measurements under controlled conditions that are usually difficult to capture in the field. The study investigated the wave force affecting the salt marsh edge through open channel basin experiments using saltmarsh samples collected in the field. Erosion rates of sampled salt marsh based on different incident wave height, water level conditions and the presence or absence of plants were tested.

3.2. Field collection of salt marsh core samples

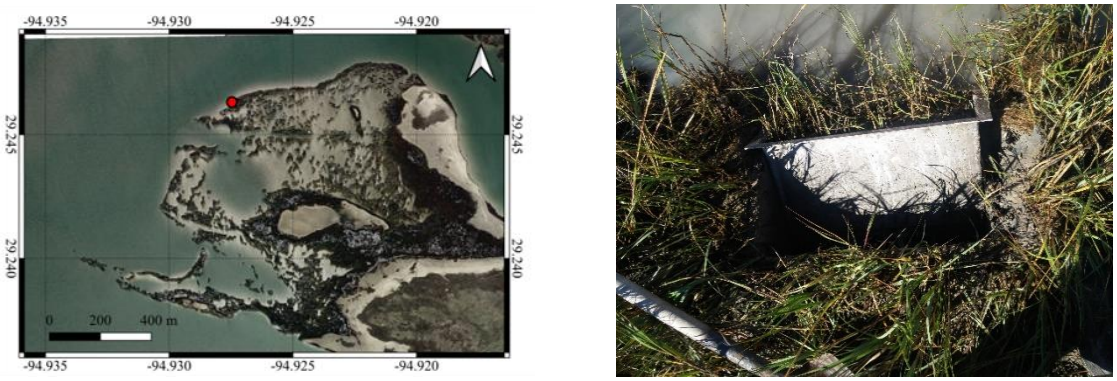

(a) **(b)**

Figure 3-1 Field test site location at the Galveston Bay (a) and sampled core at the site location (b)

The core sample site located at 29° 14' 46.55"N and 94° 55' 38.26"W, Melager Cove, where the saltmarsh boundaries present in the West Galveston Bay side of

Galveston Islands (Figure 3.1a). The wetlands are affected by regular tides and waves generated by cold fronts blowing winds across the 6 km fetch.

(a) **(b)** **(c)**

Figure 3-2 A sampled core extracted by aluminum core (a,b) and stored in wooden box (c)

The samples were extracted by the wooden box with outer dimensions of 65 cm long, 30 cm wide and 37.5 cm tall. The box was constructed out of 3/4th-inch plywood, as shown in Figure 3-2 (c). Cored samples were extracted several centimeters from the edge of the salt marsh, including the plant *Spartina alterniflora*. Six vegetated samples were extracted for the experiment.

3.3. Shallow water 3D basin experimental set-up

The 3D basin wave tests were done at the Haynes Coastal Engineering Laboratory at Texas A&M University. The laboratory has a shallow water wave basin (22.9 m wide, 36.6 m long, and 1.2 m deep) with a directional wave generator that operates in up to 1.0 m water depth and capable of generating regular and irregular waves.

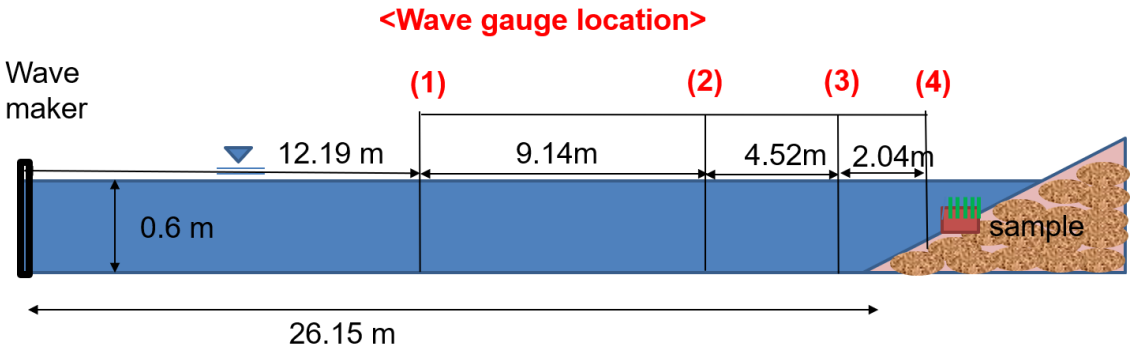

Figure 3-3 Experimental setup at three-dimensional wave basin

Four-wave gauges were installed in the tank; sample and gauge locations are shown in Figure 3-3. The first wave gauge was located in the middle of the basin. The second wave gauge was located 3/4 from the wavemaker, and the remaining two-wave gauges were located in front of the sample at different distances.

The regular wave has a period range of 0.5 to 5 seconds. The propagation angle also can be specified from 0 to 60 degrees. As the spectrum of waves, the facility can use JONSWAP (Carter, 1982), Pierson-Moskowitz (Alves et al., 2003), or other spectral shapes. The wave generator also includes a wave absorption system to remove re-reflected waves, the downwave end of the basin used a rock slope to absorb waves. The

wave absorption material is sometimes used to absorb waves contacting the side walls of the 3D wave basin.

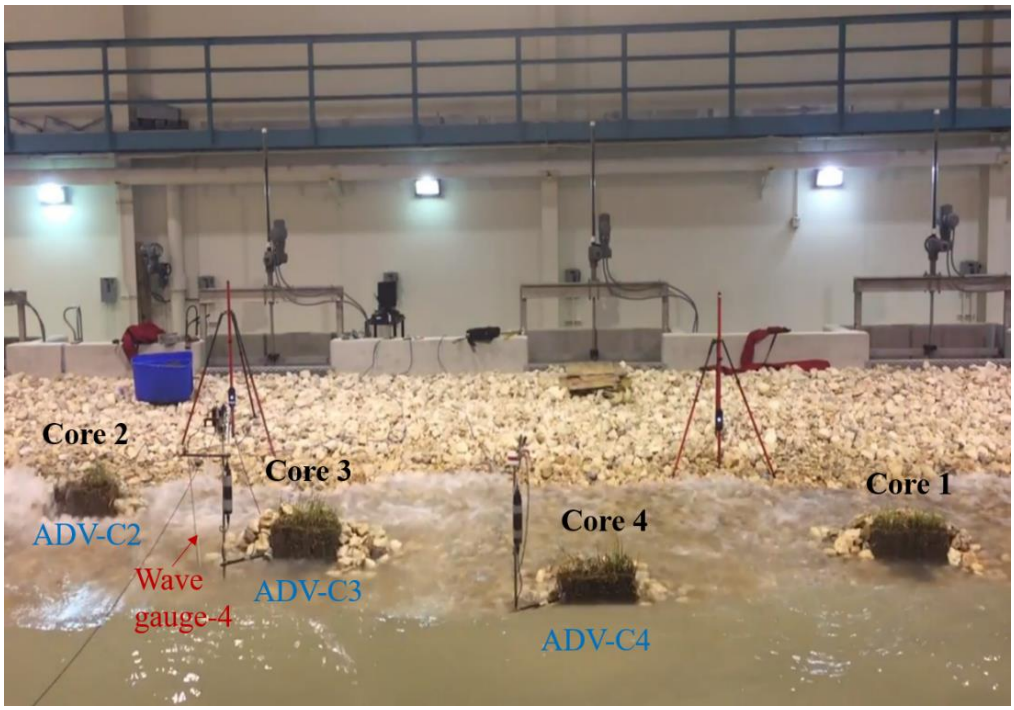

Figure 3-4 Test core samples fixed on the wave absorption material, a wave gauge and ADVs fixed in front of the samples

The sample cores were fixed by surrounding rocks. The relationship between core samples and adjacent wave gauges is summarized in Table 3-1.

Table 3-1 Water depth of the core samples, adjacent wave gauges, and ADVs

Sample Core No.	Water depth (m) at toe	Adjacent wave gauges	ADV
Core-1	0.17	Wave gauge-4	
Core-2	0.05	-	ADV-C2
Core-3	0.15	Wave gauge-4	ADV-C3
Core-4	0.26	Wave gauge-3	ADV-C4

Test Core-1 and Core-3 were located at nearly the same water depth. Thus, it was assumed that the data for wave gauge 4, located in front of the Core-3, was applicable for Core-1. However, for Core-2, there was no adjacent wave gauge. The Core-2 was located on the top of the rock beach slope, and the water depth was approximately 0.05 m. Thus, most incident waves were breaking waves at this location, with the exception of the 8 cm wave input. For Core-2, the wave power was calculated separately based on incident wave height and the shallow water approximation. Test samples were located at different heights within the rock slope, as shown in Figure 3-4.

The experiment settings based on wave parameters are :

- Water depth: 0.6 m (Constant in every experiment)
- Input wave type: Sinusoidal wave (Progressive wave)
- Incident wave period: 2 s (0.5 Hz)
- Incident wave height: 8 cm, 12 cm, 16 cm, 20 cm, 24 cm, 32 cm

Regular sinusoidal waves were generated with a height of 8 cm, 12 cm,18 cm, 20 cm, 24 cm, and 32 cm for the test of different wave power to salt marsh samples. The time duration of a regular wave was one hour for 8 cm and 12 cm waves, 30 minutes for 16 cm and 20 cm waves, 20 minutes for 24 cm and 32 cm waves. Different water depth conditions for core samples were also conducted by adjusting sample locations on the slope in the same wave condition. These were performed by lowering the angle of the rock beach in front of the weirs and by placing samples in front of the rock absorption system.

Regular waves impacting samples were reflected by the rock beach and by the test sample. The reflected wave could not be determined by a single wave gauge. Goda and Suzuki (1976) suggested the reflection analysis using two simultaneous wave records taken at nearly adjacent locations.

Figure 3-5 Installation of an ADV measurement in the laboratory experiment

The test core sample's erosion rate was measured by Light Detection and Ranging (LIDAR) equipment. LIDAR can scan the soil volume changes of each sample surface. The erosion rate was evaluated as a function of wave height and wave number acquired from the wave gauges. The current velocity at the front of the core samples (Figure 3-5) were measured by Acoustic Doppler Velocimeter (ADV), an acoustic instrument with the potential to offer the accuracy of laboratory devices even under field conditions (Lohrmann et al., 1994). It offers unobstructed three-dimensional flow measurements at high sampling rates and with a small sample volume. Site deployments have proven that the sensor can be easily deployed with moored instruments (Anderson

and Lohrmann, 1995) or attached to a structure near the seabed (Lohrmann et al. 1995). The results of the ADV analysis are shown in Appendix A.

3.4. Wave parameters

For the analysis of wave and salt marsh interactions, it was necessary to consider the effects of water depth. Water depth regimes can be divided by deep, intermediate, and shallow water based on the relationship between wavelength and water depth. Limits for different water depth regions can be calculated by the value of kh where k is wave number, and h is water depth. In the condition of $kh < \pi/10$, the waves are in shallow water (Long wave). In $\pi/10 < kh < \pi$ condition, the waves are in intermediate water, and in $kh > \pi$, the waves are deep water waves (short wave).

Boussinesq (1877) and Korteweg and de Vries (1895) were separately developed, which led to opposite conclusions regarding wave breaking in constant depth. The confusion was resolved by Ursell (1953). Ursell has shown that the ratio provides information on the choice of approximations, which correspond to very different physics. Ursell number, defined as:

$$U_r = \frac{A}{h}\frac{1}{(kh)^2} = \frac{kA}{(kh)^3} = \frac{A\lambda^2}{h^3(2\pi)^2} \qquad 3\text{-}7$$

where A is the wave height, λ is the wavelength. Ursell number indicate the nonlinearity of the wave.

The evolution of wave shapes is important to investigate the likeliness of the wave breaking at a finite water depth (Caulliez, 2002; Young and Babanin, 2006; Kaihatu et al., 2007). The wave skewness and asymmetry are considered as inherent

characteristics of wave breaking (Babanin et al., 2007). For monochromatic waves, geometric definitions of skewness, S_k and asymmetry, A_s can be defined as:

$$S_k = \frac{a_1}{a_2} - 1 \qquad 3\text{-}8$$

$$A_s = \frac{b_1}{b_2} - 1 \qquad 3\text{-}9$$

where a_1, a_2, b_1 and b_2 are defined in Figure 3-6.

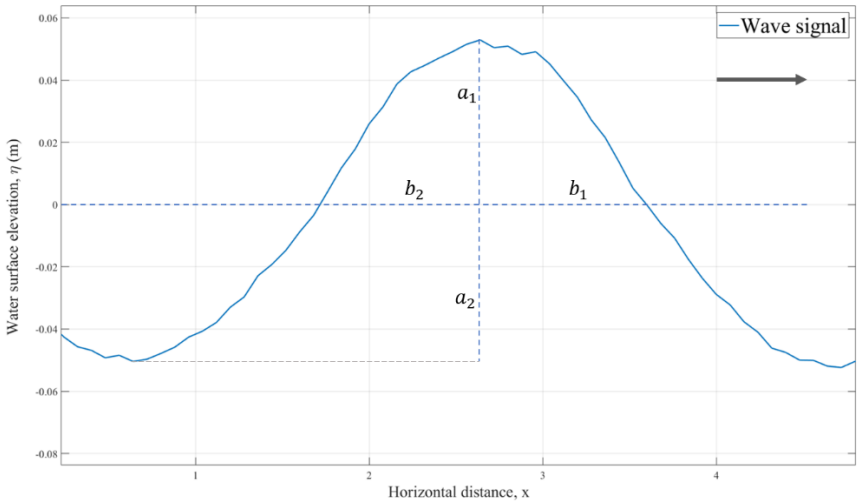

Figure 3-6 A wave signal and related geometric definitions of skewness and asymmetry

Positive skewness represents a crest sharper than the trough, and negative asymmetry represents a wave tilted forwards. Experimentally observed asymmetry A_s has been broadly associated with the wave breaking (Caulliez, 2002; Young and Babanin, 2006). The asymmetry of the wave in shallow water induces the asymmetrical forces that influence the nearshore sediments and coastal structures to a very great extent. Thus the asymmetry of the wave is important for the understanding of the shallow water wave processes.

3.5. Estimation of the incident and reflected waves

Goda and Suzuki (1976) suggested a technique to extract incident wave height from the signal of waves generated and reflected by structures and energy absorbers in the flume. If the surface elevations are recorded at two adjacent stations of x_1 and $x_2 = x_1 + \Delta l$ where Δl is the distance between two wave probes, the amplitude of superposed incident waves a_I and its reflected waves a_R can be estimated as follows.

$$a_I = \frac{1}{2|\sin k\Delta l|}\sqrt{(A_2 - A_1\cos k\Delta l - B_1\sin k\Delta l)^2 + (B_2 + A_1\sin k\Delta l - B_1\cos k\Delta l)^2}$$
$$a_R = \frac{1}{2|\sin k\Delta l|}\sqrt{(A_2 - A_1\cos k\Delta l + B_1\sin k\Delta l)^2 + (B_2 - A_1\sin k\Delta l - B_1\cos k\Delta l)^2} \quad \text{3-10}$$

There may be several methods to estimate the incident and reflected wave heights on the basis of spectral resolution. In Goda and Suzuki (1976), the effective range of resolution is set for a given gauge spacing. The lower and upper limits of frequency, f_{min} and f_{max} are better chosen by a preliminary test for progressive waves. The following guidline may be consulted:

$$f_{min} : \frac{\Delta l}{L_{max}} = 0.05,$$
$$f_{max} : \frac{\Delta l}{L_{min}} = 0.45 \quad \text{3-11}$$

In the calculation, the dispersion relation is presumed to hold.

The second step is to evaluate the energies of the resolved incident and reflected waves, E_I and E_R, contained between f_{min} and f_{max}, i.e.,

$$E_I = \int_{f_{min}}^{f_{max}} S_i(f)\ df, \quad \text{3-12}$$

$$E_r = \int_{f_{min}}^{f_{max}} S_r(f)\ df$$

The final step is to estimate the overall coefficient of reflection by

$$K_r = \sqrt{\frac{E_R}{E_I}} \qquad 3\text{-}13$$

The incident and reflected wave heights, H_I and H_R, are calculated as

$$H_I = \frac{1}{\sqrt{1 + {K_r}^2}} H_s$$
$$H_r = \frac{K_r}{\sqrt{1 + {K_r}^2}} H_s \qquad 3\text{-}14$$

3.6. Spectrum analysis and Wave power

The significant wave height (the spectrum wave height) H_{m0} and the peak period T_p were calculated by spectrum analysis using wave gauge records according to the following equations:

$$H_{m0} = H_s = 4\sqrt{\int_0^\infty S(f)df}$$
$$T_p = \frac{1}{f_p} \qquad 3\text{-}15$$

where $S(f)$ is the frequency spectrum and f_p is the spectrum peak frequency.

Schwimmer (2001) found that the marsh regression rate is correlated to the averaged wave power, defined as:

$$P_w = \left(\frac{\rho g H_s^2}{8}\right) C_g \qquad 3\text{-}16$$

where H_s is significant wave height, ρ is the water density, and C_g is the wave group velocity, where:

$$C_g = \frac{1}{2}\sqrt{\frac{g}{k}\tanh kh}\left(1 + \frac{2kh}{\sinh(2kh)}\right) \qquad 3\text{-}17$$

In shallow water (kh< π/10), $C_g = \sqrt{gh}$. For the calculation of wave power for Core-2, shallow water approximation for C_g was used in the analysis.

3.7. Wave properties and reflection of waves

Consideration of the salt marsh erosion by wind waves is a complex phenomenon. It includes mechanisms such as the continuous removal of small particle aggregates from the marsh platform and marsh edges. In addition, sudden and discontinuous detachment of marsh portions is another reason for erosion (Bendoni et al., 2014). The experiment here did not include the sudden and discontinuous detachment of marsh portions. The time duration of the waves and core samples' width (30 cm) were not targeted to reproduce the phenomenon.

First, the properties of each incident wave cases (8 cm, 12 cm, 16 cm, 20 cm, 24 cm, and 32 cm) were analyzed to verify the shallow water processes during its progress to the wetlands sample and wave energy absorber (gravel). The default water depth of the basin was 0.6 m. Based on water depth and input wave period (2 seconds), the wavenumber *k* of the entire flat floor of the basin, excluding rock beach slope, was calculated by linear dispersion relation. The *k* was calculated as 1.44, and $kh = 0.86$, which is smaller than one but not smaller than π/10. Thus the waves over the flat floor of the basin are in intermediate depth, where the nonlinearity of waves is not believed to be

significant. At the location of Core 3, placed at about near to half the height of the rock beach slope, the water depth h was 0.15 m, and k was 2.68. Here, $kh = 0.4$ and waves are still intermediate depth water waves. Thus, Core 1, 3, and 4 are in the intermediate depth regimes, and where shallow water nonlinear effects are believed to be small. However, in Core 2, the water depth was extremely low (0.053 m), and kh = 0.233, so is thus in shallow water.

The Ursell parameter of each incident wave heights at the constant depth was calculated and shown in Figure 3-7. The Ursell parameter denoted by U_r, also can be the parameter that determines the nonlinearity of the wave in addition to wave breaking. For long waves ($\lambda \gg$ h) with small Ursell number, $U_r \ll 100$, linear wave theory is applicable.

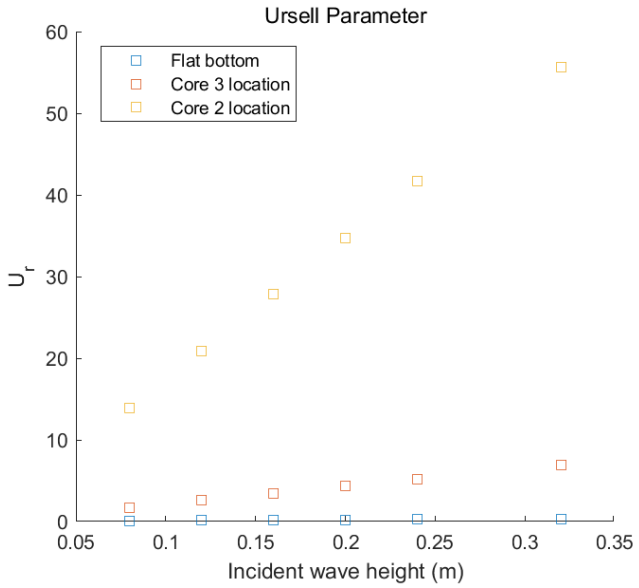

Figure 3-7 Ursell parameter of each incident wave in the experiment

At Core 2 location, with the increase in wave height, the Ursell parameter drastically increased from U_r = 13 to U_r =56, thus the nonlinearity of the wave increased. The skewness and asymmetry of each monochromatic wave were calculated based on equation 3-8 and 3-9 using wave gauges' time series records. Part of wave gauge records, skewness, asymmetry, and frequency of each incident wave input (8 cm, 12 cm, 16 cm, 20 cm, 24 cm, and 32 cm) were shown in Figure 3-8 to 3-13.

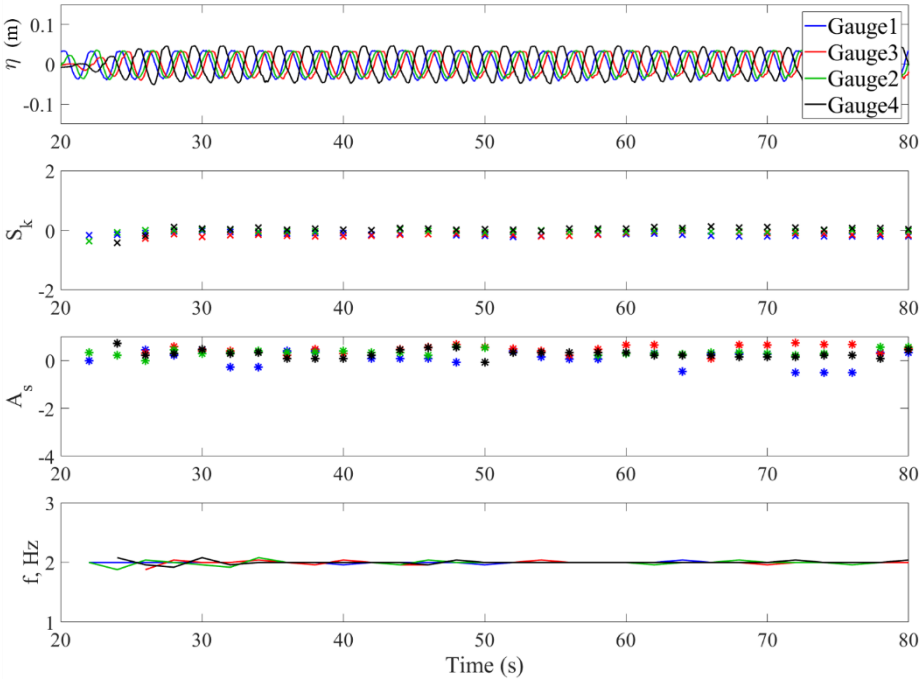

Figure 3-8 Time series of wave gauge records, skewness, asymmetry, and frequency of monochromatic waves (Input wave height: 8 cm)

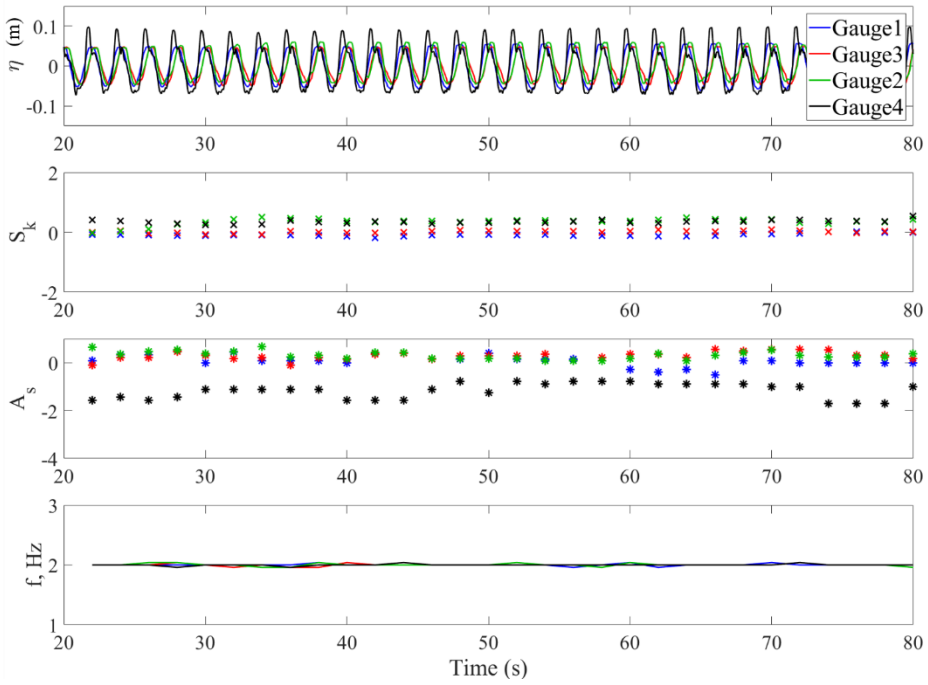

Figure 3-9 Time series of wave gauge records, skewness, asymmetry, and frequency of monochromatic waves (Input wave height: 12 cm)

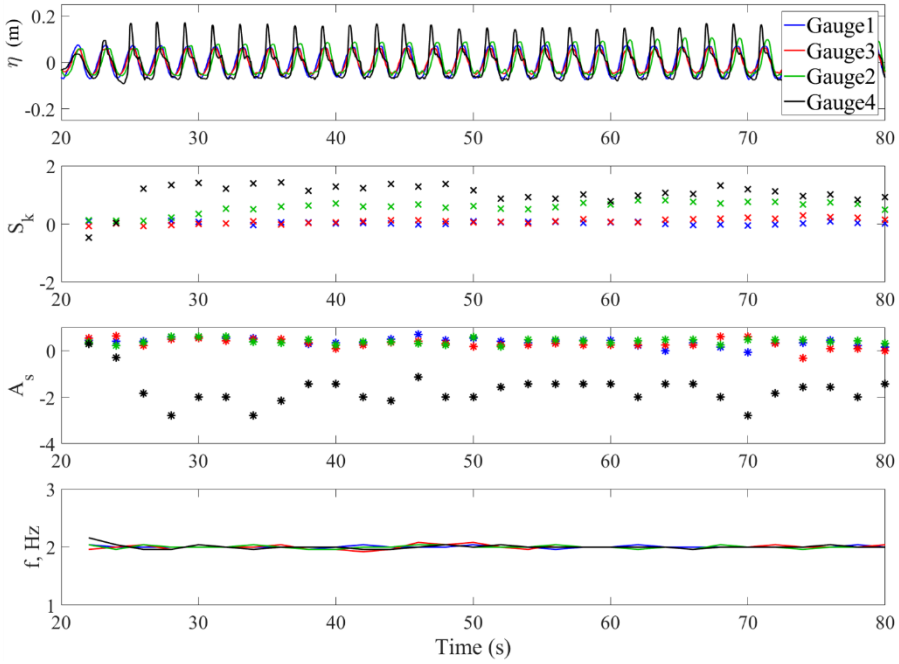

Figure 3-10 Time series of wave gauge records, skewness, asymmetry, and frequency of monochromatic waves (Input wave height: 16 cm)

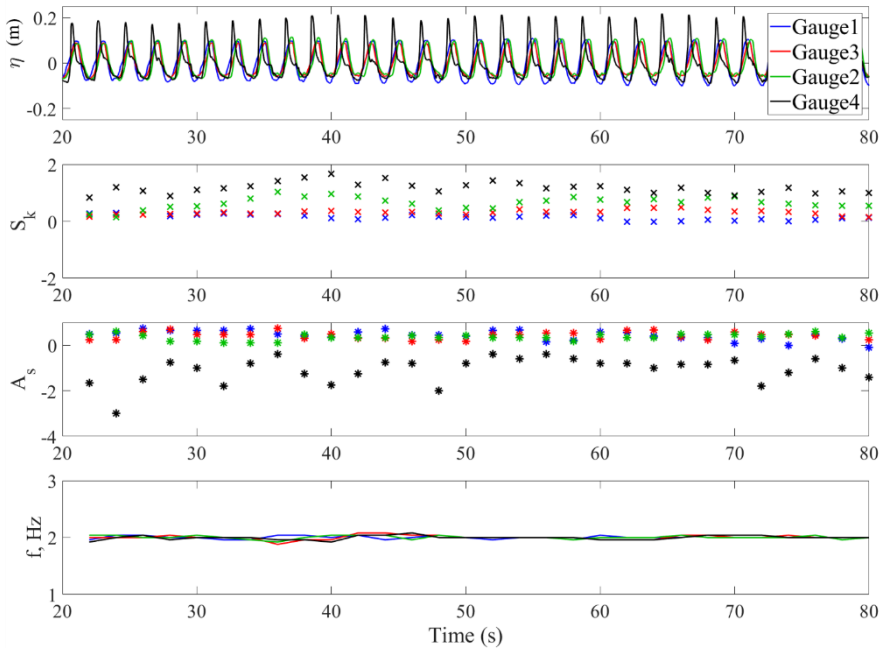

Figure 3-11 Time series of wave gauge records, skewness, asymmetry, and frequency of monochromatic waves (Input wave height: 20 cm)

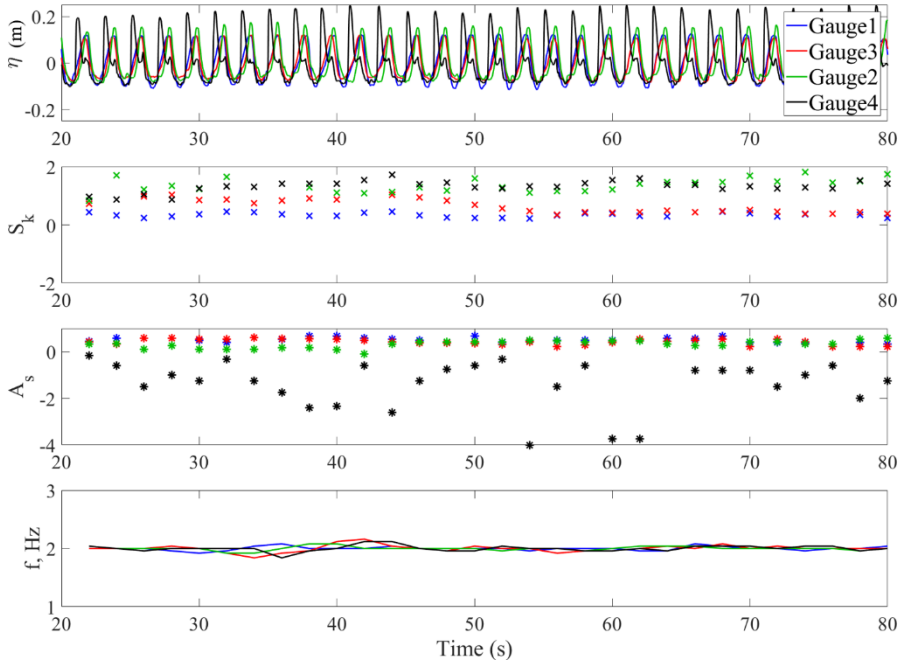

Figure 3-12 Time series of wave gauge records, skewness, asymmetry, and frequency of monochromatic waves (Input wave height: 24 cm)

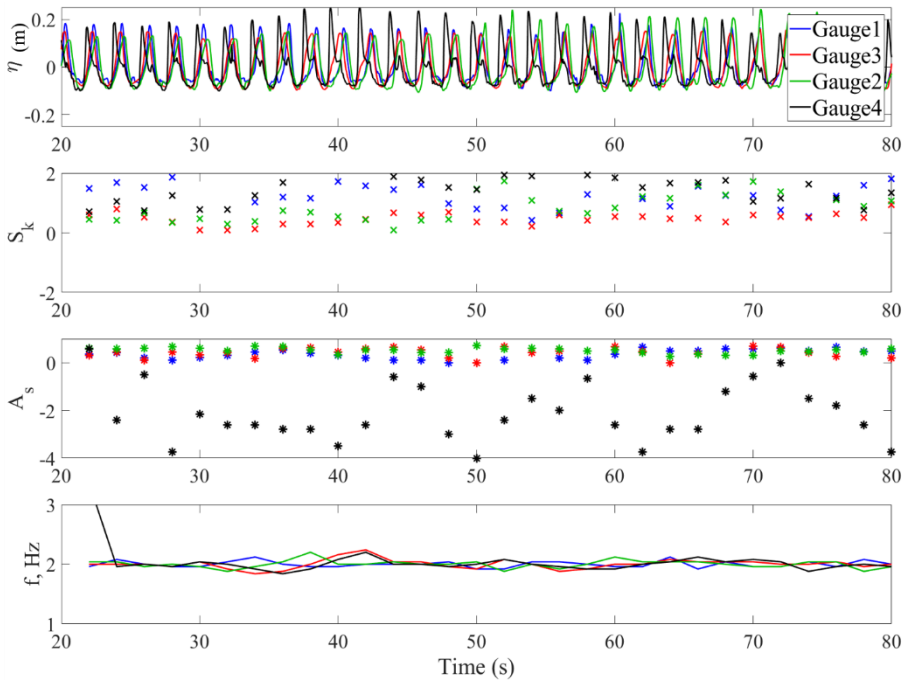

Figure 3-13 Time series of wave gauge records, skewness, asymmetry, and frequency of monochromatic waves (Input wave height: 32 cm)

The skewness of different input wave heights was calculated based on equation 3-18 from four different wave gauges. The averaged skewness of cases with the same wave height at a different distance from the wavemaker is plotted in Figure 3-14.

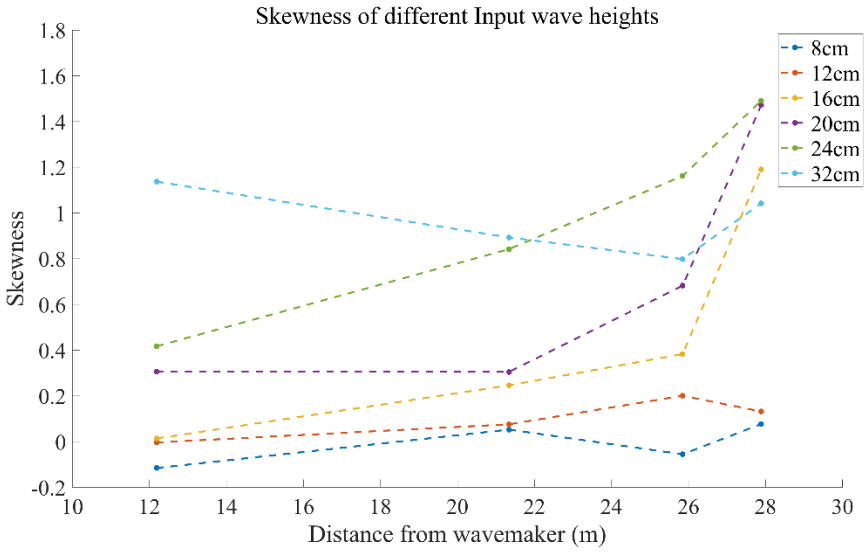

Figure 3-14 Changes in the skewness of each input wave heading to the core samples

The skewness ranged from -0.1 to 0.07 at the incident wave height of 8 cm and 12 cm. For 16 cm incident waves, the skewness significantly increased when the wave approached the rock beach slope. This indicates that the sinusoidal shape was not maintained during the approach to the rock beach over a wave height of 16cm. For the incident wave of 24 and 32 cm, the value of skewness started from 0.4 and 1.15, respectively, which is a comparatively high value compared to waves less than 24 cm. Based on the results, the incident wave heights equal and more than 24 cm were at the status of sharp crest than trough after its generation. Thus linear wave theory was not applicable for the incident wave height of more than 20 cm. The skewness of each of 16, 20, 24, and 32 cm incident waves had a peak value of 1.19, 1,47, 1.49, and 1.04, respectively, near the rock beach slope. The asymmetry of waves was plotted in Figure 3-15.

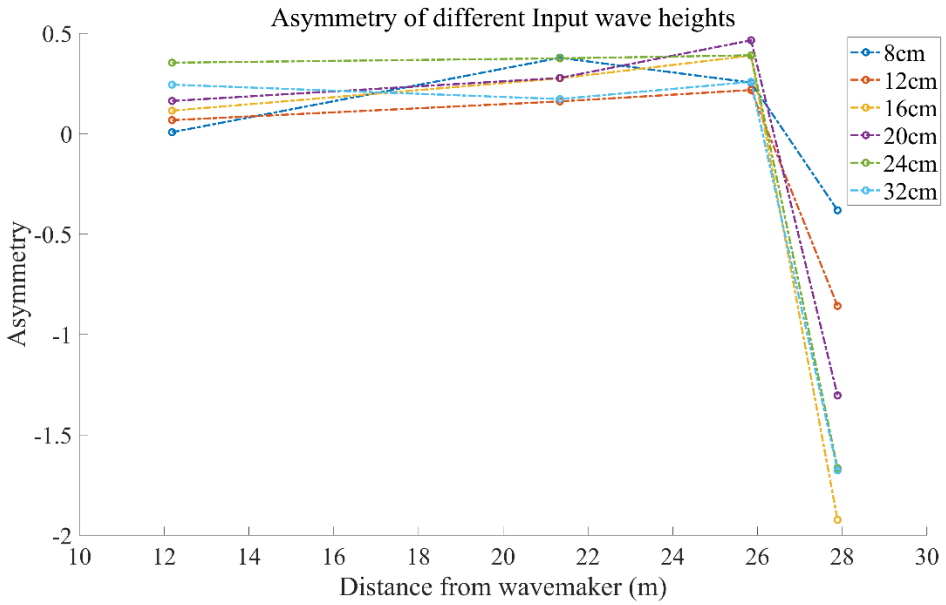

Figure 3-15 Changes in the asymmetry of each input wave heading to the core samples

From the asymmetry of the wave, it is regarded that the wave is likely to break at the location of 26~ 28m from the wavemaker where the rock beach slope is located. Wave breaking processes were recorded through the decreased asymmetry in wave gauge 4. Thus it is considered that the input sinusoidal waves were not maintained at the location of gauge 4. Subsequently, the wave energy at Core 3 needed to be calculated based on the wave gauge close to the Core 3.

The significant wave height, peak period, mean period, and absolute mean period were calculated for each test case. For the analysis, the initial 500 records were truncated to eliminate the signal before the wave generation. The incident wave's frequency is 0.5 Hz, but energy at other frequencies appears in the spectrum analysis mainly due to wave breaking, nonlinear wave-wave interaction, and spectral leakage.

With over 0.2 m of input incident wave height in the experiment, the wave tended to break immediately after the generation of the wave. Table 3-2 shows the significant wave height, peak period, mean period, and absolute mean period of wave gauge-3 located near Core 1 and wave gauge-4 located in front of Core 3.

Table 3-2 Spectrum analysis results for wave gauge-3 and 4

Input wave		H_s (cm)	T_p (s)	T_{m01} (s)	T_{m_10} (s)
8 cm	Gauge-3	9.96	2.0	1.9	2.9
	Gauge-4	13.13	2.0	1.8	2.9
12 cm	Gauge-3	14.88	2.0	1.9	2.2
	Gauge-4	19.35	2.0	1.6	2.2
18 cm	Gauge-3	19.89	2.0	1.9	2.2
	Gauge-4	26.01	2.0	1.3	2.2
20 cm	Gauge-3	26.07	2.0	1.9	2.3
	Gauge-4	34.36	2.0	1.1	17.6
24 cm	Gauge-3	23.08	2.0	1.8	7.1
	Gauge-4	24.85	2.0	1.1	10.1
32 cm	Gauge-3	35.61	2.0	1.6	2.3
	Gauge-4	27.78	2.0	1.1	5.2

Wave reflection coefficient was calculated based on equations 3-3 to 3-5 and shown in Figure 3-16. The frequency f_{max} was selected as 0.5 Hz, its input, and peak frequency. The minimum frequency f_{min} was set to 0.05 Hz. The range of K_r was between 0.1 to

0.25 depending on the input wave height. By increasing the incident wave height, K_r also tended to increase. Incident significant wave height H_I and reflected significant wave height H_r of wave gauge 3 and wave gauge 4 were calculated based on the reflection coefficient using Equation 3-7 and shown in Figure 3-17.

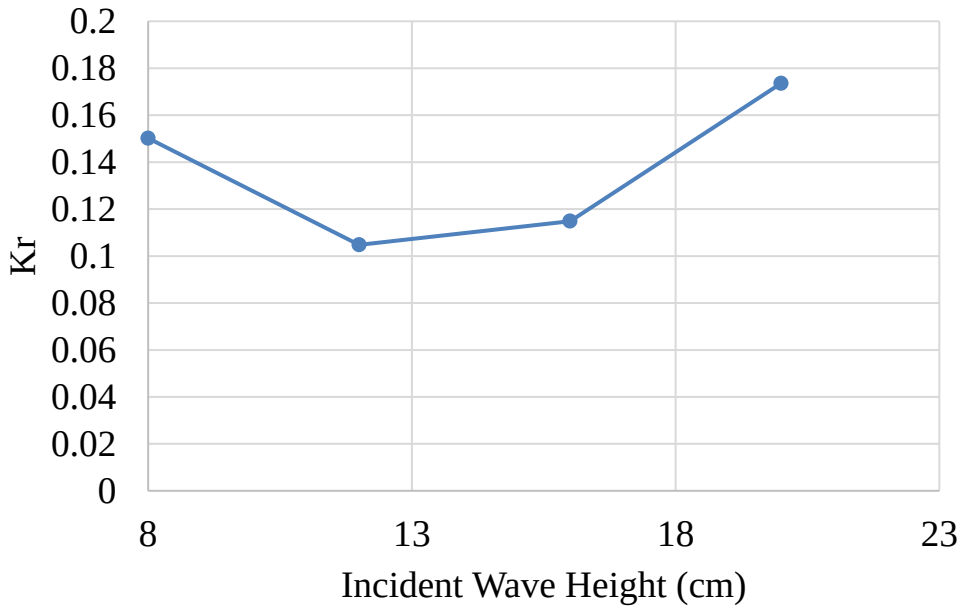

Figure 3-16 Reflection coefficient by different wave input

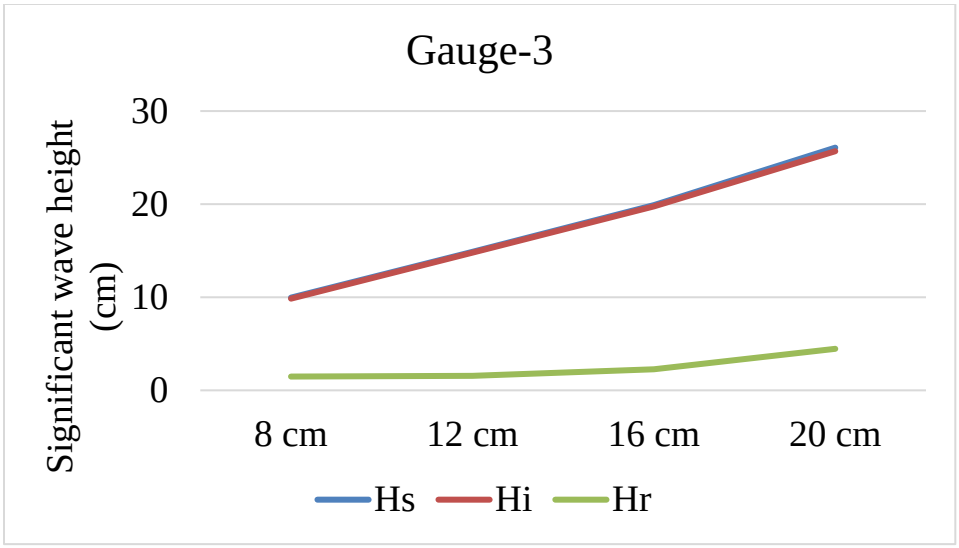

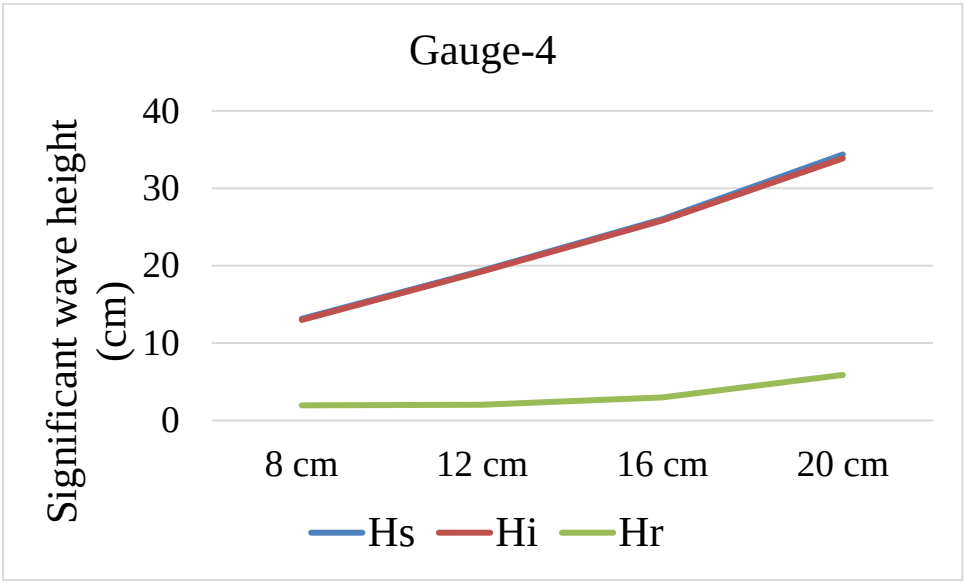

3-17 Incident significant wave height H_I and reflected significant wave height H_r of wave gauge-3 and 4

The incident wave of 24 cm and 32 cm have already started to break after its generation. Thus, it is difficult to apply the linear wave theory for those waves, and the reflection coefficient for those waves were not calculated. In subsequent calculations, 24 cm and 32 cm results were excluded for erosion analysis. Here, wave power is calculated

by two different methods, 1) wave power P_i from incident (input) wave height and 2) wave power $\bar{P}_{i-gauge}$ from spectrum analysis of wave gauges' record. Calculated P_i for different incident (input) waves were presented in Table 3-3. Calculated $P_{i-gauge}$ values based on spectrum analysis from adjacent wave gauge records are presented in Table 3-4. Wave power was calculated using the H_I in Figure 3-17. The peak wave period T_p and initial water depth of the Core-1, Core-3, and Core-4. Core-2 were excluded since there was no adjacent wave gauge.

Table 3-3 Calculated wave power $\bar{P}_i$ (W/m) based on incident (input) wave height

	Core 1	Core 2	Core 3	Core 4
8 cm	9.2	5.5	8.8	10.4
12 cm	20.8	12.4	19.9	23.3
16 cm	37.0	22.0	35.3	41.4
20 cm	57.8	34.4	55.2	64.7

Table 3-4 Calculated wave power $\bar{P}_{i-gauge}$ (W/m) based on wave gauge records and equation 3-16

	Core 1	Core 2	Core 3	Core 4
Wave gauge	Wave gauge-4	-	Wave gauge-4	Wave gauge-3
8 cm	24.5	-	23.2	16.3
12 cm	54.0	-	51.1	39.5
16 cm	96.7	-	91.6	78.4
20 cm	167.4	-	158.5	120.5

3.8. Previous studies related to the wave power and erosion rate

Many studies have suggested that a linear relationship exists between wave power and erosion rate. Schwimmer (2001) found that a positive correlation between the wave power and erosion rate is apparent with the calculated regression equation:

$$E = 0.35P^{1.1} \qquad 3\text{-}19$$

where E is the erosion rate (m/yr) in the field, and P is wave power (kW/m). The equation is based on on-site measurement of the erosion, performed by recognizing measurement of the lateral extent of the rootmat using an electronic total station. For the wave power calculation, wind, bathymetric, and fetch data were used to calculate a wind-stress factor in waves (US Army, 1984).

In Marani et al. (2011), a relationship between volumetric erosion rate ($V = E \cdot h_c$, h_c is the height of the marsh cliff with respect to the tidal flat bottom) and mean incident wave power density was suggested. The erosion rate was calculated based on three sets of aerial photographs. For the wave power calculation, a model similar to the one described by Young and Verhagen (1996) was used. The established proportionality in Marani et al. (2011) is

$$V = 0.0364\, P_i \qquad 3\text{-}20$$

where V is volumetric erosion rate ($m^2 yr^{-1}$) and P_i is wave power density (W/m) based on significant wave heights in the field. Power-law assumption ($E = 0.35P^{1.1}$) in Schwimmer (2001) is the result of a subjective interpretation of the existing data, which can be interpreted identically as a theoretically justified linear relationship between retreat and mean incident power density (Marani et al., 2011).

McLoughlin et al. (2015) investigated the erosion rate using aerial photographs and the Digital Shoreline Analysis System (DSAS). For the wave power calculation, the model in Young and Verhagen (1996) and the SWAN spectral wave model were used. The study found a stronger relationship between wave energy flux and volumetric erosion rates along the marsh edges. Leonardi et al. (2016) combined wave energy and marsh erosion data from eight different locations in the United States, Australia, and Italy and showed that the dimensionless erosion rate E^* (=E/E_{avg}) and dimensionless wave power P^* (=P/P_{avg}) have a unique relationship as follows.

$$E^* = 0.67P^* \qquad 3\text{-}21$$

3.9. Dimensional analysis

In previous studies, expressions for a margin retreat rate were investigated by the mean power density of incident waves (i.e., wave power per unit length of the marsh edge, expressed in W/m). However, these approaches do not derive the erosion rate from a theoretical framework and rely on empirical regression or temporary assumptions. To solve the problem in these approaches, Marani et al. (2011) identified the following list of variables necessary to produce a description of cliff erosion processes:

(1) E $[LT^{-1}]$: retreat rate

(2) $\bar{P}_i[MLT^{-3}]$: mean wave power density striking the cliff face

(3) $h_c[L]$: cliff face height to the tidal flat bottom

(4) $d[L]$: tidal flat bottom depth to mean sea level

(5) $c[ML^{-1}T^{-2}]$: sediment effective “cohesion”

where length, L, time, T, and mass, M are the fundamental units entering the dimensions of the variables defining the problems. By applying Buckingham's theorem of dimensional analysis (Buckingham, 1914), dimensional variables can be described in terms of non-dimensional groups. Marani et al. (2011) choose the following two non-dimensional groups:

$$\Pi_1 = \frac{Rh_c c}{\bar{P}_i}, \Pi_2 = \frac{h_c}{d}$$

Based on Π_1 and Π_2, the process of erosion then described by a relationship :

$$\frac{Eh_c c}{\bar{P}_i} = f\left(\frac{h_c}{d}\right) \quad 3\text{-}22$$

In this experiment, the cliff face height is considered to be similar for all cores (excluding vegetation height). Thus h_c (=0.375 m) is assumed to be held. The lateral erosion rate of four samples by each wave was calculated from the LiDAR analysis by Dr. Feagin's research group at Texas A&M University and is shown in Table 3-5 with the initial water depth of each core sample.

Table 3-5 Initial water depth in front of each sample and erosion rates by each incident wave

Sample No.	Core 1	Core 2	Core 3	Core 4
Initial water depth at toe (m)	0.168	0.053	0.147	0.261
Erosion rate (m/yr) (8 cm wave)	0.315	0.198	0.197	0.182
Erosion rate (m/yr) (12 cm wave)	0.171	0.581	0.170	0.125
Erosion rate (m/yr) (16 cm wave)	0.322	0.815	0.342	0.323
Erosion rate (m/yr) (20 cm wave)	0.394	0.629	0.447	0.444
Average	0.301	0.556	0.289	0.269

Based on the results of wave power and erosion rate, the linear regression of $Eh/\bar{P}_{i-gauge}$ versus h/d is then plotted in Figure 3-18.

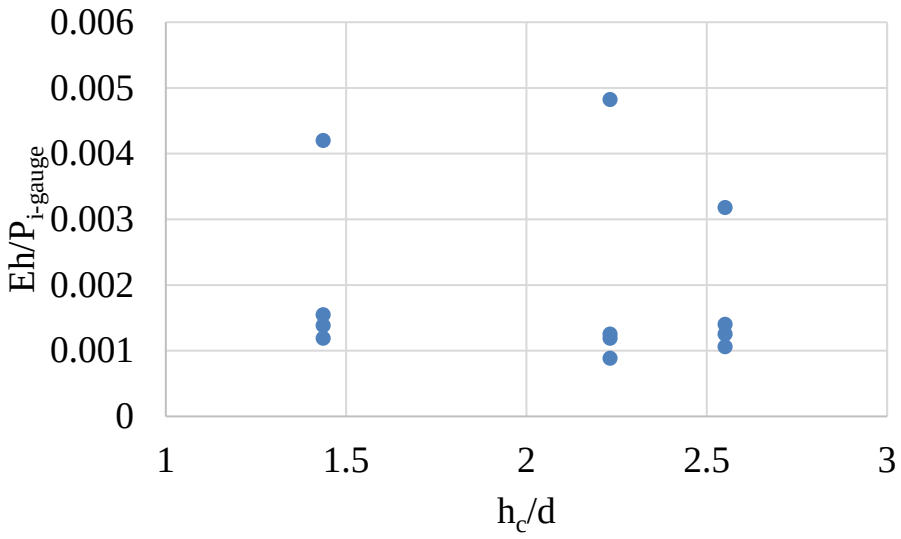

Figure 3-18 The relationship between $Eh/\bar{P}_{i-gauge}$ and h_c/d

From the result of Figure 3-18, we consider that equation 3-22 does not appreciably depend on h/d in the experiment. Thus, it is possible to take $\frac{1}{c}f\left(\frac{h_c}{d}\right)$ as approximately constant: $\frac{1}{c}f\left(\frac{h_c}{d}\right) \approx a$. This simplifies the description of the relationship between erosion rate and incident wave power,

$$E = \frac{V}{h} = \frac{a}{h}\bar{P}_i \qquad 3\text{-}23$$

Based on equation 3-23, the erosion rate and incident wave power were plotted for Core-2. Incident wave information and shallow water approximation were used for wave power calculation affecting Core-2. The results for Core-2 are shown in Figure 3-19.

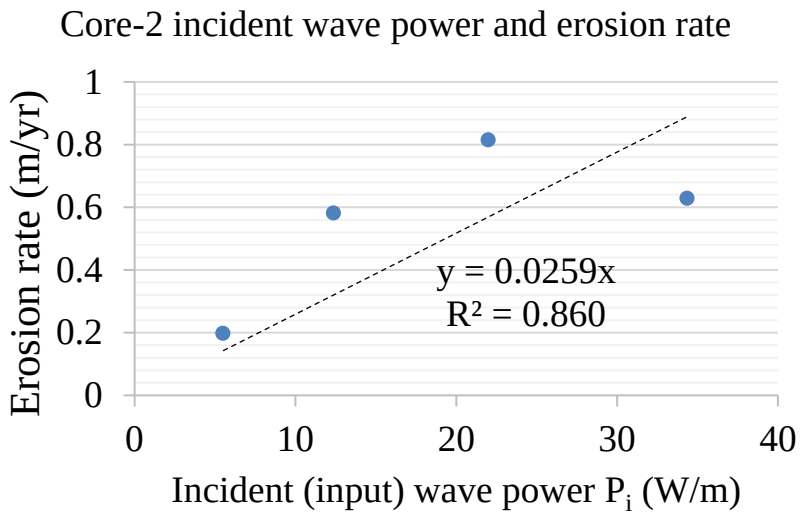

Figure 3-19 Relationships between incident (input) wave based P_i and erosion rate in the laboratory experiment for Core-2

In the results, the relationship between erosion rate (m/yr) and wave power (W/m) was calculated for Core-2, and the value of R^2 was calculated as 0.86. relating to erosion rate and incident (input) wave power of Core-2, the following relationship can be derived.

$$E = 0.026\bar{P}_i \qquad 3\text{-}24$$

The waves propagating Core-2 were considered as breaking waves due to the low water depth and rock beach slope. The orbital velocity recorded by the ADV in front of Core-2 was calculated in Appendix A. For Core-1, 3, 4, the relationship between erosion rate (m/yr) and incident (input) wave power (W/m) was plotted and shown in Figure 3-20. The following relationship can be derived to relate to Core-1,3, and 4's erosion rate and incident (input) wave power.

$$E = 0.008\bar{P}_i \qquad 3\text{-}25$$

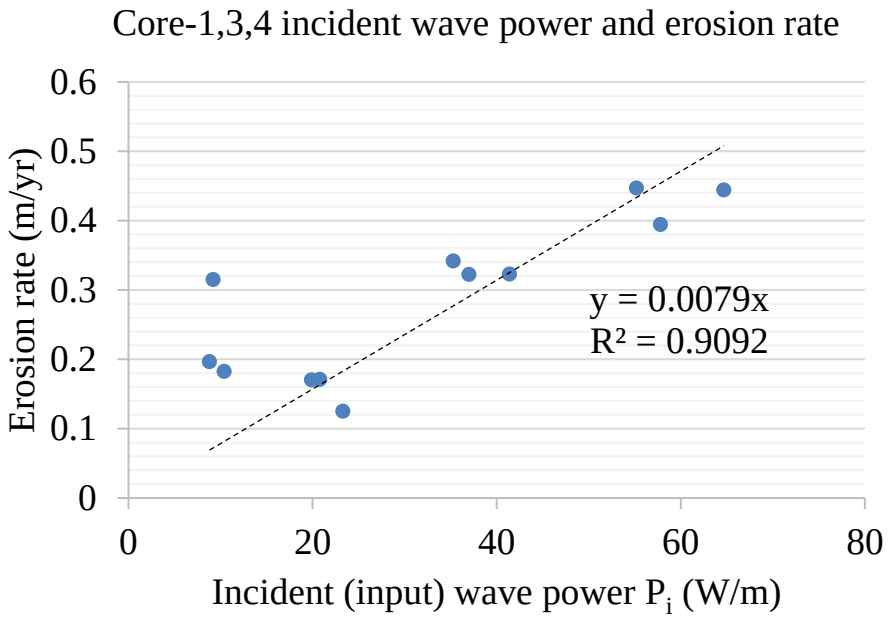

Figure 3-20 Relationships between incident (input) wave based P_i and erosion rate in the laboratory experiment for Core-1,3, and 4

For Core-1, 3, 4, the wave gauge records were available, and the significant wave height was calculated using spectrum analysis and reflection coefficient. Based on the calculated significant wave height, reflection coefficient, and water depth at toe, the wave power $\bar{P}_{i-gauge}$ was calculated. Wave power, based on records from the wave gauges was written $\bar{P}_{i-gauge}$ to distinguish from the incident (input) wave power $\bar{P}_i$. The relationship between erosion rate (m/yr) and wave gauges' wave power $\bar{P}_{i-gauge}$ (W/m) was plotted in Figure 3-21.

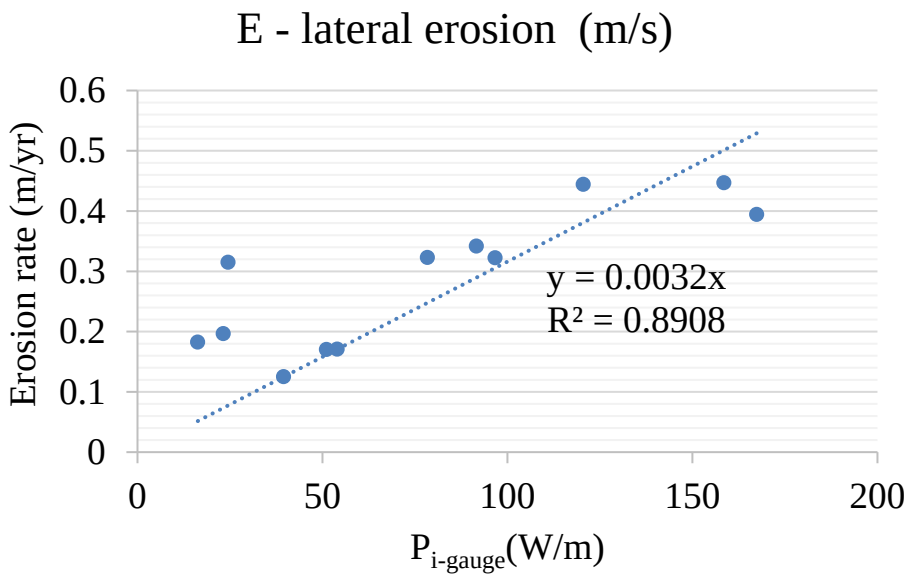

Figure 3-21 Relationships between wave gauges' $P_{i\text{-}gauge}$ and Erosion rate in the laboratory experiment

In the results, a linear relationship between erosion rate and wave power was calculated, and the value of R^2 was calculated as 0.89. From the results, the following relationship was derived in the experiment in the wave flume.

$$E = 0.003\bar{P}_{i-gauge} \qquad 3\text{-}26$$

The coefficient 0.003 was less than 0.008, the value derived based on the input incident wave height.

3.10. Discussion

Salt marsh erosion by the incident wave was investigated in this chapter through a laboratory experiment. Each incident wave's property was investigated in terms of their wave properties, such as Ursell parameter, skewness, and asymmetry. Based on the Ursell parameter results, the Ursell parameter for the location of Core-2 is dramatically

increased when the incident wave height increases. This is due to the Core-2's shallow water depth condition (0.05 m) on the rock beach bottom. 8 cm, 12 cm, and 16 cm incident waves showed less than skewness of 0.4 before it reached the rock beach bottom. Thus, it can be seen that the shape of the incident wave was relatively well maintained when it reached wave gauge-3, before the rock beach bottom. However, at the wave gauge-4's location, most skewness of waves were more than 1.0 except for 8 and 12 cm incident waves. Based on this fact, it was confirmed that the sinusoidal shape of the wave was not maintained at the position of the Wave gauge-4 in front of Core-3. At the location of Wave gauge-4, waves' asymmetry showed a significant difference compared to other wave gauges. The asymmetry of most of the waves ranged from 0.0 to 0.5. However, in wave gauge-4, asymmetry ranged from -2 to -0.5. This is an indication of the likeliness of the wave breaking at wave gauge-4's location.

When the linear wave theory is valid, the relationship between wave power and volumetric erosion rate can be considered to have a linear relationship. This relationship was verified through the dimensional analysis in 3.9. According to the dimensional analysis, a linear relationship between erosion rate and wave power was calculated based on incident (input) wave power and wave gauge records' wave power. Incident (input) wave power can underestimate the wave power since it does not consider the shoaling effect, wave breaking, and likeliness of wave breaking on the rock beach bottom. However, wave power based on wave gauge records can overestimate the wave power, due to the undetected reflected wave energy component. In addition, wave power based on wave gauge records is sometimes not appropriate for sinusoidal waves. This is

because the significant wave height from spectrum analysis assumes the statistical distribution of the individual wave heights (Rayleigh distribution). Nevertheless, calculating the significant wave height based on the wave gauge data is important because it corresponds to the significant wave height obtained in the field experiment. Thus, $\bar{P}_i$ can be used as reference wave power for experimental purpose in the basin whereas $\bar{P}_{i-gauge}$ is appropriate when compared to the field's observation data. $\bar{P}_{i-gauge}$ can be more appropriate here since the wave's sinusoidal shape was not maintained when the wave approached the core samples. The relationship between erosion rate and wave power was generally done in the field rather than in the wave basin experiment (Schwimmer, 2001; Marani et al., 2011).

Fore Core-1,3 and 4, the linear relationship between erosion rate E (m/yr) and incident (input) wave power (W/m) was $E = 0.008\bar{P}_i$. For Core-2, the coefficient was 0.026. This is mainly due to the high averaged erosion rate of 0.556 (m/yr) of Core-2. The high erosion rate is considered due to the breaking wave effects due to the low water depth at the Core-2 location located further behind Wave gauge-4. Depth-induced wave breaking is considered to generate wave shear stress (Zou et al., 2006), and it is possible to cause additional particle by particle erosion.

Based on the wave gauges' records, the wave power $\bar{P}_{i-gauge}$ was calculated for Core-1, Core-3, and Core-4. The coefficient was calculated as 0.003, which is much less than 0.008. This difference is considered to illuminate the difference between the field measurements and wave flume laboratory results in marsh edge erosion.

In Schwimmer (2001), $E = 0.00017{P_i}^{1.1}$ (P_i is in W/m) and in Marani et al. (2011), $E = 0.097P_i$ (When h_c=0.375). The coefficients in the experiment (0.026, 0.008, 0.003) were in the range between Schwimmer (2001) and Marani et al. (2011), but much less than Marani et al. (2011)'s 0.097. This chapter's wave flume experiment considered only the particle by particle erosion, so the coefficient between erosion rate and wave power can be underestimated. Depending on the region, the particle by particle erosion can account for a low percentage of total erosion in the field compared to the erosion by small-scale slides on the bank and toppling failures. However, due to the absence of accurate bathymetric information, fetch length, and water depth data, the wave power calculation could be erroneous in many studies. In addition, depending on the region, sediment effective "cohesion" can differ. Sediment effective "cohesion" is deeply related to the coefficient between erosion rate and wave power, is usually unknown for specific core samples or salt marsh edges in the field.

3.11. Summary and conclusions

The laboratory experiment of this chapter focused on salt marsh retreat processes due to particle by particle erosion induced by monochromatic waves in the wave flume. In the wave analysis, as the waves progressed toward core samples, there was a strong tendency to break on the rock beach slope. This was evidenced by the rapid decrease in asymmetry at the location of wave gauge-4. Core-2, located inside the rock beach slope more than the wave gauge-4 location, showed a higher erosion rate than the other core samples. This is considered due to wave shear stress generated in the wave breaking processes.

Overall, laboratory observations show that the wave power and erosion had a close to a linear relationship. The laboratory simulations have demonstrated that the conditions of (1) different water depths, (2) different input wave heights. Different water depth was not shown as a critical factor for erosion rate in the dimensional analysis except when low water depth makes the wave breaking. Different input wave height is the most important parameter for the erosion rate since the square of the significant wave height is proportional to the wave power and directly affects the erosion rate. As future research tasks, the present experimental model could be extended to cover the 1) erosion rate in different sediment types with different “cohesion” properties and 2) the triggering mechanism for tension crack formation at the salt marsh edge.

4. MONITORING OF SALTMARSH SHORELINES USING STRUCTURE FROM MOTION BY UAV IMAGES

4.1. Introduction

Salt marshes are valuable in their ecosystem services and potential coastal hazard mitigation ability (Shepard et al., 2011). They regenerate the ecosystem's status by cycling nutrients, provide nutrients for fishes and shellfishes, and reduce carbon emission by sequestering carbon (Chmura et al., 2003; Sousa et al., 2010). Unfortunately, salt marshes are continuously compromised by human interferences (Gedan et al., 2009; Deegan et al., 2012; Kirwan and Megonigal, 2013), as well as sea-level rise (Alizad et al., 2016) and lack of sediment supplies (Ganju et al., 2017).

To originate the cause of salt marsh loss, measuring their coverage and boundary toward the ocean at high spatial resolutions and temporal frequency is essential. Progress has been made for discrete marsh surfaces in recognizing unvegetated and vegetated territories to figure out the fate of salt marshes using remote sensing techniques (Ganju et al., 2017; Defne et al., 2020). Nonetheless, tracking the short-term salt marsh edge erosion has been less developed.

There have been many studies that investigate marsh shorelines. The Coastal Mapping Program (CMP) (https://www.ngs.noaa.gov/RSD/cmp.shtml) run by NOAA National Geodetic Survey (NGS) has developed procedures to delineate the shoreline. Stereo photogrammetry using tide-coordinated aerial photography controlled by kinematic Global Positioning System (GPS) techniques were used by CMP (Graham et al., 2003; Schmid et al., 2011). Kuleli et al. (2011) used multi-temporal Landsat images

and an automated image analysis technique to extract shorelines along the coastal wetlands of Turkey. White and Madsen (2016) used imagery collected by a balloon to map marsh landcover and ecological zones. Campbell and Wang (2019) analyzed salt marsh changes using object-based image analysis (OBIA). Furthermore, they classified a combination of data obtained from satellites, LiDAR as well as aerial imageries to study the extent of marsh grass and the evolution of pannes and pools.

Despite these efforts, monitoring of short-term morphodynamics at the marsh edges is rarely done (Bouma et al., 2016; Huff et al., 2019). This hampers the ability to clarify the erosion and accretion mechanism at the salt marsh boundary and predict whether a wetland restoration policy will succeed or fail. Using the advanced remote sensing technique and inexpensive instruments, quantifying the dynamics of short-term coastal changes is necessary to assess coastal resilience (Ladd et al., 2019).

Recent developments in UAV technology, along with sensor miniaturization, have facilitated remote sensing image retrieval of wetlands. Photogrammetry on unmanned aerial vehicles (UAVs) is gaining attention as an efficient and inexpensive way to survey the site. Unmanned Aerial Vehicle Systems (UAS) offer an alternative to the on-site method of surveying specific coastal areas with very high resolution (Everaerts, 2008; Anderson and Gaston, 2013; Colomina and Molina, 2014; Floreano and Wood, 2015). For UAV application to coastal wetlands monitoring, Taddia et al. (2020) used high-resolution multispectral images derived from UAV to monitor wetlands. Duffy et al. (2018) proposed a technique using a lightweight drone to produce high spatial resolution mosaics of coastal vegetation features.

The use of UAV images is particularly beneficial when combined with Structure from Motion (SfM) techniques; it provides better results of survey in terms of validation at a low cost (Westoby et al., 2012; Cook, 2017). High-resolution datasets using UAV images can capture salt wetland evolution through iterative mapping of vegetation and wetland topography. This data informs the numerical model and reveals the impact of waves, sea-level rise, and storms on salt wetlands.

UAV-derived photogrammetry using SfM offers significant advantages over conventional surveying techniques in 4D terrain change studies. However, the technique requires a Ground Control Point (GCP) to extend and orient the photogrammetric models to the real coordinate system even though the dependency is often unrealistic (James and Robson, 2014; Smith et al., 2016). Previous studies have shown that the amount and distribution of GCPs can significantly affect the final accuracy of photogrammetric products. For example, as the number of GCPs decreases, the gap between the GCPs increases, terrain error has increased. (Tahar, 2013; James and Robson, 2014; Johnson et al., 2014; Shahbazi et al., 2015; Tonkin and Midgley, 2016).

Ground control also limits one of UAVs' unique advantages: It allows observing terrain remotely and accurately. It is otherwise difficult and hazardous to access on the ground. The difficulty of creating these networks can also be seen in wetland studies, in which GCPs are not easy to install because of field accessibility. Due to the difficulty of building GCP networks in salt marsh environments, alternative methods are often applied to photogrammetry products. These methods include using tie points to connect

data sets geodetically and using onboard navigation GPS location information to provide additional external constraints.

Recent developments in lightweight, low-cost GNSS (Global Navigation Satellite System technology) have led to the proliferation of new techniques for accurately locating images and subsequent photogrammetry products using differential carrier phase GNSS positioning (Chudley et al., 2019). This technique, known as GNSS-assisted aerial triangulation (Benassi et al., 2017), has been shown to have sub-GSD (Ground Sampling Distance) horizontal accuracy without using GCP (Benassi et al., 2017; Van der Sluijs et al., 2018).

In this work, drone images of the Galveston Island wetlands with camera position and GPS data were collected and used for the GNSS-supported aerial triangulation (AT) based UAV Photogrammetry. By comparing wetlands maps generated from measured data at different times, the topographical difference in salt marsh boundary between the measurements was analyzed, and the boundary lateral erosion rate was verified. Monitoring the salt marsh boundaries using UAS over short and long-term periods can provide more detailed and accurate assessments of changes in salt marsh edge.

Much research has been done to determine the extent to which waves affect salt marsh edge lateral erosion using wave estimation using wind data. Fagherazzi et al. (2010) used a standard formulation for wave generation in shallow water (Young and Verhagen, 1996) to deduce the non-dimensional wave energy affecting salt marshes in shallow bays. McLoughlin et al. (2015) used the SWAN spectral wave model to estimate the wave power and correlate it to the salt marsh retreat rate.

To analyze the wave effect on the marsh edge retreat rate, wind and wave climate in the area also investigated using wind records and wave data derived from a single domain numerical simulation using Delft3D and SWAN. Based on the wave data and water level data in the model, wave power was calculated and compared with the erosion data calculated by UAV image analysis. The aims of this chapter are to (i) apply GNSS-supported aerial triangulation (AT) using a low-cost, custom-built airframe suitable for the study of estuary environments, (ii) modify the GNSS-AT process to allow surveys to be undertaken at salt marsh boundaries far from suitable GPS reference stations and compare with the results from geodetically connected data sets using tie points, (iii) recognize and calculate marsh boundary retreat rates of Galveston Bay, (iv) correlate the cumulative wave power with marsh edge retreat measured from UAV images. Here, we demonstrate the suitability of GNSS-AT assisted UAV photogrammetry for assessing salt marsh lateral erosion.

4.2. Galveston Bay and the study area

Galveston Bay, the second-largest estuary along the Gulf of Mexico (Fig. 1), has a surface area of 1600 km2, is 50-km long, and 27-km wide (Santschi, 1995). The bathymetry is relatively flat with a mean depth of ~3 m, except in the dredged Houston Ship Channel, a 140-m-wide and 12-m-deep cut through the Bay. Because of the shallowness of Galveston Bay and the relatively small tidal range, surface-waves provide a dominant physical forcing mechanism affecting water-currents and pollutant dispersion, regulating sediment transport, driving nutrient fluxes, influencing the shoreline, and flushing oyster-beds (Dupuis and Anis, 2013).

The natural coastline of Galveston Bay is made up of 61 % marshes, 35 % steep clay bluffs ranging from 1.5 to 10.7 meters in height, and 4 % sand and shell beaches (excluding manmade shorelines). Most of the marsh shoreline is located on East and West Bays, while the bluffs are in Trinity and Galveston Bays (Shipley et al., 1994). Galveston Bay salt marshes are experiencing significant lateral boundary erosion in the last 50 years. The calculated erosion rate based on the surface area analysis was 1.02% per year from 2006 to 2011 (Entwistle et al., 2018).

The natural causes of shoreline erosion in Galveston Bay include: 1) wind-driven waves by hurricanes, tropical storms, and northern cold fronts; 2) sea-level rise (Shipley et al., 1994). Human activities such as local subsidence by groundwater extraction also cause the subsidence of the wetlands and its boundary erosion. The construction of upland reservoirs has probably contributed to the acceleration of marsh erosion by blocking the fluvial sediment inputs to Galveston Bay (Shipley et al., 1994). In addition, reduced erosion rates due to changing land use in the upper watershed may also be responsible for reducing sediment supply to the bay (Ward and Armstrong, 1992).

The wind climate in Galveston Bay generally has a predominant wind direction from the southeast. However, wind patterns vary from summer to winter. Summer patterns are marked by relatively constant winds from the south, while winter winds are dominated by short, intense northern winds that can bring wind speeds of over 17 m/s out of the north and northwest. These two wind regimes are critical processes controlling the circulation in Galveston Bay. About ten percent of the days are calm from March to November, and almost half of the days have southerly, southeasterly, or easterly winds.

However, about half of strong winds occur from the north, northwest, or northeast and alternate with weak or calm southerly winds from December to February (Shipley et al., 1994).

The study areas are the wetlands near the Sea Grass Lane close to Jamaica beach on Galveston Island. Another study area is the wetlands near the San Luis Pass as shown in Figure 4-1. According to the analysis of satellite images, these are areas where erosion of the wetland boundary has been active. These areas were selected as targets because they are located in places adjacent to the take-off and landing site of the drone. Preliminary erosion analysis was done for Sea Grass Lane (Figure 4-1b) and Bay Breeze (Figure 4-1c) area. The results of the analysis for the Bay Breeze area based on Google Earth (Gorelick et al., 2017) aerial image are shown in Figure 4-2. The average annual retreat rate was calculated as 2.67 m/ year. Benker et al. (2011) investigated the accuracy of coordinates in Google Earth in the Big Bend region of Texas. In the analysis, a horizontal position accuracy of 2.64 m RMSE was determined for the Google Earth terrain model. Considering the human error can occur in recognizing boundaries in relatively low resolution Google images, the offset distance error of 3.0 m was considered in the analysis. The lateral erosion of the Sea Grass Lane area based on satellite image analysis was shown in Figure 4-3.

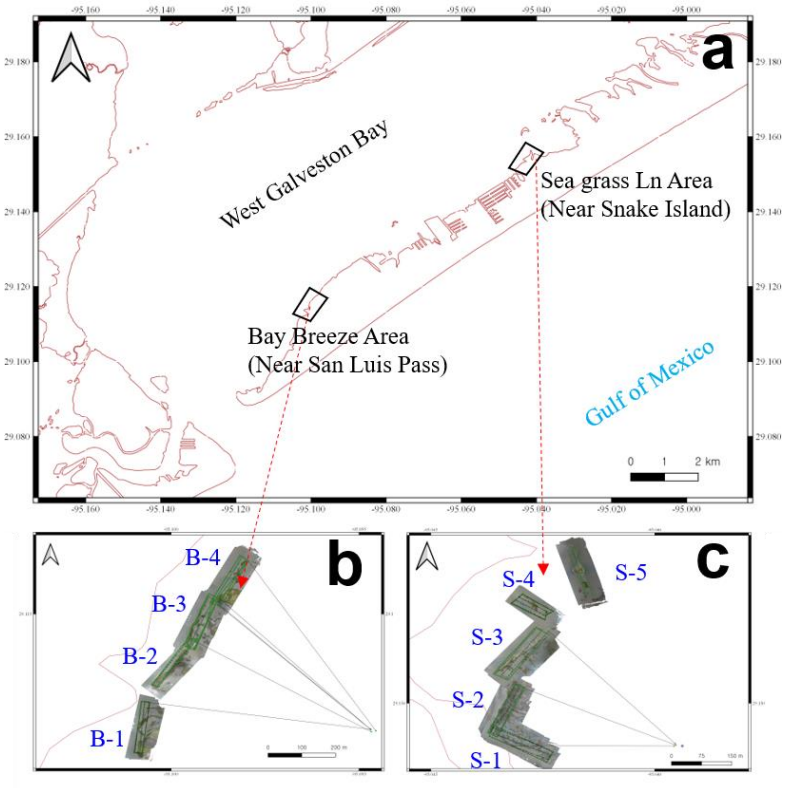

Figure 4-1 (a) Drone survey sites on Galveston Island (b) Bay breeze area drone route (c) Sea Grass lane area drone route

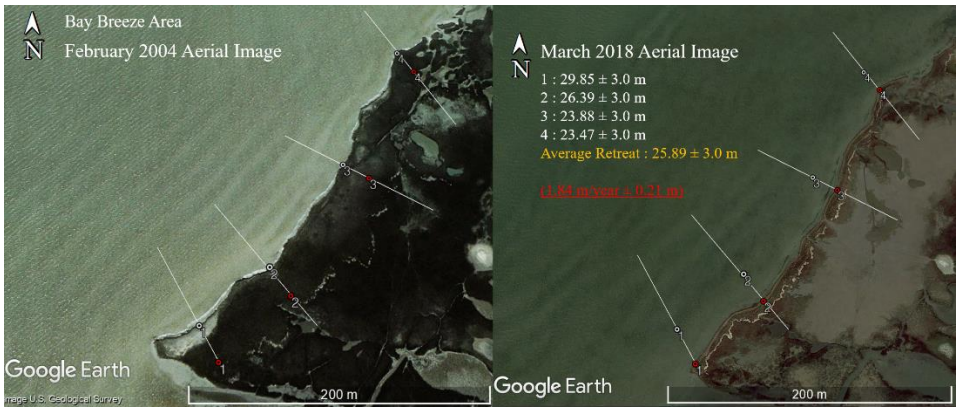

Figure 4-2 Lateral erosion of the Bay Breeze area from Feb 2004 to Mar 2018

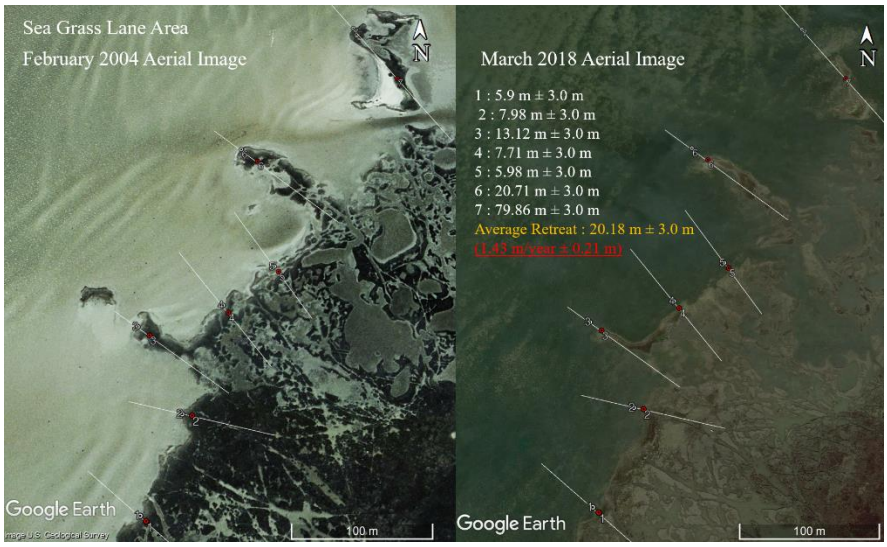

Figure 4-3 Lateral erosion of the Sea Grass Lane area from Feb 2004 to Mar 2018

Wetland boundaries protruding forward to the west bay such as No.3, 6 and 7 in Figure 4-3, showed higher lateral erosion (13.12 m, 20.71 m, 79.86 m). In contrast, the other area shows less than 10 m lateral erosion from February 2004 to March 2018 (less than yearly erosion of 1 m).

4.3. Field experiment overview

Wetland photography using drones was performed seven times from AUG 2019 to OCT 2020. The area that can be captured per day depends on the number of batteries for the UAV. In addition, the portable power station can significantly increase the operation time of UAVs. The photographing dates for each region are shown in Table 4-1. The water level condition during the measurement periods at the Galveston Railroad Bridge tide gauge was summarized in Table 4-2.

Table 4-1 Timeline of drone survey date in each region and number of shots

Location	AUG 3, 2019	NOV 1, 2019	DEC 2, 2019	MAR 6, 2020	AUG 25, 2020	SEP 12, 2020	OCT 30, 2020
S-1		1		1		1	1
S-2	1	1	2	1			1
S-3		4	2	1		1	3
S-4		2	2	1		1	3
S-5		1	2	1		1	3
B-1				1		1	
B-2				1	1	1	
B-3					1	1	
B-4				1	1	1	

Table 4-2 Reference tide level and wind condition at Galveston Railroad Bridge (8771486) during the drone flight days

Date		Start time	End time	Wind condition
AUG 3, 2019	Time (UTC)	21:00	22:00	21:00
	Tide level (m) (NAVD 88)	0.47	0.49	2.3 m/s
NOV 1, 2019	Time (UTC)	18:13	23:00	18:13
	Tide level (m) (NAVD 88)	0.18	0.32	5.4 m/s

Table 4-2 Continued.

Date		Start time	End time	Wind condition
DEC 2, 2019	Time (UTC)	21:12	23:33	21:12
	Tide level (m) (NAVD 88)	-0.31	-0.24	5.8 m/s
MAR 6 2020	Time (UTC)	20:39	23:07	20:39
	Tide level (m) (NAVD 88)	0.32	0.38	5.6 m/s
AUG 25, 2020	Time (UTC)	19:04	20:47	19:04
	Tide level (m) (NAVD 88)	0.4	0.32	6.5 m/s
SEP 12, 2020	Time (UTC)	22:23	23:55	22:23
	Tide level (m) (NAVD 88)	0.30	0.26	3.4 m/s
OCT 30, 2020	Time (UTC)	15:56	19:32	15:56
	Tide level (m) (NAVD 88)	0.15	0.25	5.9 m/s

4.4. Material and methods

The aerial surveys were performed using a recent model of a multi-copter: the DJI Phantom 4 Advanced, a compact and lightweight UAV. DJI Phantom 4 Advanced carries a DJI FC6310 camera with an 8.8 mm nominal focal length and a 1” CMOS 20-

megapixel sensor with 2.41 x 2.41 µm nominal pixel size. The DJI FC6310 camera features an image of 5472 x 3648 pixels, corresponding to 13.2 x 8.8 mm. (Peppa et al., 2019)

In the field, the take-off and landing of the drone were controlled automatically using DroneDeploy software as a mobile (or a desktop) application. DroneDeploy provides UAV mapping plans for the site of interest. It also provides an automatically generated drone path according to the region and resolution desired by the user. The DroneDeploy decides the number and location of camera shot sets based on the designated resolution. In the case of 3D mapping, many pictures from different angles are required. In general, the more images are provided to SfM, the more accuracy of 3D mapping can be derived.

The flight was performed without the aid of GPS waypoints for navigation but with altitude fixed at 30, 35 m, and 40 m depending on the area. The lower the altitude, the more pictures are required in the same area. Based on the drone operation times, altitude was selected not to exceed more than 15 minutes of the fight. This is due to the drone's maximum flight time limited by the battery capacity of the drone. The official maximum flying time of the DJI Phantom 4 Advanced is 30 minutes. However, for the safety of the drone operation, the flight time was adjusted so that the battery level does not fall below 30%.

For the accurate survey without using GCPs, post-processing kinematic (PPK) was used. GNSS receivers attached to the drone and the base GPS on the ground were used for PPK. The details of the UAS-GNSS-PPK system in the study are shown in

Figure 4-4. Global navigation satellite systems include the well-known global positioning system operated by the United States and satellite navigation systems operated by other countries, such as GLONASS, Galileo, and BeiDou. These devices use aspects of the GNSS (called code-based) signals to provide precision that can approach 10 cm–20 cm. In comparison, survey-grade systems use carrier- or phase-based aspects of the signal with some form of correction data.

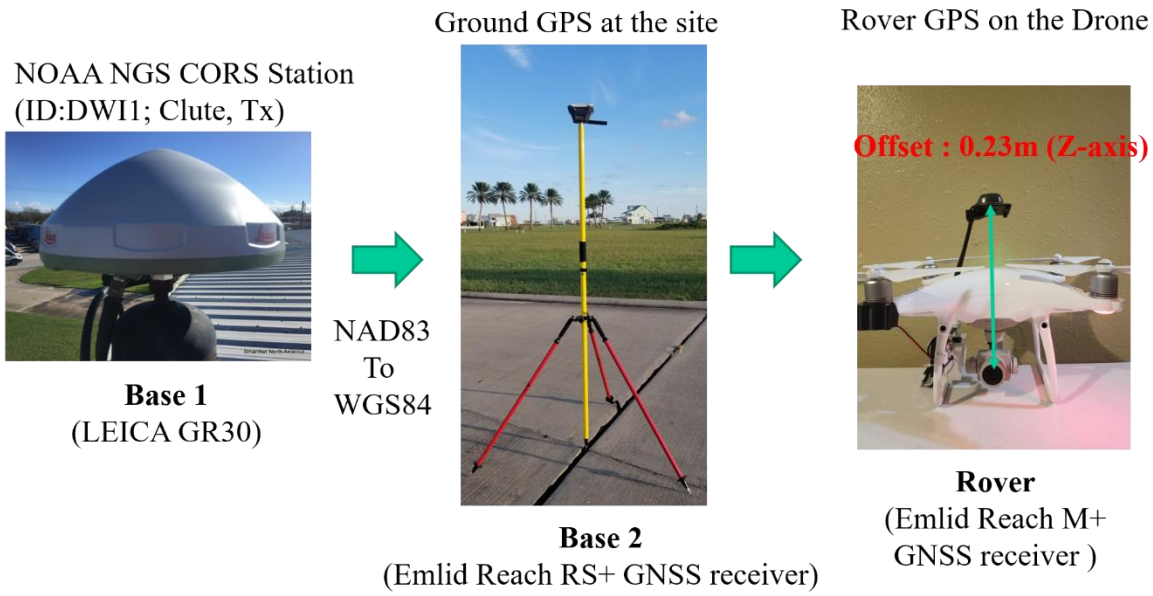

Figure 4-4 UAS-GNSS-PPK system

In the drone, a phototransistor detects the blink of front LEDs on a drone, and a time mark is recorded in the rover GPS's log file. The time marks are extracted and combined with the UAV images as precision geotags. The SfM–Multi-View Stereo (MVS) photogrammetry can be performed using sensor orientation (InSO), where ground based GCPs provide external constraints (Benassi et al., 2017). The other method is direct sensor orientation (DSO, also known as “direct georeferencing”). GNSS and an

inertial measurement unit (IMU) provide external orientation parameters. DSO combines camera orientation values (e.g., from the IMU) with accurate camera position data from a GNSS receiver (Cucci et al., 2017; Chudley et al., 2019). However, InSO methods using ground based GCPs have prevailed in UAV-based surveying because the inexpensive GNSS and IMU used in commercial UAVs are not accurate enough to provide more than sub-meter-level accuracy (James et al., 2017).

This study takes advantage of the recent availability of low-cost, lightweight carrier-phase GNSS receivers for direct georeferencing in a wetland observation. The implementation described here is a subset of DSO referred to as GNSS-supported aerial triangulation (GNSS-AT), which requires position data from GNSS receiver (Benassi et al., 2017) and camera orientation data. To provide high accuracy of position data, both a ground-based GNSS receiver and an onboard GNSS receiver are used in the study.

In the first step, absolute coordinates of Base 2 (drone launch site) is calculated by the Post-Processed Kinematic (PPK) technique based on the GPS data (Base 1) from Continuously Operating Reference Station (CORS) and the ground GPS raw data (Base 2). The second step generates PPK solutions for rover GPS raw data with the Ground GPS raw data (Base 2) and its absolute coordinate. Finally, photos taken by the camera of the drone are georeferenced with the results from the PPK analysis of rover GPS on the drone.

Agisoft Metashape (https://www.agisoft.com/) software was used in the study to generate Digital Elevation Models (DEMs) and orthorectified images from near-nadir photos acquired during the flights. In the first step, the software aligns the photographs

using an SfM algorithm (Ullman, 1979), which identifies image feature points and subsequently monitors the movement of those points throughout the image dataset. Estimation of the camera position is one of the main components in SfM (Hartley and Zisserman, 2003; Szeliski, 2010). Outputs of this first step are (1) a three-dimensional point cloud representing the geometry of the study area; (2) relative camera positions at the moment of image acquisition; (3) internal calibration parameters (focal length, principal point location, three radial, and two tangential distortion coefficients). Because these first processing steps estimate the calibration parameters, there is no real need to apply calibrated cameras and optics during the image acquisition stage (Verhoeven 2011). The second step builds a dense point cloud. In coastal zone surveys, most images partially cover the sea. For computation efficiency, sea areas are better to be excluded from the land topography. This can be done by resizing the interest region. In the third step, the algorithms operate on the pixel values to build the majority of geometric details. All pixels are utilized in the Multi-View Stereo (MVS) reconstruction algorithm (Scharstein and Szeliski 2002; Seitz et al. 2006). The software applies an algorithm based on an advanced computer vision solution that creates high-quality three-dimensional content from a series of overlapping aerial images (Verhoeven 2011). The details of the processing workflow for image georeferencing, SfM, and point clouds generation are shown in Figure 4-5.

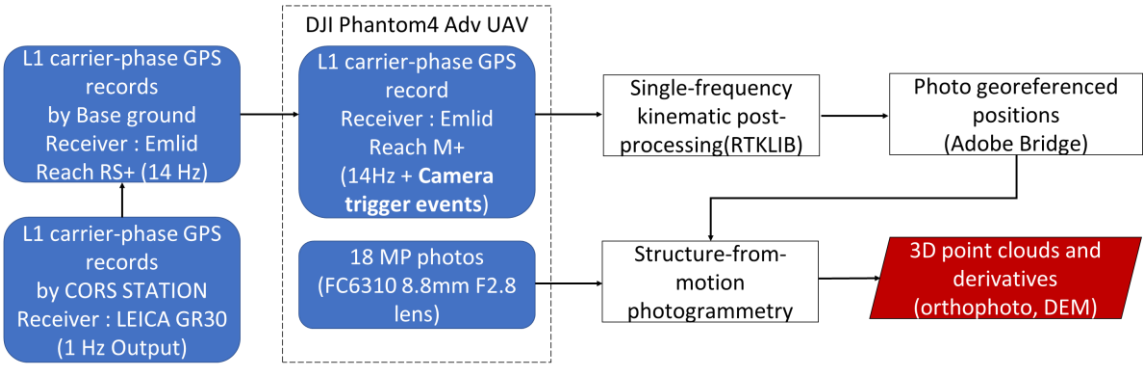

Figure 4-5 GNSS-AT Based UAV Photogrammetry Processing Workflow

4.5. Uncertainty analysis

4.5.1. PPK solution accuracy verification

A comprehensive set of uncertainty checks were executed using the total system comprising of UAV and GNSS receivers. The accuracy of the absolute coordinate of the base GPS location influences the accuracy of entire maps generated by the drone images. Thus, for the quality of the final accuracy of salt marsh boundary mapping, verification of the GPS coordinate of base location is needed to be cautiously calculated by measuring over a long period and by setting it to the exact same place in every survey on different days.

Verification of base GPS (here, work as a fixed rover for CORS station) accuracy was done with CORS station as a reference location for a known GCP coordinate. A known GCP by NOAA National Geodetic Survey is located near San Luis Pass, named as MOTTO (PID: AW0646, https://www.ngs.noaa.gov/cgi-bin/ds_mark.prl?PidBox=AW0646). MOTTO's NAD 83 coordinate was converted to

WGS 84. MOTTO's image and installed base GPS on the MOTTO are shown in Figure 4-6.

Figure 4-6 MOTTO Station (GCP) by the National Geodetic Survey and installed base GPS on the MOTTO station

The baseline length between CORS DWI1 station (Clute, TX) and MOTTO (GCP) is 29.86 km. Following is the Post Processing Kinematic settings for the base GPS station.

Table 4-3 PPK analysis settings in the study

Positioning Mode	Static
Elevation Mask	5°~25°
SNR Mask	None
Frequency / Filter type	L1 / Combined filter
AR filter	On
CORS DWI1 Location Input (WGS 84/ Ellipsoidal)	29.013605000, -95.403660500, -18.7130

The coordinate of PPK results at the MOTTO's location and MOTTO's location data in the NGS datasheet are presented in Table 4-3. The results showed that the error of base location estimation using PPK solution is approximately 4.7 mm for latitudinal direction and 4.3 mm for longitudinal direction. Even though the distance between the CORS station is relatively long at 30 km, the PPK solution had an accuracy of less than 1 cm. The accuracy of the PPK solution using the base GPS for the Sea Grass Lane area was also tested. Figure 4-7 shows the setting of the base GPS at the Sea Grass Lane site. PPK was performed using ground GPS data and CORS GPS records.

Table 4-4 Horizontal accuracy check of the base GPS on a known GCP

	Latitude (deg)	Longitude (deg)
MOTTO's location data in the NGS datasheet	29.09589366	-95.1111676
PPK results	29.09589323	-95.1111672
Difference (m)	0.004731987	-0.004377252

Figure 4-7 The process of the base GPS location on the fixed location in every drone survey

Due to the absence of the GCP at the area, verification of the accuracy of the absolute coordinate of fixed base location using PPK solution has been performed. The baseline length from the CORS station to the base GPS location is 38.49 km. The starting time of the base GPS data at the location in Figure 4-7 was NOV 1, 2019, 18:09:49.19, and the end time of ground GPS data was NOV 1, 2019, 23:05:33.00 (duration: 4 hours and 55 minutes). The location of the bottom of the pole was calculated as 29.013605000 (Latitude, deg), -95.403660500 (Longitude, deg), -18.7130 (Height, Ellipsoidal, m). This coordinate was used for every survey in this area to minimize the relative errors that can come from the PPK.

4.5.2. Uncertainty analysis for rover GPS

During fieldwork, 5 points have also been signalized on the ground by a solid black and white target (Figure 4-8). The cross size was designed for easy detection on each acquired image. The points were deployed as Check Points (CPs) to assess both the

horizontal and vertical accuracy of the models. The uncertainty of PPK based GNSS drone survey system using the ground GPS and rover GPS had been tested using CPs located near the drone launch site. The uncertainty includes the errors from the rover GPS in the PPK solution, and structure from motion (SfM) error, and nonlinear errors in the point cloud generation. The images of the initial setting for the CPs at the base point of the Sea Grass Lane area are shown in Figure 4-8. Figure 4-9 is the final product of maps of the survey area for the system uncertainty validation.

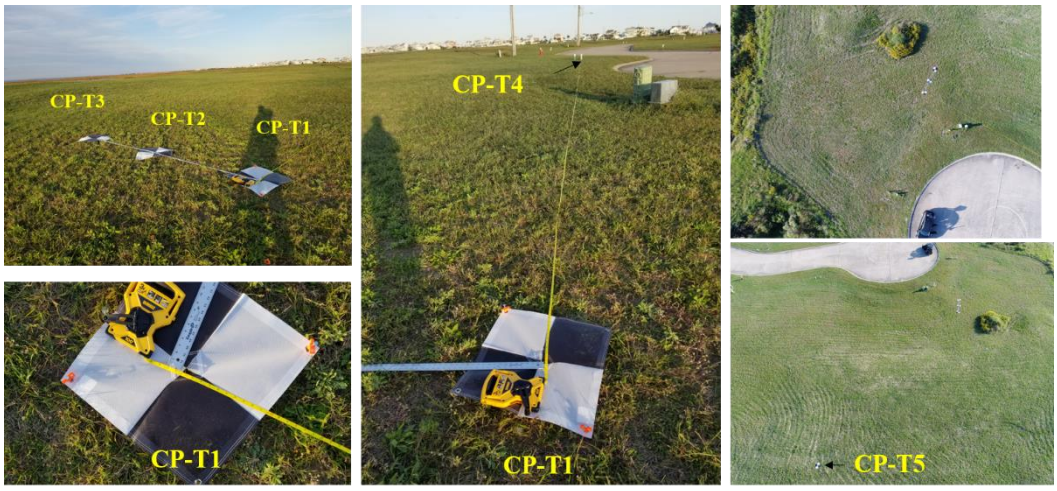

Figure 4-8 CPs distributed near the drone launch site of Sea Grass Lane area

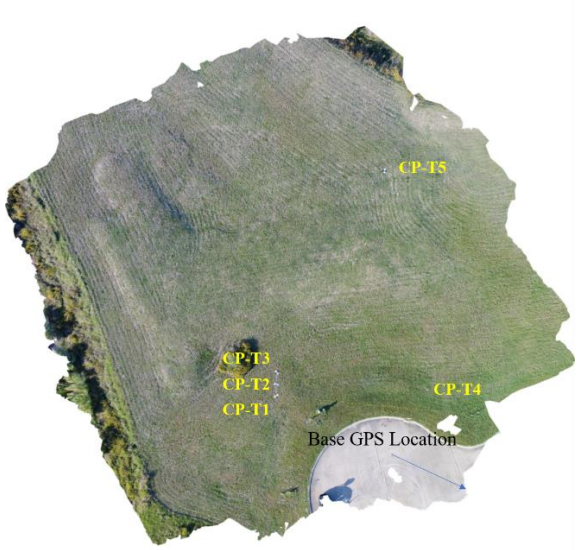

Figure 4-9 Location of the CPs in the generated map by the drone images

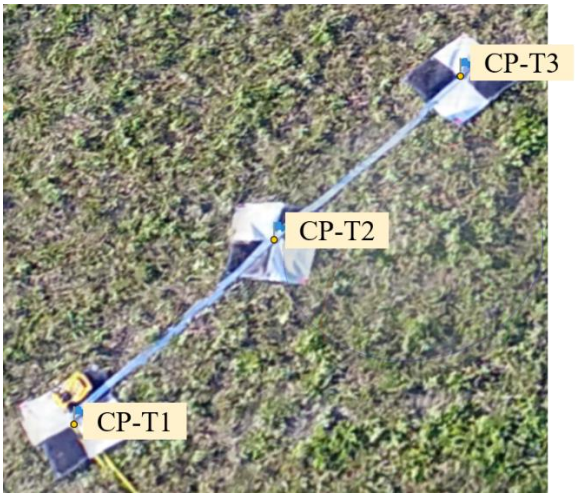

Figure 4-10 Sample of selected CPs on the final 3D map products

The RMSE was calculated based on the coordinate of CPs on the 8 trials. The errors also tend to include human error by selecting the center of the target manually. The difference in CPs coordinates in different drone surveys is shown in Table 4-5

(Longitude) and Table 4-6 (Latitude). Overall, the average longitudinal error was 1.6 cm, and the average latitudinal error was 1.2 cm.

Table 4-5 Longitudinal errors for different drone trials (total 8 trials) using CPs

Longitude	RMSE (Decimal Degree)	RMSE (m)
CP-T1	9.95221E-07	0.011
CP-T2	8.80827E-07	0.010
CP-T3	8.18481E-07	0.009
CP-T4	3.18138E-06	0.035
CP-T5	1.4606E-06	0.016
Average	1.4673E-06	0.016

Table 4-6 Latitudinal errors for different drone trials (total 8 trials) using CPs

Latitude	RMSE (Decimal Degree)	RMSE (m)
CP-T1	1.07219E-06	0.012
CP-T2	9.10276E-07	0.010
CP-T3	8.26779E-07	0.009
CP-T4	1.34494E-06	0.015
CP-T5	1.12583E-06	0.013
Average	1.056E-06	0.012

4.6. Verification of the salt marsh boundary images

4.6.1. Uncertainty analysis based on same date drone survey

Based on the images generated by the drone survey, an accuracy check was done for drone images generated by different drone surveys on the same days. Due to the inaccessibility, GCPs and CPs were not available at the salt marsh boundary area. Thus, natural CPs were used for the uncertainty of the drone survey. The surveys were done on NOV 1, 2019 for the S3 in the Sea Grass Lane site. The natural CPs in S3 are selected as following in Figure 4-11. The STD and RMSE were calculated for three surveys in the same day in NOV 2019 and presented in Table 4-7.

Figure 4-11 Selected natural CPs in same day surveys

Table 4-7 Longitudinal, latitudinal, and altitudinal errors for different drone trials using CPs located inside of the salt marsh in the S3 area

Location		STD (m)	RMSE (m)
Natural CP-S3-T1	Lon	0.004	0.003
	Lat	0.010	0.008
	Height	0.116	0.095
Natural CP-S3-T2	Lon	0.003	0.002
	Lat	0.016	0.013
	Height	0.062	0.050

The calculated STD for Longitude and Latitude ranged from 0.002 m to 0.01 m. However, the STD for height ranged from 0.062 m to 0.116 m. Due to the high uncertainty in height, the height data was not used for the analysis of lateral erosion in the study.

4.6.2. Uncertainty analysis for drone surveys on different days

To analyze the uncertainty of the accuracy of coordinates on different dates in the drone survey, natural CPs were selected. Natural CP can be moved from its original position by external factors, so caution must be taken when choosing a natural CP. The images of selected natural CPs are shown in Figure 4-12. The UAV images were taken on NOV, DEC 2019, MAR 2020, and OCT 2020.

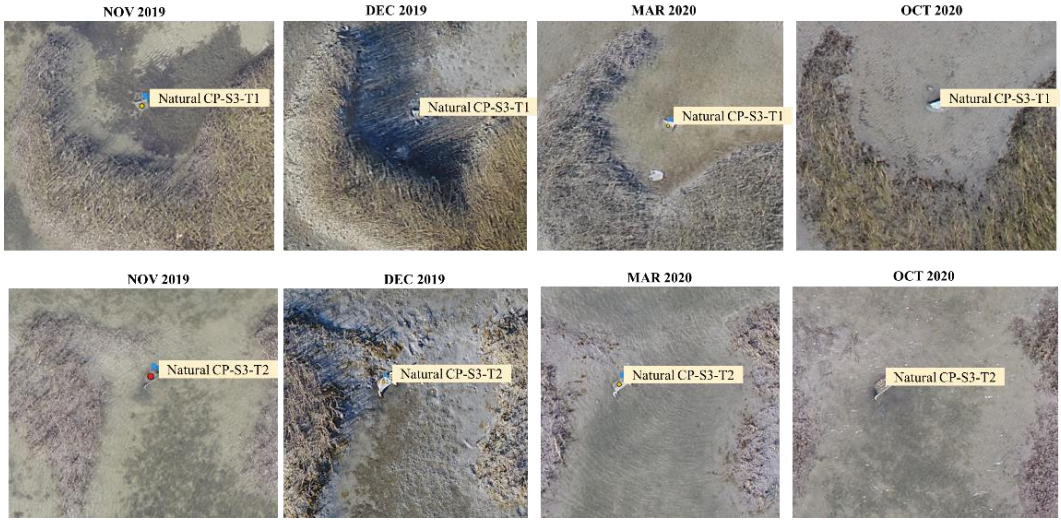

Figure 4-12 Selected natural CPs on different days in S3

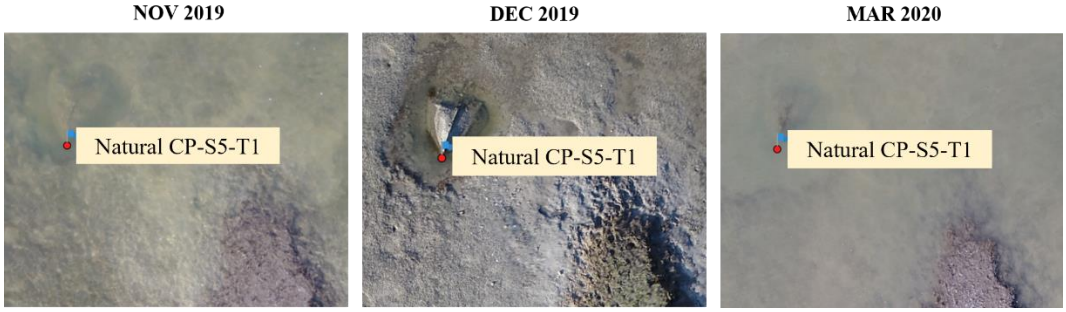

Figure 4-13 Selected natural CPs on different days in S5

According to images in MAR 2020 for Natural CP-S5-T1 in Figure 4-13, turbidity in water was noticeable; however, the natural CP was recognized. However,

due to the high turbidity of the bay water, Natural CP-S5-T1 was not recognized. The changes in the water depth among the drone flights on different days, the natural CP was noticeable in every flight. The STD and RMSE were calculated for the CP and presented in Table 4-8.

Table 4-8 STD and RMSE of the natural CP-S3, S5 on different days

Location		STD (Meters)	RMSE (Meters)
Natural CP-S3-T1	Lon.	0.016	0.003
	Lat.	0.012	0.008
	Height	0.107	0.095
Natural CP-S3-T2	Lon.	0.009	0.002
	Lat.	0.014	0.012
	Height	0.146	0.050
Natural CP-S5-T1	Lon.	0.025	0.020
	Lat.	0.005	0.004
	Height	0.921	0.752

The averaged longitudinal, latitudinal RMSE for three natural points in Table 4-8 were 1.3 cm, 1.0 cm, respectively. Natural CP-S5-T1 was on the seabed, so it was inundated in most surveys except during the DEC 2020 survey. Because of this situation, the height error was higher than other natural CPs. On the other hand, the height errors of the other two CPs were 9.5 cm and 5 cm, which is much higher than the horizontal error.

4.7. Erosion analysis based on UAV Orthomosaic maps

Boundary erosion was measured based on the analysis by drawing a path on the salt marsh edge using the Google Earth platform. The recognition of the boundary was done manually. Thus, some errors can be expected to relate to this process. The erosion was compared by selecting only the edges with shadows or clear lines to minimize the

error. The analysis was done for small island wetlands in the S3, S4, and S5 area of the Sea Grass Lane. The results are shown in Figure 4-14~16. In area S4, the retreat of the salt marsh boundary was clearly recognized for the specific areas.

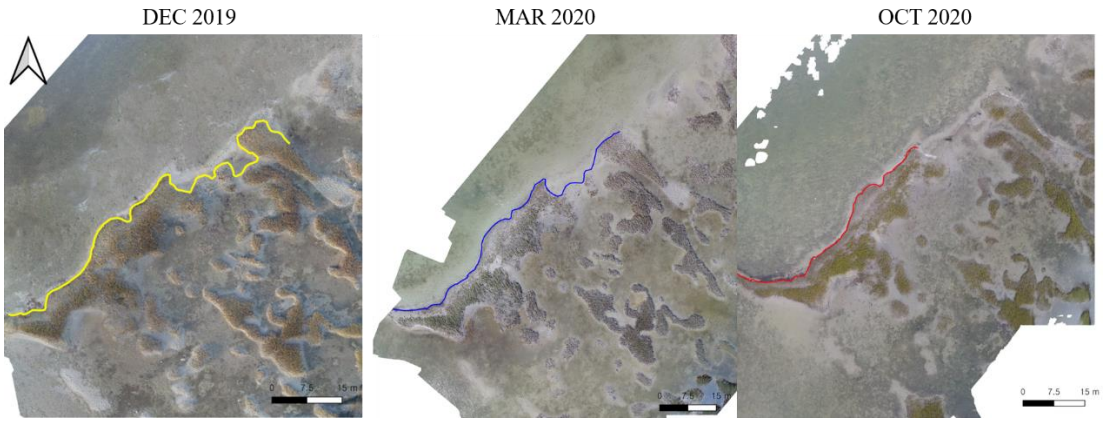

Figure 4-14 Recognized boundary of the salt marsh island in the S3 area of the Sea Grass Lane

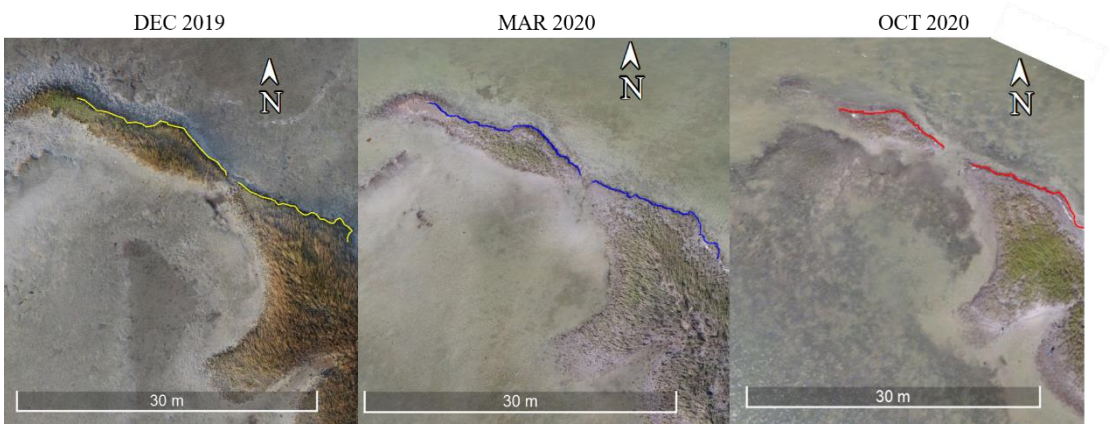

Figure 4-15 Recognized boundary of the salt marsh island in the S4 area of the Sea Grass Lane

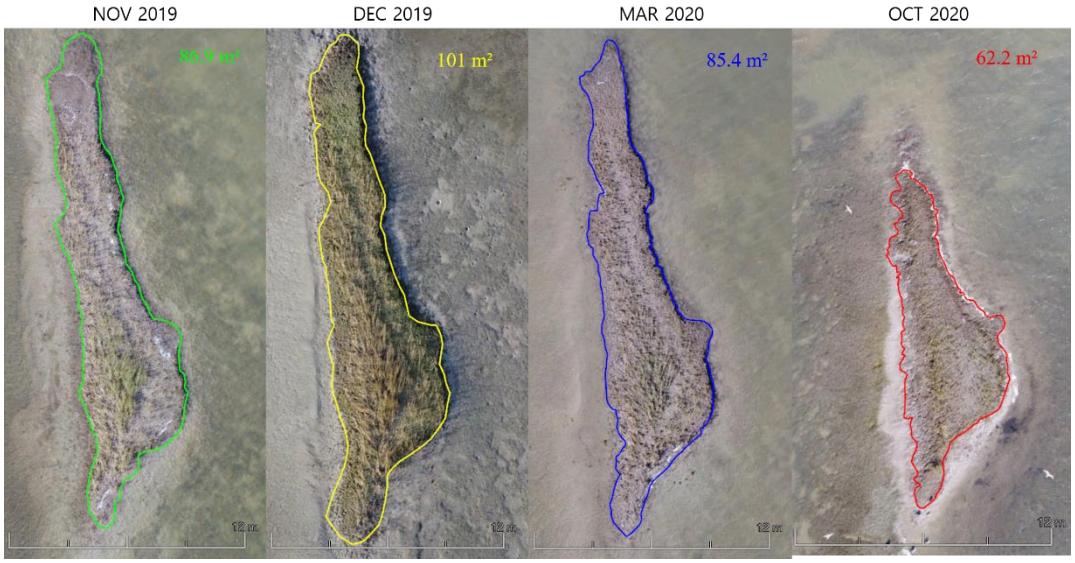

Figure 4-16 Recognized boundary of the salt marsh island in the S5 area of the Sea Grass Lane

The total area of salt marsh island in S5 was increased slightly due to accretion or vegetation growth from NOV to DEC 2019 but decreased around 16.4 m^3 from DEC 2019 to MAR 2020. The vegetation density was also decreased with the erosion of the marsh boundary from DEC 2019 to MAR 2020. The total area was significantly decreased from MAR 2020 to OCT 2020. The overlapped boundaries for S3 and S4 from DEC 2019 to SEP 2020 are shown in Figure 4-17 and Figure 4-18. The polylines drawn along the wetland edge of S5 from MAR to SEP 2020 are shown in Figures 4-19.

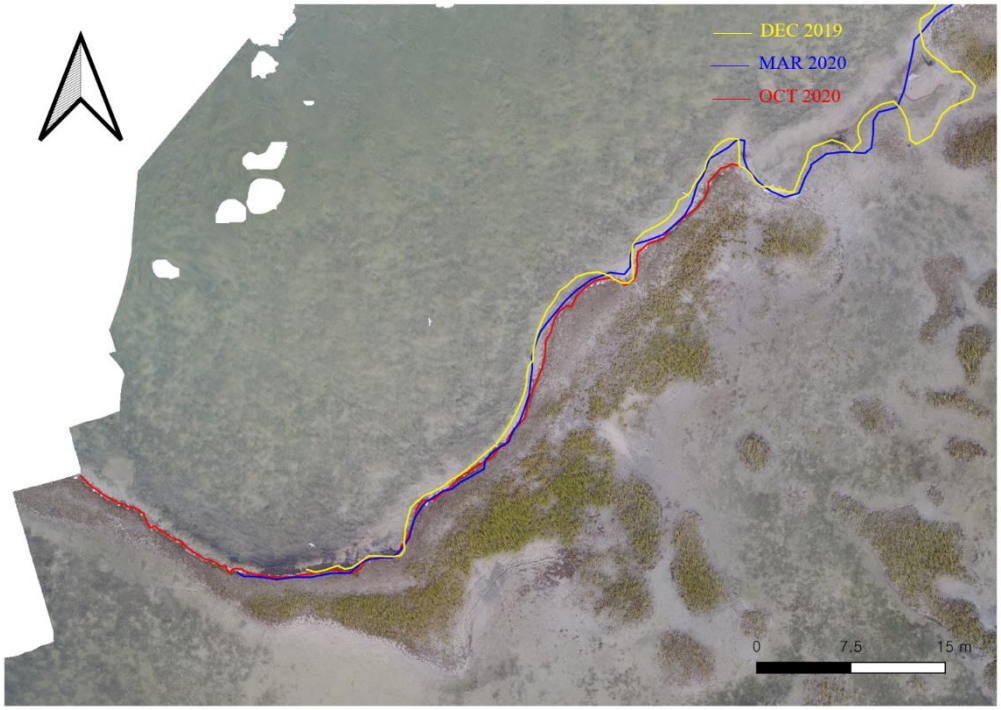

Figure 4-17 Overlap of shorelines of salt marsh in the different drone survey measurements of the part of the S3 area

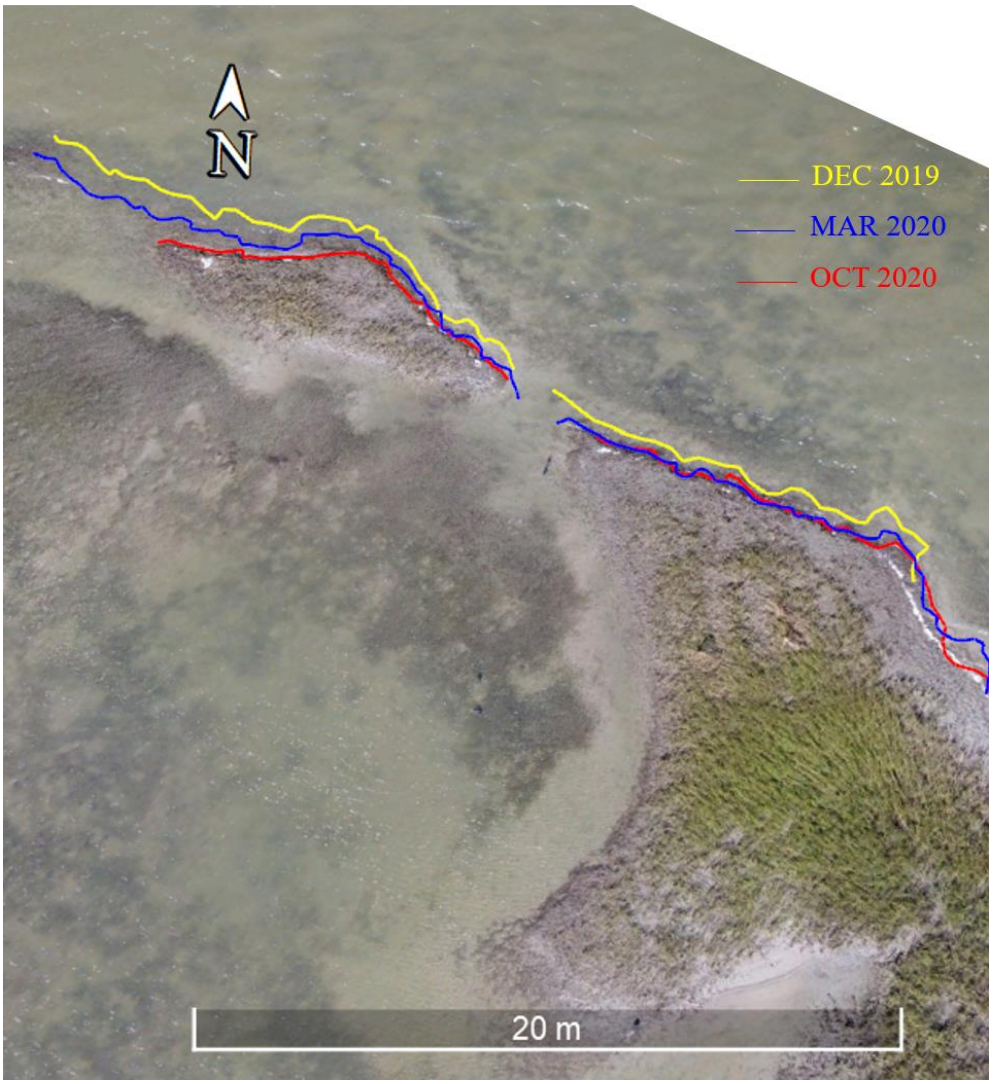

Figure 4-18 Overlap of shorelines of salt marsh in the different drone survey measurements of the part of the S4 area

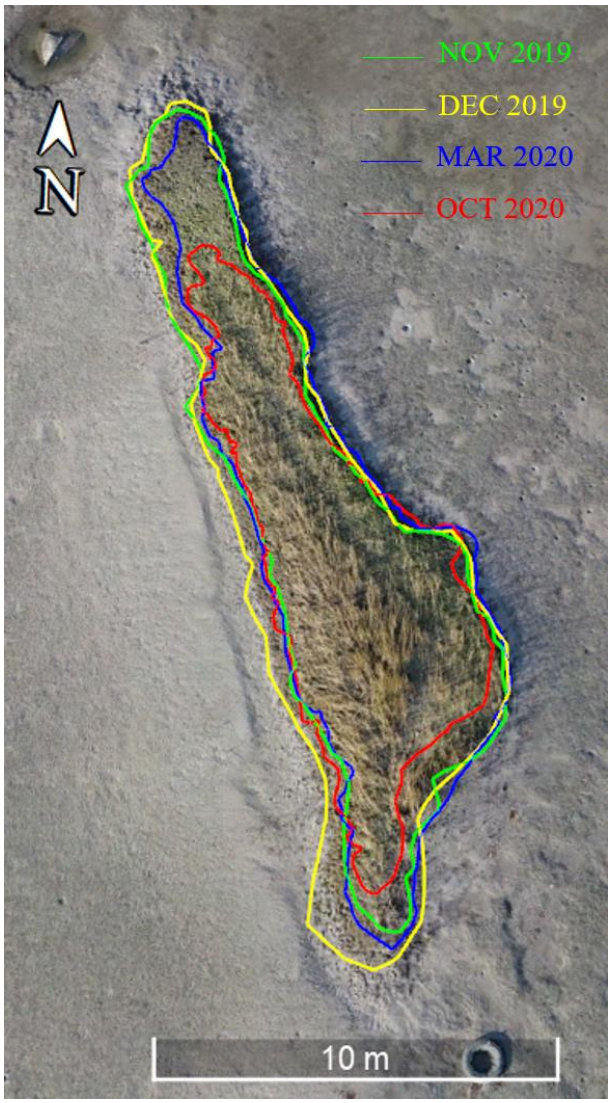

Figure 4-19 Overlap of shorelines of salt marsh island in the different drone survey measurements of the part of the S5 area

4.8. Wind and wave climate in the bay during the measurement period

The wind condition was investigated based on the wind data from the NOAA weather station in the Galveston Railroad Bridge (Station ID: 8771486), Texas. Averaged wind speed was determined by a 2-minute scalar average of 1-second wind speed measurements collected prior to each tenth hour. The monthly wind rose from

DEC 2019 to OCT 2020 was presented in Figure 4-20. Winds from the Galveston Railroad Bridge wind station, measured at 8.44 m above mean sea level, were corrected to the standard 10 m height using the following equation.

$$U_{10} = u(\frac{10}{z_r})^{0.11} \quad (4.1)$$

where u is the wind speed (m/s) at a reference height z_r, and U_{10} is the wind speed at 10 m neutral stability conditions, an exponent of 0.11 is more appropriate over open water (e.g., for the offshore area) than 0.143, which is more applicable over open land surfaces (Hsu et al., 1994).

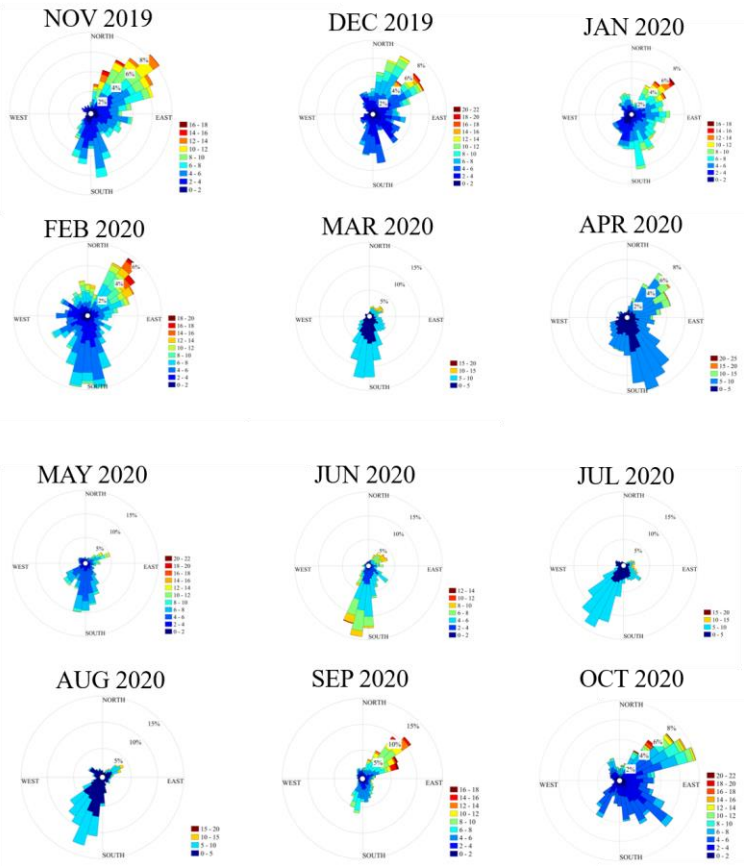

Figure 4-20 Wind data at Galveston Railroad Bridge during the UAV survey period (NOV 2019 - OCT 2020)

From NOV 2019 to FEB 2020, winds from the northeast were very active, and relatively strong winds were blowing that range from 10 m/s to 22 m/s. It is considered that cold fronts during this period generated higher wind velocity. From JUN to AUG 2020, winds from south, southeast, and southwest were very active, but most of their speed was less than 10 m/s. Based on the wind data, wave climate was investigated preliminarily using the equation based on Young and Verhagen (1996). The equation in Young and Verhagen (1996) can calculate the wave power in the field with a short computation time. The wave power can be calculated as $P = Wc_g$, where W is wave energy, $W = \rho g H^2/8$, and c_g is the group velocity. The dimensionless wave energy, $\varepsilon = g^2 W/U^4$, and peak frequency, $\nu = FU/g$, are related to the nondimensional fetch $\chi = gx/U^2$ and dimensionless water depth $\delta = gd/U^2$ through the expression

$$\varepsilon = 3.64 \cdot 10^{-3} (tanh A_1 tanh \left[\frac{B_1}{tanh A_1}\right])^{1.74} \tag{4.2}$$

where U is the reference wind velocity at an elevation of 10 m, F is the wave frequency, x is the fetch, d is the water depth, $A_1 = 0.493\delta^{1.01}$ and $B_1 = 3.13 \cdot 10^{-3}\chi^{0.57}$. The dimensionless peak frequency is

$$\nu = 0.133 \left\{tanh A_2 tanh \left[\frac{B_2}{tanh A_2}\right]\right\}^{-0.37} \tag{4.3}$$

where $A_2 = 0.331\delta^{1.01}$ and $B_2 = 3.13 \cdot 10^{-4}\chi^{0.73}$.

The maximum fetch length corresponding to each direction was selected, and the wave power of the North, South, West, and East was calculated based on the location of

salt marshes in the Sea Grass Lane area. The calculated maximum fetch lengths are presented in Table 4-9.

Table 4-9 Calculated fetch length based on the location of the salt marsh boundary

Location	Water Depth (m)	Fetch to North (m)	Fetch to South (m)	Fetch to West (m)	Fetch to East (m)
S5 area	0.3	19,120	680	12,750	1,680

The monthly calculated waves for one year by the Young and Verhagen (1996)'s method from AUG 2019 to SEP 2020 was presented in Figure 4-21. Cumulative bulk wave power was the highest in SEP 2020. It is also noticeable that the waves from north and east affecting salt marsh were active from OCT 2019 to APR 2020 (excepting Mar 2020). However, waves from the south were active from MAR 2020 to AUG 2020. Wave climate is also calculated using the hydrodynamic and wave model of Delft3D. The model grid was generated as a medium-scale model covering the entire Galveston Bay and the offshore part of Galveston Bay. The model uses an equidistant grid and the grid size is 370 m. The grid and bathymetry of the model are shown in Figure 4-22.

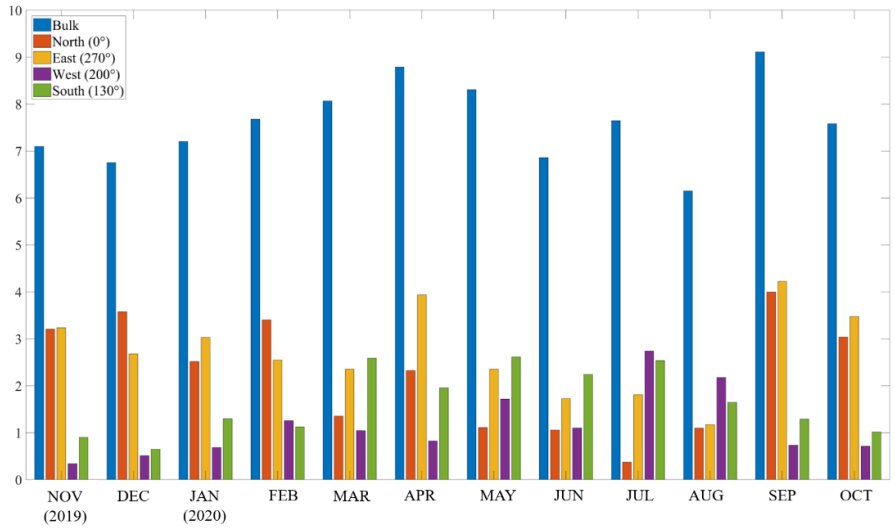

Figure 4-21 Calculated monthly averaged wave power (W/m) from NOV 2019 to OCT 2020

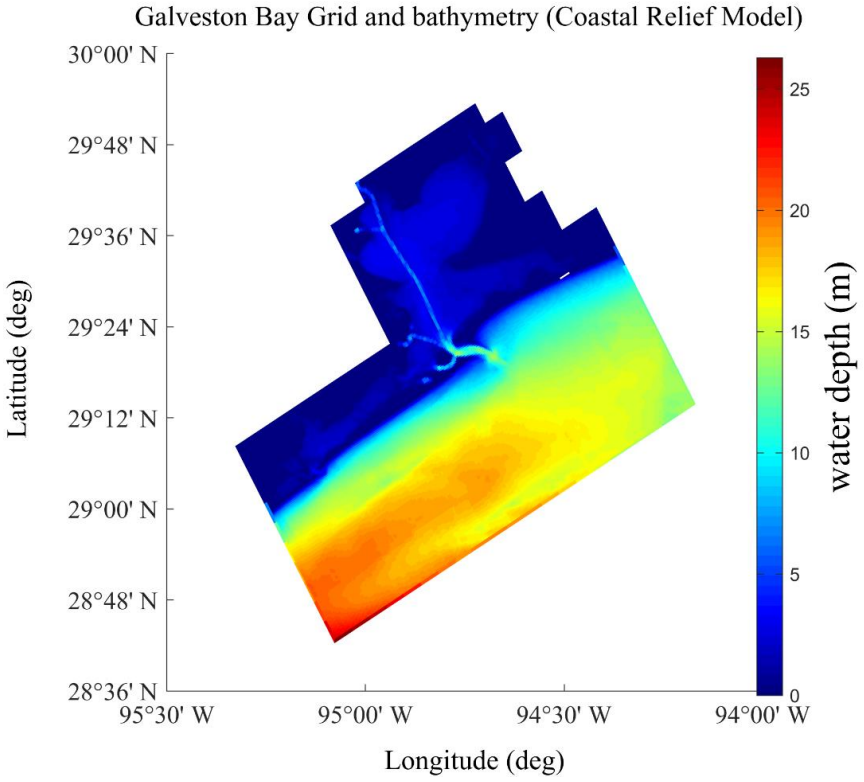

Figure 4-22 Galveston Bay grid and bathymetry in Delft3D model

The wind data from Galveston Railroad Bridge (Station ID: 8771486), Texas, was used as wind input for the domain. The DELFT3D model suite was configured to allow the hydrodynamic flow model (Delft3D-FLOW) and the SWAN wave model to communicate every one hour during the simulation. The time step of the DELFT3D-FLOW model was 1 minute and the SWAN time step and coupling interval with the flow is one hour. The wave directional spectra in SWAN model are discretized into 72 directional bins of constant 5-degree width, and the frequencies are discretized over 24 frequency bins, in the range of 0.05-1 Hz, which is the default in SWAN. The hindcast uses the wind input formulation based on Snyder et al. (1981), the modified whitecapping expression of Rogers et al. (2003), and quadruplet nonlinear interactions via the discrete interaction approximation (Hasselmann et al., 1985). For the shallow-water source terms, depth-induced breaking is computed with a spectral version of the model of Battjes and Janssen (1978) with the breaking index γ= 0.73. Wave refraction is enabled in regions where the resolution of the bathymetry is sufficient to prevent spurious wave refraction. Both models were run on the same computational grid, thus eliminating the need for interpolation between models. The monthly wind and wave rose, bulk and effective wave power at Sea Grass Lane area based on the Delft3D was presented in Figure 4-23 during the drone measurement period.

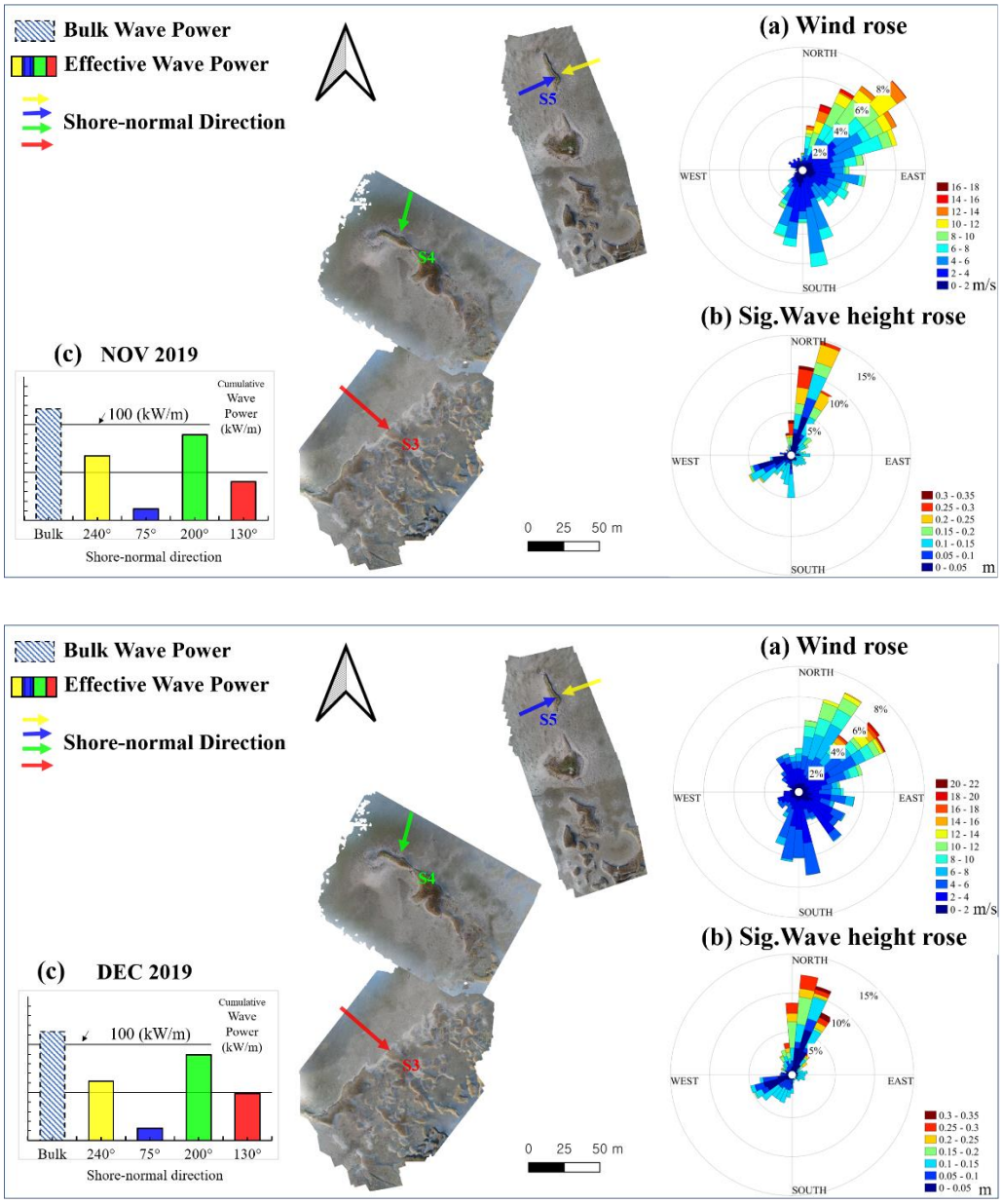

Figure 4-23 Monthly (a) wind and (b) wave rose, (c) cumulative bulk and effective wave power by different shore-normal direction from NOV 2019 to OCT 2020

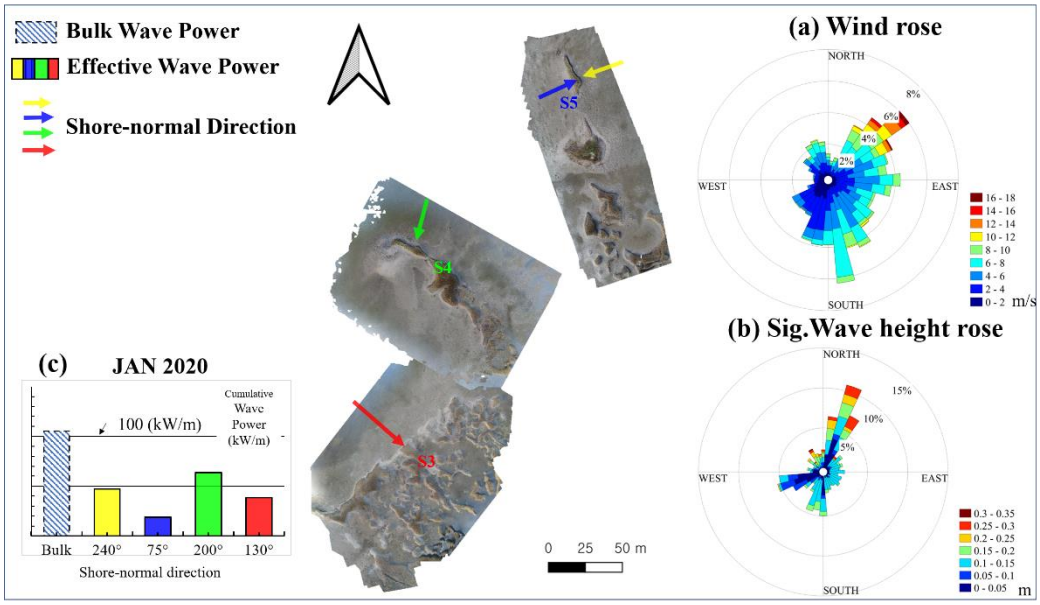

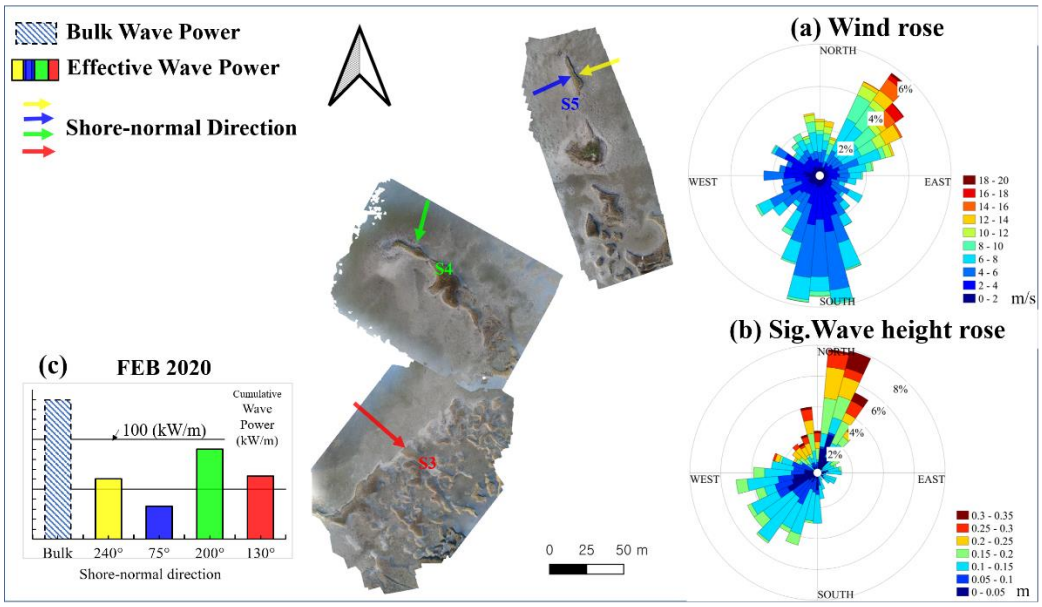

Figure 4-23 Continued.

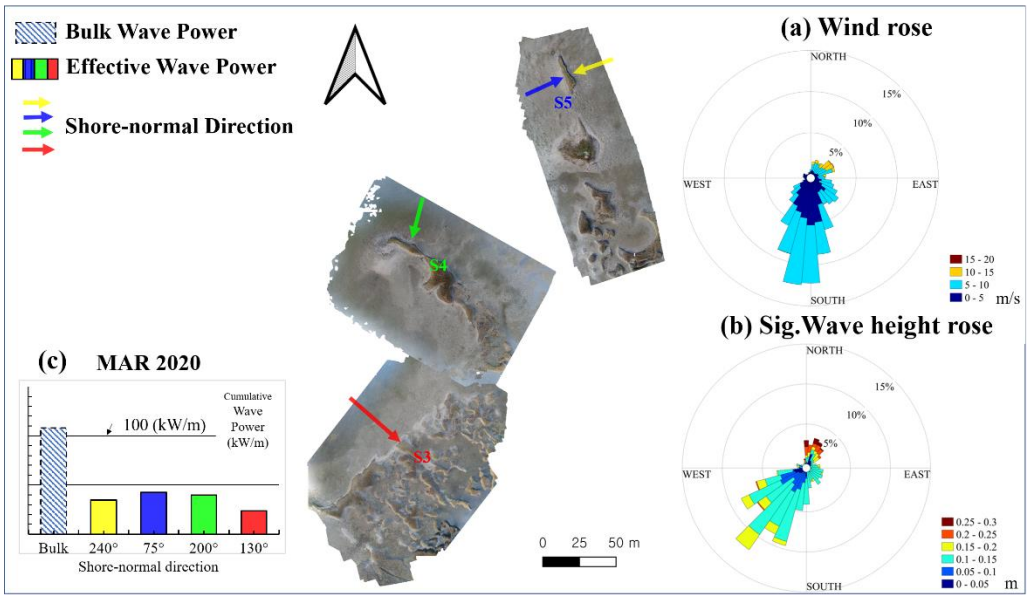

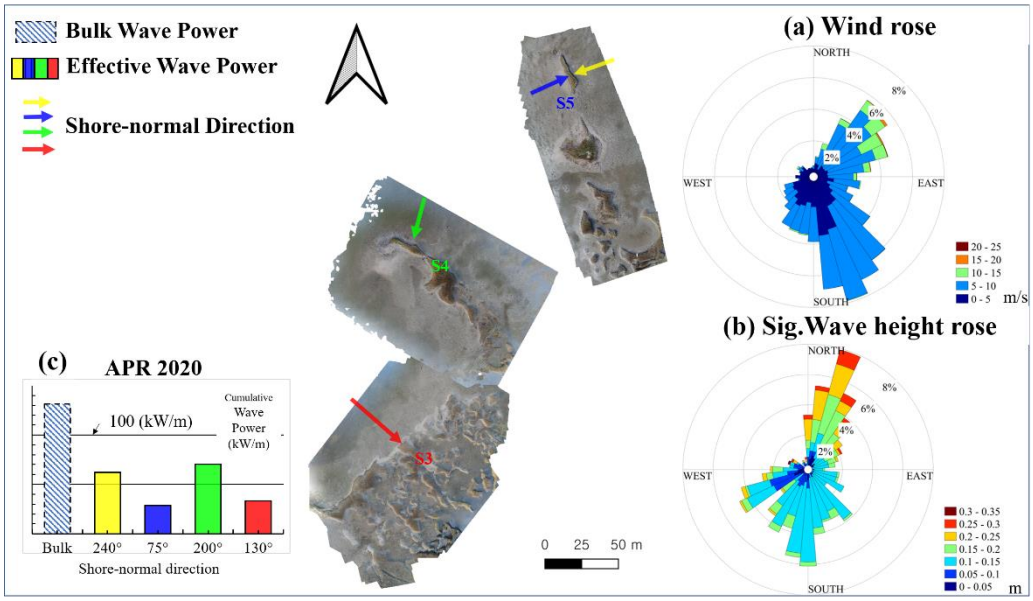

Figure 4-23 Continued.

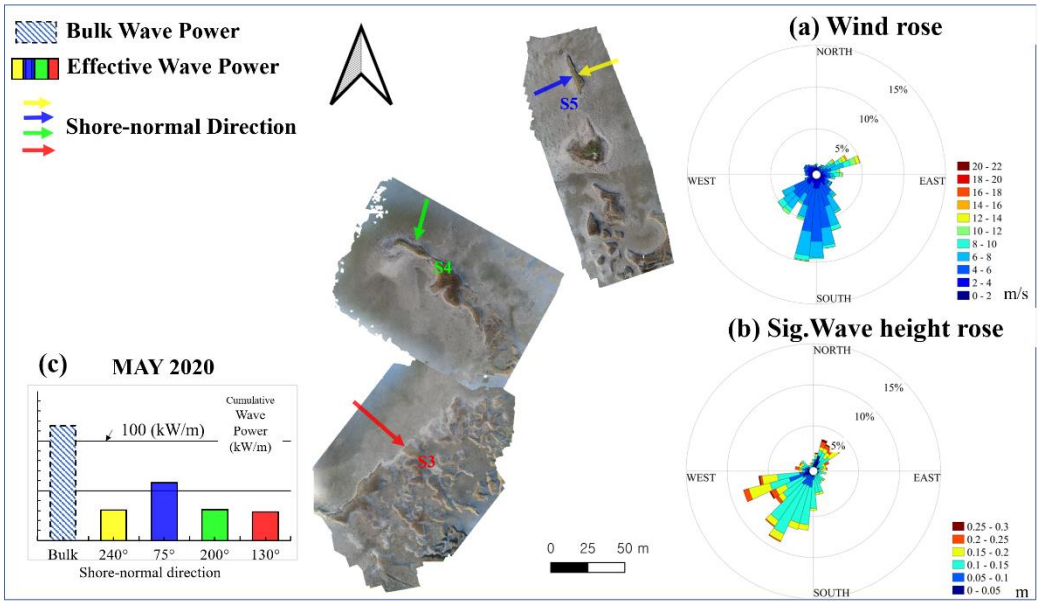

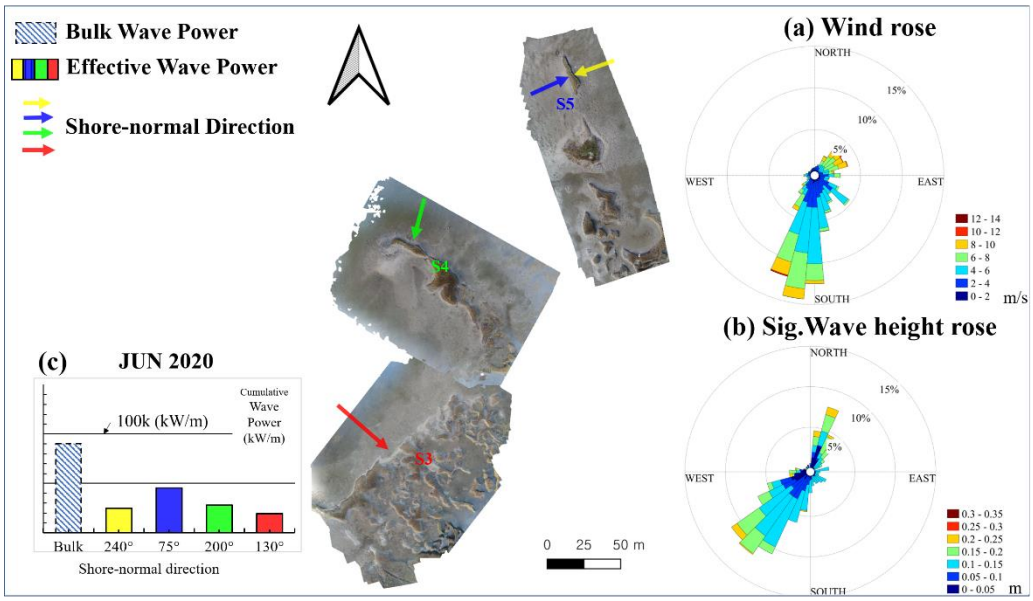

Figure 4-23 Continued.

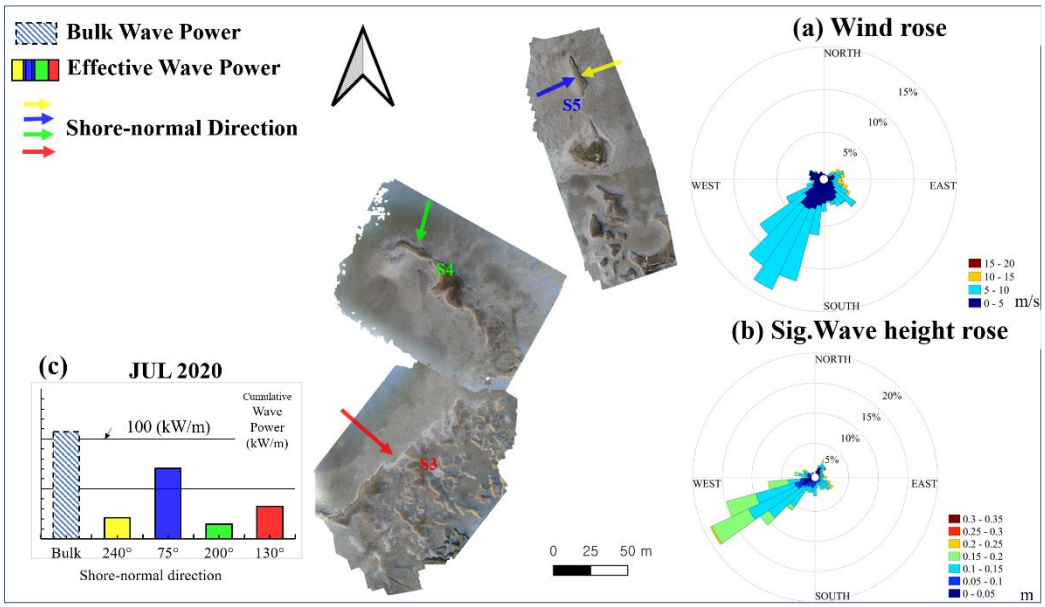

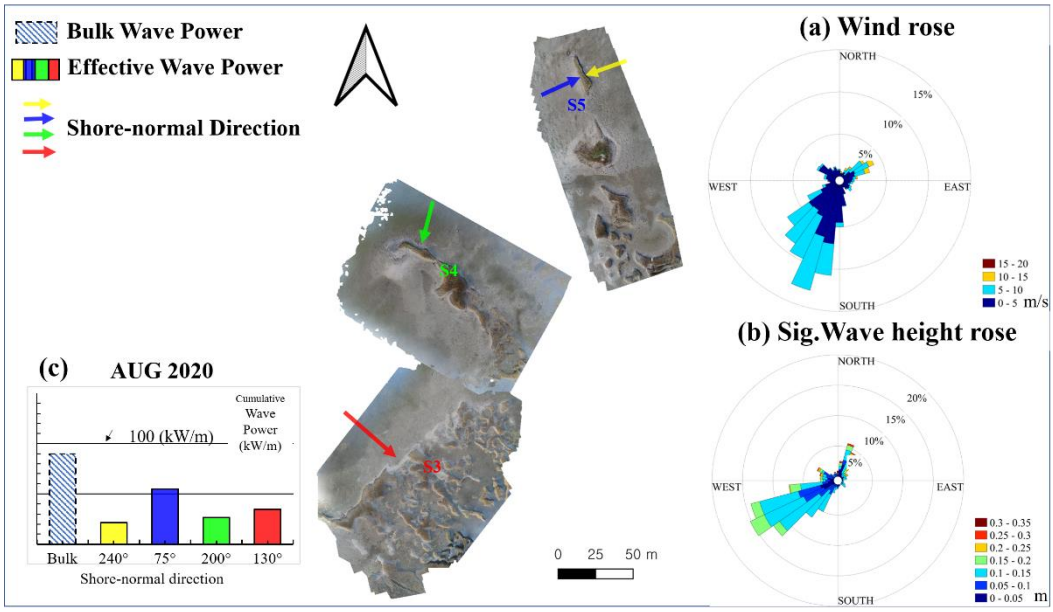

Figure 4-23 Continued.

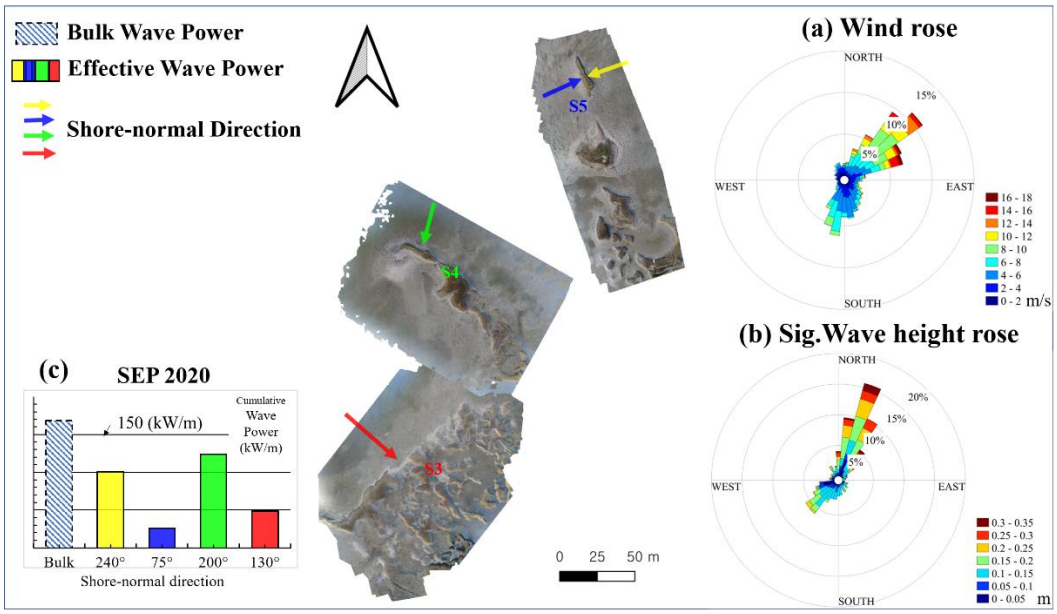

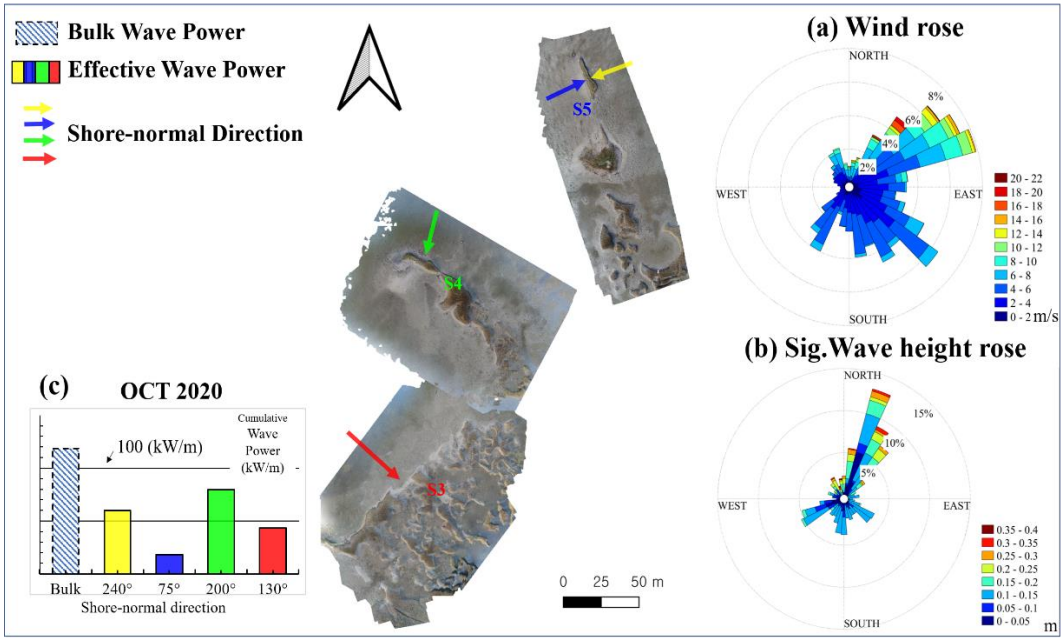

Figure 4-23 Continued.

As for the difference between wind and waves, the wind direction was broadly distributed in the range of wind blowing from the north and east, but the rate of waves mainly propagated from the northeast was the highest. From MAR 2020 to SEP 2020,

the proportion of wind blowing from the south, southwest, and southeast was higher than in other directions. However, the majority of the winds in these periods were less than 10 m/s.

Over entire periods, the wave direction showed relatively similar trends. The proportion of waves flowing from the south or from the east was relatively small, or their significant wave height was generally less than 0.1 m. This is because the south-east direction is the back-barrier direction. From NOV 2019 to FEB 2020, the proportion of wind blowing from the northeast was the highest. Accordingly, the waves from the northeast to the southwest were also observed the most in the simulation.

In the wave rose from MAR 2020 to SEP 2020, the waves generated in the southeast direction and proceeding toward the northwest hardly appear, which is thought to be related to the orientation of Galveston Island (WWS to EEN). Waves from southwest and south to northeast and north were observed frequently. However, most of the significant wave heights did not exceed 0.2 m from these directions due to relatively weak winds.

In order to analyze the effect of wave direction on wetland erosion, the cumulative effective wave energy was calculated for the four directions normal to the salt marsh edges in the site. During the survey period, the cumulative effective wave energy of waves propagating from the northeast (200 degrees) to southwest was the highest, followed by the waves propagating from the northeast (240 degrees) to the southwest. In summary, monthly cumulative bulk and effective wave power are plotted in Figure 4-24.

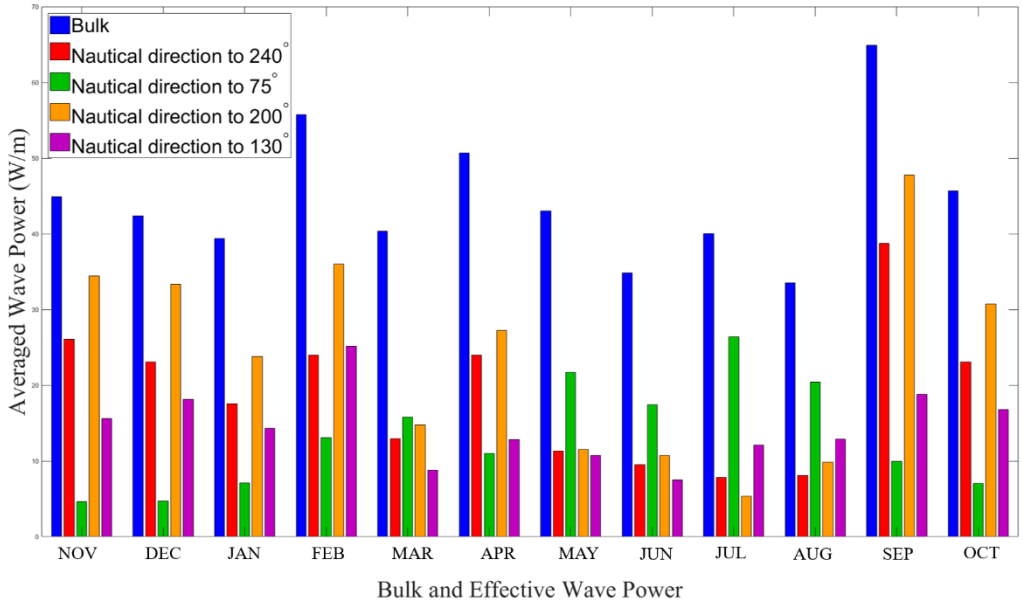

Figure 4-24 Monthly cumulative bulk and effective wave power from NOV 2019 to OCT 2020

Cumulative bulk wave power was the highest during SEP 2020. The lowest cumulative bulk wave power was during the summer, in AUG 2020 and JUN 2020. From autumn to spring (NOV 2019 to APR 2020), cumulative wave power of shore-normal direction of 200° and 240° were calculated higher than the other direction (75° and 130°). During the summer (From MAY 2020 to AUG 2020), cumulative wave power of shore-normal direction of 75° was calculated higher than the other direction (200°, 240°, and 130°).

4.9. Erosion analysis based on wave climate

Erosion of the S3, S4, and S5 area was calculated based on the shoreline orientation of the salt marsh. The erosion calculation was calculated to be parallel to the direction of the specified wave direction in the area. In deriving the relationship between erosion rate and wave energy, the amount of erosion was classified and calculated from the drone survey on March 16. Therefore, erosion from DEC 2019 to MAR 2020 was calculated, and erosion from MAR 2020 to OCT 2020 was calculated separately.

The drone survey of NOV 2019 was not used here. This is because the change between NOV 2019 and DEC 2019 was too small, and it was difficult to judge erosion due to possible accretion or growth of vegetation. In order to measure the erosion rate, lines parallel to the oncoming wave's direction were marked between two different shorelines at regular intervals, as shown in Figure 4-25, and their average value was derived. The calculated erosion(-)/ accretion(+) during the survey period are presented in Table 4-10.

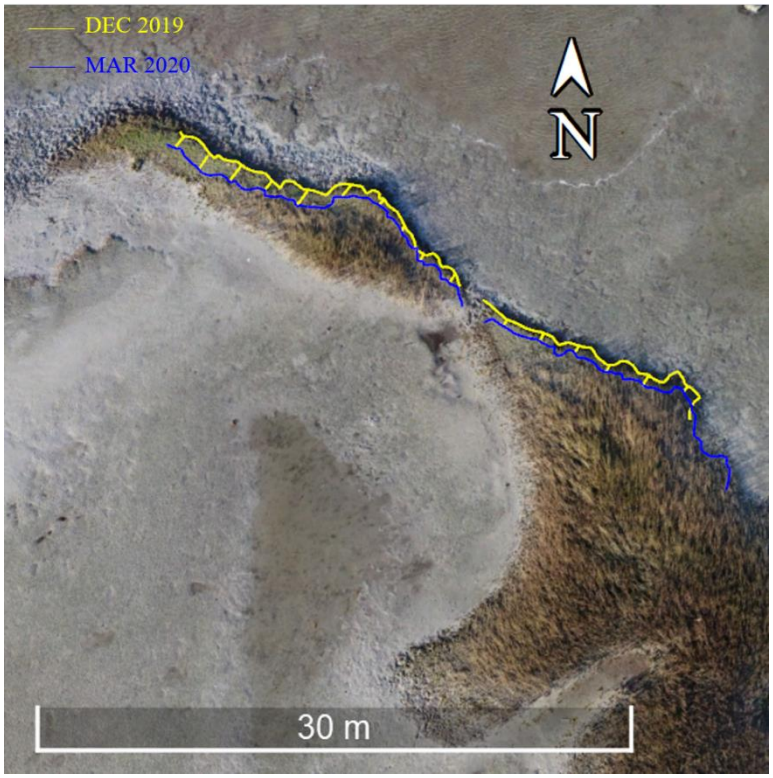

Figure 4-25 The method used in the calculation of edge erosion of the salt marsh in the S4 area

Table 4-10 Erosion during the UAV image measurement periods

Area	Wave direction	Erosion (-) / accretion (+)		
		DEC 1, 2019 to MAR 6, 2020 (m)	MAR 6, 2020 to OCT 30, 2020 (m)	Total Erosion (m)
S3	130°	-0.50	-0.32	-0.82
S4	200°	-0.59	-0.59	-1.18
S5	240°	-0.18	-0.37	-0.54
	75°	-0.46	-0.05	-0.51
Average		-0.43	-0.33	-0.76

For the wave power, the cumulative bulk and effective wave power from DEC 1, 2019 to MAR 6, 2020, and from MAR 6, 2019 to SEP 12, 2019 were calculated for each wave direction (240°, 75°, 200°, and 130°). Erosion was observed the most at the direction of 75° in the S5 area and the least at 130° in the S3 area. While the elapsed date from MAR 6 to SEP 12, 2020 is 238 days, the elapsed date from DEC 1, 2019 to March 6, 2020 is 96 days. Despite this period difference, more erosion occurred from DEC 1, 2019 to MAR 6, 2020, except for the 240° direction of S5. It is believed that the influence of strong winds blowing from the north and northeast directions from DEC 2019 to FEB 2020 has affected the erosion rate.

Table 4-11 Calculated time-averaged wave power with and without inundation consideration for each wave directions relate to the survey areas

Area	Wave direction	Time-averaged wave power (W/m)			
		DEC 1, 2019 to MAR 6, 2020		MAR 6, 2020 to OCT 30, 2020	
		No inundation consideration	Inundation considered	No inundation consideration	Inundation considered
S3	130°	21.2	13.6	16.8	10.6
S4	200°	8.5	8	16.4	15.5
S5	240°	30.6	21	19.4	12.5
	75°	18.9	15.3	12.5	9.7

In Table 4-11, inundation was considered based on tide gauge data at Galveston Railroad Bridge. Water level data records in the model and UAV images taken in AUG

2019. The salt marsh boundaries were inundated at 21:00 (UTC) on AUG 3, 2019, as shown in Figure 4-26. At the same time, the water level at the tide gauge was 0.462 m (NAVD). When the tide gauge level was 0.46 m (NAVD88), the model had a water depth of 0.74 m. When submerged, the waves will not affect lateral erosion of the wetland boundary. However, when the tide gauge level was 0.32 m (NAVD88), the wetland boundary was not submerged, as shown in Figure 4-26. Therefore, the wave power generated above 0.74m of the water depth was nullified (P=0) and shown in Table 4-11.

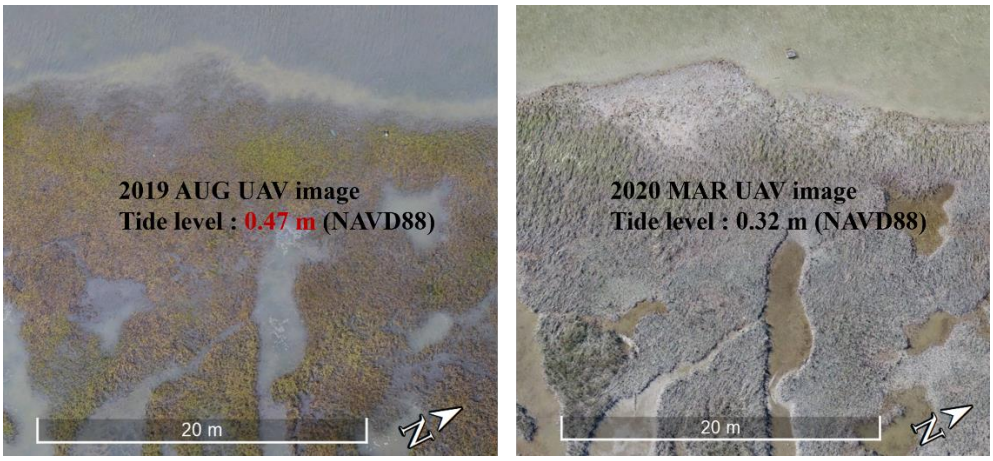

Figure 4-26 Tide level marsh boundary conditions on AUG 3, 2019 and on MAR 16, 2020 in S2 area

The relationship between erosion and wave power was investigated from erosion and time-averaged wave power results during the measurement period. The results are shown in Figure 4-27 when the effect of inundation is not considered. One set of values that deviates the most was excluded in the calculation. In the results, the averaged wave power P (W/m) and Erosion rate R (m/yr) generally has a relationship of R = 0.0457P. The results after the consideration of inundation are shown in Figure 4-28. The averaged

wave power P (W/m) and Erosion rate R (m/yr) generally has a relationship of R = 0.1012P when the inundation was considered. Although there was no obvious increase in linearity tendency, it was confirmed that P to R's proportionality coefficient increased by about 2.2 times compared to the case with no consideration of inundation.

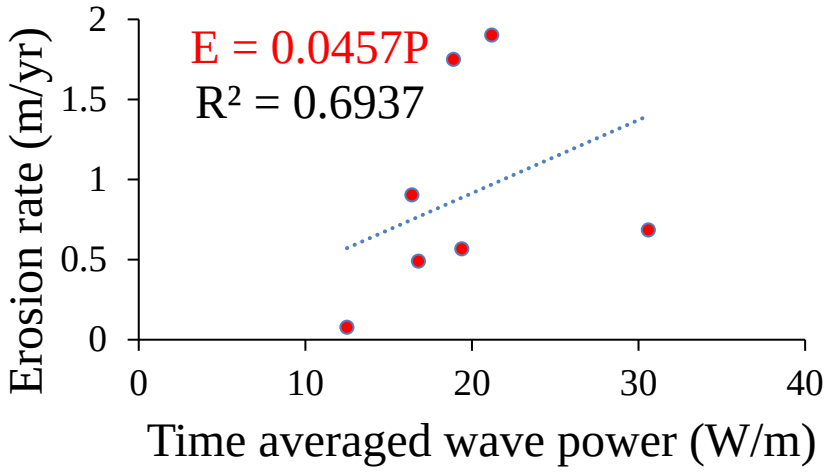

Figure 4-27 Relationship between erosion rate and wave power based on UAV images and numerical model

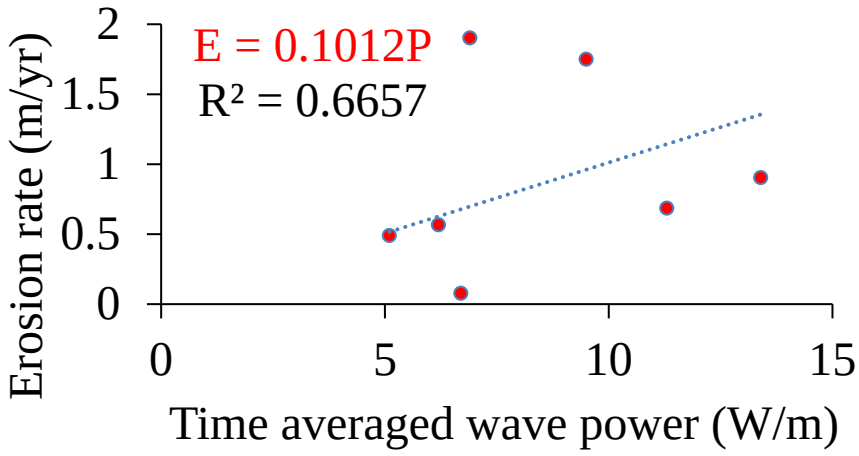

Figure 4-28 Relationship between erosion rate and wave power based on UAV images and numerical model after consideration of flooding

4.10. Discussion

4.10.1. Environment and variables for UAV survey

In this chapter, short-term erosion analysis of wetlands using UAV was conducted. In order to obtain accurate coordinate values of the wetland boundary, PPK analysis was performed through a GNSS receiver installed on the ground and a GNSS receiver attached to the drone. Changes in the boundary of the wetland area were observed through UAV surveys for one year. There were difficulties encountered in this field survey as follows. Planning operations at coastal sites is challenging since it can be hard to find (and to access) a suitable takeoff and landing area. In addition, since GCP cannot be installed readily, other methods are required to maintain accuracy. In this chapter, a method combining GNSS receivers and the use of tie points using a checkpoint was adopted and implemented. In order to minimize the coordinate error with other periods, a fixed ground GPS location should always be used. Using the PPK solution for GNSS receivers, the camera's positional accuracy in the UAV was calculated as sub-centimeter-level accuracy. However, this accuracy may vary depending on the time zone in which the image is photographed by UAV. This is because the number of possible satellites varies depending on the time zone. Only GPS satellites were used for the maximum data recording frequency (14 Hz) in GNSS receivers. Accordingly, when there were insufficient satellites (mainly 7 or less) in the designated mask angle, the final map's error tends to be slightly larger due to the coordinate errors of images.

The tide level greatly influences the recognition of the salt marsh edge. In the case of UAV surveying at high tide, the boundaries of wetlands can hardly be distinguished. On the contrary, at low tide, it is possible to survey the surrounding bathymetry as well as the edge of the wetland. The UAV image in DEC 2019 (Appendix Figure B2-3) was taken at the lowest tide, and accordingly, the surrounding seabed bathymetry was additionally observed. However, the images taken in AUG 2019 (Appendix Figure B2-1) were difficult to distinguish wetlands boundaries due to a high tide and high turbidity of the water. In order to solve this problem, only the recognizable edges of wetlands were analyzed to avoid the difficulty of dividing boundaries caused by flooding. Therefore, a survey during the low tide is recommended for recognizing the wetlands boundaries. However, it is challenging to survey the boundary at the identical water level condition to another survey, especially during low tide conditions. This is because a relatively low tide does not occur much in Galveston Bay than a high tide despite the advantages. During December 2019, the tide gauge of the Galveston Railroad bridge fell below -0.3 m (NAVD) 3 times (good for UAV SfM survey), and the number of times it went above 0.3 m (NAVD) 23 times.

4.10.2. Boundary erosion measurements and wave climate

The boundaries of the wetlands were recognized manually by a human. Farris et al. (2019) developed the marsh edge from the elevation data (MEED) method to calculate an objective proxy for a salt marsh shoreline using elevation data. However, this method requires accurate elevation data. The reported RMSE errors between the MEET method to manual digitization was 0.43 m. It is considered that these error values

are not yet suitable for interpreting the short-term erosion of the wetland boundary. The advantages that the manual boundary recognition method can have over the automatic boundary identification method are as follows. The manual recognition is possible to distinguish a point where it is difficult to recognize, for example, if there is no "marsh scarp" with a gentle slope. In addition, there is an advantage when more detail is required in the boundary recognition due to the vegetation at the boundary of the wetland. However, if the boundary is recognized manually, errors can occur according to human judgment. When a high-resolution 3D model is obtained through topographic data using LiDAR or SfM, the wetland boundary recognition can be more accurate.

In the results, the erosion of the wetland boundary was clearly observed during the measurement period from UAV image analysis with GNSS information. The most eroded place was in S4. Especially, erosion at the outer edge of the S4 was very active. This trend was also found in the wetland island of the S5 area. The protruding edge is considered vulnerable to waves coming from various directions. Thus, the erosion of these ends is one of the results proving wave energy's effect on boundary erosion.

The wave power was calculated using the hydrodynamics and wave model to derive the relationship between wave energy and erosion rate. This value was compared with the salt marsh edge erosion rate based on the UAV image analysis. From the results, there was a weak correlation between wave energy and erosion rate. For one reason, the erosion rate of protruding areas, such as the S4 or S5 area, increased the overall erosion rate. However, when the wave energy was high, the increase in the erosion rate was remarkable. This is considered to be an important result to infer that

wave energy has more influence on erosion amid repeated erosion and accretion. This is because the erosion accelerated from the part where wave energy was concentrated. Repeated high-resolution topographic surveys can provide evidence to spatially map wetland erosion and deposition rates and patterns (Goodwin et al., 2018). Accumulated topographic data by UAV images can provide insight into these processes and a challenging baseline of model validations.

The winds coming from the northeast direction were active from NOV 2019 to FEB 2020, and therefore, waves from the northeast to the southwest were actively generated during this period. The wave direction was similar to the wind direction, but the wave energy toward southeast direction was the least since this is the back marsh direction. In most periods, waves were coming from the northeast. Consequently, the salt marsh's erosion facing northeast direction can be considered the most affected salt marsh boundary in the area. However, for the correlation between salt marsh erosion and the effective wave power by different directions, further investigation is necessary.

From the perspective of the numerical model, the following cause may have influenced the results. The resolution and model parameter of the numerical model near the region of interest can affect wave power calculation accuracy. In the case of a hydrodynamic model over a period of time over a year, using a detailed model requires a lot of computation time. The Delft3d model used in this chapter has a grid resolution of 370 m, and the computation time was over 3 days for a 1-year simulation (NOV 2019 ~ OCT 2020). For the detailed model used in Chapter 2, it is expected that approximately 121 days of simulation time will be required for a 1-year simulation (Operating

condition: 16 CPU cores). Although a highly resolved model requires more computational power than the model in this chapter, it is important to derive the wave power through a model in which the region of interest is highly refined. This is because the detailed model can consider refraction of waves, protection from surrounding areas, and fetch conditions more precisely.

4.11. Conclusions

In this chapter, the application of an alternative SfM-MVS geolocation method known as GNSS-supported aerial triangulation was presented in the UAV survey. By using an on-board carrier-phase GNSS receiver to geolocate UAV images, the need for GCPs was significantly reduced. The uncertainties in the salt marsh surface reconstruction can be reduced to an average of 1 ~ 1.3 cm horizontally when flying at ~45 m above ground level. The erosion of salt marsh boundary over a year was analyzed using high-precision wetland images obtained through the drone surveys with GNSS receivers, and compared with the wave energy generated during that time. The averaged coordinate RMSE of the final orthomosaic maps produced by a GNSS receiver equipped UAV was 1 to 1.3 cm in the horizontal direction.

The wind data near the survey area was used to predict the wave environment based on the standard equation and the SWAN model. The direction of wind and waves showed a distinct difference between winter and summer. Based on the erosion records in the UAV orthomosaic images and the calculated effective wave power based on the numerical model, their relationship was investigated. The retreat rate of the salt marsh edges of the surveyed area over a year was -0.76 m. In addition, the erosion from DEC

2019 to MAR 2020 was higher than the erosion from MAR 2020 to OCT 2020. The difference in erosion was likely influenced by the high proportion of northeast to southwest wind from DEC 2019 to MAR 2020.

Salt marshes in Galveston Bay are continuously threatened by global sea level rise and anthropogenic stresses such as excessive groundwater pumping. To effectively implement the wetland conservation policy, accurate data for the analysis of the progress of wetland erosion is needed. In this respect, periodic high-precision measurements using UAVs can play an important role in future wetland conservation policies.

5. SEDIMENT TRANSPORT DURING COLD FRONT PASSAGE AFFECTING THE MORPHODYNAMIC OF SALT MARSHES IN SHALLOW BAY

5.1. Introduction

Salt marshes are usually formed by biogeographical morphological feedback processes, which is bidirectional interactions between biological and physical processes (Bouma et al., 2016). Sediments flooded on the salt-marsh platform can be trapped by vegetation because of its ability to reduce the hydrodynamic energy (Leonard and Luther, 1995; Bouma et al., 2005; Temmerman et al., 2007; Temmerman et al., 2012), which allow the plants to grow well on the salt marsh (Bruno, 2000). Therefore, it becomes more effective at capturing more sediment, providing positive feedback. (Fagherazzi et al., 2012; Kirwan and Megonigal, 2013).

Previous studies have shown that sediment supply from marine or stream sources can reduce the risk of erosion if sediment builds up and raises tidal flats, given sufficient sediment. For example, the Bay of Fundy's wetlands, a large tidal flat in Canada, are resistant to erosion. Because new sediments are carried to the tidal flat's edge by large-amplitude tides in ice rafting (van Proosdij et al., 2006).

Increasing sea-level rise and severity of storms and river floods act collectively to increase water depth and wave / tidal currents on the salt marsh boundary, thereby increasing the likelihood of initiating lateral wetland erosion. (Hu et al., 2015; Mariotti & Carr, 2014; Mariotti & Fagherazzi, 2010). However, recent results show that wetlands

can keep pace with sea level rise in different scenarios by trapping sediments on the marsh surface and growing vertically (Kirwan et al., 2016).

The adaptation of wetlands can be related to long-term trends in external forcing (e.g., increased shipping, shifted the position of estuarine channels, sea-level rise, or altered sediment supply) due to the periodic behavior of salt marsh by alternating lateral expansion and retreat stages. On the other hand, wind-induced waves are thought to cause the lateral erosion of the marsh edge (Mariotti and Fagherazzi, 2010; Marani et al., 2011; Mariotti and Fagherazzi, 2013; Mariotti and Carr, 2014). The erosion by waves can also be the cause of the periodic behavior of salt marshes.

In general, understanding the mechanisms of wetland edge morphodynamics is critical to understanding wetland's vulnerability to the loss in response to global sea-level rise and land subsidence. To address the net effect of mild storms on the morphology of tidal flats, it is necessary to identify the causes of sediment supply to coastal wetlands and take appropriate measures to balance sediment. This requires analysis through hydrodynamic and morphodynamic numerical modeling along the wetlands area. Since observation alone has limitations in understanding these processes. Accuracy of modeled accretion rates is susceptible to the suspended sediment concentration (SSC) (Kirwan et al., 2010) and the bay-centric processes that affect sediment availability. In Galveston Bay, Ravens et al. (2009) suggested the importance of sediment supply for sediment accretion rates in West Galveston Bay marshes through the radiochemical analysis.

Recent experiments have investigated the processes that trigger the initiation of wetland boundary migration (Bouma et al., 2016). Bouma et al. (2016) suggest that the transition from steady-state to progression or erosion may be related to short-term fluctuations in sediment dynamics and bed elevation. Specifically, lateral erosion is triggered when short-term sediment dynamics create a significant height difference between marsh areas and surrounding tidal flats. Short-term sediment dynamics can also cause bed level changes, which are too high to allow establishment of seedlings and associated marsh progradation.

Although there have been many field studies, model prediction has not been able to keep pace. Specifically, processes involving morphological dynamics in adjacent bays have not been incorporated into regional models of wetland evolution (Wiberg et al., 2020). For example, many studies (Liu et al., 2018; Zang et al., 2018; Defne et al., 2019) have been done to model sediment transport and morphodynamic processes for shallow bay shorelines during hurricane passage. However, no study has verified the erosion and accretion processes from mild storms such as cold front passages using a large scale model and high-resolution topography of salt marshes.

In this chapter, we use the sediment transport module in Delft3D-FLOW, combined with the SWAN wave model. Delft3D-FLOW is capable of sediment dynamics and morphological processes in shallow water environments (Horstman et al., 2015). The details of Delft3D-FLOW and SWAN are described in Chapter 2. In Delft3D-FLOW, sediment transport and sedimentation are calculated simultaneously

with the hydrodynamics, facilitating direct feedback between fluid forcing and morphology (Lesser et al., 2004).

The purpose of this chapter is to investigate the short-term sediment transport processes during the cold front passage and its effect on salt marsh boundary accretion and erosion with and without relative sea level rise. During the cold front passage in the simulation period, the changes in water level and waves in the Galveston Bay due to the wind forcings were relatively high. This chapter assesses the changes in sediment supply to the wetland area caused by the cold front. In addition, the morphological changes by sediments around the edge of the wetland that change due to relative sea level rise were investigated.

5.2. Galveston bay and sediment transport

Sediments in Galveston Bay are delivered from several sources, including rivers, erosion at the edge of the bay, and Gulf sediments transported through the inlets (Newell et al., 1994). Some sediments are transported from the southwest by longshore currents since the entrance to Galveston Bay is near the banks of the Mississippi River (Newell et al., 1994). The bottom of the bay is formed by various sediment sources and physical processes, including ocean currents and wave energy. Overall, the predominant sediment types of the bay are fine-grained: mud, muddy sand, and sandy mud, as shown in Figure 5-1 based on usSEABED 2006 results (Buczkowski et al., 2006; Williams et al., 2007).

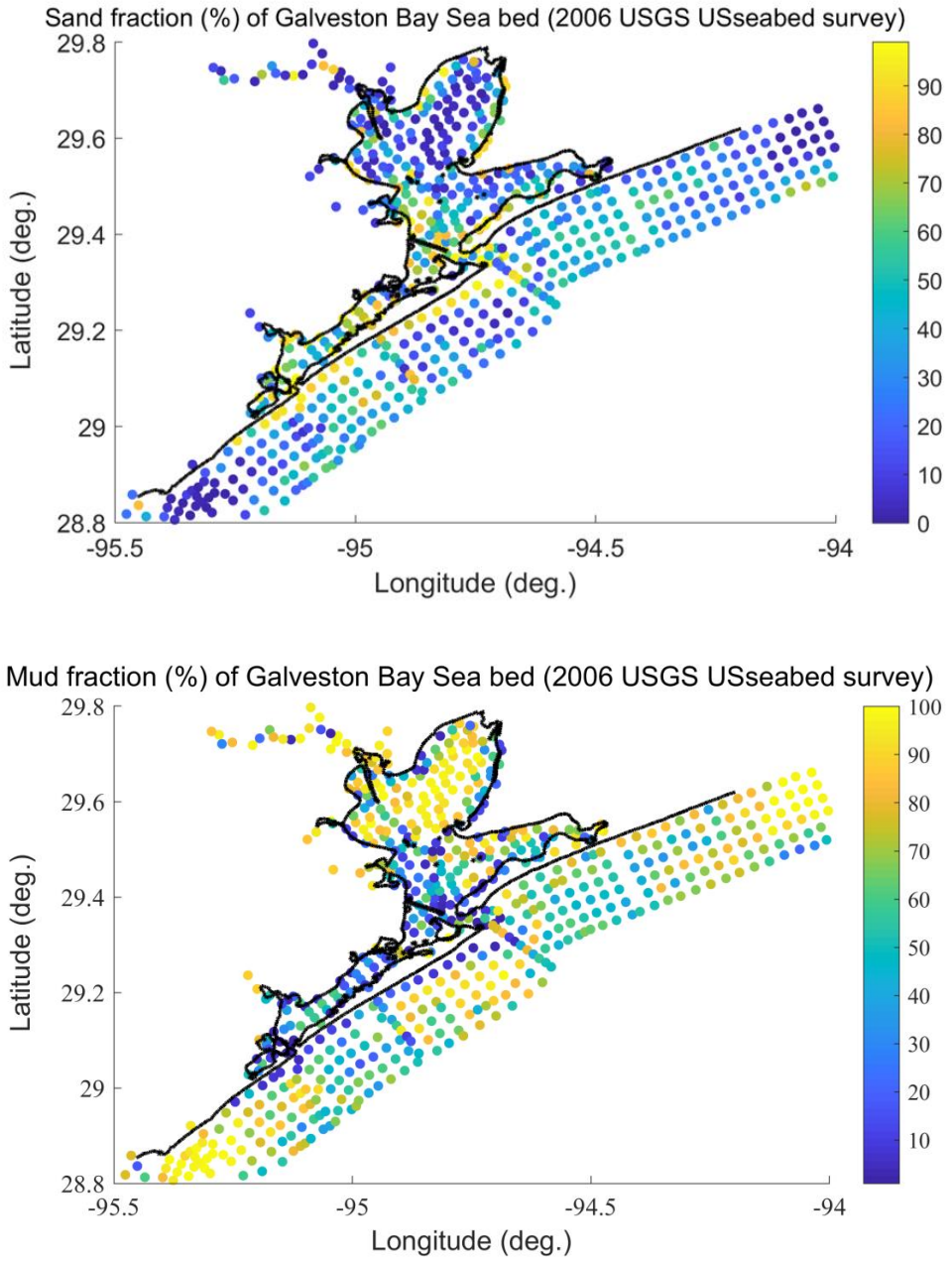

Figure 5-1 Sediment texture (sand and mud fraction) in Galveston Bay

Areas with high wave and current energy have mainly coarse-grained sediments (sand, gravel, and shell) since fine-grained material (mud and silt) remains suspended. The result is often a beach or bar composed of shell hash or sand. Relatively high energy

areas include lower Galveston Bay near Bolivar Roads. Other factors affect circulation and sediment distribution patterns, locally forming a patchwork-like appearance of different sediments on the bay floor. Some of the main impacts on sediment in certain parts of the bay are: oyster reefs, artifact barrier islands and delta formed during the pre-sea level decline 30,000 years ago, dredge material islands, the impact of sand sources on the Bolivar Peninsula and Galveston Islands on water flow, and infrequent but intense storm events (Newell et al., 1994).

5.3. Sediment transport in Delft3D model

5.3.1. Delft3D and SWAN model setting

This chapter uses the same model in Chapter 2 for the hydrodynamic and wave forcing. The details of hydrodynamic processes and wave climates during the simulation period were already discussed in Chapter 2. The details of the model parameter in Delft3D-Flow and SWAN are also described in Chapter 2. The following parameters are the default parameter settings for Delft3D-FLOW and WAVE simulation. The time step of the DELFT3D-FLOW model is 1 min and the SWAN time step and coupling interval are 30 min in the default model. The SWAN model calculates the wave energy spectrum; the wave directions are discretized into 72 directional bins of constant width 5 degrees, and the frequencies are discretized over 24 frequency bins, in the range of 0.05-1 Hz. For the shallow-water source terms in SWAN, depth-induced breaking is computed with a spectral version of Battjes and Janssen (1978) model with the breaking index $\gamma = 0.73$. Wave refraction is enabled in regions where the resolution of the bathymetry is sufficient to prevent spurious wave refraction over one spatial element,

specifically in Galveston Bay. In the coupling of DELFT3D-FLOW and SWAN, both models run on the same grid, thus eliminating the need for interpolation between the model. The model grids are presented in Figure 2-4 of Chapter 2.

5.3.2. Bed load transport in Delft3D model

The formulations of Van Rijn et al. (1993) and Partheniades and Krone formulations (Partheniades, 1965) are used for non-cohesive and cohesive sediment, respectively.

(1) Van Rijn et al. (1993)

$$q_b = 0.25 d_{50} u_{*,c} D_*^{-0.3} T^{1.5} \tag{5.1}$$

in which $T = \frac{\tau_{b,cw} - \tau_{b,cr}}{\tau_{b,cr}}$, $D_* = \left[\frac{(s-1)g}{v^2}\right]^{1/3} d_{50}$, $s = \rho_s/\rho$, $u_{*,c} = \sqrt{\tau_{b,cw}/\rho}$

where q_b is instantaneous bed-load transport, d_{50} is median particle diameter, $u_{*,c}$ is shear stress velocity, s is specific gravity, ρ_s is sand density, ρ is water density, D_* is dimensionless particle parameter, T is dimensionless bed -shear stress, v is kinematic viscosity coefficient, g is gravity acceleration, $\tau_{b,cw}$ is instantaneous grain-related bed-shear stress due to both current and waves, $\tau_{b,cr}$ is critical bed-shear stress. Critical shear stress and shear velocity are calculated using particle Reynolds number:

$$Re_p = \frac{d\sqrt{sgd}}{\nu} = 4 \times 10^6 d^{3/2} \tag{5.2}$$

In the formulation of Cao et al. (2006), the critical shear parameter can be obtained with particle Reynolds number:

$$\theta_c = 0.1414 {Re_p}^{-0.2306}, \qquad 0 < Re_p < 6.61$$

$$\theta_c = \frac{\left[1 + (0.0223 Re_p)^{2.8358}\right]^{0.3542}}{3.0946 {Re_p}^{0.6769}}, \qquad 6.61 < Re_p < 282.84 \tag{5.3}$$

$$\theta_c = 0.045 Re_p, \qquad 282.84 < Re_p < \infty$$

Critical shear stress and shear velocity is given by :

$$\tau_{oc} = \theta_c (\rho_s - \rho) g d \tag{5.4}$$

$$u_{*c} = \sqrt{\frac{\tau_{oc}}{\rho}} = \sqrt{\frac{\theta_c d}{0.062}} \tag{5.5}$$

(2) Partheniandes and Krone formulations (Partheniades, 1965)

$$E^{(l)} = M^{(l)} \cdot S(\tau_{b,cw}, {\tau_{cr,e}}^{(l)}) \tag{5.6}$$

$$D^{(l)} = {w_s}^{(l)} {c_b}^{(l)} S'(\tau_{b,cw}, {\tau_{cr,d}}^{(l)}) \tag{5.7}$$

in which

$$S(\tau_{b,cw}, {\tau_{cr,e}}^{(l)}) = \begin{cases} \left(\frac{\tau_{b,cw}}{{\tau_{cr,e}}^{(l)}} - 1\right), \tau_{b,cw} > {\tau_{cr,e}}^{(l)} \\ 0\,, \tau_{b,cw} < {\tau_{cr,e}}^{(l)} \end{cases} \tag{5.8}$$

$$S(\tau_{b,cw}, {\tau_{cr,d}}^{(l)}) = \begin{cases} \left(1 - \frac{\tau_{b,cw}}{{\tau_{cr,d}}^{(l)}}\right), \tau_{b,cw} > {\tau_{cr,d}}^{(l)} \\ 0\,, \tau_{b,cw} \geq {\tau_{cr,d}}^{(l)} \end{cases} \tag{5.9}$$

where E(l) is Erosion flux, M(l) is Erosion parameter and S,S′ are step functions

5.3.3. Suspended load transport in Delft3D

Delft3D resolves suspended sediment transport through an advection-diffusion formulation (Deltares, 2018).

$$\frac{\partial c}{\partial t} + \frac{\partial uc}{\partial x} + \frac{\partial vc}{\partial y} + \frac{\partial (w - w_s)c}{\partial z} = \frac{\partial}{\partial x}\left(D_H \frac{\partial c}{\partial x}\right) + \frac{\partial}{\partial y}\left(D_H \frac{\partial c}{\partial y}\right) + \frac{\partial}{\partial z}\left(D_v \frac{\partial c}{\partial z}\right) \tag{5.10}$$

where, c is suspended sediment concentration, u, v, w are velocity components, w_s is sediment's settling velocity, D_H is horizontal eddy diffusivity and D_v is vertical eddy diffusivity.

For cohesive sediment, Partheniades-Krone equations (Partheniades, 1965)

$$D_r = w_s c_b S'(\tau_b, \tau_{cr,d})$$
$$E_r = MS(\tau_b, \tau_{cr,e}) \tag{5.11}$$

where c_b is near-bed sediment concentration, τ_b is bed shear stress, $\tau_{cr,d}$ and $\tau_{cr,e}$ are critical bed shear stress, which refers to the erodibility of the bed materials. Finally, the morphological change (i.e., net deposition) is calculated by subtracting the time-integrated deposition and erosion rates.

5.3.4. Cohesive and non-cohesive sediment parameters in the model

Two sediment types, mud, and sand were considered in our model. The initial composition of mud and sand on the bed of Galveston Bay was extracted from the usSEABED data. Figure 5-2 shows the average grainsize of the Galveston Bay sediment. The grain size in millimeter was calculated from Phi characteristic grain size in

usSEABED extracted data. The median grainsize of the sand for the Delft3D-FLOW model input was selected based on the usSEABED data. The D_{50} of sand was calculated from the data points (24 points) where the proportion of sand was more than 95 %. Figure 5-3 shows the 24 data points have more than 94.9 % of sand fraction.

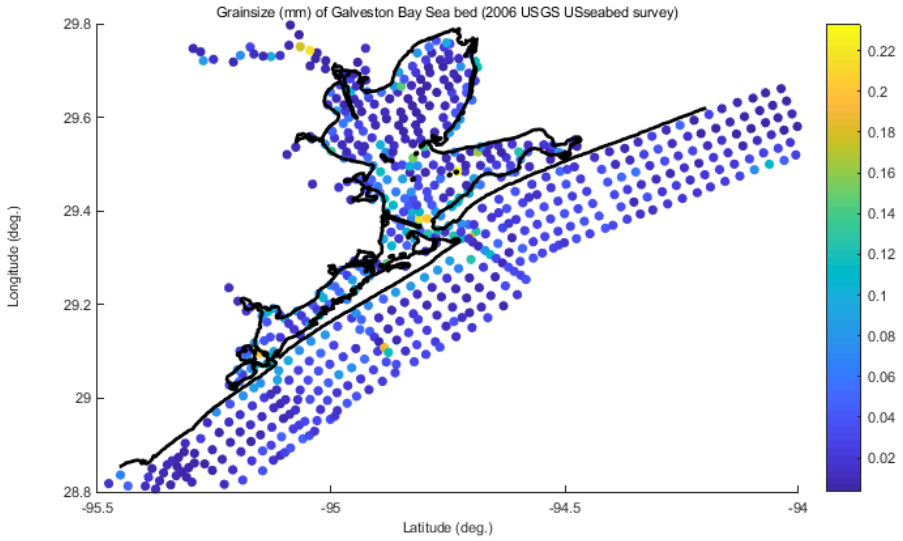

Figure 5-2 Median grainsize of the sea bed in the Galveston Bay area (2006 USGS usSEABED survey)

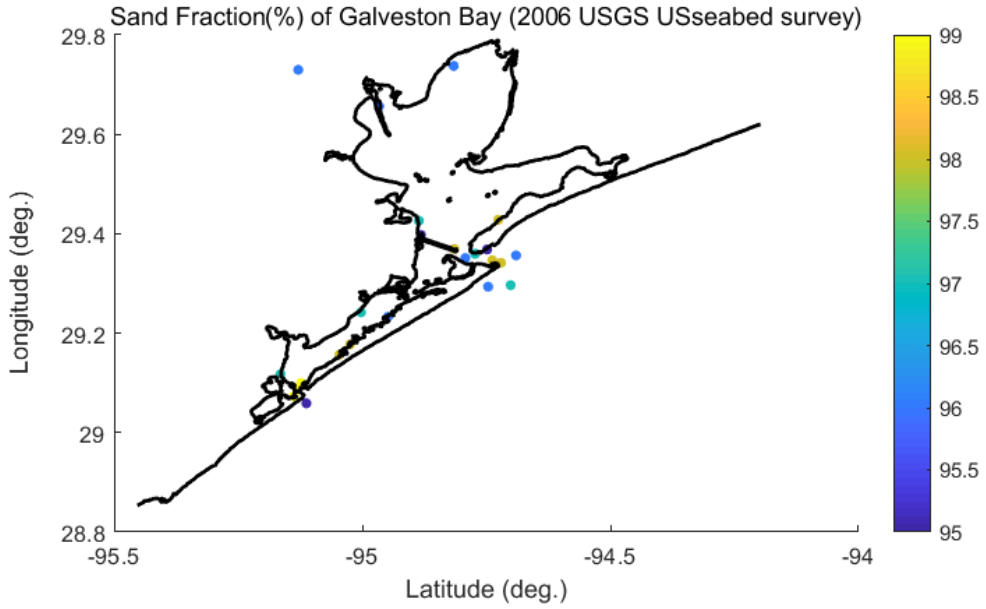

Figure 5-3 The locations of samples that exceed 94.9% of the sand fraction

Based on the grain size of those 24 data points the average median grain size (D_{50}) of 24 data was approximately 0.1049 mm. We use 0.1 mm as a D_{50} of sand in the model based on this averaged data. As can be seen in figure 5-3, data sets in which the sand fraction is above 94.9% are distributed all around Galveston Bay. Other parameters such as the settling velocity (ϖ_s), critical shear stress (τ_{crit}), and erosion parameter (E) of mud are important in simulating sediment transport processes in the model. Settling velocity (ϖ_s) of mud is selected as 0.25 mm/s. Based on the sensitivity test, the overall errors between 0.1 mm/s and 0.25 mm/s (default) for settling velocity were less than 1 mm in erosion and deposition result at the end of the simulation. This result is consistent with Liu et al. (2018)'s result. Thus in this chapter, the default settling velocity value of 0.25 mm/s was used.

Erosion parameter of 0.5, 1.0 and 5.0×10^{-4} kg/m^2/s were tested, and 5.0×10^{-4} kg/m^2/s showed much less erosion where the erosion occurred at the end of the simulation. The difference between erosion parameter of 0.5 and 1.0×10^{-4} kg/m^2/s was 2 cm at the salt marsh edge at the end of the simulation period. Since the erosion parameter of mud in the West Bay is not a measurable quantity, the default value of 1.0×10^{-4} kg/m^2/s for the erosion rate of mud was used here. However, validation is required when evaluating absolute erosion values. For critical shear stress of mud, 0.1 Pa was chosen based on the numerical studies in the Texas-LA continental shelf (Xu et al., 2016). For the vegetated wetland surface, the critical shear stress was set to 1.0 Pa to account for vegetation root's effects on the soil layer (Liu et al., 2018). Critical shear stress of the vegetated wetland surface area and the other areas include the shelf in the bay are shown in Figure 5-4.

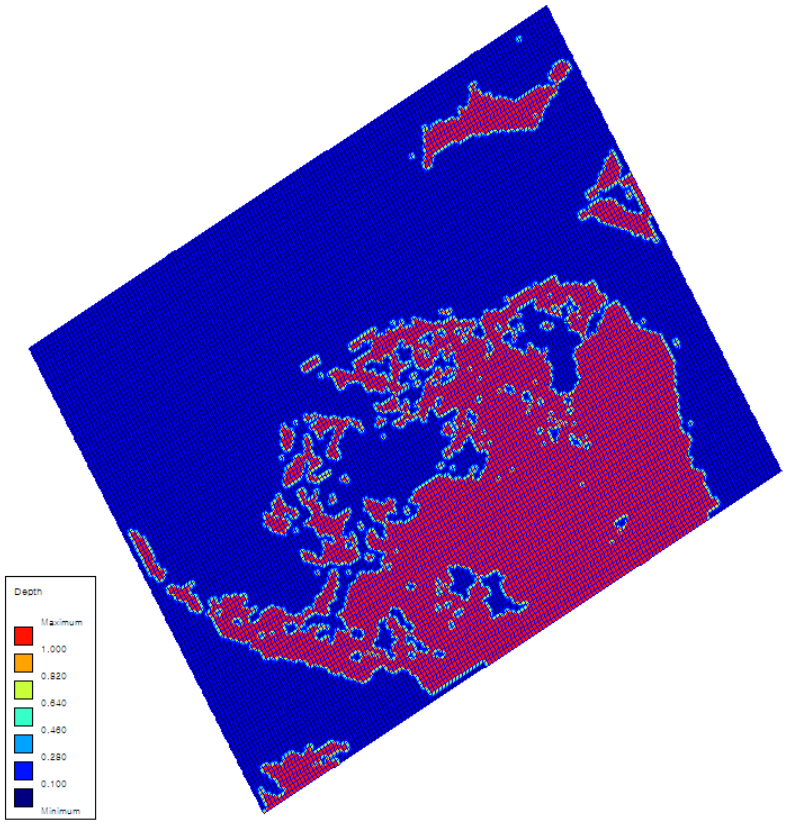

Figure 5-4 Space-varying critical shear stress (Pa) setting for vegetated wetland surface and the other areas

In some parameter settings, if the initial sediment thickness is not large enough, the rate of erosion may be overestimated during the simulation and the sediment supply at the bottom of the water body may be depleted. Therefore, an initial sediment layer of 5 m was assumed in the model to prevent the removal of the sediment reservoir (Liu et al., 2018). No sediment concentration was prescribed to all domains. The fluxes between the water phase and the bed are calculated with the Partheniades-Krone formulations (Partheniades, 1965). The method in Van Rijn (2000) was chosen to account for erosion and deposition of sand. The sediment concentration in the water column was assumed to

be zero at the beginning of the simulation. The sediment properties for sand and mud used in the model were summarized in Table 5-1 and 5-2. an erosion parameter of 10^{-4} $kg/m^2/s^1$ and a settling velocity of 0.25 mm/s for mud was defined as the baseline model.

Table 5-1 A summary of non-cohesive sediment parameters used in the baseline model

Sediment Type	Layer Thickness (m)	D50 (mm)
Sand	5	0.1

Table 5-2 A summary of cohesive sediment parameters used in the baseline model

Sediment Type	Critical shear stress (Pa)	Layer Thickness (m)	Settling velocity (mm/s)	Erosion rate (kg/m2/s)
Mud	0.1/1.0	5	0.25	0.0001

5.3.5. Sediment supply from fluvial inputs

According to the investigation regarding major fluvial yields, San Jacinto River, Buffalo Bayou and Cedar Bayou occupy 66% of fluvial sediment input to Galveston Bay (Greiner, 1982). In addition to these three major fluvial sediment inputs, fluvial input from Chocolate Bayou was considered in this case study. Fluvial input from San Jacinto River was calculated based on the record of USGS USGS 08068000 W Fk San Jacinto River near Conroe, TX. For Buffalo Bayou fluvial input to Galveston Bay, the sum of USGS 08074000 Buffalo Bayou at Houston, TX and USGS 08074500 Whiteoak Bayou at Houston, TX records were used for the calculation of discharge and mean discharge. Relate to Buffalo Bayou fluvial input, real-time discharge data on USGS 08076700

Greens Bayou at Ley Rd, Houston, TX was not used since the data was not available during the simulation period. Fluvial input from Cedar Bayou was calculated and used in the model based on the record at USGS 08067500 Cedar Bayou nr Crosby, TX.

In order to include the sediment supply from fluvial inputs such as an adjacent estuary, modeling of the river discharges with sediments are considered in the model. USGS Current conditions monitoring station, 08078000 Chocolate Bayou near Alvin, TX, located 10 miles away from Chocolate Bayou, where the freshwater and sediments flow into West Bay. The USGS 08078000 station provides daily discharge and gauge height of the river channel. Due to the limit of the model grid boundary, the discharge point was moved from Chocolate Bayou near Alvin, TX to the end of Chocolate Bayou.

Sediment density and flow rates from the Chocolate Bayou are determined based on data from Greiner (1982) and the monitored data at 08078000 Chocolate Bayou near Alvin, TX. The estimated average fluvial sediment inputs to Galveston Bay from Chocolate Bayou is 37,000 tons/year. The annual mean discharge was 4.5 m^3/sec in 2015. Thus the calculated sediment density of fluvial input from the Chocolate Bayou is 0.262 kg/m^3. The fluvial sediment input per year (tons/year), yearly mean discharge (m^3/year), calculated sediment density (kg/m^3) for four fluvial sediment inputs in the model (Trinity River, Buffalo Bayou, Cedar Bayou, Chocolate Bayou) are summarized in Table 5-3.

Table 5-3 Fluvial sediment input to Galveston Bay in the model

Name	Fluvial Yields (tonnes/year)	Yearly mean discharge in 2015 (m^3/s)	Calculated Sediment density input (kg/m^3)
San Jacinto River	1,016,000	32.7	0.98
Buffalo Bayou	290,000	81.7	0.11
Cedar Bayou	144,000	4.2	1.10
Chocolate Bayou	37,000	4.5	0.26

Figure 5-5~9 shows the discharge records used as daily discharge data at five locations from DEC 7, 2015 to Dec 20, 2015. Daily discharge data at USGS 08074000 Buffalo Bayou was not available from DEC 7 to DEC 15, 2015, gauge data and its relation with discharge trends was used for the estimation of the discharge data. Overall, the daily discharge was increased on DEC 13, 2015, due to the rainfall accompanied by the first cold front passage. The discharge Buffalo Bayou was highest during the simulation period, recorded more than 6,000 ft3/s.

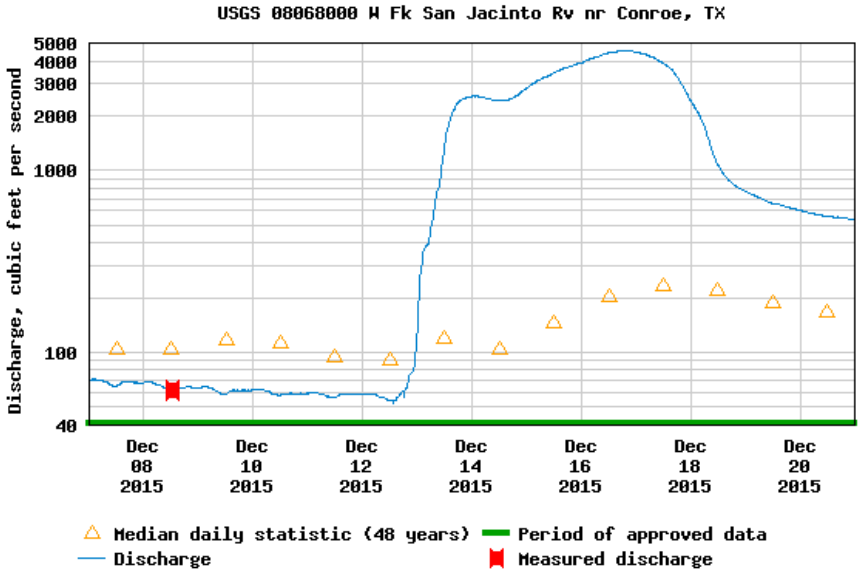

Figure 5-5 Daily discharge records at USGS 08068000 W Fk San Jacinto River near Conroe, TX from DEC 07 to DEC 20, 2015

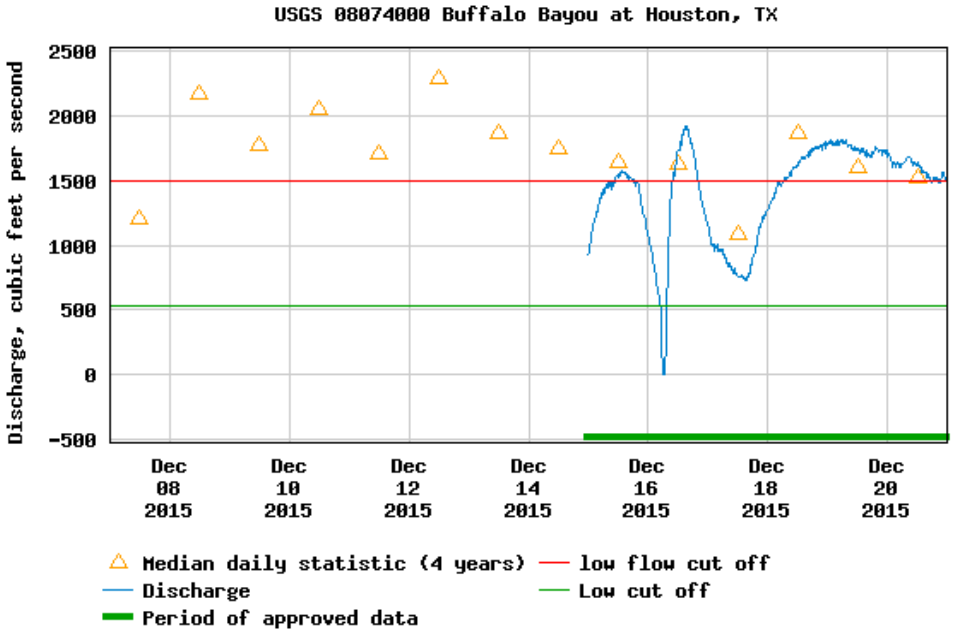

Figure 5-6 Daily discharge records at USGS 08074000 Buffalo Bayou at Houston, TX from DEC 07 to DEC 20, 2015

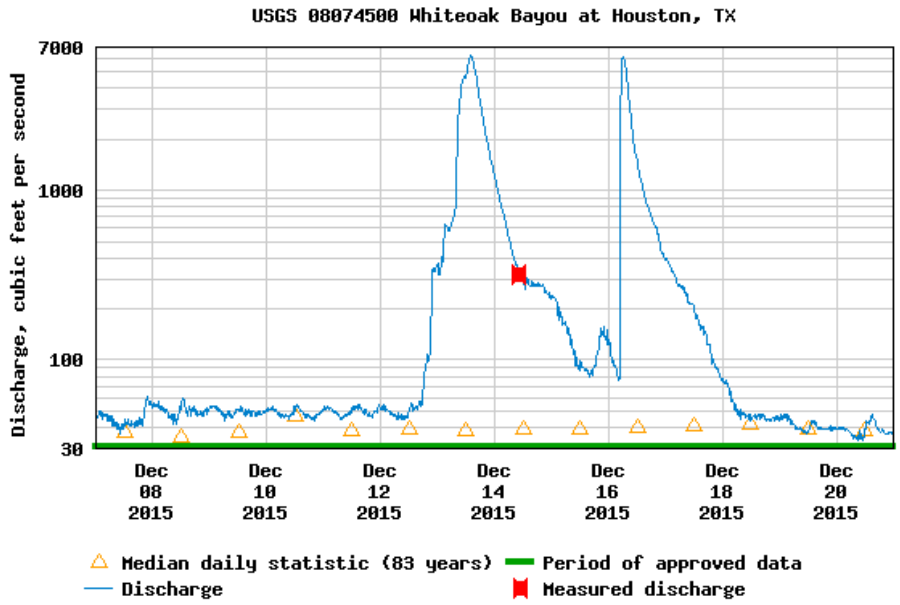

Figure 5-7 Daily discharge records at USGS 08074500 Whiteoak Bayou at Houston, TX (as a branch of Buffalo Bayou) from DEC 07 to DEC 20, 2015

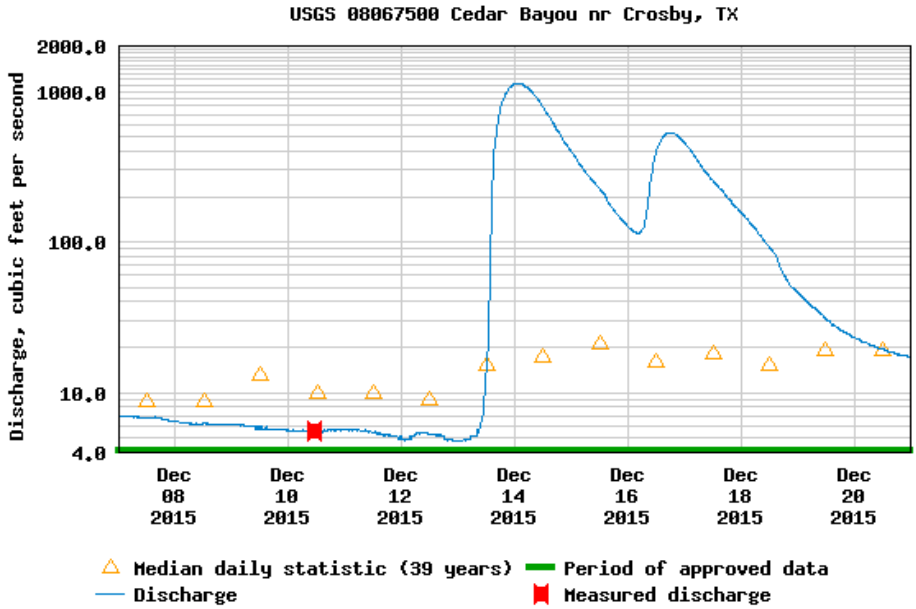

Figure 5-8 Daily discharge records at USGS 08067500 Cedar Bayou near Crosby, TX from DEC 07 to DEC 20, 2015

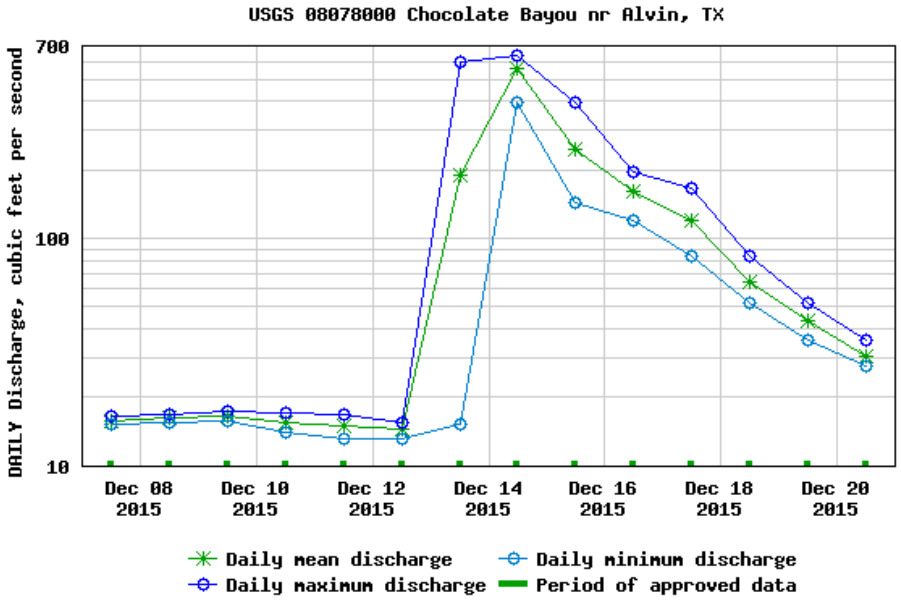

Figure 5-9 Daily discharge records at USGS 08078000 Chocolate Bayou near Alvin, Tx from DEC 07 to DEC 20, 2015

5.3.6. Sea-level rise and land subsidence

Relative sea level rise (RSLR), measured at any tide gauge, is the combination of absolute sea level rise (ASLR) due to land subsidence and global warming. The land subsidence occurs due to tectonic downward movement caused by subsurface fluid withdrawal and creep of soil and rock (Liu et al., 2020). Flood risk in Galveston Bay is elevated in part because RSLR in this region is about four times greater than Global Mean Sea Level Rise (GMSLR).

Since 1900, GMSLR has been rising at a rate of approximately 1.7 $\pm$ 0.3 mm/yr as recorded by tide gauges (Church 2011; Nicholls and Cazenave 2010). From satellite altimetry data, beginning in the early 1990s, measurements suggest that this rate has

increased to approximately 3.3 $\pm$ 0.4 mm/yr. (Ablain, M. 2009; Church 2011; Nicholls and Cazenave 2010). While current and future GMSLR are associated with global warming, the primary cause of local RSLR in the Houston–Galveston region during the past 50 years has been land subsidence associated with groundwater extraction (Liu et al., 2020).

The local secondary consolidation subsidence was estimated to be 2.67 mm/yr at the Galveston Pier 21 tide gauge (Liu et al., 2019). Annual sea level rise at Galveston Pier 21 and its acceleration by subsidence due to primary compaction and absolute sea level rise (ASLR) was estimated. Estimation from 1992 to 2018 with a regression coefficient of 0.98 is shown in the following Equation 5.12 suggested in Liu et al. (2020).

$$AMSL = 4.60t - 1877.03 + 0.1349(t - 1992)^2 \qquad (5.12)$$

The annual mean sea level (AMSL) in 2015 and 2016 were 7463.3 mm and 7474.3 mm respectively, and its difference was 11 mm. In this chapter, a different initial water level model was tested to consider the RSLR effect on sediment transport processes. Here, we set the 55 mm of RSLR as a proxy for five years of sea level change. Based on the fact that land subsidence is occurring in the Galveston Bay area, a mean sea level rise of 17.5 mm and land subsidence of 37.5 mm was applied for the Galveston Island grid in the RSLR model. For the Gulf of Mexico grid, GMSLR of 17.5 mm was applied. Land subsidence was applied by adjusting each grid's bathymetry level in the Galveston Bay except for the Gulf of Mexico grid. From the RSLR model results,

it is possible to evaluate the process of relatively gradual change in sediment transport by the RSLR, including land subsidence.

5.4. Results

5.4.1. Sediment fluxes and balance

To evaluate the overall sediment flux during the cold front passages, sediment exchange within the system from the Gulf of Mexico to Galveston Bay, five cross-sections were applied as shown in Figure 5-10. The cross sections are located near San Luis Pass inlet (W1), Galveston Bay Entrance Inlet (G1, Bolivar Road), an inlet near Galveston Pier 21 tide gauge (G2, Galveston Channel), cross section near Chocolate Bay (W2), and cross section near Galveston Railroad bridge (W3). The time series of the instantaneous transport (suspended and bed load sediment transport) over the defined cross sections are shown in Figure 5-11. Overall, Instantaneous Transport along the G1 had the largest peak in the area. This location is by the water inflow and outflow at the inlet of Galveston Bay leading to the Houston Ship Channel. During the first cold front passage, inflow and outflow of sediment to the West Bay were prominent, considering records of the entire period of W2 and W3. The details of net sediment transport over different cross sections during the first cold front and the second cold front are shown in Figure 5-12 and Figure 5-13, respectively.

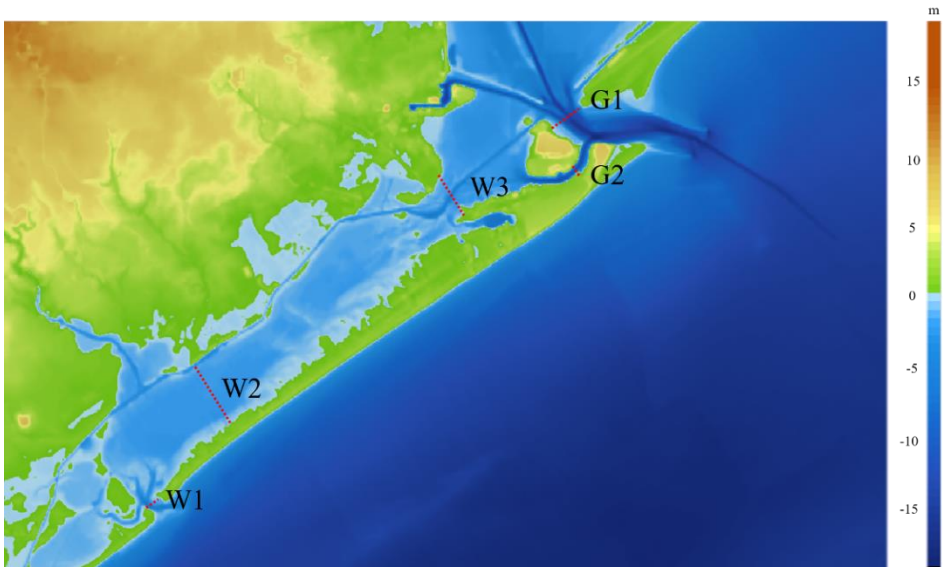

Figure 5-10 The cross sections in Galveston Bay for monitoring sediment fluxes (W1-San Luis Pass, W2-Chocolate Bay, W3-Galveston Railroad bridge, G1-Galveston Bay Entrance, G2-Galveston Channel)

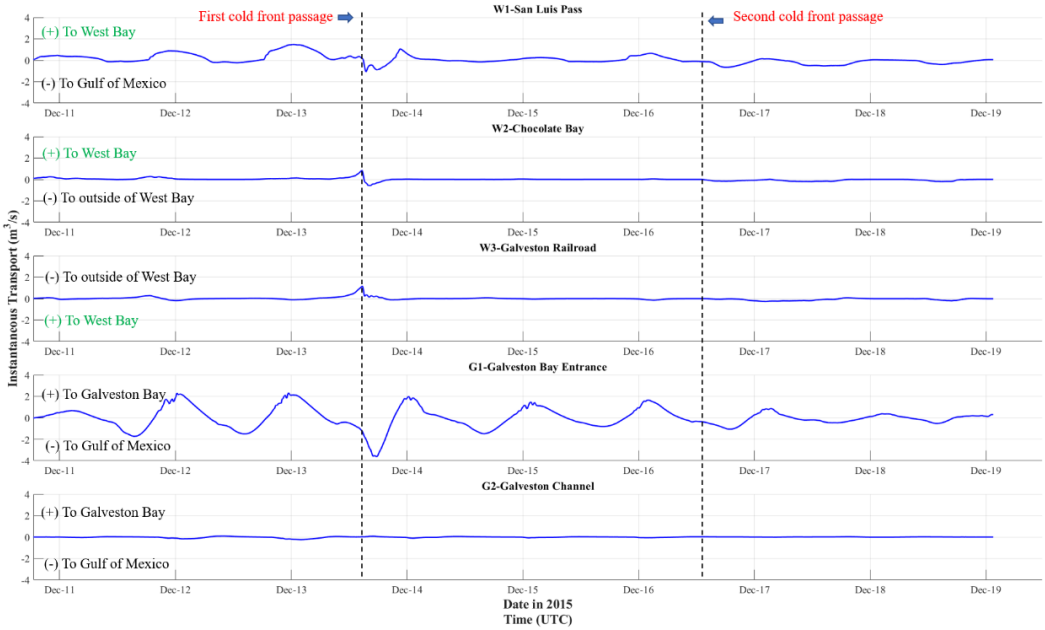

Figure 5-11 The time series of the instantaneous (suspended and bed load sediment) transport over the defined cross sections

(A) 1st Cold front **Prefrontal**

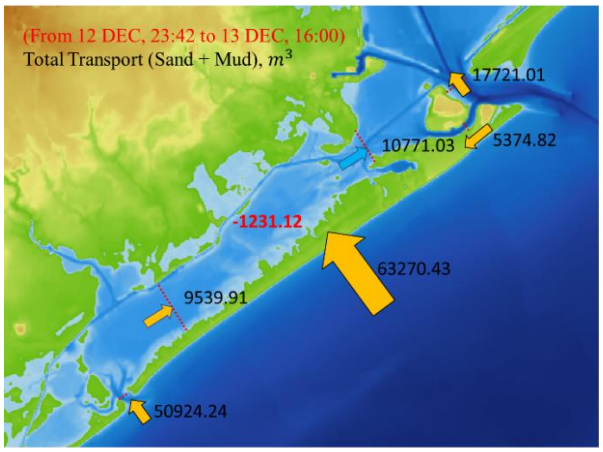

(B) 1st Cold front **Postfrontal**

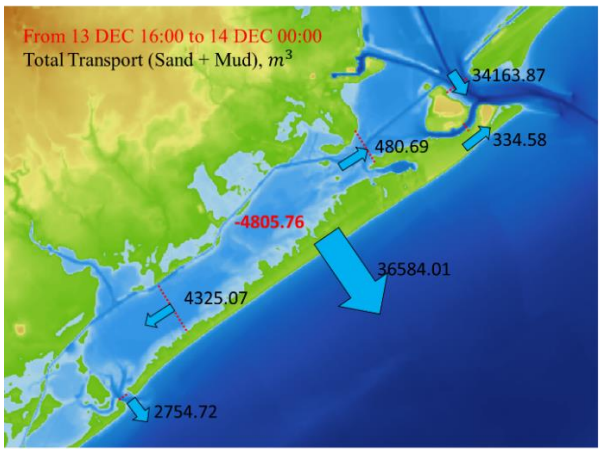

(C) 1st Cold front **Entire period**

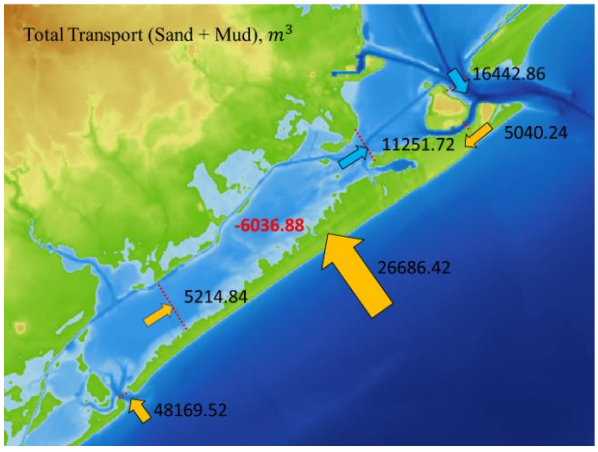

Figure 5-12 The net sediment transport over different cross sections in Galveston Bay during the first cold front passage (yellow means the direction towards the west bay and blue means the direction outside the west bay)

(A) 2nd Cold front **Prefrontal**

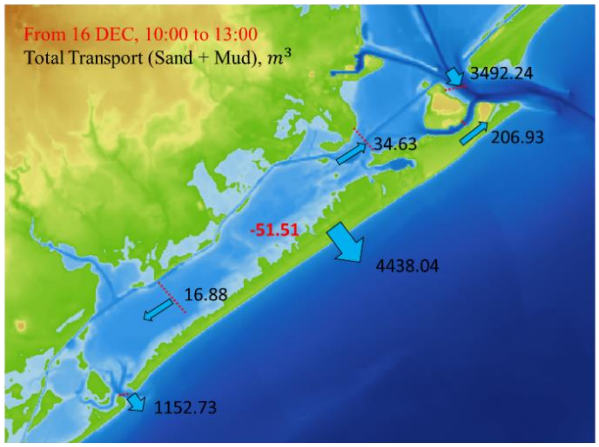

(B) 2nd Cold front **Postfrontal**

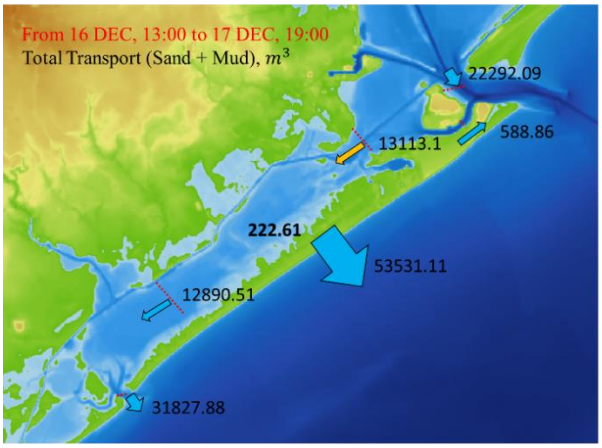

(C) 2nd Cold front **Entire period**

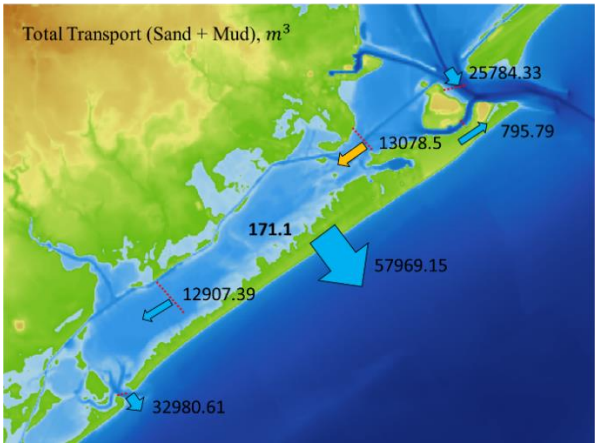

Figure 5-13 The net sediment transport over different cross sections in Galveston Bay during the second cold front passage (yellow means the direction towards the west bay and blue means the direction outside the west bay)

The inflow of sediment was greatest in the prefrontal phase of the first cold front (Figure 5-12a), and least in the prefrontal phase of the second cold front (Figure 5-12a). The first cold front had significant sediment inflow into Galveston Bay (Figure 5-12c), whereas the second front had significant sediment outflow out of Galveston Bay (Figure 5-13c). In West Bay, in the prefrontal phase of the first cold front, the inflow from the Chocolate Bay cross section (W2) and the outflow to the Galveston Railroad bridge cross section (W3) were significant. On the other hand, in the postfrontal phase of the second cold front, the inflow from the Galveston Railroad bridge cross section (W3) and the outflow from the Chocolate Bay cross section (W2) were significant. Overall, the sediment flow during the prefrontal period of the first cold front increased dramatically. In the second cold front, the sediment flow during the postfrontal period increased sharply. The sediment fluxes at the end of the two cold fronts proceeded in opposite directions since the prevailing winds from each cold front were different.

5.4.2. Morphodynamics along the salt marsh edge

The net morphological change in the bed sediment layer after the simulation period is presented in Figure 5-14. Deposition (red color in Figure 5-14) along the ship channel and in tidal inlets (San Luis Pass, Galveston Bay Entrance) was significant during the simulation period. The erosion also (blue color in Figure 5-14) occurred on the coastline of the west bay, including the coast of Galveston Island. Along the beach of Galveston Island, erosion was noticeable. However, there is a tendency for a mixture of erosion and deposition on the West Bay sea bed, including the shoreline of the wetlands to appear. For the detailed morphodynamics changes along the salt marsh edges in the site of interest, erosion and deposition results in the most refined grid are plotted in Figure 5-15.

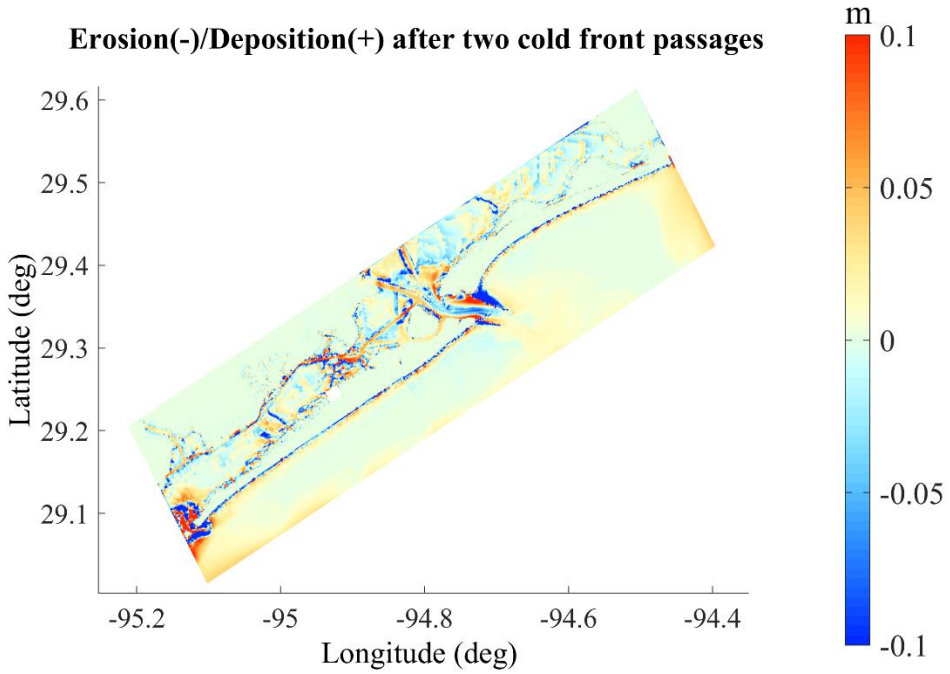

Figure 5-14 The modeled net erosion (-)/deposition (+) in the West Bay and near the Galveston Bay Entrance

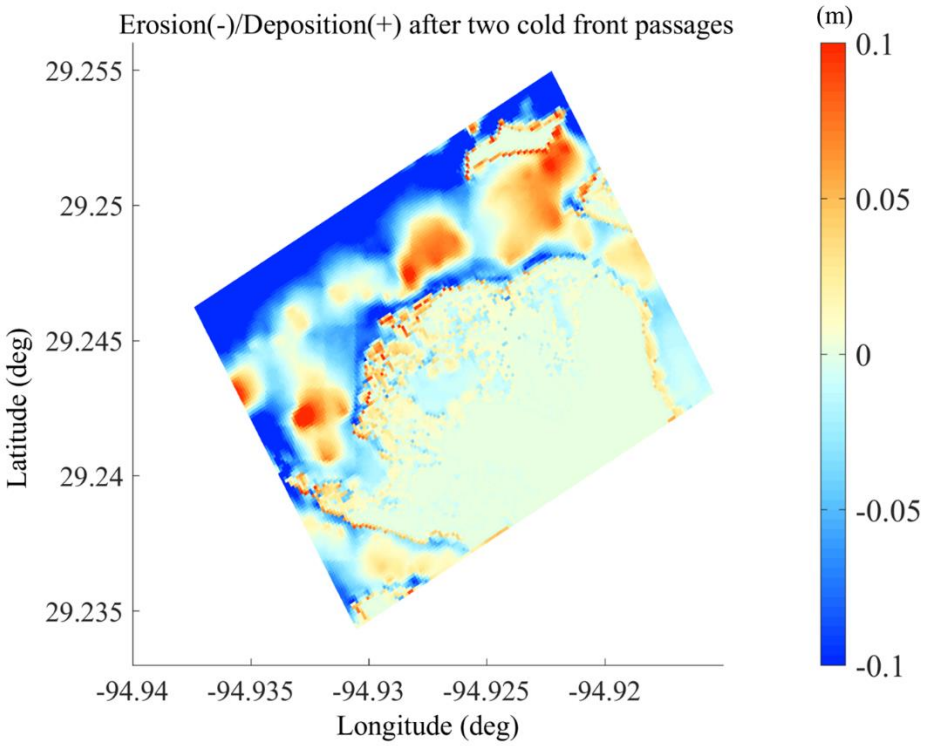

Figure 5-15 The modeled net erosion (-)/deposition (+) near the site of interest (salt marsh edges)

Although the trends of erosion and sedimentation were visible, it was confirmed that the accretion occurred on the specific platforms at the boundary of the wetland, especially in the outer boundary of the salt marshes. In contrast, erosion occurred on the sea bed located at the front of salt marsh boundaries. Local deposition often occurred a lot in the coastal area adjacent to the wetland boundary, where the water depth is slightly deeper than the neighboring areas.

In order to examine the forcing driving the sediment transport processes during the simulation period, depth-averaged current speeds during the cold front passages

around the site of interest are shown in Figure 5-16. In Figure 5-16(b), when the first cold front had just passed, the current velocities were high, and the surrounding flow has penetrated the wetland boundary and circulated within the inner part of the wetland.

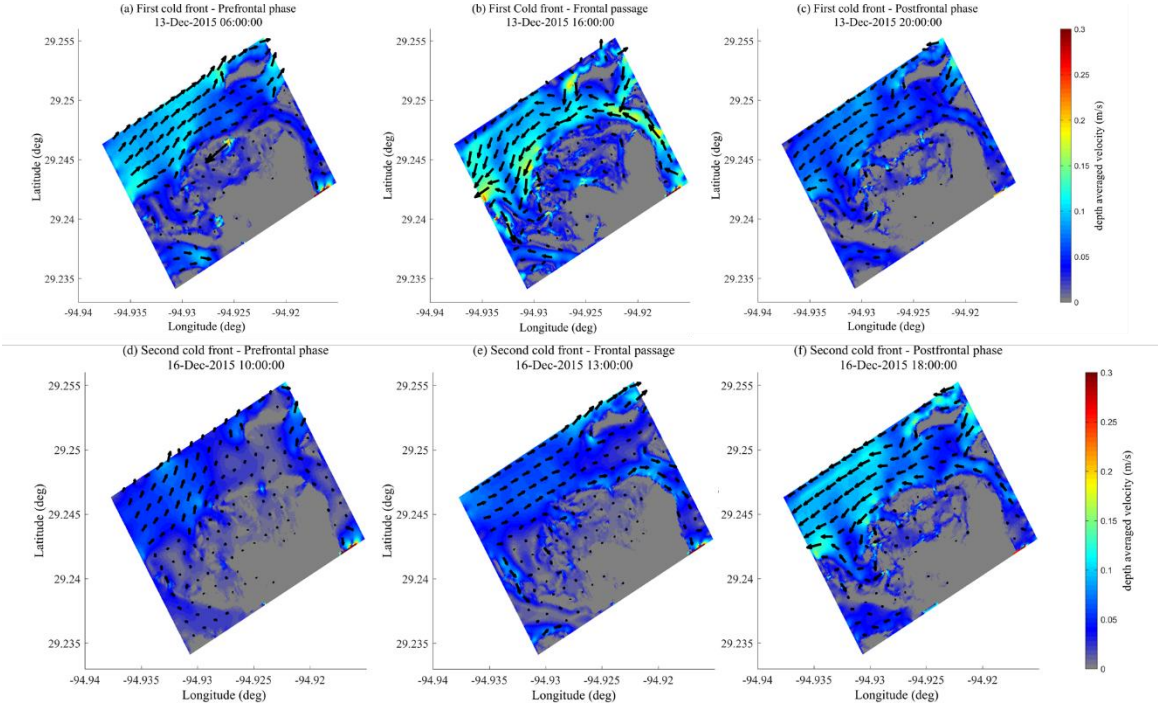

Figure 5-16 Depth averaged velocity (current velocity) and its direction in different phases during the first cold front passage, (a) 13-DEC 06:00 UTC (prefrontal phase), (b) 13-DEC 17:00 UTC (frontal Passage), (c) 13-DEC 20:00 UTC (postfrontal phase) and during the second cold front passage, (d) 16-DEC 10:00 UTC (prefrontal phase), (e) 16-DEC 13:00 UTC (frontal Passage), (f) 16-DEC 18:00 UTC (postfrontal phase)

The observation points were selected within the site of interest (wetlands along the bay side of Galveston Island). Although their positions were very close to each other, the three points represent three types of landscape characteristics. M01 is located bayside from the salt marsh edge (inundated), M02 is located on the salt marsh edge, and M03 is located on the salt marsh platform about 50 m away from the salt marsh edge. The

locations of the three monitoring points are shown in Figure 5-17. Modeled hydrodynamics processes and morphological processes in M01, M02 and M03 are shown in Figure 5-19.

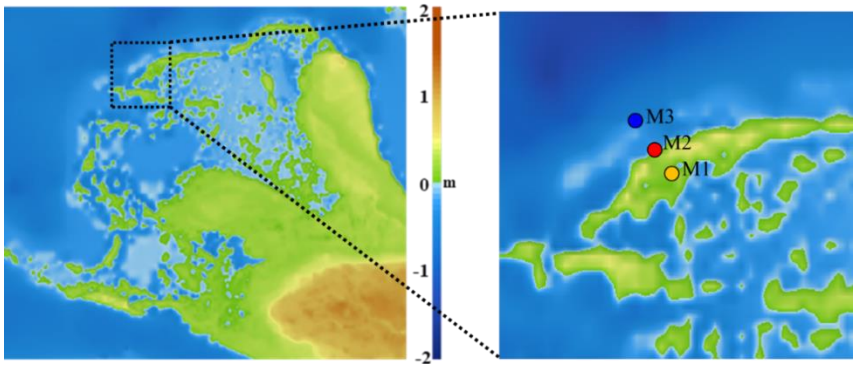

Figure 5-17 Location of monitoring points near the salt marsh edge

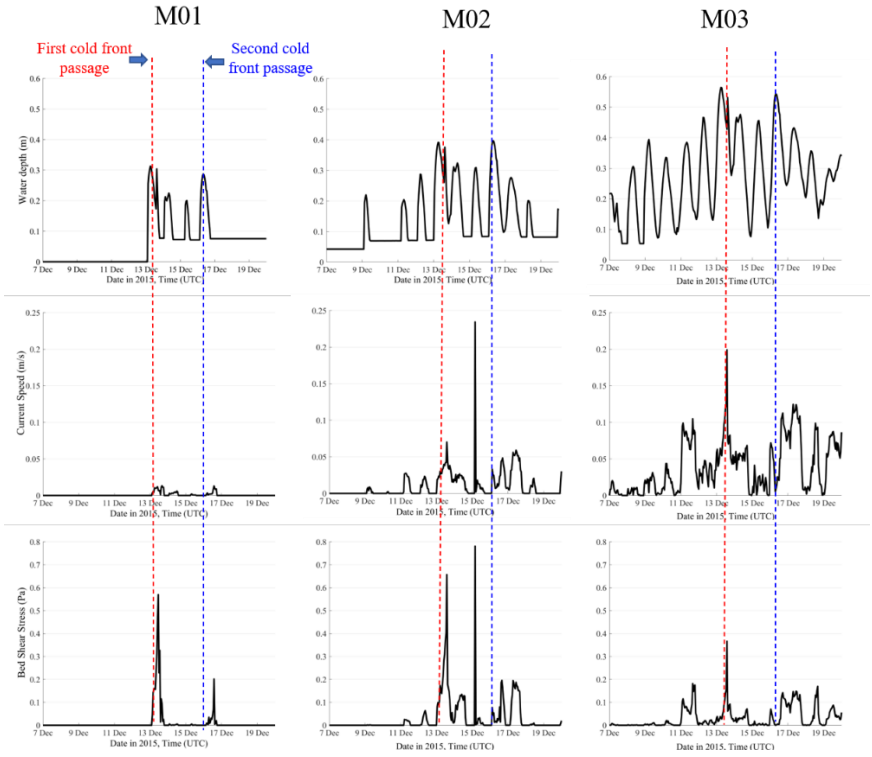

Figure 5-18 Modeled (a) water depth, (b) Current speed, and (c) bed shear stress at M01, M02, and M03

The water depth was highest when the first cold front passed in the three regions, followed by the second cold front passage. The current speed in M01 was not significant most of the period since M01 was a dry point at the start of the simulation. In M01, the water level exceeded 0.2 m during the cold front passages, but after the passage of the front, the water level was less than 0.1 m. Thus, no current and bed shear stress occurred except during cold front passages. The depth-averaged current velocity in M02 was slightly active than the M01. M02 was also a dry point, but became inundated during the high tide over the entire simulation period. Thus the bed shear stress during the high tide was recorded. M03 was initially inundated, and its water depth was approximately 0.2 m. During the first cold front passage, the water depth was 0.55 m, and the current speed was around 0.2 m/s. During the second cold front passage, the current speed was approximately 0.1 m/s. Bed shear stress in M03 was less than M02.

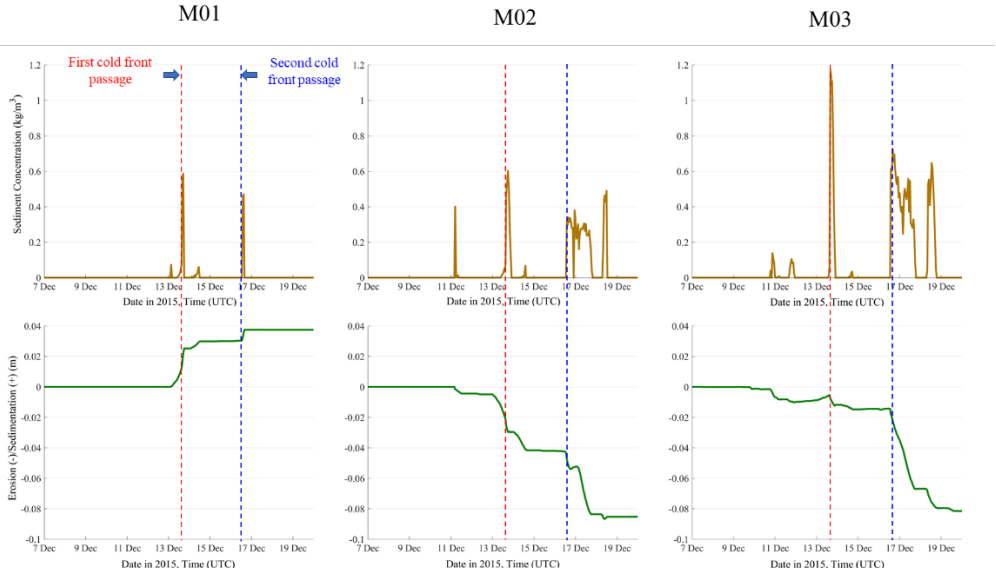

Figure 5-19 Modeled (a) sediment concentration, (b) erosion (-)/ accretion (+) at M01, M02, and M03

For the entire period, deposition occurred at M01. The point M01 is not inundated except during the cold front passages. During the inundation, most of the deposition occurred on the salt marsh platform at M01. Erosion was recorded for M02 and M03, especially during the cold front period. The point M02 experienced 0.04 m of erosion during the first cold front passage, whereas M03 experienced less than 0.01 m of erosion during the first cold front passage. During the second cold front, significant erosion was recorded both in M02 and M03. The point M02 experienced another 0.04 m of erosion, and M03 experienced approximately 0.06 m of erosion during the second cold front. The records of SSC at M01, M02, and M03 of mud and sand were plotted and shown in Figure 5-20. The increase in SSC was related to wind activity. During the first cold front passage, the mud SSC and sand SSC had a peak value of 3.5 kg/m^3 and 0.18 kg/m^3, respectively. The high SSC during the second cold front passage was also confirmed. During the cold front passages, the SSC was high in the order of M01, M02, and M03.

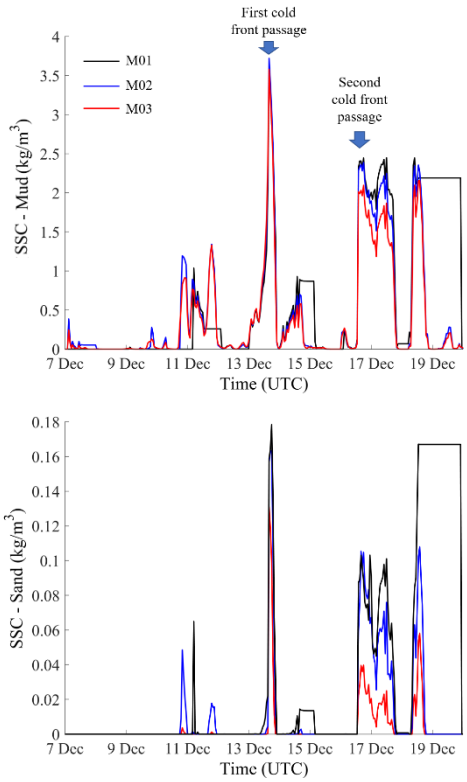

Figure 5-20 SSC records of mud and sand at M01, M02 and M03

For the detailed analysis for bed level changes in the wetlands area, five monitoring cross section lines were selected along the monitoring line. The cross section includes a shallow bay in front of the salt marsh edge, the salt marsh edge, and the salt marsh platform inside of the wetlands. The locations of cross section lines are shown in Figure 5-21. The bed level changes during the first and second cold front on each cross section line were investigated and plotted in Figure 5-22~26.

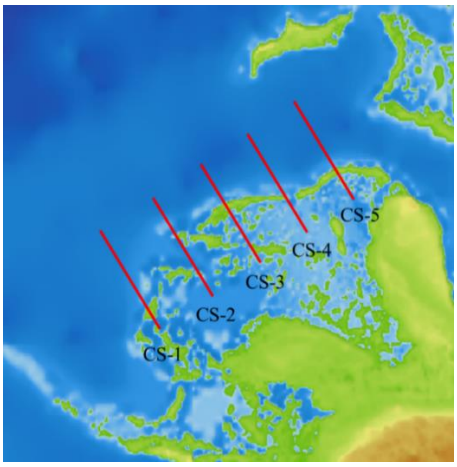

Figure 5-21 The locations of cross section monitoring lines

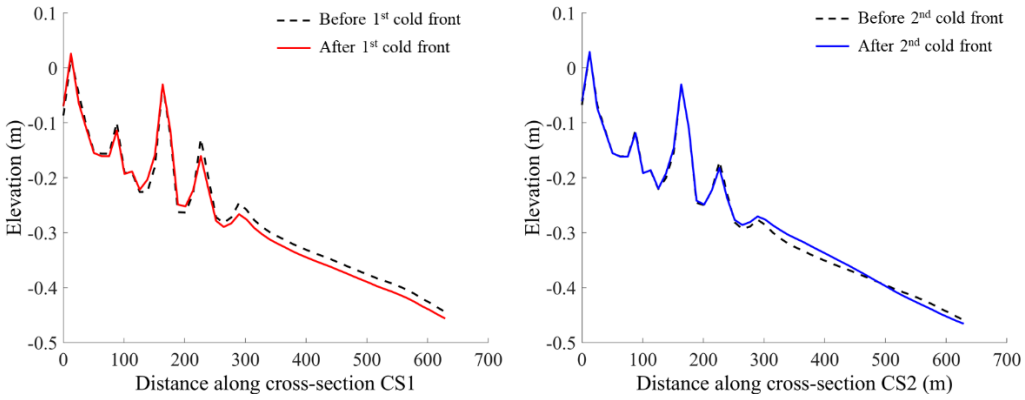

Figure 5-22 Bed level changes after cold front passages along CS1

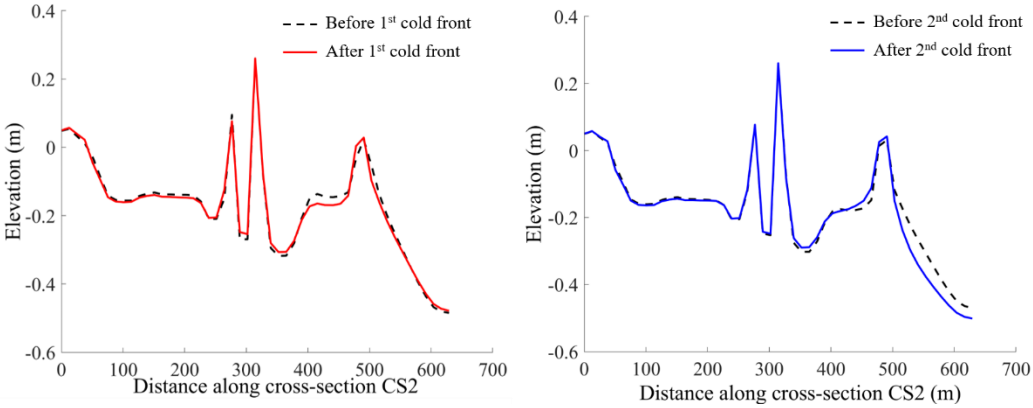

Figure 5-23 Bed level changes after cold front passages along CS2

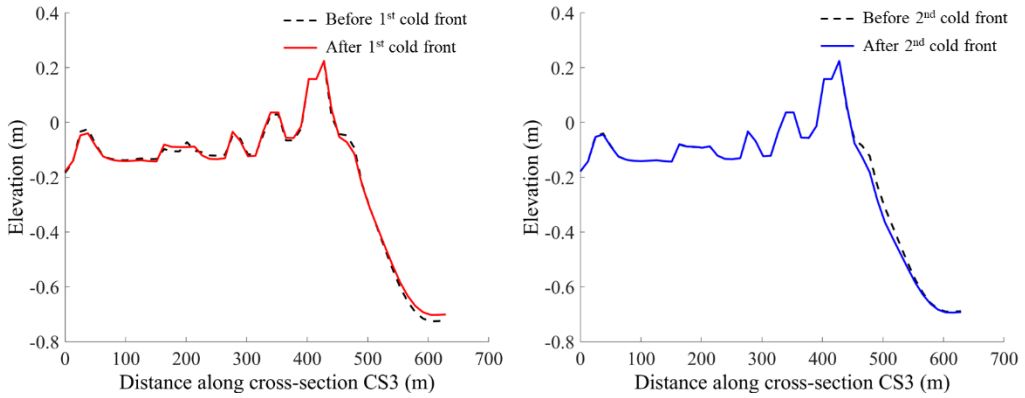

Figure 5-24 Bed level changes after cold front passages along CS3

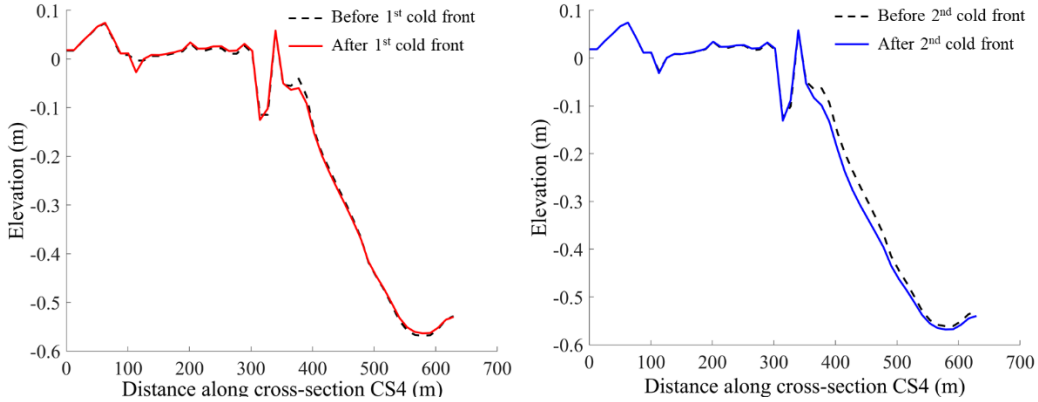

Figure 5-25 Bed level changes after cold front passages along CS4

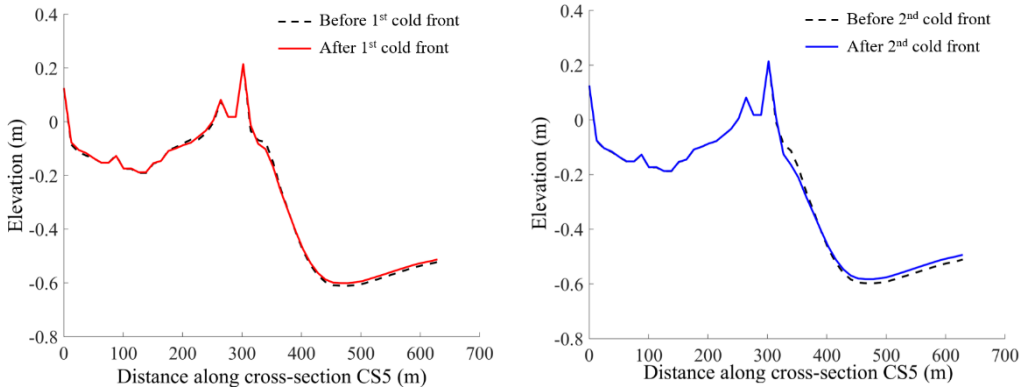

Figure 5-26 Bed level changes after cold front passages along CS5

The results show that the deposition on the platform inside the wetland occurred most prominently during the first cold front passage. However, when the second cold front passed, erosion was active at the edge of the wetland and in the immediate front. The erosion created by the second cold front is also correlated with the potential erosion possibility calculated by the cumulative wave power in Chapter 2.

After the first cold front passage, changes in bed level at the inner part of the salt marshes were observed. The changes are related to the flooding of the area caused by the prefrontal winds during the first cold front passage. Some erosion of the sea bed in front of the salt marsh was also found. After the second cold front passage, it was confirmed that the coastal floor in front of the wetland boundary was more eroded than the first cold front.

5.4.3. Sea level rise sensitivity

The difference in sediment fluxes in the RSLR model was investigated on the cross section monitoring point in Figure 5-11. Differences in sediment fluxes compared to the baseline model in each cross section were calculated and shown in Figure 5-27 (at the end of the first cold front) and Figure 5-28 (at the end of the second cold front). Due to the RSLR, there was a significant difference in sediment fluxes along the Galveston bay inlets and inside of the West Bay. During the first cold front, sediment influx from W1 was significantly increased (59.8 %). Sediment supply to West Bay (W2) was also increased (21.3 %). During the second cold front, sediment outflux from Galveston Bay to Gulf of Mexico was significantly increased (W1 - 18.5 %, G1 - 23.7 %). Overall,

sediment fluxes out of San Luis Pass and Galveston Bay entrance increased, and sediment passing through West Bay decreased in the RSLR model.

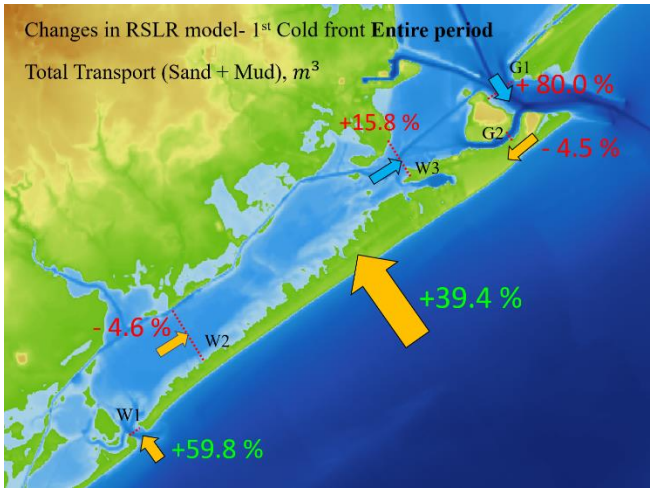

Figure 5-27 Changes of sediment fluxes along cross sections in the RSLR model compare to the baseline model at the end of the first cold front (yellow means the direction towards the west bay, and blue means the direction outside the west bay)

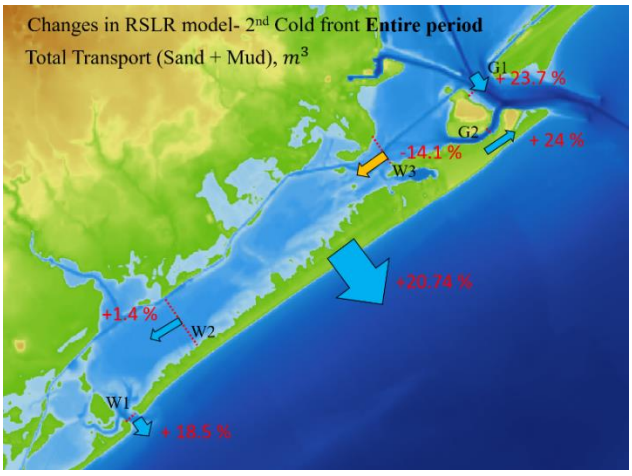

Figure 5-28 Changes of sediment fluxes along cross sections in the RSLR model compare to the baseline model at the end of the second cold front (yellow means the direction towards the west bay, and blue means the direction outside the west bay)

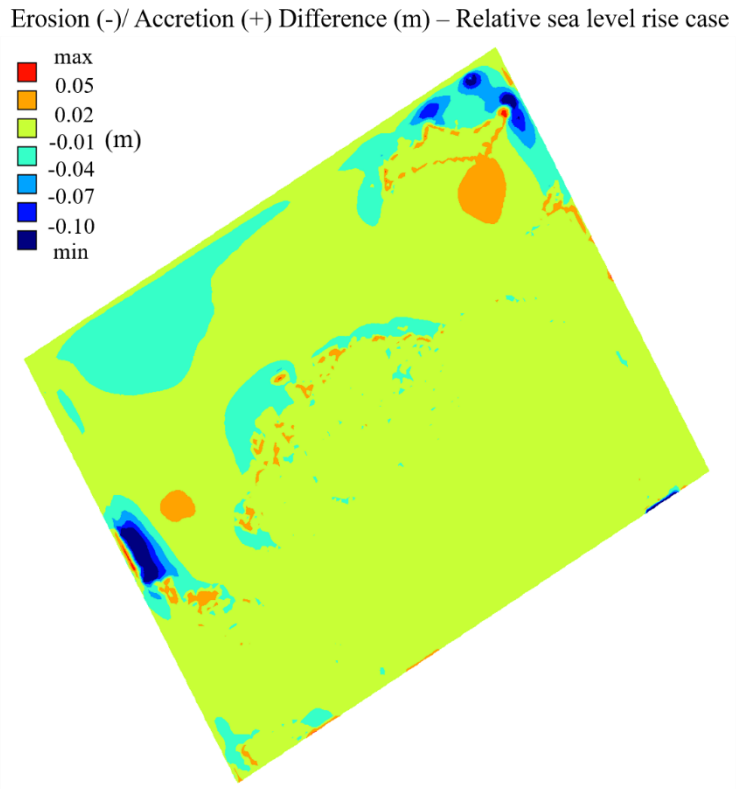

Figure 5-29 Erosion (-)/ accretion (+) difference between the baseline model and the RSLR model at the end of the simulation period (DEC 20, 2015)

The effect of RSLR on morphodynamics around the wetland boundary was verified. The erosion (-)/ accretion (+) difference between the baseline model and the RSLR model (37.5 mm local subsidence + 15 mm global sea level rise) was calculated and shown in Figure 5-29. More accretion was observed along the salt marsh edge compared to the default model, around 0.02 m at the end of the simulation period. On the other hand, more erosion was observed at sea beds in front of the salt marsh edge. Little changes in erosion/accretion were seen in the inner part of the wetland, but an overall increase in erosion of less than 0.01 m was found. This is considered due to the

possibility of flooding by the water level increase in the RSLR model. Monitoring cross sections were set around the most refined grid, as shown in Figure 5-30 to track the sediment influx and outflux to the salt marsh areas. The cumulative total transport along the cross sections was compared between the baseline model and the RSLR model. The results along SLT-1, SLT-2, and SLT-3 are shown in Figure 5-31~33.

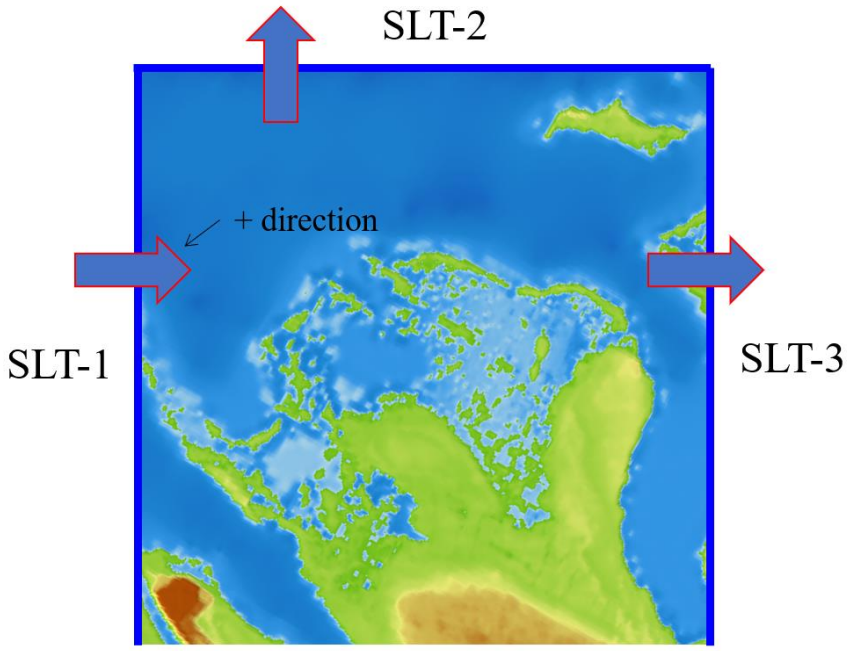

Figure 5-30 Cross sections along salt marsh area near the site of interest

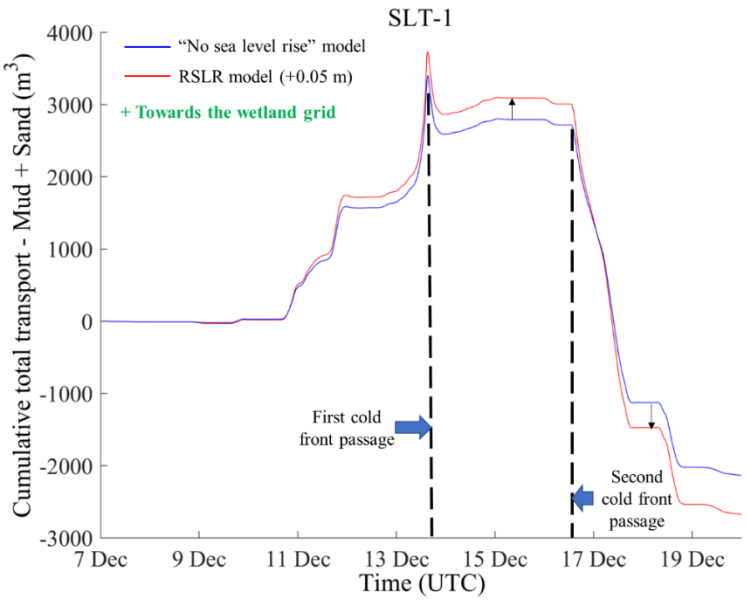

Figure 5-31 Differences in cumulative total transport between the baseline model and the RSLR model at SLT-1

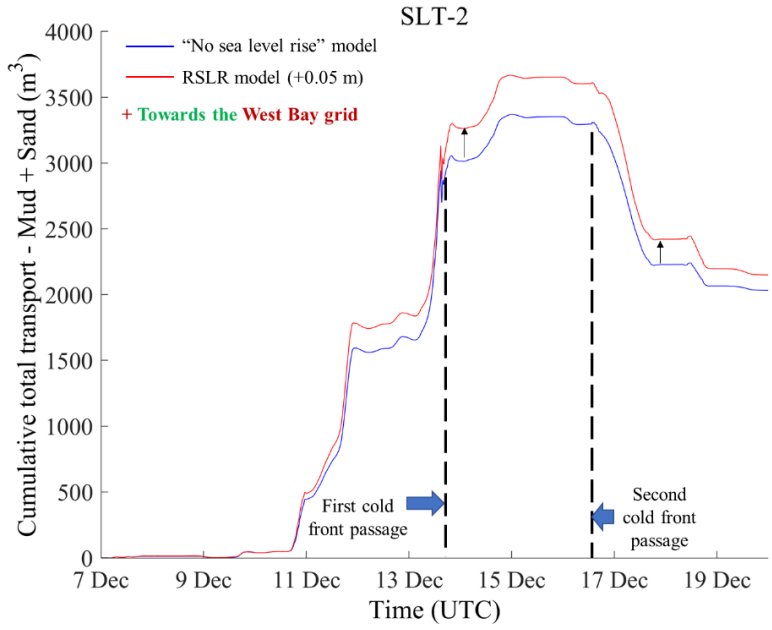

Figure 5-32 Differences in cumulative total transport between the baseline model and the RSLR model at SLT-2

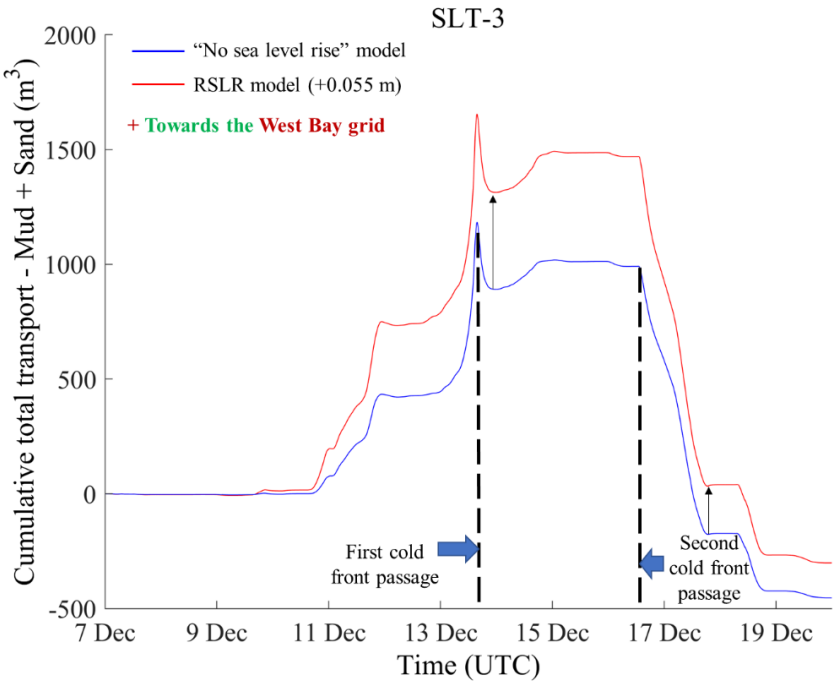

Figure 5-33 Differences in cumulative total transport between the baseline model and the RSLR model at SLT-3

The amount of sediment supplied to the salt marsh has decreased due to the RSLR. However, at the end of the first cold front, the amount of sediment supplied from the southwest (SLT-1) was increased. This is due to the increase in sediment influx into Galveston Bay during the first cold front in the RSLR model. During this period, outflows to West Bay along STL-2 and STL-3 were increased. After the second cold front passage, postfrontal winds (winds from the north) were affected for a long time. At the boundary of SLT-1 and SLT-2, the outflow of sediments from the salt marsh area was very significant during the second cold front period. RSLR was found to make the sediment spill worse since sediment outflux has increased in all directions compared to the baseline model.

5.5. Discussion

5.5.1. Sediment flux and morphological changes

According to the sediment flux results, sediment exchange between Galveston Bay and the Gulf of Mexico was active on DEC 12 and DEC 13, and during the first cold front passage. On DEC 12 and DEC 13, the outflow of sediment flux from the Galveston Bay was active at Galveston Bay entrance and San Luis Pass cross section. However, during the first cold front passage, significant outflux of the sediments to the Gulf of Mexico along the W1 (San Luis pass) and G1 (Galveston Bay Entrance) was observed. The sediment run-off in G1 is more periodic than other monitoring sections, suggesting that the sediment is transported by tidal ebb and flow along the ship channel.

The instantaneous sediment transport along W2 and W3 in West Bay was relatively small compared to W1 and G1. This is due to the relatively shallow water depth in the entire of West Bay sea bed. During the first cold front passage, the instantaneous sediment transport was relatively high along W2 and W3 compared to all other periods. This is related to the increase in water depth and ocean current velocity due to the wind during the first cold front.

From the entire simulation period, significant erosion and deposition was confirmed along the ship channel and along the boundary between the Gulf of Mexico and Galveston Bay. Deposition occurred during the simulation period near the boundary of vegetated wetlands, where critical shear stress in the model is much higher. However, it was confirmed that erosion occurred at the bottom of the front part of the wetland, which is likely due to the bed shear stress created by the waves. The inner parts of the

wetland boundary were not flooded until the first cold front approached. During the flooding, bed shear stress was recorded, and relatively low current speed was recorded. Low enough current speed less than settling velocity can induce the mud deposition, evidenced by the accretion inside the salt marsh boundary during the first cold front passage. The salt marsh edge platform was periodically flooded by high tide and cold front induced wind set-up. Due to the low water depth, the current velocity was less than 5 mm/s on the marsh edge platform.

SSC is an important parameter deciding the accretion availability of the salt marsh boundary. The results show that approximately more than 8 m/s wind velocity generated a high SSC of mud. The SSC level was highest during the first cold front passage, and the relatively high SSC tended to persist during the second cold front passage. Therefore, the passage of the cold front contributed to the increase in SSC. Furthermore, it also activated an environment causing both erosion and accretion to the salt marsh edges and the inner part of the salt marsh.

5.5.2. Model sensitivities and limitations

For the sediment characteristics, default values were used for sand except for the site information of D_{50}. The characteristics of mud were not based on the actual sediment found near the Galveston Island wetlands, so that the sediment may differ substantially from the model. Default values were used for parameters for mud. The erosion parameters, settling velocity, and critical shear stress are fundamental in defining the cohesive sediment. Differences among these parameters can affect the salt marsh boundary erosion and accretion. However, there is no detailed report on the properties of

the mud in the West Bay area. In general, with a larger erosion rate, more sediment can be suspended material is more likely to be transported for enough to reach the shoreline before it settles down again. In terms of the contributions of coastal bays to deposition in salt marshes, the settling velocity is an important parameter since it is related to deposition on the salt marsh platform.

In this study, different settling velocities of 0.1 mm/s and 0.25 mm/s were tested to verify the impact of the mud's settling velocity. The results showed that the impact of settling velocity change on erosion and deposition is minimal (less than 1 mm). However, with less settling velocity, the suspended material is more likely to be transported outside of the salt marshes. Erosion rate (parameter) is an important parameter for deciding sediment suspension from the bed. To verify the impact in the erosion rate difference in salt marsh morphodynamics, two erosion rates of 0.5 and 1.0 $\times 10^{-4}$ kg/m^2/s were tested. The results showed that the erosion rate of 1.0×10^{-4} kg/m^2/s was more sensitive to the erosion near the salt marsh boundary. In reality, critical shear stress could vary in space and time, and settling velocity and erosion rate are also variables depending on sediment properties and flow conditions. However, they were simplified to be constants in time and a uniform value for sediment under water and on the vegetated wetlands, respectively. The scarcity of data for these parameters highlights the need for a more detailed sediment dataset on Galveston Bay.

No recent data was available for the fluvial input from the rivers in Galveston Bay. In the results, the river discharge and sediment input did not make a difference in sediment transport to the site of interest. The river discharge records were also based on

the single gauge located away from the estuary. Therefore, there may be a difference in the amount of discharge.

In the Delft3D-Flow model, the process of drying and flooding is represented by removing grid points from the flow domain that become “dry” when the tide falls and by adding grid points that become “wet” when the tide rises. In addition, the inundation threshold for sedimentation calculation can also affect the morphodynamic, especially when significant bed shear stresses are existing due to waves. The model used here adopted a default inundation threshold of 0.1 m. The current model used depth-averaged grids for hydrodynamic simulation. If density stratification is important for sediment suspension and transport, a 3D model is required. In Liu (2016), the 3D model’s magnitudes of the sediment fluxes at cross-sections between the estuaries and wetlands were smaller than those appeared in the 2D model. However, it was reported that their difference is in a reasonable range compared to measurement data from the field.

5.5.3. Sea level rise case

Comparisons between models were performed assuming ground subsidence and sea level rise five years after the simulation year. Based on the reference data, a sea level rise of 37.5 mm and 17.5 mm of the ground settlement was assumed after five years from 2015. In the sea level rise model, some sediment transport changes between Galveston Bay and the Gulf of Mexico were observed. During the first cold front, sediments flowing into Galveston Bay were increased. However, this increase in inflows did not help to increase sediment volumes in the West Bay area. This is because most of the sediment entering the San Luis Pass has not reached the West Bay, or the amount

discharged from the other side has increased relatively. In addition, sediment fluxes move towards the Galveston Bay Entrance or Trinity Bay has been increased. At the end of the second cold front, an overall increase in sediment outflux to the Gulf of Mexico was found in the RSLR model. The second cold front had generated the winds from north to south for a long time during the postfrontal phase, and its effects combined with RSLR ensured to have accelerated sediment runoff. This trend is important since the outflow of sediment can be accelerated by the cold front when RSLR is in progress.

In the vicinity of the wetland boundary, differences occurred between the salt marsh edge and the inner side of the salt marsh. Less than 0.01 m of increase in erosion has occurred throughout the wetland area due to RSLR during the simulation period spanning from DEC 7 to DEC 19, 2015 (12 days). The sea bed in front of the wetland boundary also showed a higher increase in erosion due to the increase in shear stress caused by waves in the RSLR model. At the edge of the salt marsh, increased accretion occurred at the edge of the wetland. Even though in RSLR, there was a trend to maintain the bed level at the edge of the wetland. The adaptation of salt marsh to the RSLR was also reported in Kirwan et al. (2016)'s model tests.

5.6. Conclusions

The examination of cold front-induced sedimentation in coastal wetlands was performed through a coupled wind, tide, wave and sediment transport modeling system in the present study. The simulations showed that the circulation of sediment fluxes to the West Bay was increased during the first cold front. The extensive flooding of the first cold front had a relatively large effect on the supply of sediments to the wetlands. In

contrast, the transport of sand was relatively negligible during the cold front. The model prediction of wetland erosion and deposition was sensitive to some sediment properties in the model, i.e., erosion rate. Among them, uncertainty in erosion rate constituted the major part of the predicted accretion and erosion variance.

The hypothesis about the salt marsh platform's sea level adaptation was verified by comparing the baseline model and the RSLR model. At the outermost part of the wetland boundary, there was a trend to adapt to sea-level rise during the simulation period. In the RSLR model, increased sediment runoff was observed at the salt marsh area when the north to south winds were dominant during the cold front passage.

The implication of the present study for wetland restoration in West Galveston Bay is that keeping sediments from the inner side Bay is essential. As the properties of the mud and sand in the West Bay are not accurately identified. Thus, collecting these properties will contribute to improving the morphodynamic model accuracy. The change in SSC in the West Bay is also related to the survival fate of the future RSLR. Thus, it is necessary to measure SSC's temporal change in the West Bay estuary through the field measurement and the remote sensing technique.

6. CONCLUSIONS AND FUTURE RESEARCH DIRECTION

6.1. Conclusions

This dissertation aims to verify the impact of ocean waves on the erosion of salt marsh boundaries. In addition, sediment transport affecting salt marsh morphodynamics was considered to understand better the entire accretion and erosion processes near salt marsh boundaries. Wave energies affecting salt marsh were investigated through a numerical and experimental model in Chapter 2 and Chapter 3. Chapter 2 aims to verify and quantify the wave energies to the salt marsh in the actual field through hindcast simulation. Chapter 3 investigates the wave energies' effect on salt marsh surface erosion to connect Chapter 2's wave energy information with the lateral erosion rate of salt marsh. In Chapter 4, observation of salt marsh boundaries in Galveston Bay was done over a year through actual field UAV surveys. From the survey results, Chapter 4 tried to verify Chapter 2 and Chapter 3's investigations related to wave power and erosion rate relationships. In addition, Chapter 5 investigates sediment transport's role in the erosion and accretion of the salt marsh to understand the overall morphological change of salt marsh edges by supplementing the contents of chapters 2-4. In hindcast simulation in Chapter 2 and Chapter 5, a specific focus is on cold front induced waves and currents affecting the salt marsh boundary. The detailed research outcomes of each chapter are described as follows.

To begin with, Chapter 2 investigated the cold front induced waves propagating into the wetland using a large scale hydrodynamic and wave model. The model's wave and water level results were validated based on the wave gauge records installed near the

Galveston Island wetland boundary during December 2015. The model and observation results were in good agreement. In the simulation period, the passage of two cold fronts generated relatively high wave energies and increased Galveston Bay's water level. In the model, wind gusts input leads to improved predictions of cold-front driven surface waves over averaged wind input. The wave power affecting the salt marsh edge was calculated and found that wetlands inundation caused by coincident cold front-driven water levels and high tide weakens the impact of energetic waves on marsh edge. Calculated cumulative effective wave power results revealed that a slow-moving cold front (the second cold front) leads to more energetic waves in confined bays and a greater probability of salt marsh erosion.

In Chapter 3, the erosion by the experimentally generated waves on the wetland core samples was investigated through experiments. The amount of erosion was measured for each incident wave of a different height. First, the characteristics that the incident wave changes as it proceeds to the rock beach slope on which the sample is placed were analyzed. Through wave characteristic analysis, it was found that the wave tends to break as it goes up the slope. From dimensional analysis, it was confirmed that there is a linear relationship between wave power and erosion rate. Based on the spectrum analysis of the wave gauge, wave power was calculated and compared with each core sample's erosion rate. The results confirmed that the erosion rate coefficient was high in a sample core location where the wave breaking occurs easily.

In Chapter 4, the lateral erosion of the salt marshes in Galveston Island wetlands were investigated through the field UAV surveys. Using a GNSS receiver on the ground

and a GNSS receiver attached to the UAV, the highly accurate location information for the UAV images were derived through the PPK analysis. Based on the UAV images with location information, Structure from Motion (SfM) by GNSS-supported aerial triangulation was conducted to generate the wetlands' orthomosaic map. Drone surveys have been conducted a total of 7 times over a year, and the boundary erosions for each period were calculated. The final orthomosaic maps' averaged error was 1~1.3 cm in the horizontal direction. The average wave power was calculated by investigating the wave climate of the survey area through a simplified numerical model. Then the relationship between wave power and erosion rate was summarized. The average amount of erosion from 2019 DEC to 2020 MAR, where winds from north to south were dominant, was higher than that from 2020 MAR to 2020 OCT. Much erosion was observed in the protruding part of the wetland. This is caused by waves coming from many directions surrounding these parts, and the erosion of this part had a significant influence on the averaged erosion rate of the survey areas.

Chapter 5 focuses on analyzing the effects of sediment transport on wetland erosion and accretion along the boundary. Using the model verified in Chapter 2, after inputting the sediment information of the Galveston area that can be secured, we analyzed the movement of these sediments in Galveston Bay. As a result, when the cold front passed, it was possible to confirm a large inflow or outflow of sediment to the boundary between the Gulf of Mexico and Gulf of Galveston. In addition, through comparison with the RSLR model, the effect of global sea level rise and land subsidence on sediment transport at the edge of the wetland was analyzed. As a result, the platform

at the edge of the wetland tended to maintain the surface level despite the subsidence and increase in water depth. This proves that sediment sedimentation at the wetland boundary increased due to RSLR.

6.2. Future research direction

Based on the results obtained in this dissertation, several future research directions are identified and proposed. Below are examples for each chapter.

In Chapter 2, a highly refined resolution for salt marsh area using a flexible grid model can enhance the model reproducibility. The improved results can play an important role in predicting future progress in wetlands boundaries. This requires higher resolution wind data and topographic and bathymetric data. It is essential to test these input data and check their validity based on observations. This chapter analyzed the wave environment for a short period of time. However, it is important to understand the trend of wave energy changes and water level changes along salt marsh boundaries over a long period of time. In addition, although this study investigated the wetland facing north of Galveston Island, it is necessary to analyze the long-term wave energy trend for the wetland facing south or the wetland facing other directions in the Galveston Bay.

In chapter 3, additional derivation of the relationship between wave energy and erosion using random waves similar to the actual site condition can be an important reference. In terms of measurement, attaching several pressure transducers to the salt marsh edge sample helps to quantify the effects of wave force. In addition, another direction of research is to analyze the images of wave breaking, via the Bubble Image Velocimetry (BIV) technique (Ryu et al., 2005), to quantify the surface shear stress

generated by wave breaking. Finally, it is important to distinguish the role of erosion among tension crack, mass failure, and particle by particle erosion. This requires a laboratory experiment with long-term exposure to waves. If this is not feasible, a method of photographing the wetland edge surface directly in the field may also be considered.

In chapter 4, additional analysis for the 3d image of the salt marsh based on the UAV images can enhance the accuracy of the boundary recognition. This also makes it possible to evaluate the volume erosion of salt marsh edges based on 3D data obtained from SfM. From a hardware perspective, the performance of GNSS receivers (increased number of satellites) or improved performance of the antenna attached to the UAV can play an important role in reducing the errors of the final result. Regarding wetland boundary recognition, developing an automatic recognition algorithm with a low margin of error can help efficiency. An example is recognizing wetland boundaries using Region Based Convolutional Neural Networks (RCNN), known as an object detection algorithm. It is also essential to observe changes in vegetation on the salt marsh edge platform using a near-infrared camera. From the normalized difference vegetation index (NDVI) results, it is possible to distinguish whether a decline in vegetation could affect boundary erosion and vice versa. Finally, the method of obtaining DEM of wetland platform through LiDAR, obtaining 3D images through SfM, and classifying vegetation through NDVI will be most effective to assess overall changes of the salt marsh in time.

In Chapter 5, large uncertainties exist in some of the sediment properties. Future efforts to better link ongoing field studies with model parameters should be undertaken to improve model prediction skills. Validating the modeled accretion/erosion by

observation data through direct or indirect (remote sensing) is essential. Indirect methods include satellite image and UAV image observation. Based on the comparison of measured values and model results, the amount of erosion/accretion of the marsh edge can be verified. To make this clear, long-term simulations and observations need to be done.

REFERENCES

Adam, P. (1993). Saltmarsh ecology, Cambridge University Press.

Alizad, K., S. C. Hagen, J. T. Morris, S. C. Medeiros, M. V. Bilskie and J. F. Weishampel (2016). "Coastal wetland response to sea-level rise in a fluvial estuarine system." Earth's Future.

Allen, J. R. (2000). "Morphodynamics of Holocene salt marshes: a review sketch from the Atlantic and Southern North Sea coasts of Europe." Quaternary Science Reviews **19**(12): 1155-1231.

Alves, J. H. G., M. L. Banner and I. R. Young (2003). "Revisiting the Pierson–Moskowitz asymptotic limits for fully developed wind waves." Journal of Physical Oceanography **33**(7): 1301-1323.

Anderson, K. and K. J. Gaston (2013). "Lightweight unmanned aerial vehicles will revolutionize spatial ecology." Frontiers in Ecology and the Environment **11**(3): 138-146.

Anderson, S. and A. Lohrmann (1995). Open water test of the SonTek acoustic Doppler velocimeter. Proceedings of the IEEE Fifth Working Conference on Current Measurement, IEEE.

Babanin, A., D. Chalikov, I. Young and I. Savelyev (2007). "Predicting the breaking onset of surface water waves." Geophysical Research Letters **34**(7).

Battjes, J. A. and J. Janssen (1978). Energy loss and set-up due to breaking of random waves. Coastal Engineering 1978**:** 569-587.

Becker, J., D. Sandwell, W. Smith, J. Braud, B. Binder, J. Depner, D. Fabre, J. Factor, S. Ingalls and S. Kim (2009). "Global bathymetry and elevation data at 30 arc seconds resolution: SRTM30_PLUS." Marine Geodesy **32**(4): 355-371.

Benassi, F., E. Dall'Asta, F. Diotri, G. Forlani, U. Morra di Cella, R. Roncella and M. Santise (2017). "Testing accuracy and repeatability of UAV blocks oriented with GNSS-supported aerial triangulation." Remote Sensing **9**(2): 172.

Bendoni, M., S. Francalanci, L. Cappietti and L. Solari (2014). "On salt marshes retreat: Experiments and modeling toppling failures induced by wind waves." Journal of Geophysical Research: Earth Surface **119**(3): 603-620.

Benker, S. C., R. P. Langford and T. L. Pavlis (2011). "Positional accuracy of the Google Earth terrain model derived from stratigraphic unconformities in the Big Bend region, Texas, USA." Geocarto International **26**(4): 291-303.

Booij, N., R. C. Ris and L. H. Holthuijsen (1999). "A third-generation wave model for coastal regions: 1. Model description and validation." Journal of geophysical research: Oceans **104**(C4): 7649-7666.

Bouma, T., J. Van Belzen, T. Balke, J. Van Dalen, P. Klaassen, A. Hartog, D. Callaghan, Z. Hu, M. Stive and S. Temmerman (2016). "Short-term mudflat dynamics drive long-term cyclic salt marsh dynamics." Limnology and oceanography **61**(6): 2261-2275.

Bouma, T., M. D. Vries, E. Low, L. Kusters, P. Herman, I. Tanczos, S. Temmerman, A. Hesselink, P. Meire and S. Van Regenmortel (2005). "Flow hydrodynamics on a mudflat and in salt marsh vegetation: identifying general relationships for habitat characterisations." Hydrobiologia **540**(1-3): 259-274.

Boussinesq, J. (1877). Essai sur la théorie des eaux courantes, Impr. nationale.

Bruno, J. F. (2000). "Facilitation of cobble beach plant communities through habitat modification by Spartina alterniflora." Ecology **81**(5): 1179-1192.

Buckingham, E. (1914). "On physically similar systems; illustrations of the use of dimensional equations." Physical review **4**(4): 345.

Buczkowski, B. J., J. A. Reid, C. J. Jenkins, J. M. Reid, S. J. Williams and J. G. Flocks (2006). usSEABED: Gulf of Mexico and Caribbean (Puerto Rico and US Virgin Islands) offshore surficial-sediment data release, US Department of the Interior, US Geological Survey.

Cahoon, D. R. (2006). "A review of major storm impacts on coastal wetland elevations." Estuaries and Coasts **29**(6a): 889-898.

Campbell, A. and Y. Wang (2019). "High spatial resolution remote sensing for salt marsh mapping and change analysis at Fire Island National Seashore." Remote Sensing **11**(9): 1107.

Carter, D. (1982). "Prediction of wave height and period for a constant wind velocity using the JONSWAP results." Ocean Engineering **9**(1): 17-33.

Caulliez, G. (2002). "Self-similarity of near-breaking short gravity wind waves." Physics of Fluids **14**(8): 2917-2920.

Chmura, G. L., S. C. Anisfeld, D. R. Cahoon and J. C. Lynch (2003). "Global carbon sequestration in tidal, saline wetland soils." Global biogeochemical cycles **17**(4).

Chudley, T., P. Christoffersen, S. H. Doyle, A. Abellan Fernandez and N. Snooke (2019). "High-accuracy UAV photogrammetry of ice sheet dynamics with no ground control."

Colomina, I. and P. Molina (2014). "Unmanned aerial systems for photogrammetry and remote sensing: A review." ISPRS Journal of photogrammetry and remote sensing **92**: 79-97.

Cook, K. L. (2017). "An evaluation of the effectiveness of low-cost UAVs and structure from motion for geomorphic change detection." Geomorphology **278**: 195-208.

Cox, D. T., P. Tissot and P. Michaud (2002). "Water level observations and short-term predictions including meteorological events for entrance of Galveston Bay, Texas." Journal of waterway, port, coastal, and ocean engineering **128**(1): 21-29.

Cucci, D. A., M. Rehak and J. Skaloud (2017). "Bundle adjustment with raw inertial observations in UAV applications." ISPRS Journal of photogrammetry and remote sensing **130**: 1-12.

Dahl, T. E. and C. E. Johnson (1991). Wetlands, status and trends in the conterminous United States, mid-1970's to mid-1980's: first update of the national wetlands status report, US Department of the Interior, Fish and Wildlife Service.

Deegan, L. A., D. S. Johnson, R. S. Warren, B. J. Peterson, J. W. Fleeger, S. Fagherazzi and W. M. Wollheim (2012). "Coastal eutrophication as a driver of salt marsh loss." Nature **490**(7420): 388-392.

Defne, Z., A. L. Aretxabaleta, N. K. Ganju, T. S. Kalra, D. K. Jones and K. E. Smith (2020). "A geospatially resolved wetland vulnerability index: Synthesis of physical drivers." PloS one **15**(1): e0228504.

Defne, Z., N. K. Ganju and J. M. Moriarty (2019). "Hydrodynamic and Morphologic Response of a Back-Barrier Estuary to an Extratropical Storm." Journal of geophysical research: Oceans **124**(11): 7700-7717.

DiMego, G. J., L. F. Bosart and G. W. Endersen (1976). "An Examination of the Frequency and Mean Conditions Surrounding Frontal Incursions into the Gulf of Mexico and Caribbean Sea." Monthly Weather Review **104**(6): 709-718.

Donatelli, C., N. K. Ganju, T. S. Kalra, S. Fagherazzi and N. Leonardi (2019). "Changes in hydrodynamics and wave energy as a result of seagrass decline along the shoreline of a microtidal back-barrier estuary." Advances in Water Resources **128**: 183-192.

Donatelli, C., X. Zhang, N. K. Ganju, A. L. Aretxabaleta, S. Fagherazzi and N. Leonardi (2020). "A nonlinear relationship between marsh size and sediment trapping capacity compromises salt marshes' stability." Geology.

Duarte, C. M., W. C. Dennison, R. J. Orth and T. J. Carruthers (2008). "The charisma of coastal ecosystems: addressing the imbalance." Estuaries and Coasts **31**(2): 233-238.

Duffy, J. P., L. Pratt, K. Anderson, P. E. Land and J. D. Shutler (2018). "Spatial assessment of intertidal seagrass meadows using optical imaging systems and a lightweight drone." Estuarine, Coastal and Shelf Science **200**: 169-180.

Dupuis, K. and A. Anis (2013). "Observations and modeling of wind waves in a shallow estuary: Galveston Bay, Texas." Journal of waterway, port, coastal, and ocean engineering **139**(4): 314-325.

Duran-Matute, M., T. Gerkema and M. G. Sassi (2016). "Quantifying the residual volume transport through a multiple-inlet system in response to wind forcing: The case of the western D utch W adden S ea." Journal of geophysical research: Oceans **121**(12): 8888-8903.

Egbert, G. D. and S. Y. Erofeeva (2002). "Efficient inverse modeling of barotropic ocean tides." Journal of Atmospheric and Oceanic Technology **19**(2): 183-204.

Entwistle, C., M. A. Mora and R. Knight (2018). "Estimating coastal wetland gain and losses in Galveston County and Cameron County, Texas, USA." Integrated environmental assessment and management **14**(1): 120-129.

Everaerts, J. (2008). "The use of unmanned aerial vehicles (UAVs) for remote sensing and mapping." The International Archives of the Photogrammetry, Remote Sensing and Spatial Information Sciences **37**(2008): 1187-1192.

Fagherazzi, S., M. L. Kirwan, S. M. Mudd, G. R. Guntenspergen, S. Temmerman, A. D'Alpaos, J. Van De Koppel, J. M. Rybczyk, E. Reyes and C. Craft (2012). "Numerical models of salt marsh evolution: Ecological, geomorphic, and climatic factors." Reviews of Geophysics **50**(1).

Fagherazzi, S., G. Mariotti, J. Porter, K. McGlathery and P. Wiberg (2010). "Wave energy asymmetry in shallow bays." Geophysical Research Letters **37**(24).

Fagherazzi, S. and P. Wiberg (2009). "Importance of wind conditions, fetch, and water levels on wave-generated shear stresses in shallow intertidal basins." Journal of Geophysical Research: Earth Surface **114**(F3).

Farris, A. S., Z. Defne and N. K. Ganju (2019). "Identifying salt marsh shorelines from remotely sensed elevation data and imagery." Remote Sensing **11**(15): 1795.

Feagin, R., S. M. Lozada-Bernard, T. M. Ravens, I. Moller, K. M. Yeager and A. H. Baird (2009). "Does vegetation prevent wave erosion of salt marsh edges?" Proceedings of the National Academy of Sciences of the United States of America(106).

Feagin, R. A., M. L. Martinez, G. Mendoza-Gonzalez and R. Costanza (2010). "Salt marsh zonal migration and ecosystem service change in response to global sea level rise: a case study from an urban region." Ecology and Society **15**(4).

Floreano, D. and R. J. Wood (2015). "Science, technology and the future of small autonomous drones." Nature **521**(7553): 460-466.

Francalanci, S., M. Bendoni, M. Rinaldi and L. Solari (2013). "Ecomorphodynamic evolution of salt marshes: Experimental observations of bank retreat processes." Geomorphology **195**: 53-65.

Ganju, N. K., Z. Defne, M. L. Kirwan, S. Fagherazzi, A. D'Alpaos and L. Carniello (2017). "Spatially integrative metrics reveal hidden vulnerability of microtidal salt marshes." Nature communications **8**(1): 1-7.

Gedan, K. B., B. R. Silliman and M. D. Bertness (2009). "Centuries of human-driven change in salt marsh ecosystems."

Gibeaut, J. C. (2003). "Changes in Bay Shoreline Position, West Bay System, Texas. A Report of the Texas Coastal Coordination Council pursuant to National Oceanic and Atmospheric Administration Award No. NA07OZ0134. GLO Contract Number 02-225R."

Goda, Y. and Y. Suzuki (1976). Estimation of incident and reflected waves in random wave experiments. Proceedings of 15th conference on Coastal Engineering, ASCE.

Goodwin, G. C., S. M. Mudd and F. J. Clubb (2018). "Unsupervised detection of salt marsh platforms: a topographic method." Earth surface dynamics. **6**(1): 239-255.

Google-Earth-Pro 7.3.3.7786 (Feb 2004, Mar 2018), Galveston Island, TX USA, 29° 9'5.80"N, 95° 2'32.98"W, Borders and labels; places layers, US Geological Survey 2004 (Accessed Jan 19, 2021).

Gorelick, N., M. Hancher, M. Dixon, S. Ilyushchenko, D. Thau and R. Moore (2017). "Google Earth Engine: Planetary-scale geospatial analysis for everyone." Remote Sensing of Environment **202**: 18-27.

Graham, D., M. Sault and C. J. Bailey (2003). "National ocean service shoreline—Past, present, and future." Journal of Coastal Research: 14-32.

Greiner, J. H. (1982). "Erosion and sedimentation by water in Texas: Average annual rates estimated in 1979." Report/Texas Department of Water Resources (USA).

Hanson, J. L., B. A. Tracy, H. L. Tolman and R. D. Scott (2009). "Pacific hindcast performance of three numerical wave models." Journal of Atmospheric and Oceanic Technology **26**(8): 1614-1633.

Hartley, R. and A. Zisserman (2003). Multiple view geometry in computer vision, Cambridge university press.

Hasselmann, K., T. Barnett, E. Bouws, H. Carlson, D. Cartwright, K. Enke, J. Ewing, H. Gienapp, D. Hasselmann and P. Kruseman (1973). "Measurements of wind-wave growth and swell decay during the Joint North Sea Wave Project (JONSWAP)." Ergänzungsheft 8-12.

Hasselmann, S., K. Hasselmann, J. Allender and T. Barnett (1985). "Computations and parameterizations of the nonlinear energy transfer in a gravity-wave specturm. Part II: Parameterizations of the nonlinear energy transfer for application in wave models." Journal of Physical Oceanography **15**(11): 1378-1391.

Hofland, B., X. Chen, C. Altomare and P. Oosterlo (2017). "Prediction formula for the spectral wave period Tm-1, 0 on mildly sloping shallow foreshores." Coastal Engineering **123**: 21-28.

Hope, M. E., J. J. Westerink, A. B. Kennedy, P. Kerr, J. C. Dietrich, C. Dawson, C. J. Bender, J. Smith, R. E. Jensen and M. Zijlema (2013). "Hindcast and validation of Hurricane Ike (2008) waves, forerunner, and storm surge." Journal of geophysical research: Oceans **118**(9): 4424-4460.

Horstman, E., M. Dohmen-Janssen and S. Hulscher (2013). Modeling tidal dynamics in a mangrove creek catchment in Delft3D. Coastal dynamics.

Horstman, E. M., C. M. Dohmen-Janssen, T. J. Bouma and S. J. Hulscher (2015). "Tidal-scale flow routing and sedimentation in mangrove forests: Combining field data and numerical modelling." Geomorphology **228**: 244-262.

Hsu, S., E. A. Meindl and D. B. Gilhousen (1994). "Determining the power-law wind-profile exponent under near-neutral stability conditions at sea." Journal of Applied Meteorology **33**(6): 757-765.

Huff, T. P., R. A. Feagin and A. Delgado (2019). "Understanding Lateral Marsh Edge Erosion with Terrestrial Laser Scanning (TLS)." Remote Sensing **11**(19): 2208.

Hydraulics, D. (2006). "Delft3D-FLOW user manual." Delft, the Netherlands.

James, M. R. and S. Robson (2014). "Mitigating systematic error in topographic models derived from UAV and ground-based image networks." Earth Surface Processes and Landforms **39**(10): 1413-1420.

James, M. R., S. Robson and M. W. Smith (2017). "3-D uncertainty-based topographic change detection with structure-from-motion photogrammetry: precision maps for ground control and directly georeferenced surveys." Earth Surface Processes and Landforms **42**(12): 1769-1788.

Johnson, K., E. Nissen, S. Saripalli, J. R. Arrowsmith, P. McGarey, K. Scharer, P. Williams and K. Blisniuk (2014). "Rapid mapping of ultrafine fault zone topography with structure from motion." Geosphere **10**(5): 969-986.

Kaihatu, J. M., J. Veeramony, K. L. Edwards and J. T. Kirby (2007). "Asymptotic behavior of frequency and wave number spectra of nearshore shoaling and breaking waves." Journal of geophysical research: Oceans **112**(C6).

Karimpour, A., Q. Chen and R. R. Twilley (2016). "A field study of how wind waves and currents may contribute to the deterioration of saltmarsh fringe." Estuaries and Coasts **39**(4): 935-950.

Keen, T. R. (2002). "Waves and currents during a winter cold front in the Mississippi bight, Gulf of Mexico: Implications for barrier island erosion." Journal of Coastal Research: 622-636.

Kerr, P., A. Donahue, J. J. Westerink, R. Luettich Jr, L. Zheng, R. H. Weisberg, Y. Huang, H. V. Wang, Y. Teng and D. R. Forrest (2013). "US IOOS coastal and ocean modeling testbed: Inter-model evaluation of tides, waves, and hurricane surge in the Gulf of Mexico." Journal of geophysical research: Oceans **118**(10): 5129-5172.

Kirwan, M. L., G. R. Guntenspergen, A. D'Alpaos, J. T. Morris, S. M. Mudd and S. Temmerman (2010). "Limits on the adaptability of coastal marshes to rising sea level." Geophysical Research Letters **37**(23).

Kirwan, M. L. and J. P. Megonigal (2013). "Tidal wetland stability in the face of human impacts and sea-level rise." Nature **504**(7478): 53-60.

Kirwan, M. L., S. Temmerman, E. E. Skeehan, G. R. Guntenspergen and S. Fagherazzi (2016). "Overestimation of marsh vulnerability to sea level rise." Nature Climate Change **6**(3): 253-260.

Kulawardhana, R. W., R. A. Feagin, S. C. Popescu, T. W. Boutton, K. M. Yeager and T. S. Bianchi (2015). "The role of elevation, relative sea-level history and vegetation transition in determining carbon distribution in Spartina alterniflora dominated salt marshes." Estuarine, Coastal and Shelf Science **154**: 48-57.

Kuleli, T., A. Guneroglu, F. Karsli and M. Dihkan (2011). "Automatic detection of shoreline change on coastal Ramsar wetlands of Turkey." Ocean Engineering **38**(10): 1141-1149.

Ladd, C. J., M. F. Duggan-Edwards, T. J. Bouma, J. F. Pagès and M. W. Skov (2019). "Sediment supply explains long-term and large-scale patterns in salt marsh lateral expansion and erosion." Geophysical Research Letters **46**(20): 11178-11187.

Leonard, L. A. and M. E. Luther (1995). "Flow hydrodynamics in tidal marsh canopies." Limnology and oceanography **40**(8): 1474-1484.

Leonardi, N., Z. Defne, N. K. Ganju and S. Fagherazzi (2016). "Salt marsh erosion rates and boundary features in a shallow Bay." Journal of Geophysical Research: Earth Surface **121**(10): 1861-1875.

Leonardi, N. and S. Fagherazzi (2015). "Effect of local variability in erosional resistance on large-scale morphodynamic response of salt marshes to wind waves and extreme events." Geophysical Research Letters **42**(14): 5872-5879.

Leonardi, N., N. K. Ganju and S. Fagherazzi (2016). "A linear relationship between wave power and erosion determines salt-marsh resilience to violent storms and hurricanes." Proceedings of the national Academy of Sciences **113**(1): 64-68.

Lesser, G. R., J. v. Roelvink, J. Van Kester and G. Stelling (2004). "Development and validation of a three-dimensional morphological model." Coastal Engineering **51**(8-9): 883-915.

Lester, J., L. A. Gonzalez, T. Sage and A. Gallaway (2002). The state of the bay: A characterization of the Galveston Bay ecosystem, Galveston Bay Estuary Program.

Liu, K. (2016). "Numerical Simulations of Wind Effects on Wave Nonlinearity and Hurricane-Induced Sediment Transport on Louisiana Coast."

Liu, K., Q. Chen, K. Hu, K. Xu and R. R. Twilley (2018). "Modeling hurricane-induced wetland-bay and bay-shelf sediment fluxes." Coastal Engineering **135**: 77-90.

Liu, Y., J. Li and Z. N. Fang (2019). Sea Level Rise and Its Projection in the Galveston Bay of Mexico Gulf. World Environmental and Water Resources Congress 2019: Groundwater, Sustainability, Hydro-Climate/Climate Change, and Environmental Engineering, American Society of Civil Engineers Reston, VA.

Liu, Y., J. Li, J. Fasullo and D. L. Galloway (2020). "Land subsidence contributions to relative sea level rise at tide gauge Galveston Pier 21, Texas." Scientific reports **10**(1): 1-11.

Lohrmann, A., R. Cabrera and N. C. Kraus (1994). Acoustic-Doppler velocimeter (ADV) for laboratory use. Fundamentals and advancements in hydraulic measurements and experimentation, ASCE.

Mann, K. H. and J. R. Lazier (2013). Dynamics of marine ecosystems: biological-physical interactions in the oceans, John Wiley & Sons.

Marani, M., A. D'Alpaos, S. Lanzoni and M. Santalucia (2011). "Understanding and predicting wave erosion of marsh edges." Geophysical Research Letters **38**(21).

Mariotti, G. and J. Carr (2014). "Dual role of salt marsh retreat: Long-term loss and short-term resilience." Water Resources Research **50**(4): 2963-2974.

Mariotti, G. and S. Fagherazzi (2010). "A numerical model for the coupled long-term evolution of salt marshes and tidal flats." Journal of Geophysical Research: Earth Surface **115**(F1).

Mariotti, G. and S. Fagherazzi (2013). "Critical width of tidal flats triggers marsh collapse in the absence of sea-level rise." Proceedings of the national Academy of Sciences **110**(14): 5353-5356.

Mathieson, S., A. Cattrijsse, M. Costa, P. Drake, M. Elliott, J. Gardner and J. Marchand (2000). "Fish assemblages of European tidal marshes: a comparison based on species, families and functional guilds." Marine Ecology Progress Series **204**: 225-242.

McLoughlin, S. M., P. L. Wiberg, I. Safak and K. J. McGlathery (2015). "Rates and forcing of marsh edge erosion in a shallow coastal bay." Estuaries and Coasts **38**(2): 620-638.

Möller, I., M. Kudella, F. Rupprecht, T. Spencer, M. Paul, B. K. Van Wesenbeeck, G. Wolters, K. Jensen, T. J. Bouma and M. Miranda-Lange (2014). "Wave attenuation over coastal salt marshes under storm surge conditions." Nature Geoscience **7**(10): 727-731.

Möller, I. and T. Spencer (2002). "Wave dissipation over macro-tidal saltmarshes: Effects of marsh edge typology and vegetation change." Journal of Coastal Research **36**(sp1): 506-521.

Moulton, D. W. and J. S. Jacob (1997). Texas coastal wetlands guidebook, Texas A & M University. Sea Grant College Program.

Nerem, R. S., B. D. Beckley, J. T. Fasullo, B. D. Hamlington, D. Masters and G. T. Mitchum (2018). "Climate-change–driven accelerated sea-level rise detected in the altimeter era." Proceedings of the national Academy of Sciences **115**(9): 2022-2025.

Newell, D., J. Charles, S. R. Hanadi, B. B. Philip, S. S. Frank and W. M. Robert (1994). The State of the Bay: A characterization of the Galveston Bay ecosystem, Cambridge Scientific Abstracts for Food and Agriculture Organization of the ….

NOAA (2020). "Meteorological observations-measurement specifications." from https://tidesandcurrents.noaa.gov/publications/CO-OPS_Measurement_Spec.pdf.

Parker, B., D. Milbert, K. Hess and S. Gill (2003). National VDatum–The implementation of a national vertical datum transformation database. Proceeding from the US Hydro'2003 Conference.

Partheniades, E. (1965). "Erosion and deposition of cohesive soils." Journal of the Hydraulics Division **91**(1): 105-139.

Peppa, M., J. Hall, J. Goodyear and J. Mills (2019). "Photogrammetric assessment and comparison of DJI Phantom 4 pro and phantom 4 RTK small unmanned aircraft systems." ISPRS Geospatial Week 2019.

Priestas, A. M., G. Mariotti, N. Leonardi and S. Fagherazzi (2015). "Coupled wave energy and erosion dynamics along a salt marsh boundary, Hog Island Bay, Virginia, USA." Journal of Marine Science and Engineering **3**(3): 1041-1065.

Ramesh, R., Z. Chen, V. Cummins, J. Day, C. D'Elia, B. Dennison, D. Forbes, B. Glaeser, M. Glaser and B. Glavovic (2015). "Land–ocean interactions in the coastal zone: Past, present & future." Anthropocene **12**: 85-98.

Ravens, T. M., R. C. Thomas, K. A. Roberts and P. H. Santschi (2009). "Causes of Salt Marsh Erosion in Galveston Bay, Texas." Journal of Coastal Research **2009**(252): 265-272, 268.

Roberts, H., O. Huh, S. Hsu, L. Rouse and D. Rickman (1987). Impact of cold-front passages on geomorphic evolution and sediment dynamics of the complex Louisiana coast. Coastal sediments, ASCE.

Roberts, H. H., R. D. DeLaune, J. R. White, C. Li, C. E. Sasser, D. Braud, E. Weeks and S. Khalil (2015). "Floods and cold front passages: impacts on coastal marshes in a river diversion setting (Wax Lake Delta Area, Louisiana)." Journal of Coastal Research **31**(5): 1057-1068.

Rogers, W. E., P. A. Hwang and D. W. Wang (2003). "Investigation of wave growth and decay in the SWAN model: three regional-scale applications." Journal of Physical Oceanography **33**(2): 366-389.

Ryu, Y., K.-A. Chang and H.-J. Lim (2005). "Use of bubble image velocimetry for measurement of plunging wave impinging on structure and associated greenwater." Measurement Science and Technology **16**(10): 1945-1953.

Saha, S., S. Moorthi, X. Wu, J. Wang, S. Nadiga, P. Tripp, D. Behringer, Y.-T. Hou, H.-y. Chuang and M. Iredell (2014). "The NCEP climate forecast system version 2." Journal of climate **27**(6): 2185-2208.

Santschi, P. H. (1995). "Seasonality in nutrient concentrations in Galveston Bay." Marine Environmental Research **40**(4): 337-362.

Schmid, K. A., B. C. Hadley and N. Wijekoon (2011). "Vertical accuracy and use of topographic LIDAR data in coastal marshes." Journal of Coastal Research **27**(6A): 116-132.

Schwimmer, R. A. (2001). "Rates and processes of marsh shoreline erosion in Rehoboth Bay, Delaware, USA." Journal of Coastal Research: 672-683.

Schwimmer, R. A. and J. E. Pizzuto (2000). "A model for the evolution of marsh shorelines." Journal of Sedimentary Research **70**(5): 1026-1035.

Sebastian, A., J. Proft, J. C. Dietrich, W. Du, P. B. Bedient and C. N. Dawson (2014). "Characterizing hurricane storm surge behavior in Galveston Bay using the SWAN+ ADCIRC model." Coastal Engineering **88**: 171-181.

Seibt, C., F. Peeters, M. Graf, M. Sprenger and H. Hofmann (2013). "Modeling wind waves and wave exposure of nearshore zones in medium-sized lakes." Limnology and oceanography **58**(1): 23-36.

Shahbazi, M., G. Sohn, J. Théau and P. Menard (2015). "Development and evaluation of a UAV-photogrammetry system for precise 3D environmental modeling." Sensors **15**(11): 27493-27524.

Shepard, C. C., C. M. Crain and M. W. Beck (2011). "The protective role of coastal marshes: a systematic review and meta-analysis." PloS one **6**(11): e27374.

Shipley, F. S., R. W. Kiesling, C. J. Newell, H. Rifai, P. Bedient and R. McFarlane (1994). "State of the Bay: A Characterization of the Galveston Bay Ecosystem."

Smith, M., J. Carrivick and D. Quincey (2016). "Structure from motion photogrammetry in physical geography." Progress in Physical Geography **40**(2): 247-275.

Snyder, R., F. Dobson, J. Elliott and R. Long (1981). "Array measurements of atmospheric pressure fluctuations above surface gravity waves." Journal of Fluid mechanics **102**: 1-59.

Sousa, A. I., A. I. Lillebø, M. A. Pardal and I. Caçador (2010). "Productivity and nutrient cycling in salt marshes: contribution to ecosystem health." Estuarine, Coastal and Shelf Science **87**(4): 640-646.

Szeliski, R. (2010). Computer vision: algorithms and applications, Springer Science & Business Media.

Taddia, Y., F. Stecchi and A. Pellegrinelli (2020). "Coastal Mapping using DJI Phantom 4 RTK in Post-Processing Kinematic Mode." Drones **4**(2): 9.

Tahar, K. (2013). "An evaluation on different number of ground control points in unmanned aerial vehicle photogrammetric block." ISPAr: 93-98.

Taylor, L. A., B. W. Eakins, K. S. Carignan, R. R. Warnken, T. S. Sazonova and D. C. Schoolcraft (2008). "Digital elevation model of Galveston, Texas: procedures, data sources and analysis."

Temmerman, S., T. Bouma, J. Van de Koppel, D. Van der Wal, M. De Vries and P. Herman (2007). "Vegetation causes channel erosion in a tidal landscape." Geology **35**(7): 631-634.

Temmerman, S., P. Moonen, J. Schoelynck, G. Govers and T. J. Bouma (2012). "Impact of vegetation die-off on spatial flow patterns over a tidal marsh." Geophysical Research Letters **39**(3).

Tilburg, C. E. and R. W. Garvine (2004). "A simple model for coastal sea level prediction." Weather and forecasting **19**(3): 511-519.

Tonelli, M., S. Fagherazzi and M. Petti (2010). "Modeling wave impact on salt marsh boundaries." Journal of geophysical research: Oceans **115**(C9).

Tonkin, T. N. and N. G. Midgley (2016). "Ground-control networks for image based surface reconstruction: An investigation of optimum survey designs using UAV derived imagery and structure-from-motion photogrammetry." Remote Sensing **8**(9): 786.

Ullman, S. (1979). "The interpretation of structure from motion." Proceedings of the Royal Society of London. Series B. Biological Sciences **203**(1153): 405-426.

Ursell, F. (1953). The long-wave paradox in the theory of gravity waves. Mathematical Proceedings of the Cambridge Philosophical Society, Cambridge University Press.

US Army (1984). "Shore protection manual." US Army Engineer Waterways Experiment Station, US Government Printing Office, Washington (DC), USA.

Valentine, K. and G. Mariotti (2019). "Wind-driven water level fluctuations drive marsh edge erosion variability in microtidal coastal bays." Continental Shelf Research **176**: 76-89.

Van der Sluijs, J., S. V. Kokelj, R. H. Fraser, J. Tunnicliffe and D. Lacelle (2018). "Permafrost terrain dynamics and infrastructure impacts revealed by UAV photogrammetry and thermal imaging." Remote Sensing **10**(11): 1734.

van der Wal, D. and K. Pye (2004). "Patterns, rates and possible causes of saltmarsh erosion in the Greater Thames area (UK)." Geomorphology **61**(3-4): 373-391.

Van Rijn, L. (2000). "General view on sand transport by currents and waves: data analysis and engineering modelling for uniform and graded sand (TRANSPOR 2000 and CROSMOR 2000 models)." Z2899.

Walker, N. D. and A. B. Hammack (2000). "Impacts of winter storms on circulation and sediment transport: Atchafalaya-Vermilion Bay region, Louisiana, USA." Journal of Coastal Research: 996-1010.

Ward, G. and N. Armstrong (1992). "Galveston Bay National Estuary Program, ambient water and sediment quality of Galveston Bay: present status and historical trends." Center for Research in Water Resources, University of Texas at Austin: 19-20.

Westoby, M. J., J. Brasington, N. F. Glasser, M. J. Hambrey and J. M. Reynolds (2012). "'Structure-from-Motion'photogrammetry: A low-cost, effective tool for geoscience applications." Geomorphology **179**: 300-314.

White, S. M. and E. A. Madsen (2016). "Tracking tidal inundation in a coastal salt marsh with Helikite airphotos: Influence of hydrology on ecological zonation at Crab Haul Creek, South Carolina." Remote Sensing of Environment **184**: 605-614.

White, W. A., T. A. Tremblay, R. L. Waldinger and T. R. Calnan (2004). Status and trends of wetland and aquatic habitats on barrier islands, upper Texas Coast, Galveston and Christmas Bays, University of Texas at Austin.

Wiberg, P., S. Fagherazzi and M. L. Kirwan (2020). "Improving Predictions of Salt Marsh Evolution Through Better Integration of Data and Models." Annual Review of Marine Science **12**(1): 389-413.

Wiberg, P. L. and C. R. Sherwood (2008). "Calculating wave-generated bottom orbital velocities from surface-wave parameters." Computers & Geosciences **34**(10): 1243-1262.

Williams, S. J., M. A. Arsenault, B. J. Buczkowski, J. A. Reid, J. Flocks, M. A. Kulp, S. Penland and C. J. Jenkins (2007). Surficial sediment character of the Louisiana offshore Continental Shelf region: a GIS Compilation, US Geological Survey.

Xiaoming, Y., J. Yujian and L. Yonghong (2011). "MATLAB simulation and analysis of the Welch method in the classical power spectrum estimation." Electronic Test **30**(11): 101-104.

Xu, K., R. C. Mickey, Q. Chen, C. K. Harris, R. D. Hetland, K. Hu and J. Wang (2016). "Shelf sediment transport during hurricanes Katrina and Rita." Computers & Geosciences **90**: 24-39.

Young, I. R. and A. V. Babanin (2006). "Spectral distribution of energy dissipation of wind-generated waves due to dominant wave breaking." Journal of Physical Oceanography **36**(3): 376-394.

Young, I. R. and L. Verhagen (1996). "The growth of fetch limited waves in water of finite depth. Part 1. Total energy and peak frequency." Coastal Engineering **29**(1-2): 47-78.

Zang, Z., Z. G. Xue, S. Bao, Q. Chen, N. D. Walker, A. S. Haag, Q. Ge and Z. Yao (2018). "Numerical study of sediment dynamics during hurricane Gustav." Ocean Modelling **126**: 29-42.

Zou, Q., A. J. Bowen and A. E. Hay (2006). "Vertical distribution of wave shear stress in variable water depth: Theory and field observations." Journal of geophysical research: Oceans **111**(C9).

APPENDIX A

<ADV Data Analysis of Wave Flume>

Near-bed wave orbital velocities and shear stresses are important parameters in many sediment-transport and hydrodynamic models of the coastal ocean, estuaries. Wiberg and Sherwood (2008) suggested several methods estimating wave-generated bottom orbital velocities from near-bed velocity data, surface-wave spectra, and surface-wave parameters based on linear dispersion relation. For acoustic Doppler velocimeters, they suggested an approach for calculating bottom orbital velocity based on near-bottom velocity spectra. The method estimates the spectra, S_{uu} and S_{vv}, for the u and v components of velocity using the Welch method in Matlab (Xiaoming et al., 2011) and determines the representative bottom orbital velocity u_{br} as

$$u_{br} = \sqrt{2\sum_{i} S_{uv,i}\Delta f_i} \qquad \text{A-1}$$

where $S_{uv} = S_{uu} + S_{vv}$ is the combined horizontal spectrum.

The advantage of the spectral approach is that it can be used to estimate surface-wave heights as

$$H_s = 4\left(\sum_{i} \frac{S_{uv,i}\Delta f_i}{\left(\frac{2\pi f_i \cos\left(k_i z_{uv}\right)}{\sinh(k_i h)}\right)}\right)^{1/2} \qquad \text{A-2}$$

where z_{uv} is the elevation (above the bottom) of the velocity measurements. The orbital velocity was calculated based on Equation 3-7 using acoustic Doppler velocimeters records in front of core 2, 3, and 4. The results are shown in Figure A-1. Channel direction is the horizontal direction opposite to the wave propagation direction.

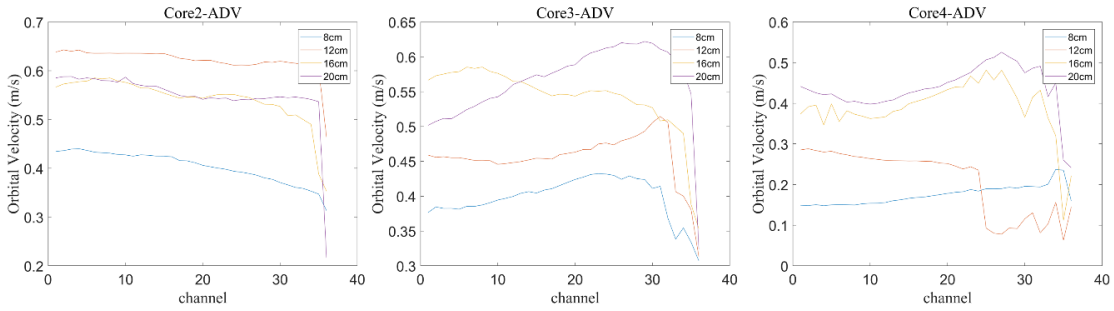

Figure A-1 Calculated orbital velocity from acoustic Doppler velocimeter's horizontal (x and z-direction in the experiment) profiles in front of Core 2, 3 and 4

Thus, the channel values are averaged to get the average orbital velocity and plotted in Figure 3-13 with the erosion rate.

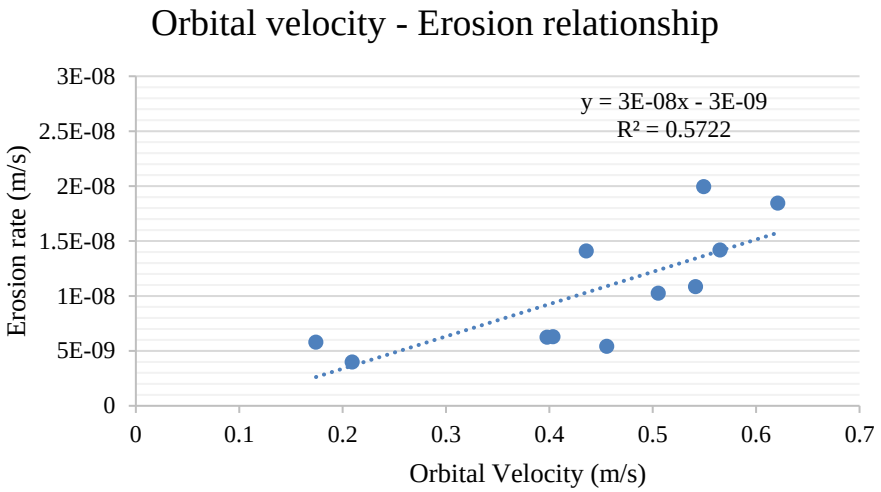

Figure A-2 Relationship between orbital velocity and erosion rate in Core 2, 3 and 4

A linear relationship between orbital velocity and erosion rate was also derived and its R^2 was 0.5722. The significant wave height was indirectly calculated using

orbital velocity, water depth, and distance between ADV and the bottom. The results are shown in Figure A-3 and compared to the significant wave height directly calculated from wave gauges. The wave gauge 3 was close to Core 4 ADV and the wave gauge 4 was at the same location with Core 3 ADV. The distance between ADV and bottom was set to an approximate value as 1/4 of the water depth. Hs results from Core 3 ADV underestimate the directly measured Hs. This is likely due to the breaking of waves in front of the Core 3. Hs results from Core 4 ADV estimate the Hs better than Core 3 ADV case. This is likely due to the wave did not break in front of the core 4. Thus the linear wave theory was held.

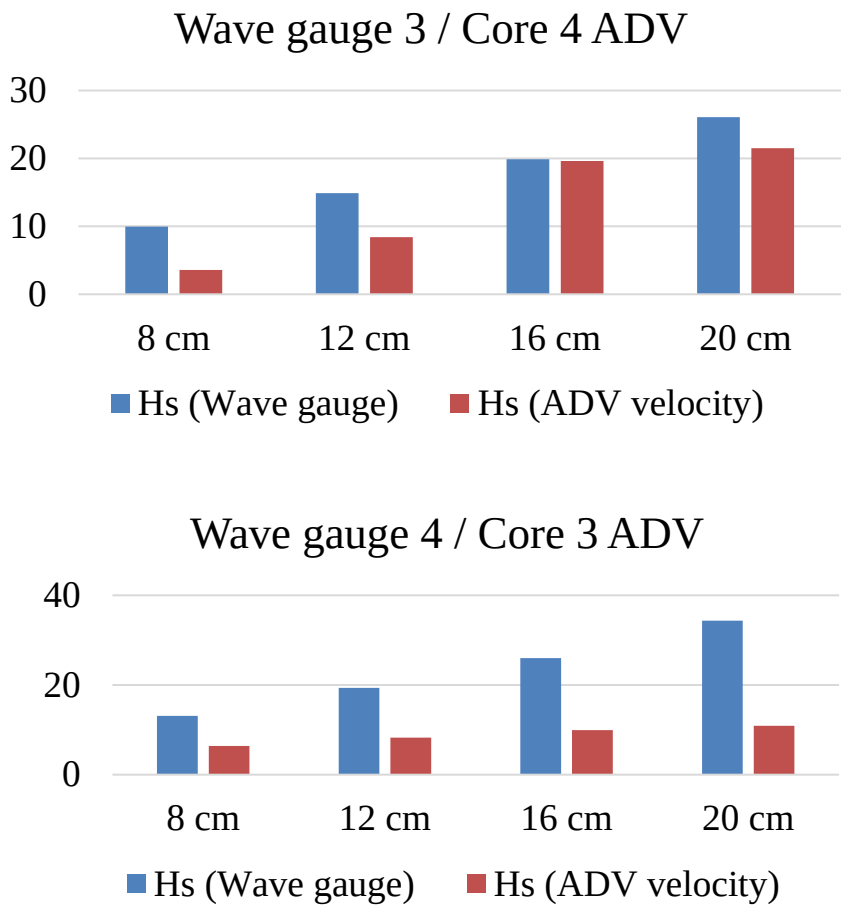

Figure A-3 Comparison of ADV based significant wave height with wave gauge

APPENDIX B

<Orthomosaic Maps of Salt Marsh Boundary by Area and Date>

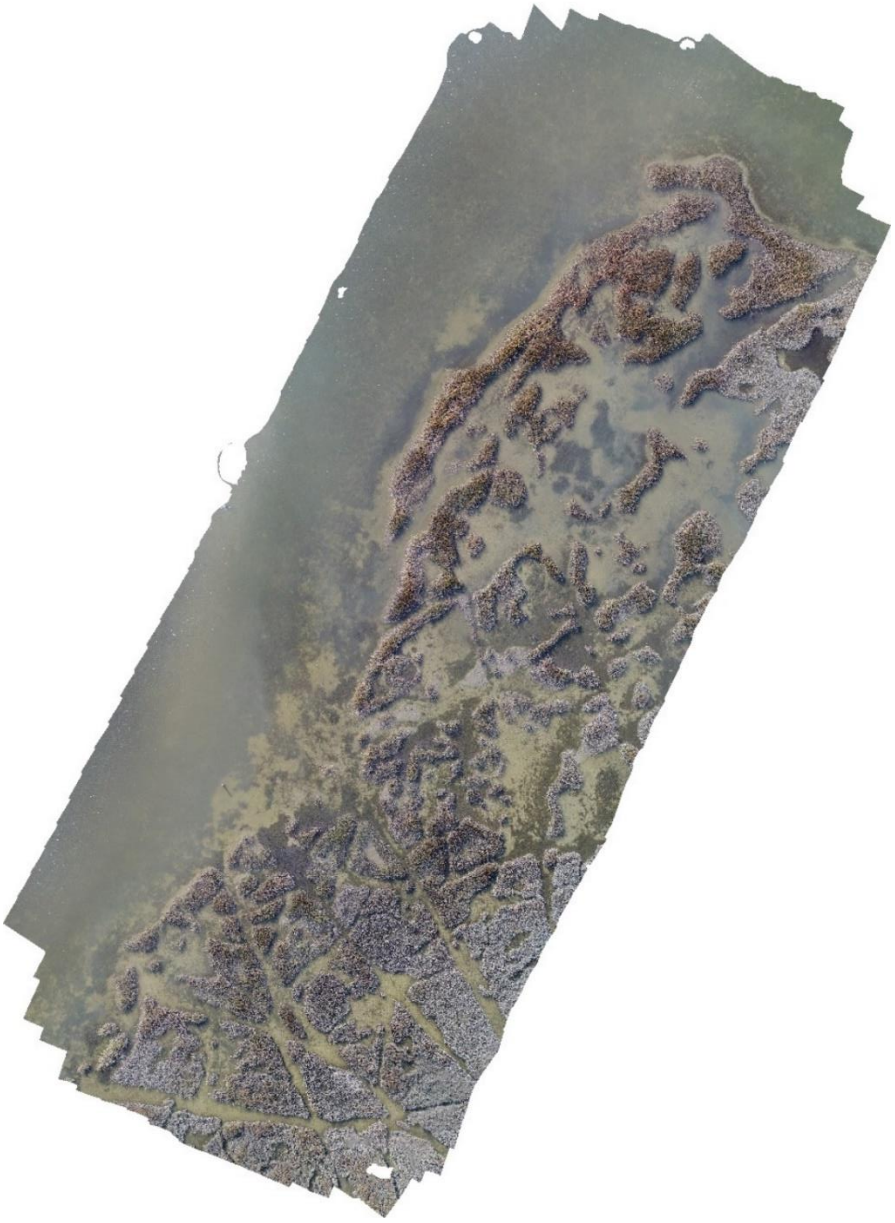

Figure B1-1 Sea Grass Lane S1 (November 1, 2019)

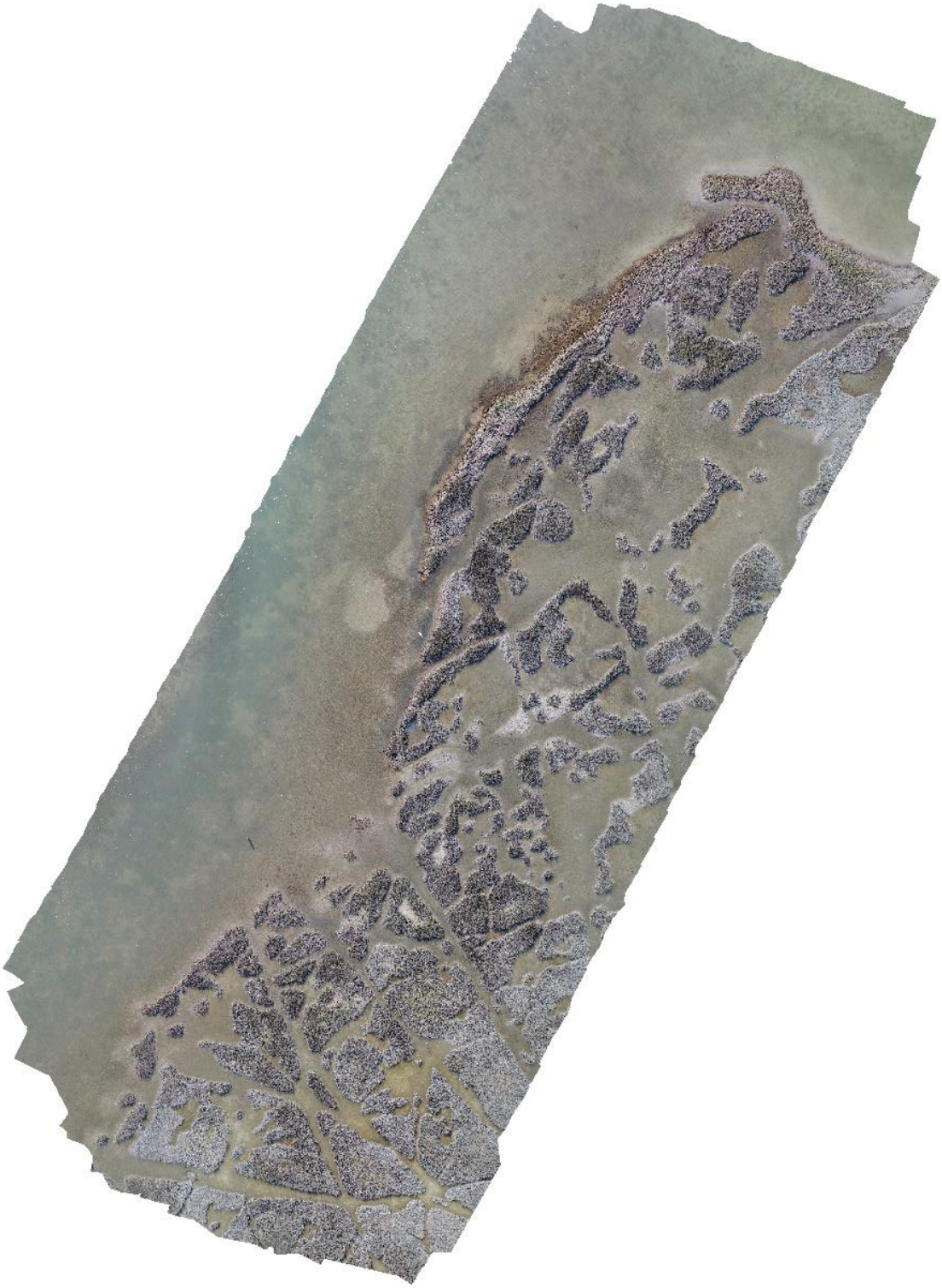

Figure B1-2 Sea Grass Lane S1 (March 6, 2020)

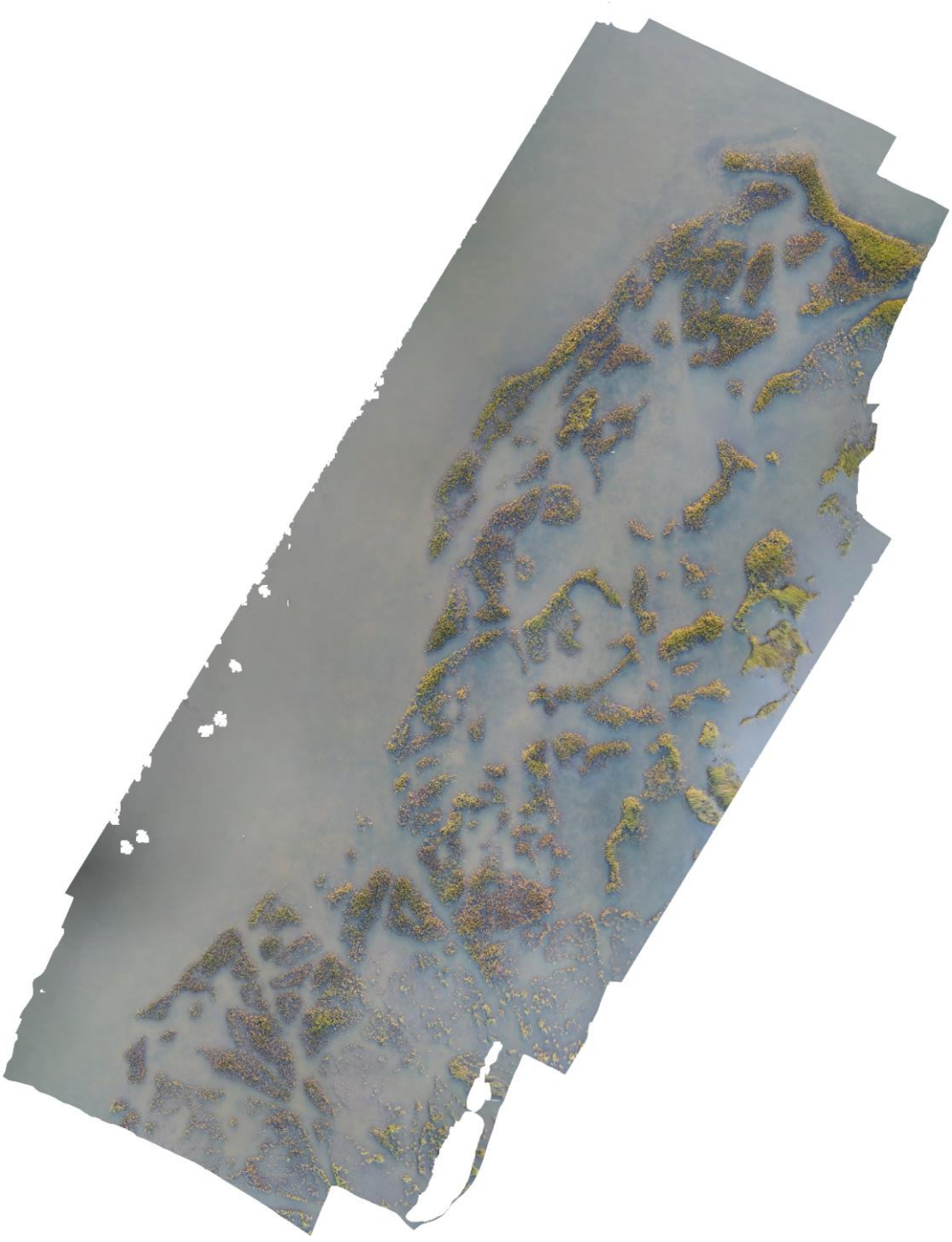

Figure B1-3 Sea Grass Lane S1 (September 12, 2020)

Figure B1-4 Sea Grass Lane S1 (October 30, 2020)

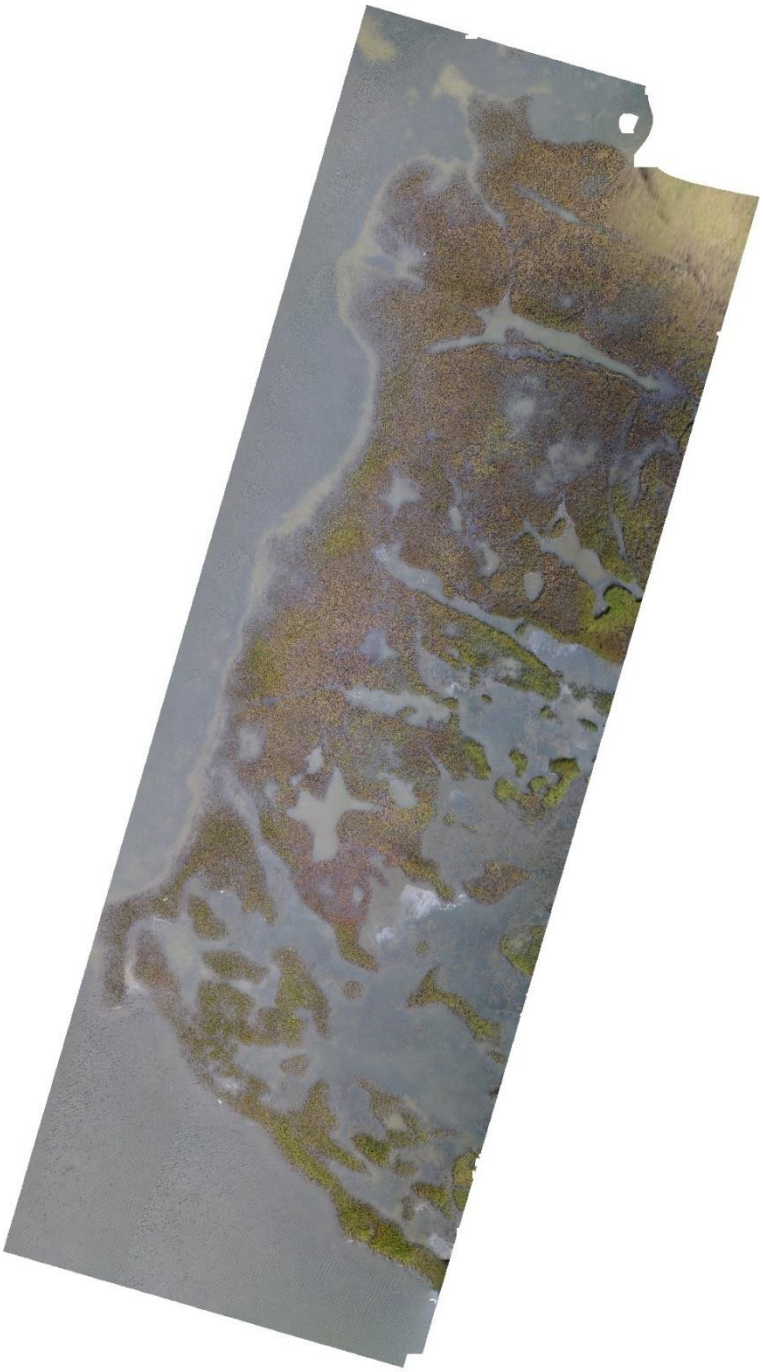

Figure B2-1 Sea Grass Lane S2 (August 3, 2019)

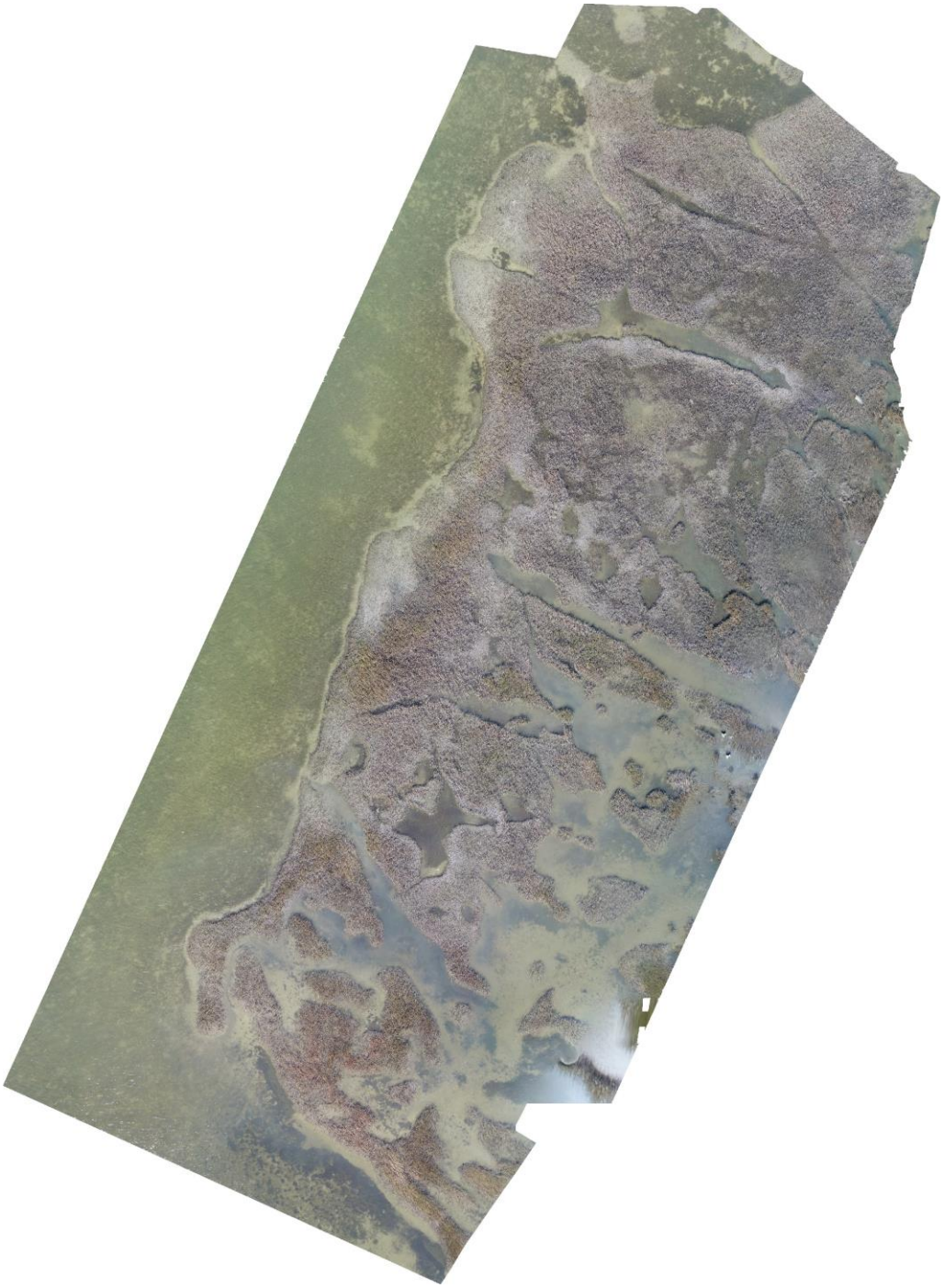

Figure B2-2 Sea Grass Lane S2 (November 1, 2019)

Figure B2-3 Sea Grass Lane S2 (December 2, 2019)

Figure B2-4 Sea Grass Lane S2 (March 6, 2020)

Figure B2-5 Sea Grass Lane S2 (October 30, 2020)

Figure B3-1 Sea Grass Lane S3 (November 1, 2019)

Figure B3-2 Sea Grass Lane S3 (December 2, 2019)

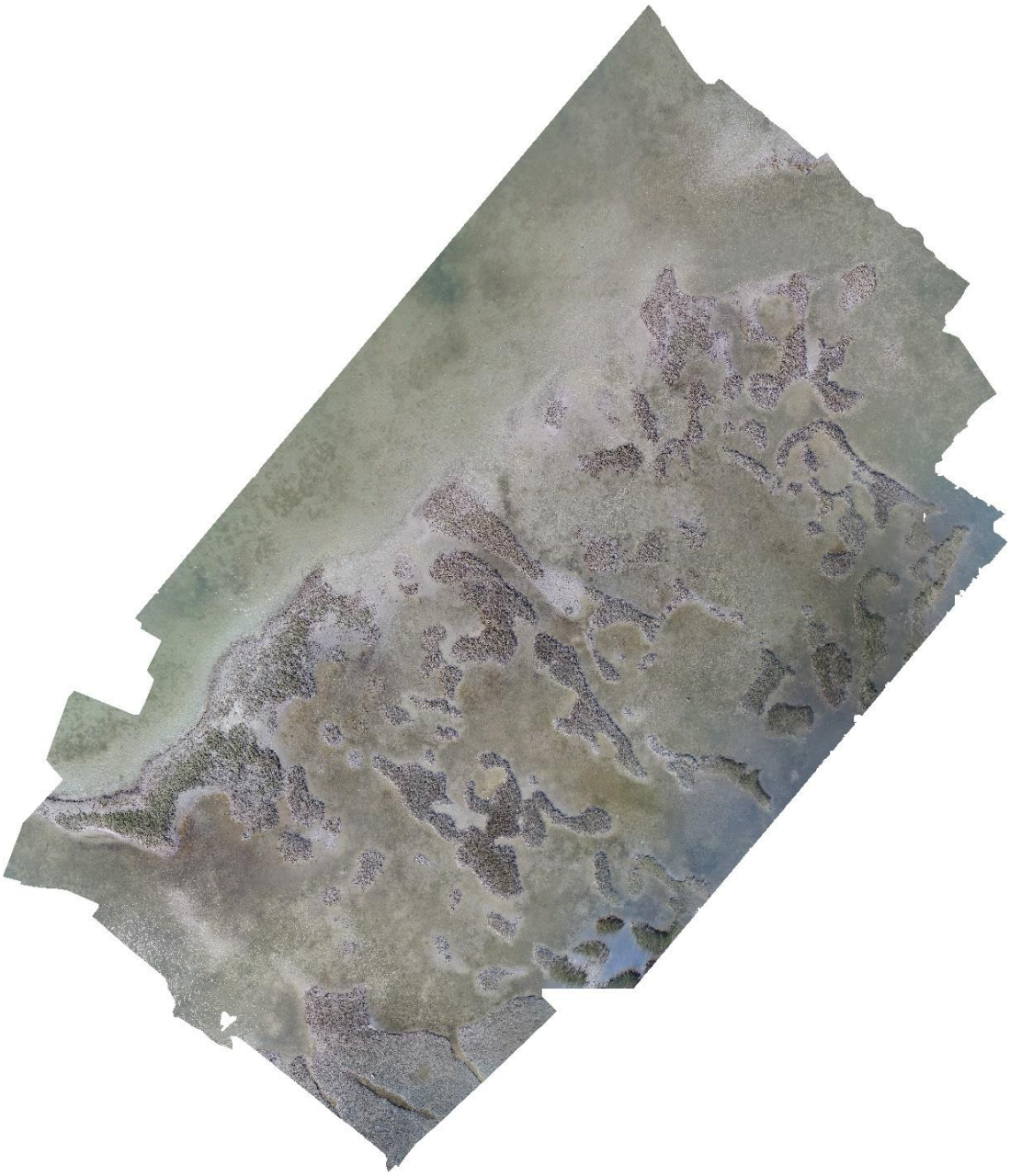

Figure B3-3 Sea Grass Lane S3 (March 6, 2020)

Figure B3-4 Sea Grass Lane S3 (September 12, 2020)

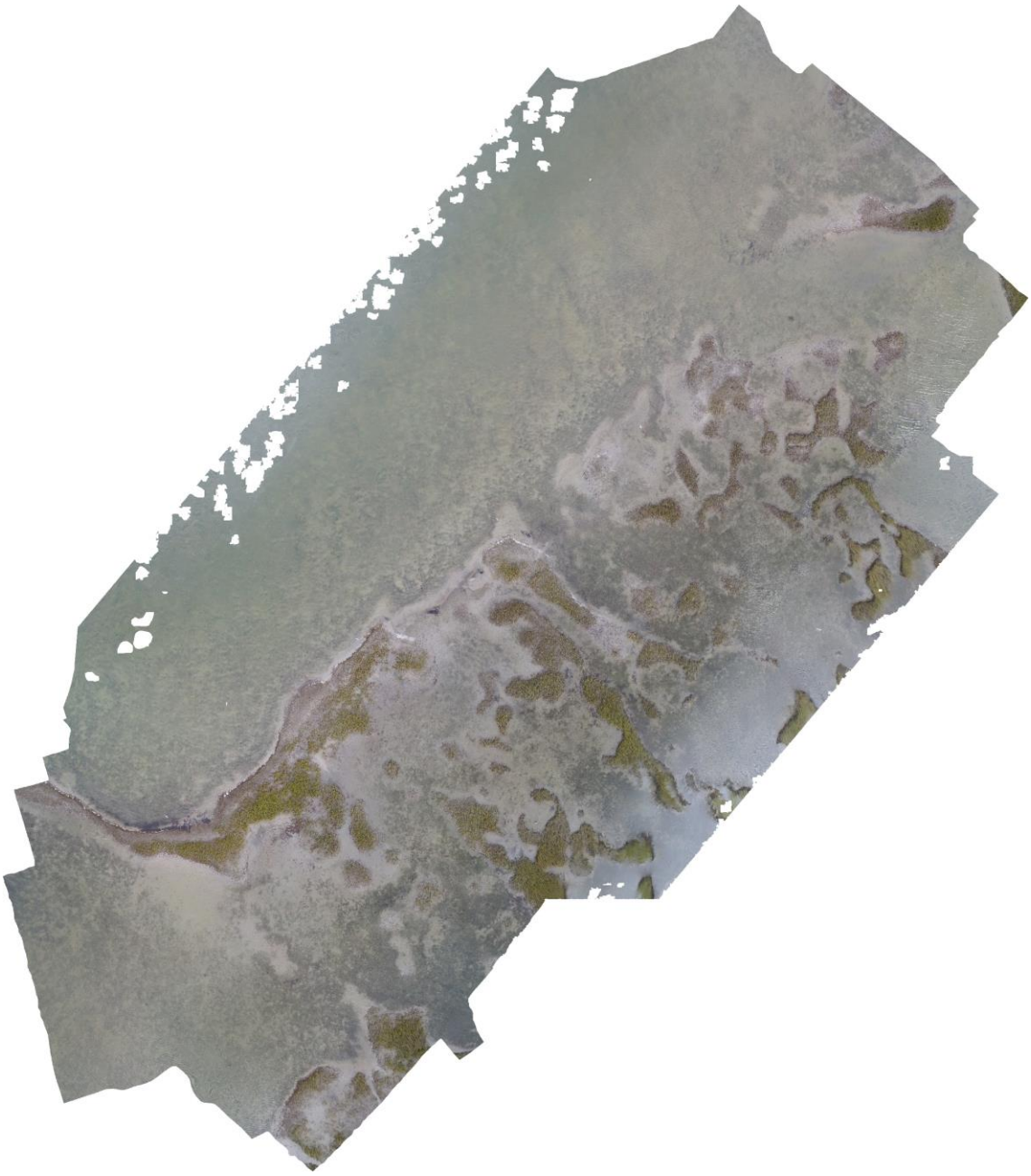

Figure B3-5 Sea Grass Lane S3 (October 30, 2020)

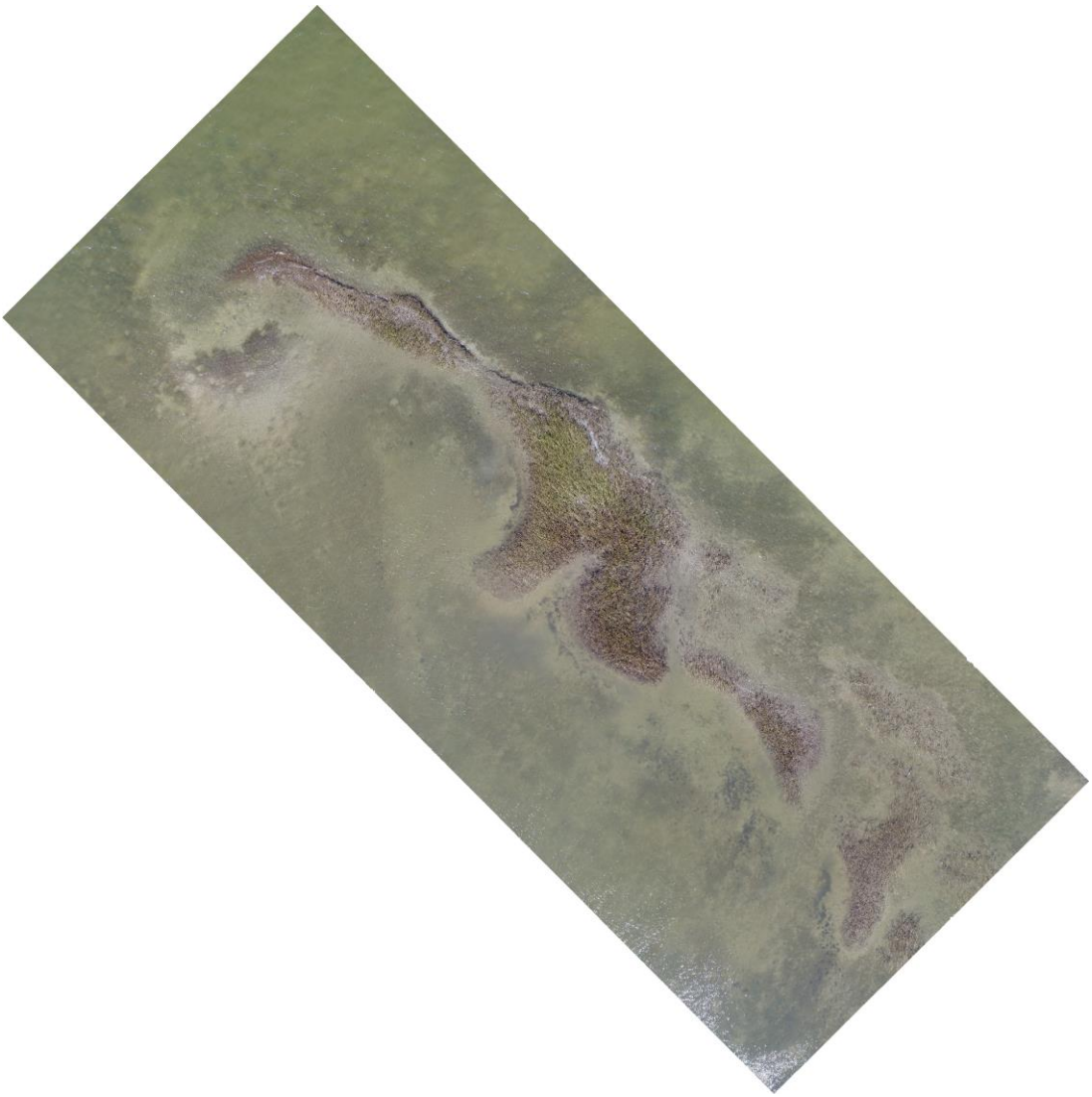

Figure B4-1 Sea Grass Lane S4 (November 1, 2019)

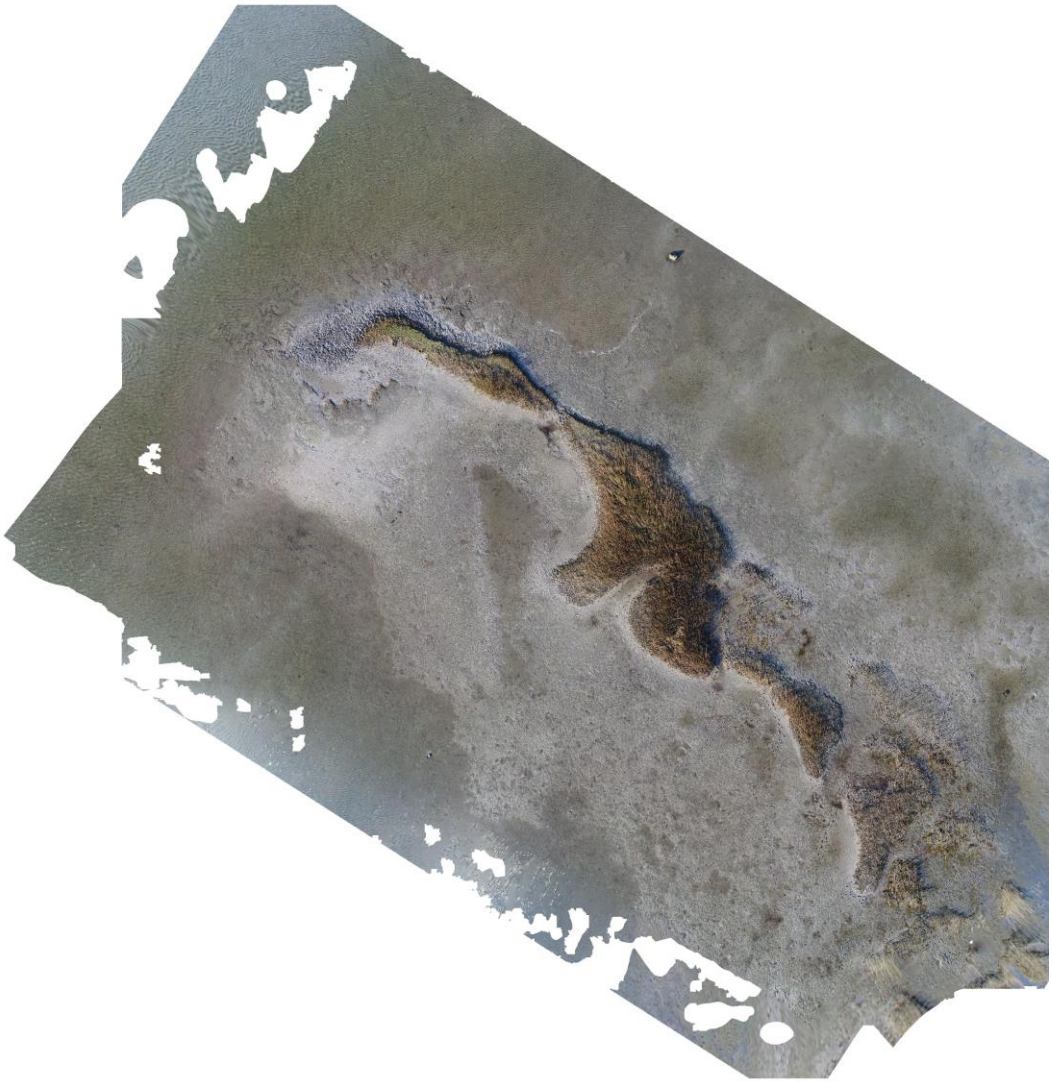

Figure B4-2 Sea Grass Lane S4 (December 2, 2019)

Figure B4-3 Sea Grass Lane S4 (March 6, 2020)

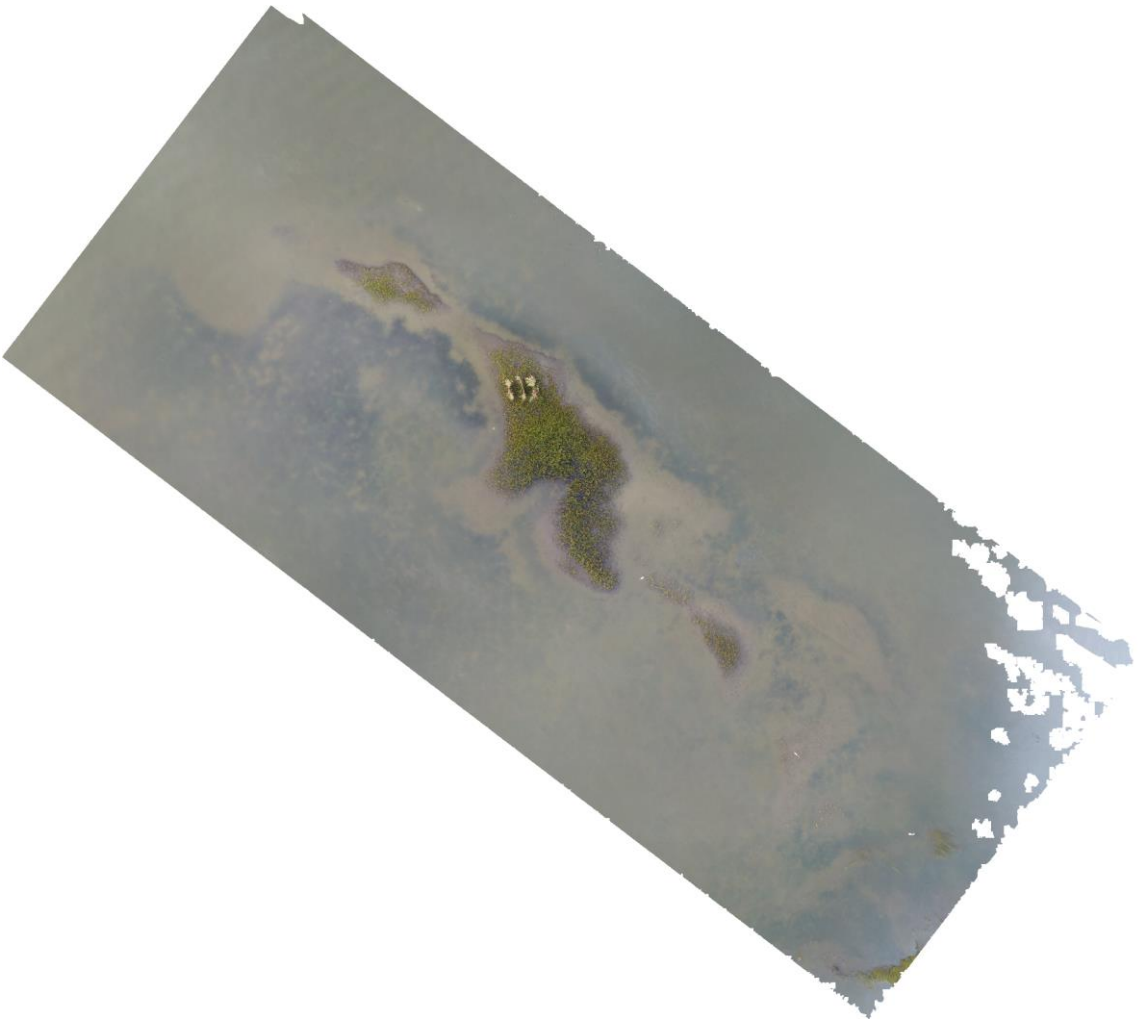

Figure B4-4 Sea Grass Lane S4 (September 12, 2020)

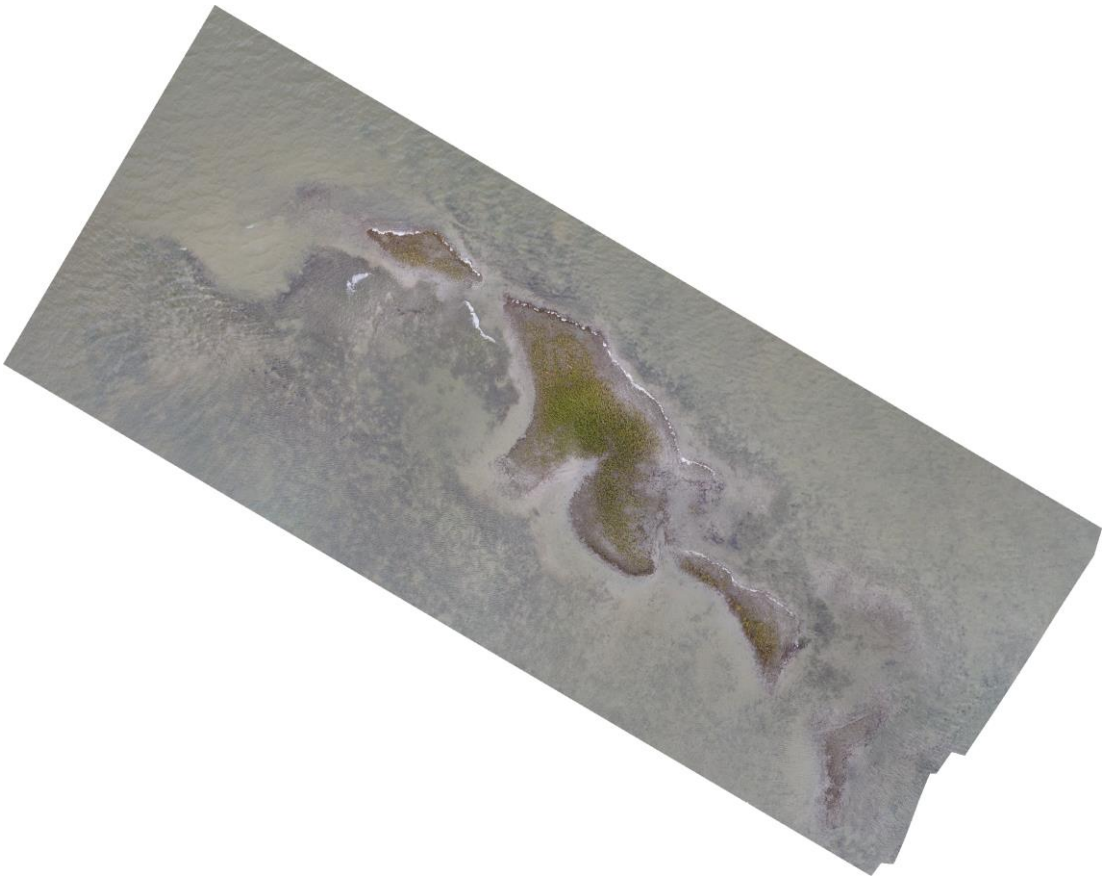

Figure B4-5 Sea Grass Lane S4 (October 30, 2020)

Figure B5-1 Sea Grass Lane S5 (November 1, 2019)

Figure B5-2 Sea Grass Lane S5 (December 2, 2019)

Figure B5-3 Sea Grass Lane S5 (March 6, 2020)

Figure B5-4 Sea Grass Lane S5 (September 12, 2020)

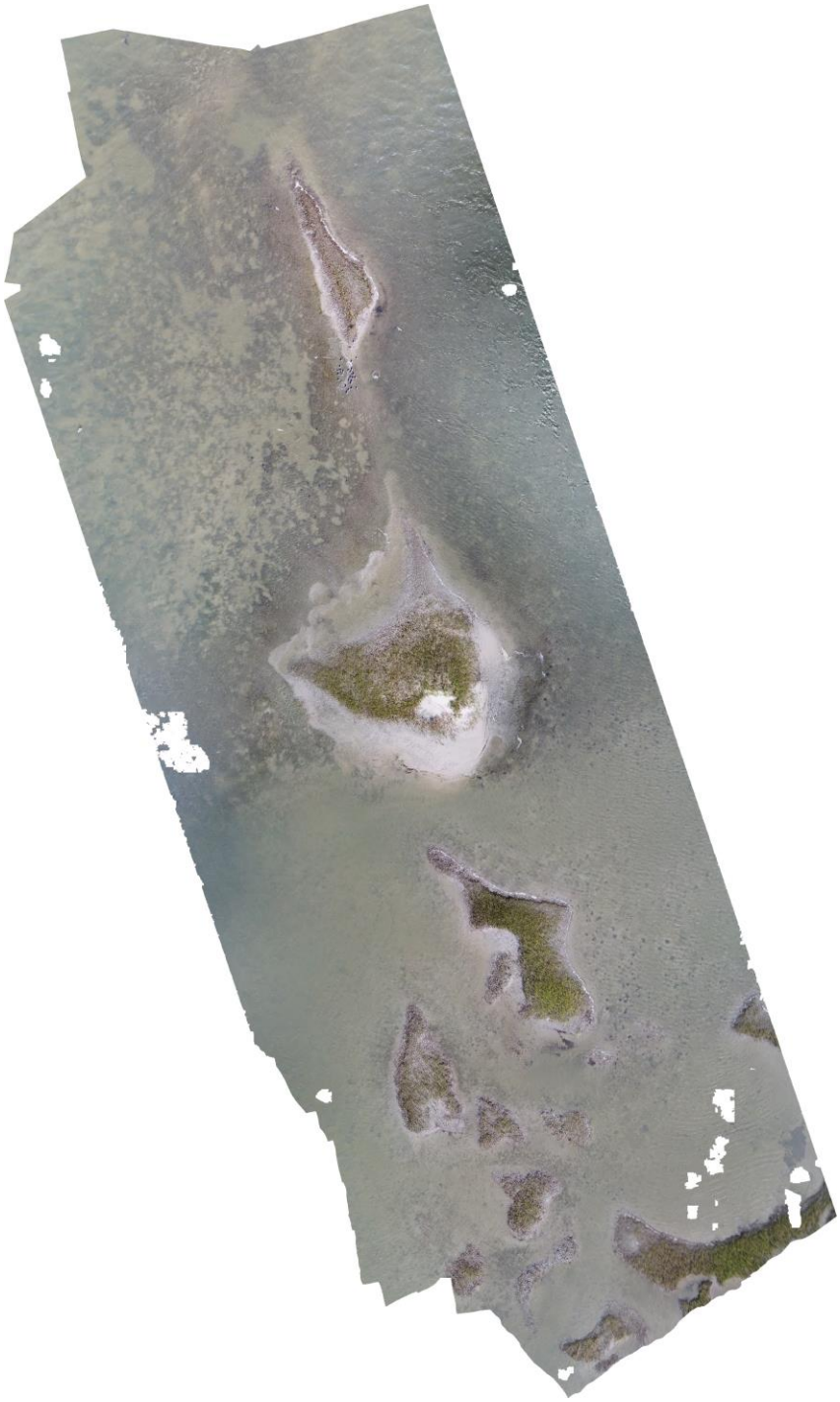

Figure B5-5 Sea Grass Lane S5 (October 30, 2020)

Figure B6-1 Bay Breeze B1 (March 6, 2020)

Figure B7-1 Bay Breeze B2 (March 6, 2020)

Figure B7-2 Bay Breeze B2 (August 25, 2020)

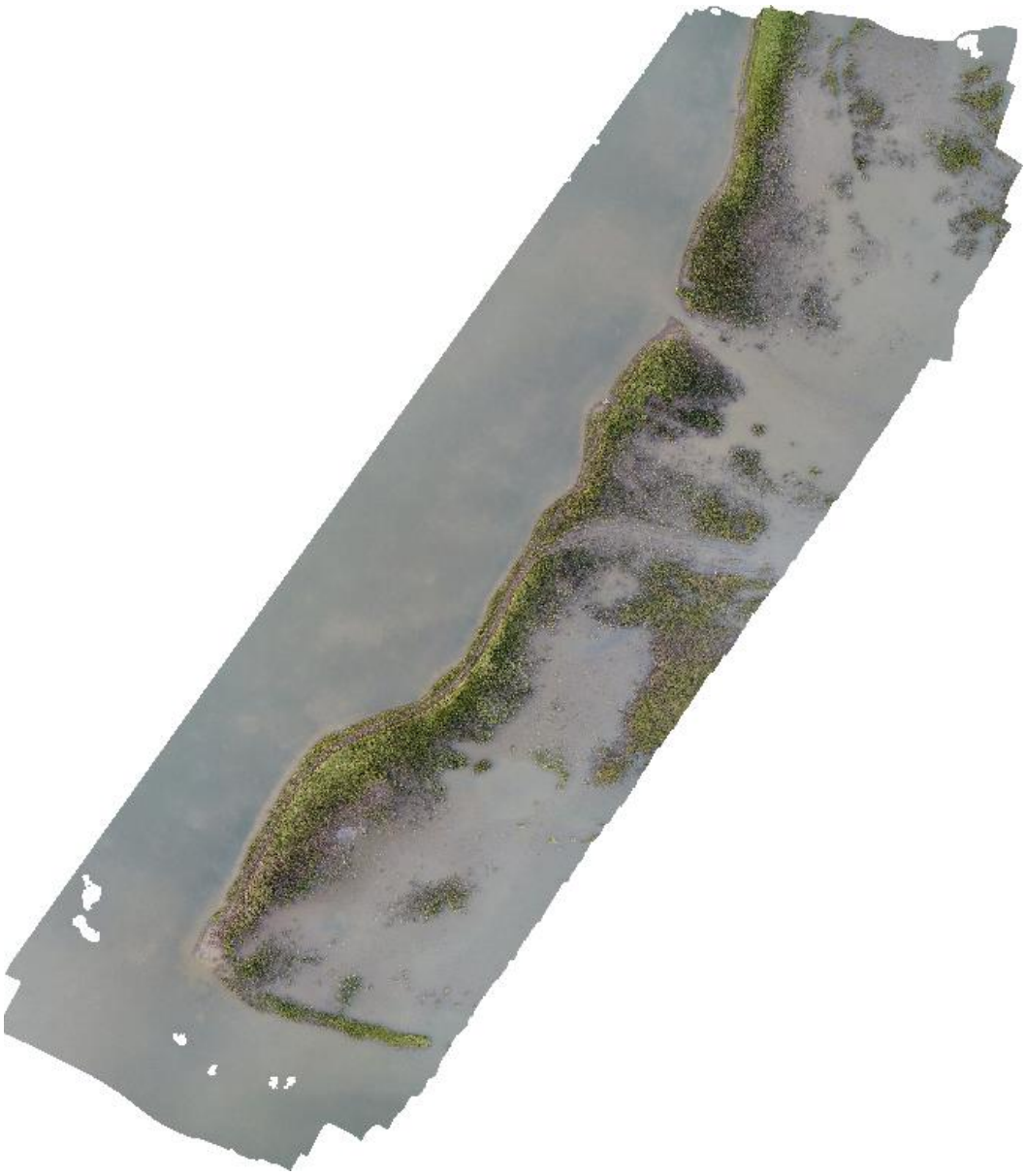

Figure B7-3 Bay Breeze B2 (September 12, 2020)

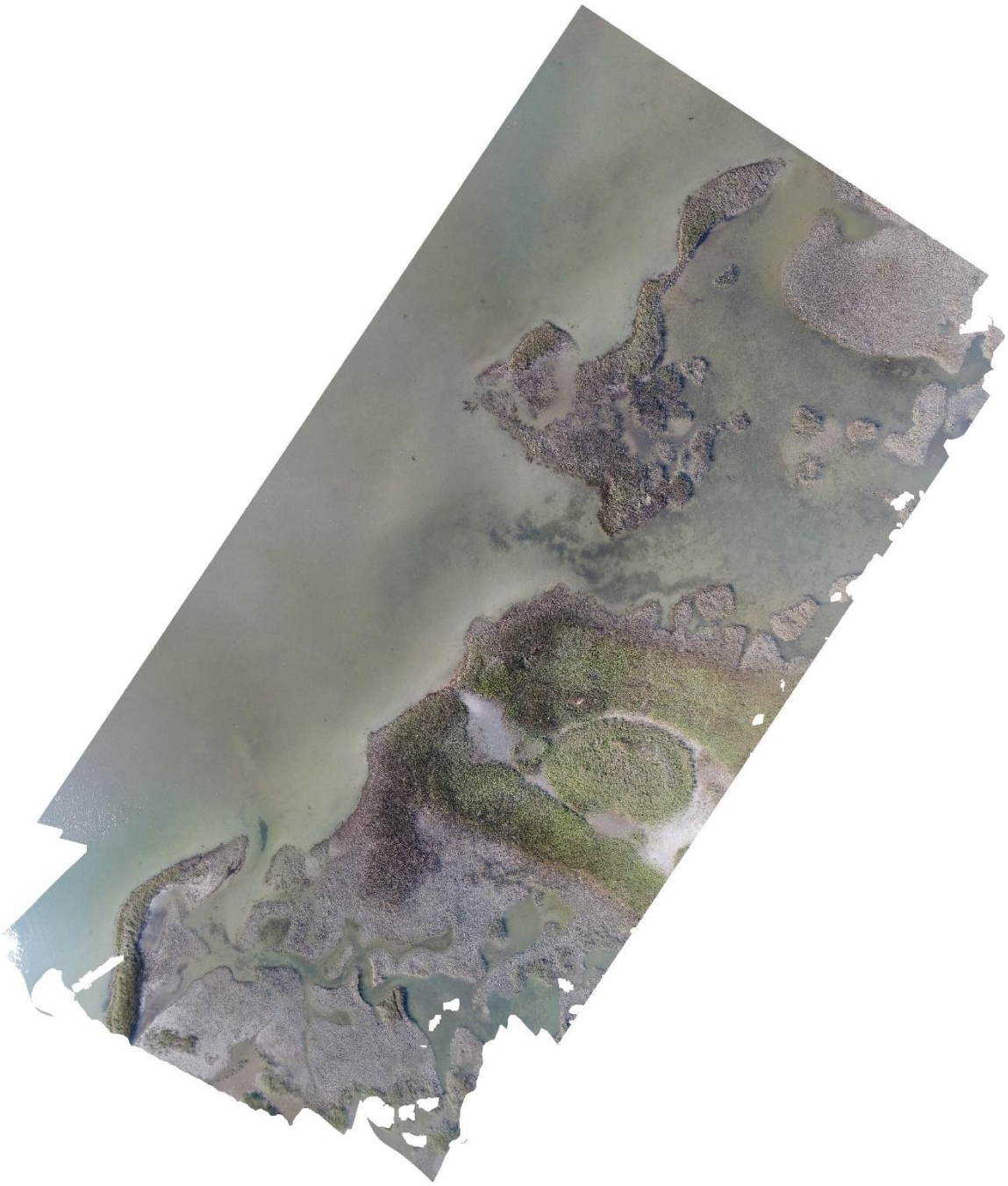

Figure B8-1 Bay Breeze B3 (March 6, 2020)

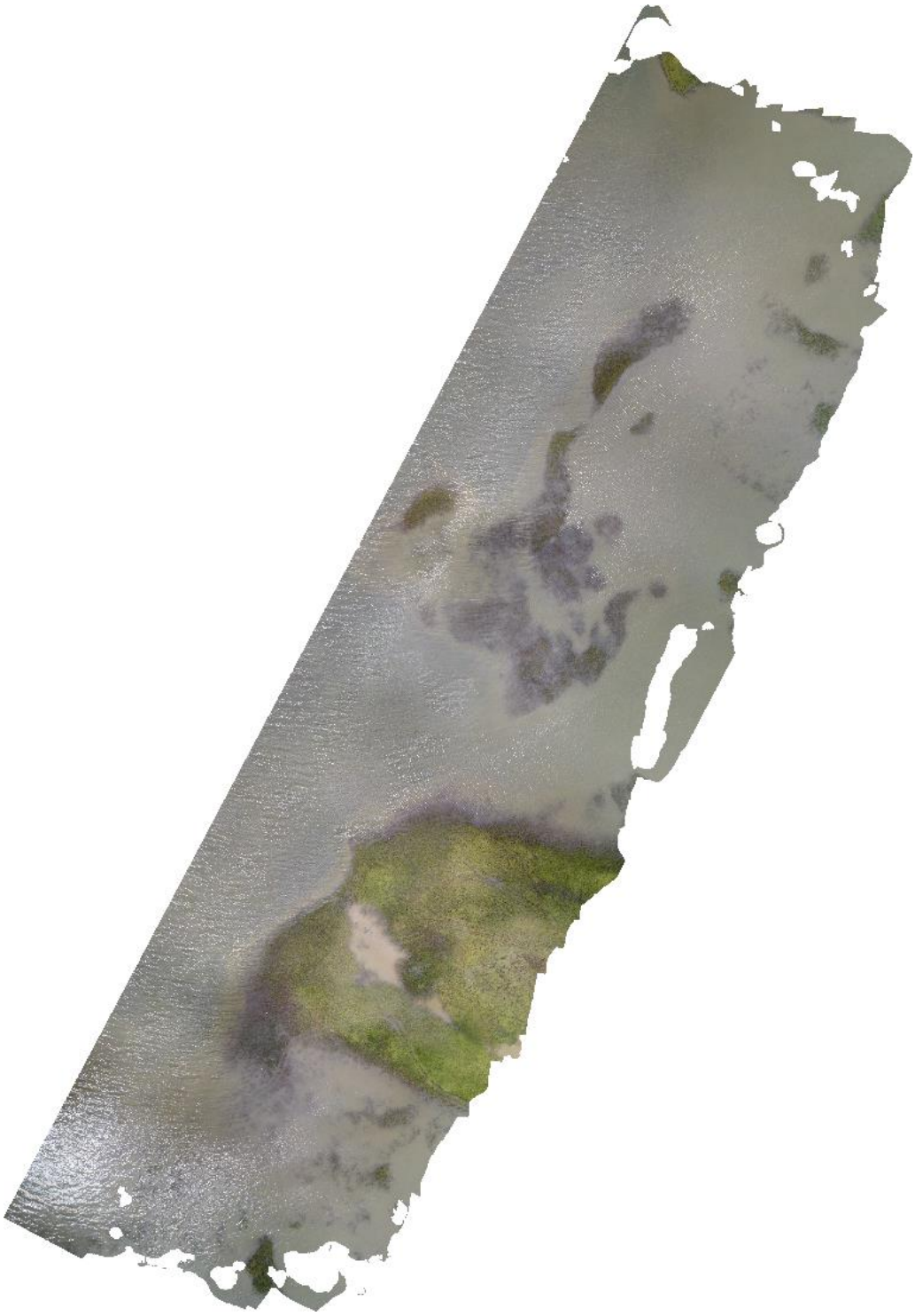

Figure B8-2 Bay Breeze B3 (August 25, 2020)

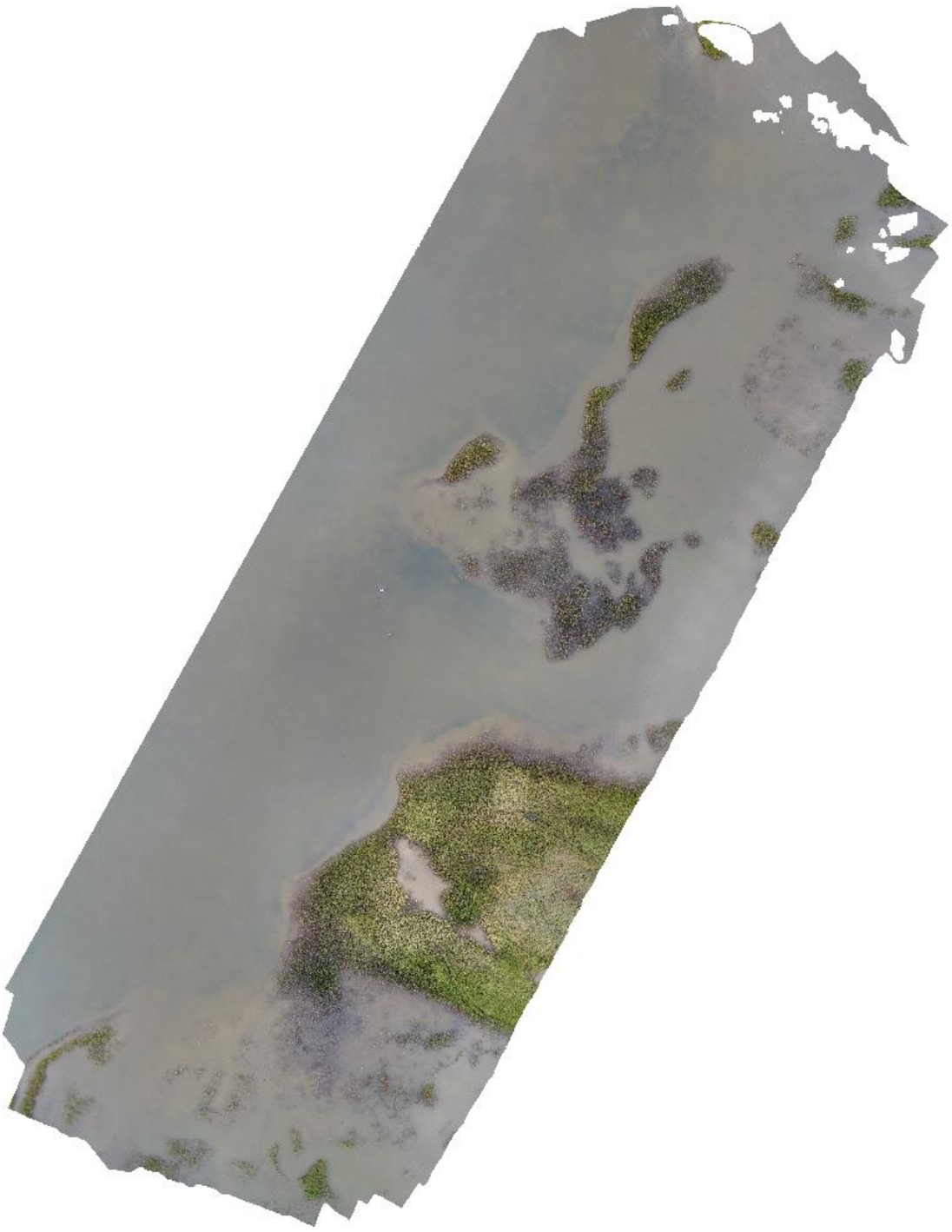

Figure B8-3 Bay Breeze B3 (September 12, 2020)